Radiation-induced Nanoparticle Formation as Novel Means of in Vivo / in Vitro Dosimetry

by

Karthik Subramaniam Pushpavanam

A Dissertation Presented in Partial Fulfillment
of the Requirements for the Degree
Doctor of Philosophy

Approved April 2019 by the
Graduate Supervisory Committee:

Kaushal Rege, Chair
Stephen Sapareto
Brent Nannenga
Matthew Green
Bin Mu

ARIZONA STATE UNIVERSITY

May 2019

ABSTRACT

Rapid development of new technology has significantly disrupted the way radiotherapy is planned and delivered. These processes involve delivering high radiation doses to the target tumor while minimizing dose to the surrounding healthy tissue. However, with rapid implementation of these new technologies, there is a need for the detection of prescribed ionizing radiation for radioprotection of the patient and quality assurance of the technique employed. Most available clinical sensors are subjected to various limitations including requirement of extensive training, loss of readout with sequential measurements, sensitivity to light and post-irradiation wait time prior to analysis. Considering these disadvantages, there is still a need for a sensor that can be fabricated with ease and still operate effectively in predicting the delivered radiation dose.

The dissertation discusses the development of a sensor that changes color upon exposure to therapeutic levels of ionizing radiation used during routine radiotherapy. The underlying principle behind the sensor is based on the formation of gold nanoparticles from its colorless precursor salt solution upon exposure to ionizing radiation. Exposure to ionizing radiation generates free radicals which reduce ionic gold to its zerovalent gold form which further nucleate and mature into nanoparticles. The generation of these nanoparticles render a change in color from colorless to a maroon/pink depending on the intensity of incident ionizing radiation. The shade and the intensity of the color developed is used to quantitatively and qualitatively predict the prescribed radiation dose.

The dissertation further describes the applicability of sensor to detect a wide range of ionizing radiation including high energy photons, protons, electrons and emissions from radioactive isotopes while remaining insensitive to non-ionizing radiation. The sensor was further augmented with a capability to differentiate regions that are irradiated and non-irradiated in two dimensions. The dissertation further describes the ability of the sensor to predict dose deposition in all three dimensions. The efficacy of the sensor to predict the prescribed dose delivered to canine patients undergoing radiotherapy was also demonstrated. All these taken together demonstrate the potential of this technology to be translatable to the clinic to ensure patient safety during routine radiotherapy.

ACKNOWLEDGMENTS

I would like to start by thanking my mentor Dr. Kaushal Rege, for all the support and guidance he has given me during my time at Arizona State University. I know that his advice has been a crucial part of my success for which I am truly grateful.

I would also like to give a very special thanks to Dr. Stephen Sapareto, Dr. Brent Nannenga, Dr. Matthew Green and Dr. Bin Mu for their willingness to work on my committee. I am grateful to Dr. David Taylor, Dr. James Ramos, Dr. Matthew Christensen, Dr. Sai Pavan Gandhi, Candace Rae Walker, Beatrice Tamakloe, Dr. Thrimoorthy Potta, Dr. Jacob Elmer, Dr. Bhavani Miryala, Dr. Sudhakar Godeshala, Dr. Sheba Goklany, Russell Urie, Rajeshwar Nitiyanandan, Subhadeep Dutta, Inam Ridha, Deepanjan Ghosh, Amar Thaker, Sanjitarani Santra, Brian Thompson and Bohan Shan with whom I have had the pleasure of working with. I would like to acknowledge the excellent students that I have had the pleasure of working with during my research including Caesario Sutiyoso, Eshwaran Narayanan and Sahil Inamdar.

I would like to give a very special thanks to the physicists and clinicians at Banner-MD Anderson Cancer Center for their continued support of the research and guiding me all the way. These individuals include Tomasz Bista, Thaddeus Sokolowski, Chelsea Page, Alek Rapchak and Dr. John Chang. I would like to thank Dr. Eric Boshoven for working with us and facilitating the canine studies conducted as part of the research.

Lastly, I am truly grateful to my family for their continued support and encouragement during my stay at Arizona State University.

TABLE OF CONTENTS

Page

LIST OF TABLES

Table Page

LIST OF FIGURES

Figure Page

Figure Page

Figure Page

Figure Page

Figure Page

Figure Page

Figure Page

Figure Page

Figure Page

Figure Page

Figure Page

Figure Page

Figure Page

Figure Page

Figure Page

Figure Page

Figure Page

Chapter 1 INTRODUCTION

Radiation therapy or Radiotherapy (RT), using ionizing radiation (X-rays and gamma rays), is a first line of treatment for several types of cancer diseases, although protons and low atomic weight ions are also used (Hardon therapy).[1] External-beam radiotherapy (EBRT) is commonly employed in the clinic, although other methods including brachytherapy, intra-operatory radiation therapy (IORT) and metabolic radiation therapy are also used.[1] The cumulative dose delivered depends on the type of cancer and often ranges between 20 and 70 Gy (1 Gy = 1 Joule of radiation energy absorbed / kg of matter). In conventional procedures, the cumulative dose is delivered over several fractions with a typical dose close to 2 Gy. The entire treatment lasts several weeks, with up to five fractions delivered every week. Several variations of fractionated radiotherapy have been explored in order to maximize the efficiency of treatment and facilitate patient tolerance. A dose range of 0.5-1.8 Gy is employed in hyperfractionated radiotherapy[2, 3]. In hypofractionated radiotherapy, doses ranging from 3-10 Gy, which are higher than the conventional 2 Gy dose, are delivered[4]. This has been made possible by advanced methods including volumetric-modulated arc therapy (VMAT). In addition, stereotactic RT, which is a kind of EBRT, has been employed in conjunction with imaging to deliver higher radiation doses, between 6 and 25 Gy[1], specifically to well-defined small tumors in a single treatment or smaller number of fractions.[5]

Although radiotherapy possesses several advantages for cancer treatment, radiation-induced toxicity and tissue damage are causes for concern. For example, radiation-induced

fatigue, skin problems, proctitis[6], esophagitis[7], osteonecrosis[8] and other complications have been reported. Clinical cases of accidental overdose[9] and inaccurate dosing[10] due to errors in machine calibration have been reported. In addition, cases of overdose due to error have also been known to occur[11]. These issues highlight the importance of appropriately dosing cancerous tumors so as to avert any adverse effects of radiation-induced toxicity.

Several technologies have been investigated for monitoring and quantifying ionizing radiation in order to potentially facilitate accurate dosing in patients. For example, small ionization chambers, silicon diodes, metal-oxide semiconductor field effect transistors (MOSFETs), thermo-luminescent dosimeters (TLDs), optically stimulated luminescence dosimeters (OSLDs), diamonds and films are used for radiation dose determination. Existing dosimeters can be classified into non-implantable devices for in vivo measurements and implantable devices for measurements inside the target in the body. Non-implantable systems find application in procedures using standard fractions of ≈2 Gy per session of fractionated radiotherapy. Diodes, TLDs, films and some MOSFETs are the most commonly used non-implantable systems, and are often used for entry dose measurement. On the other hand, implantable dosimeters are introduced into the body via natural cavities or less commonly, directly into target tissues[12]; the reader is referred to other excellent papers on this for a more detailed discussion[1]. Most of these devices require electrical or optical connections for readout and are often cumbersome to use. Even in case of optical fibers, there is a need to shield optical connections as a result of the Cherenkov light produced[13]. In light of the above limitations, there is an urgent need to develop simple yet robust systems that can address existing challenges with radiation sensing and

dosimetry for clinical applications. Here, we review the latest developments in molecular and nanoscale systems for sensing ionizing radiation, with a particular focus on use in cancer radiotherapy applications. To our knowledge, this is the first comprehensive review on molecular and nanoscale dosimeters for application in clinical radiotherapy.

1.1 Molecular Systems

1.1.1 Small Molecule Systems

Emission of light from fluorescent molecules depends on the chemistry of the molecules and their local environment.[14]. Radio-fluorogenic co-polymerization is a process in which a non-fluorescent active monomer is incorporated into a growing polymer chain resulting in fluorescence of the long chain. The polymerization itself is triggered by the free radicals generated upon irradiation with ionizing radiation. Warman et al. described a two-component monomer system which includes an acrylate-based supporting molecule and a functional non-fluorescent active molecule, *N*-(1-pyrenyl)maleimide (MPy), for radiation sensing.[15] The supporting non-fluorescent medium (methyl methacrylate/tertiary-butyl acrylate) polymerizes, incorporating the active molecule MPy into the growing polymer chain, in turn making it fluorescent.[16] This incorporation of the active molecule in the polymer chain prevents diffusion and can render information on the spatial distribution of the dose. Limited diffusion of the active probe reduces false positives post-irradiation which can help define complex radiation profiles delivered. This approach of radio-fluorogenic co-polymerization (RFCP) has been shown to be applicable to a wide range of

ionizing radiation sources including ^{192}Ir radioisotope, cobalt gamma ray source, electron beam and proton beams.[17-20] The fluorescence signal reached a steady state after three minutes and was reported to be stable for at least three hours. However, approximately 60 % loss in signal was seen after a period of 28 days. This loss was attributed to the diffusion of air into the dosimeter, which was responsible for quenching the pyrene fluorescence; diffusion of the fluorescent product out of the irradiated region was not deemed to be a cause for this loss.[20] Even though RFCP-based dosimeters measure doses as low 2 Gy, the need to carefully handle toxic and flammable acrylates can be a limitation of these systems. In addition, it is difficult to obtain real time information, which may limit the ultimate application of such systems during routine radiotherapy.[20]

Benevides et al. used the principle of degradation of fluorescent molecules as a "turn-off" sensor for detecting radiation. Briefly, rhodamine 6G and fluorescein dyes were embedded in water-containing agarose hydrogels.[21] Upon irradiation, water molecules release free radicals which have oxidizing and reducing properties.[22] Upon reaction with free radicals, the dyes lose their fluorescence properties and act as an indicator of applied radiation dose[21]. Radiolytic species generated in water have short lifespans, which decreases the probability of interaction between the free radical and the fluorophore. To achieve enhanced sensitivities, the lifetime of radiolytic species was increased by the addition of NaCl. Cl^{2-} radicals generated through high energy irradiation have longer life times which led to the detection of radiation doses between 40 and 200 Gy with a resolution of 20 Gy.[21] Han et al. improved upon these fluorescence systems by developing a sensor that can detect radiation levels down to 0.01 Gy by using 4,4′-di(1H-phenanthro[9,10-d]imidazol-2-

yl)biphenyl (DPI-BP).[23] This detection capability can be relevant in a clinical setting in order to accurately target cancerous tumors with γ-radiation during therapy. DPI-BP, when solubilized in either chloroform or dichloromethane, demonstrated a strong fluorescence signal; iodinated and brominated solvents were not useful since DPI-BP did not fluoresce in them. These chlorine-based solvents result in the formation of HCl upon irradiation with ionizing radiation. This, in turn, is thought to enhance aggregation of DPI-BP due to intermolecular π–π stacking, leading to detectable quenching of the original fluorescence signal. This signal decay was used as a measure of radiation dose. A 5 % decrease in the emission of DPI-BP was seen for a radiation dose as small as 0.1 Gy and complete quenching was observed at a dose of 3 Gy. The strong quenching indicates the capability of the system for sensing low doses of ionizing radiation. Additionally, the original signal could be recovered by the addition of a strong base like NaOH which deprotonates HCl. In order to verify the need of HCl, other solvents including DMF, DMSO, THF and toluene were used without detectable changes in fluorescence even at a dose of 100 Gy. Further investigations may be necessary to determine the toxicity of these molecules for in vivo settings, particularly given the need for chlorinated solvents and formation of HCl.

A novel fluorescence technique that is based on aggregation-induced fluorescence emission of silole compounds was recently developed for the detection of gamma ray radiation.[24] In this system, the silole compound, containing a positively charged ammonium group, shows minimal emission in aqueous solutions. The solution however becomes strongly emissive upon mixing with either polymers or amphiphilic molecules that contain negatively charged moieties, which can induce the aggregation of the silole.

In one version, the silole molecule was mixed with a polyelectrolyte containing sulfone groups (−SO_2−) in the main chain and −COONa groups in the side chain. Upon exposure to gamma ray radiation, the polymer degrades by the release of SO_2 due to the relative weakness of C−S bonds in the main chain. The electrostatic and hydrophobic interactions between silole and polymer in turn weaken, inhibiting the aggregation of the silole compound. As a result, the solution containing the silole compound and polymer is weakly emissive after gamma-ray exposure. The decrease in intensity is used as a measure of radiation dose. The fluorescent complex did not lose its intensity for up to two days. In this case, a minimum dose of 130 Gy was needed for the sensor to work effectively. A "turn-on" fluorescence sensor was subsequently developed by the same group due to the relatively high radiation dose required to observe a detectable change in the previous version.[25] The synthesized molecular sensor consists of a 3,3′-dimethyl-3H-indole functional group on a tetraphenylethylene derivative dissolved in halogenated solvents including $CHCl_3$ or CH_2Cl_2. This system is weakly emissive in chloroform and dichloromethane. Following irradiation with gamma rays, these solvents produce HCl, which results in protonation of the molecular sensor. This protonated molecule demonstrates poor solubility in the solvents used, which results in its aggregation and a concomitant increase in fluorescence ("turn-on"). The limit of detection of this system was shown to be as low 0.023 Gy. A different molecular sensor with a dual-band emissive response was developed by dissolving 4-(1*H*-phenanthro[9,10-*d*]imidazol-2-yl)-*N*,*N*-diphenylaniline (PI-DPA) in chloroform.[26] PI-DPA tends to self-assemble into fibers upon interaction with HCl that is generated upon irradiation. Formation of these fibers quenches the existing fluorescence intensity and brings about a new fluorescence band at a longer

wavelength. These two signals, along with the photoconductive property of the nanofibers, were predicted to assist in developing a multimodal sensor in the detection of ionizing radiation. The sensor was projected to detect radiation doses as low as 0.006 Gy. These stimuli-responsive small molecules could potentially be applied for routine ex vivo (skin) radiotherapy due to their sensitivity and fast response. However, potential toxicity issues of these small-molecule sensors as well as the solvent will have to be determined prior to in vivo dosimetry.

1.1.2 Polymer-Based Systems

Most polymer systems used for the purpose of radiation sensing are based on the principle of modification of the polymer structure / chain length either through cross-linking or by scission of the backbone by ionizing radiation[27]. This, in turn, results in changes in the physicochemical properties (e.g. color changes or change in electrical conductivity) of the polymer used[28]. Initial studies on polymer thin films were based on poly(p-phenylene vinylene)[28]; changes in electrical conductivity, optical density and photoluminescence were observed upon exposure to X-ray irradiation. However, these changes in polymer properties were typically observed at high radiation doses (>1 kGy), which necessitated the need for polymer-based systems that were responsive to lower radiation doses. Poly (2-methoxy-5-(2′-ethyl-hexyloxy)-1,4-phenylene vinylene) (MEH-PPV) is one of the most widely studied polymer systems for detecting lower doses of ionizing radiation[29]. Two sets of formulations, MEH-PPV dissolved in chloroform and spin-coated MEH-PPV on a glass substrate as a thin film, were investigated. Upon gamma irradiation using a 1.25 MeV ^{60}Co source, MEH-PPV in chloroform showed significant spectral shifts at 38 Gy, while MEH-

PPV films were insensitive to doses as high as 114 Gy. The enhanced response could be attributed to the release of ·Cl radicals in solution which degrade the polymer leading to a loss of conjugation. Further investigation into free radical-based polymer degradation was carried out using Fukui indices. [30] The ·Cl radicals attack the vinyl bonds in the polymer backbone leading to chain scission and eventual loss of electronic conjugation. The effect of different halogenated solvents and their role in degradation of MEH-PPV was also investigated.[31] At doses as low as 1 Gy, the polymer, dissolved in bromoform and diiodomethane/dichloromethane, showed blue shifts in absorbance spectra compared to the 0 Gy condition. Significant shifts were obtained when the solvent contained higher amounts of halogen atoms. Studies with the polymer dissolved in toluene solvent showed no significant response at 30 Gy, which indicated the need for halogenated solvents in this system. Lower concentrations of the polymer were deemed to enhance the sensitivity of the dosimeter. This could be explained by the fact that at lower concentrations, the polymer is better solvated increasing the probability of reaction between the free radical and the polymer backbone. However, at higher concentrations, polymer aggregation can hinder the reaction between the radicals and the polymer, which lowers the efficacy of the detection performance. In addition to gamma radiation MEH-PPV also was shown to be responsive to a proton flux of 10^{13} ions cm^{-2} irradiation which can make this a versatile system for radiation sensing.[32] As with previous systems, biocompatibility of the polymers, solvents, and by-products of the sensing reaction will need to be elucidated before considering translation to human applications.

High Z (atomic number) elements are known to enhance the sensitivity to lower radiation doses. [33, 34] Based on this background, composites containing inorganic compounds within polymer hosts were studied for gamma scintillation. Upon irradiation, the high Z material attenuates high-energy photons resulting in the formation of an electron-hole pair. These pairs are transferred to the polymers where radiative decay occurs.[35] A luminescent polymer P-PPV and high Z materials including 1,3-diiodobenzene (DIB) and BiI_3 were blended together with a solid polymer matrix consisting of poly(trimethylolpropane trimethylacrylate) (TMPTMA).[35] The scintillation lifetimes of the nanocomposites were comparable to commonly employed scintillants $LaCl_3$ and $LaBr_3$ [36] even though the scintillation efficiencies were found to be lower with the current formulation. A similar nanocomposite for detecting radiation using fluorescence resonance energy transfer (FRET)[37] was developed. Poly[9-hexyl-9-(20-ethylhexyl)-fluorene] (HEH-PF), a blue light-emitting polymer, was mixed with red light emitting polymer DCM (4-(dicyanomethylene)-2-methyl-6-(p-dimethylaminostyryl)-4H-pyran). DIB was added to this mixture in order to enhance radiation absorption efficiency; the mixture was subsequently formulated into a thin film. This ternary composite showed radiation sensitivity for doses lower than 50 Gy based on photoluminescence readout.

An unavoidable effect of photon beam radiotherapy is the potential scattering of the dose outside the treatment beam.[38] These scattered doses of magnitudes lower than 1 Gy can induce unintended secondary effects in patients[39]. However, MEH-PPV based dosimeters do not typically respond to doses lower than 1 Gy[40]. Detection limits were improved by using an organometallic polymer 1,1'-bis(ethynyl)-4,4'–biphenyl (DEBP) with a platinum

metal center as a potential radiation dosimeter[41]. Pt-DEBP dissolved in chloroform was used further for dosimetry studies. Structural changes in Pt-DEBP arise due to Cl· free radical attack on the triple bond on the polymer chain and increase in molecular weight due to recombination of the oligomeric fragments[42]. A concomitant change in the absorbance spectra is detected above 1 Gy as a result of structural modification on the polymer. The polymer system displayed fluorescence properties due to its conjugated nature and $\pi \rightarrow \pi^*$ absorption[41]. The presence of a transition metal (Pt) renders unique structural, optical and electronic properties to the polymer. An importance feature is the presence of a delocalized π-conjugated electron cloud which extends and reaches the metal center from the polymeric backbone[40]. Chlorine incorporation reduces the spin density on Pt, thereby increasing the output fluorescence signal. This system, which uses the photoluminescence emission ratio at 420 nm and 398 nm, could detect doses between 0.1-1 Gy.

1.1.3 Single-Crystal Systems

Dielectric and wide-band gap semiconductor materials have been traditionally employed as scintillator materials[43] and in radiation detection [44]. Thermalized electrons and holes are generated in the scintillator lattice upon irradiation with a high-energy photon beam. Recombination of these electron-hole pairs lead to luminescence which is converted into an electrical signal through a photodetector.[43] The use of room-temperature synthesis protocols has made organic molecules attractive alternatives to inorganic scintillators[45]. Organic semiconducting single crystals (OSSCs) including 4-hydroxycyanobenzene (4HCB) and 1,8-naphthaleneimide (NTI) demonstrate tissue equivalent properties, and are attractive as direct X ray detectors[46]. These crystals, along with organic polymers (PDMS,

poly(dimethylsiloxane) and PEDOT:PSS, poly(ethylenedioxythiophene):poly(styrenesulfonate)) as substrates, were able to convert incoming 35 kV photons from an X-ray source directly to an electrical signal. The longevity of 4HCB crystals was investigated by (1) irradiation to a total dose of 2.1 kGy and (2) aging for a month. The electrical response of the sensor was reliable despite this significant strain. Anisotropic crystals of 4HCB require alignment of the crystal and electrode in order to manipulate charge carrier transport properties. However, 1D crystals are of practical interest because they possess only one single crystallographic direction that can be electrically accessed. Needle-shaped crystals (1D) of 1,5-dinitronaphthalene (DNN) were studied for their electrical response under irradiation.[45] Rubrene crystals were used based on the hypothesis that charge mobility might affect the sensitivity of the crystals to X-ray irradiation [47]; charge mobility of rubrene crystals is higher than that of DNN crystals by approximately two orders of magnitude. However, rubrene crystals showed lower sensitivities and slower response times for detecting ionizing radiation compared to DNN[47]. DNN could detect doses as low as 20 mGy s^{-1} while rubrene had to be irradiated with 120 mGy s^{-1} in order to achieve a similar electrical output. This demonstrated that the higher charge mobility might not be sufficient to achieve enhanced performance for radiation detection.

With flexible devices and wearable technology drawing a lot of attention, a wearable flexible detector with poly (ethylene terephthalate) (PET) as substrate and 4HCB crystals as the active ingredient was fabricated.[48] Repeated bending did not seem to affect the electrical performance of the device making them feasible for active-wear radiation

detectors. A minimum dose of 50 μGy s^{-1} was able to trigger detection. The sensitivity of the above flexible device is comparable to an existing amorphous selenium detector. Such flexible detectors could be useful in routine entry and exit dose measurements during radiotherapy.

1.2 Nanoparticle Systems

1.2.1 Quantum Dot (QD) Systems

Quantum dots are semiconductor nanoparticles (1–100 nm and demonstrate strong light absorption and luminescence properties).[49] The electronic and optical characteristics of quantum dots are determined by their size and shape; larger sized dots are known to emit longer wavelengths while smaller dots emit shorter wavelengths. Quantum dots based on CdSe/ZnS have been investigated as neutron detectors.[50] However, commercially available inorganic compounds possess low solubilities in organic and polymeric matrices, which can limit their use. Their preparation in inorganic matrices, including sol-gels, results in the formation of non-transparent materials, which can lower their efficiency as scintillating devices. Colloidal quantum dots (cQDs), which are dispersible in aqueous media, were subsequently mixed with lithiated gels to form a transparent QD gel composite and tested with a Po-210 alpha source. The scintillation pulse detected upon comparison with background radiation signal showed a performance similar to existing inorganic scintillators. Withers et al. reported the effect of ^{137}Cs gamma irradiation on photoluminescence properties of CdSe/ZnS colloidal quantum dots.[51, 52] Upon gamma

irradiation using 1.17 and 1.33 MeV energy photon beams, a decrease in fluorescence of the composite was observed at a dose as low as 0.1 Gy. At higher doses (10 Gy) the fluorescence intensity is halved with respect to the 0 Gy control sample. Based on this, the authors proposed that cQDs could be used as sensors to report for cumulative radiation doses. Colloidal quantum dots were subjected to a cumulative dose of 140 krad (1.4 kGy) using a 0.662 MeV beam; it was found that 50 % of the original optical output was lost after an exposure of 11.5 krad (115 Gy). The dose at which cQDs lost their signal was significantly higher than conventional NaI:Tl scintillator crystals, which lose their light output after an exposure to 5 Gy. Hypothetically, radiation hardness of cQDs can make them versatile for longer-term use in clinical applications without having to replace the dosimeter after every treatment. Using hexane as the solvent for cQD synthesis resulted in aggregation during prolonged storage.[52] Water-dispersible CdSe-CdS-$Cd_{0.5}Zn_{0.5}S$-ZnS core-shell colloidal quantum dots were therefore developed in order to potentially eliminate limitations with other cQD systems.[53] A linear emission behavior with radiation was observed between 0.05–3 Gy, making this system a potential candidate for detecting doses used in fractionated radiotherapy.

Colloidal quantum dots can suffer from irreversible aggregation leading to loss in fluorescence properties[54]. In order to overcome this challenge, cQDs were cast in a polymer matrix and the resulting composites were used as scintillators. Dispersion in a polymeric matrix also serves the purpose of maintaining the efficiency of cQDs while potentially lowering the costs of synthesis by using lower amounts of the inorganic scintillator[55]. A dosimeter in which CdSe/ZnS QDs were impregnated in a porous glass matrix was

fabricated; etching with hydrofluoric acid resulted in in an increase in pore size of the matrix. In addition to being sturdy and transparent, the matrix contained cavities to hold guest molecules that were also kept apart in order to prevent self-quenching[56]. Scintillation output of the nanocomposite was compared to that of rhodamine B laser dye under alpha irradiation ($^{243\text{-}244}$Cm as radiation source). Colloidal QDs were able to convert the incoming alpha radiation ($^{243\text{-}244}$Cm) to visible photons, but their scintillation output was lower than that seen with conventional rhodamine B laser dye. The output variation between the two systems was attributed to the photon transport efficiency described by their Stokes shift; the laser dye has an inherent Stokes shift while cQDs do not exhibit such a phenomenon[57]. Thus, engineering the Stokes shift in quantum dots can likely lead to more sensitive dosimeters. Radiotherapy involves photon beams with various energies ranging from keV to MeV. This warrants the development of dosimeters that can function at both ends of the energy spectrum[58]. The above cQD nanocomposites demonstrated an improvement in energy resolution by a factor of 2 when compared to standard NaI crystal (irradiation with a 59 keV Americium or ^{241}Am source) [56].

Size effects of CdSe/ZnS quantum dots were studied using a 1 MeV gamma radiation source[59]. Colloidal quantum dots (3.3 nm) showed a degradation of up to 30 % in original fluorescence emission, while larger particles showed complete recovery of their original emission properties 24 h after exposure to 5 Gy dose.[60] In a system developed by Crone and coworkers, CdSe-ZnSe cQDs were dispersed in an organic scintillator (poly[2-methoxy-5-(2′-ethylhexyloxy)-*p*-phenylene vinylene][61] Ionizing radiation generates excitations in the cQDs and these excitations are transferred to the organic host by FRET.

Cathode luminescence (CL) experiments were carried out on a composite spin-coated on gold-coated sapphire substrates in order to probe scintillation performance. At a volume fraction of 0.15, the cQD showed twice the CL intensity compared to pure MEH-PPV. Interestingly, further increase to 0.21 volume fraction led to a significant decrease in CL intensity. Aggregation of the cQDs at higher volume fractions can lead to an increase in non-radiative recombination and poor performance of the sensor, which indicates the need for uniform dispersion of cQDs in the matrix.

In addition to CdSe quantum dots, CdTe QDs have also been investigated for x-ray scintillation and imaging[62]. A lower cost reusable detector was recently developed by Gaur *et.al* in which CdTe/CdS quantum dots were impregnated within porous silica[63]. The high surface area of the silica allows for larger entrapment of the colloidal particles. Upon irradiation, the QDs are oxidized and lose their emission intensity. X-ray radiation doses as high as 1 Mrad (10 kGy) were required to decrease the peak emission intensity by half. The nanoparticles show a near-complete recovery of peak intensity when treated with a thiol-rich solution for 25 min post X-ray irradiation, while partial recovery was observed post γ-irradiation, indicating differential mechanisms by which the quantum dots interact with radiation of different energies.

Detailed studies on the mechanisms behind radiation-induced scintillation, and energy/dose rate dependency will be necessary to investigate the potential use of QDs in clinical radiation dosimetry. The relatively high cost associated with the use of such

systems and toxicity of quantum dots may also limit their use as implantable dosimeters in vivo. [64]

1.2.2 Plasmonic Nanoparticles

Surface plasmon resonance (SPR) properties of plasmonic nanoparticles including gold and silver nanoparticles, have made them attractive in a number of biomedical applications [65-67]. Nanoparticles ranging in size from 1 to 100 nm have been found to preferentially accumulate at the tumor site and are widely employed as imaging agents in oncology [67]. Very recently Dou et al demonstrated that optimally sized gold nanoparticles enhances real-time CT imaging and radiotherapy[68]. Oscillating surface plasmons in these nanoparticles can enhance surface-enhanced Raman scattering (SERS), resulting in increased efficiencies for chemical and biological sensing[69]. Alanine powder and alanine blended with polymeric binders have been investigated as dosimeters for ionizing radiation[70], which induces the formation of stable free radicals in the amino acid. These free radicals are detected using electron spin resonance (ESR)[71]. The intensity of the ESR signal is proportional to the amount of free radicals generated, and this measure is used as a reporter for radiation dose [70, 72]. Such systems are widely used in biological dosimetry applications and also serve as a reference system for other commercial dosimeters[73]. However, alanine dosimeters typically demonstrate reduced sensitivities when beam energies of the order of keV are employed. The sensitivity of alanine systems to X-rays can be enhanced by doping with high Z micro-scale materials[74]. Incorporating plasmonic nanoparticles within the matrix improved the dose enhancement factor, which is the ratio

between the mass absorption coefficient of the nanocomposite to that of pure alanine[75, 76]. Upon exposure to X-rays, metallic nanoparticles contribute to enhanced generation of free radicals within the alanine matrix[75]. Pre-synthesized silver nanoparticles were added to an aqueous solution of alanine before drying at 40^{o}C to yield nanocomposite powders[75]. These nanocomposites, when irradiated with a 90 keV beam, displayed enhanced peak-to-peak amplitude of the ESR spectra when compared with a pure alanine dosimeter. Interestingly, increasing the nanoparticle concentration from 0.01% Ag NPs to 1% Ag NPs decreased the DEF which could be attributed to particle agglomeration at higher concentrations. Similar responses were observed when gold nanoparticles were employed[76]. These nanocomposites exhibit homogeneity, nanoparticle size stability and improved sensitivity with a linear response between 1-50 Gy. However, ESR is a sophisticated detection method that requires trained professionals. This can be a limitation in translating this technology towards clinical radiotherapy.

1.2.3 Carbon Nanotubes

Carbon nanotubes (CNTs) were first investigated for detecting ionizing radiation as part of field effect transistors (FETs)[77]. Shifts in threshold voltage upon irradiation of these CNTFETs were used as a measure of ionizing irradiation. CNTFETs had similar dosimetry characteristics to already existing MOSFETs and showed longevity upon repeated exposure to radiation. Thickness of the silicon dioxide layer in the CNTFETs affects the sensitivity of the device, which is similar to that seen in conventional MOSFETs. A parallel plate ionization chamber using CNTs was developed in order to overcome this drawback [78]; the parallel plate orientation allows for the insertion of CNTs into the working chamber.

The sensor demonstrated a near linear response from 2 - 600 MU (1 MU = 1 cGy in water), when both 6 and 15 MV photon beams were employed.

A system using low density carbon fiber sheets sandwiched in between polymethylmethacrylate (PMMA) holders [79] was developed in order to potentially overcome attenuation of radiation dose by the sensor; copper electrodes were used as electrical contacts to complete the circuit. Absorption of ionizing radiation by the carbon fiber film generates electron pairs, which move in opposite directions under the influence of an initial current and reinforces the current. The change in current is used as an indirect measure of the radiation dose. A linear response between 100 and 600 MU (1–6 Gy) dose range indicates potential utility for dosimetry in fractionated radiotherapy.

SCNTs have also been shown to be responsive to proton irradiation[80]. Proton irradiation (10^{11} protons/cm^2) induces trapped charges in SiO_2 on which the CNTs are deposited. These charges in turn affect the resistivity of the CNTs which is used as a measure of radiation dose. A polymer composite containing multiwalled carbon nanotubes (MCNTs) was recently developed for detecting γ radiation[81]. Conductive MCNTs were dispersed in a non-conductive poly(olefin sulfone) matrix (**Figure 4**). Upon irradiation, the polymer network depolymerizes leading to a better contact between the MCNTs. This leads to enhanced electrical conductivity which is detected by amperometry. Doses as low as 50 Gy were detected using this method. An advantage of CNT based dosimeters for radiation sensing applications includes real time dose response unlike passive sensors (TLDs) which

have to be processed and analyzed. Subsequent generations of CNT devices may possess the versatility required for clinical dosimetry.

1.2.4 Metal Organic Frameworks

Metal organic frameworks (MOFs) are crystalline materials that contain metal clusters linked by coordinating organic groups; these organic groups are fluorescent and are often excellent scintillators. This imparts fluorescence properties to MOFs upon exposure to ionizing radiation, and the change in luminescence can be used as a measure of the radiation dose. Flexibility of synthesis and ability to modulate the scintillation properties make MOFs attractive materials for radiation dosimetry.

Several MOFs with zinc (Zn) have been evaluated for radioluminescence[82]. These MOFs were synthesized using solvothermal reaction of Zn^{II} metal ion and stilbene dicarboxylic acid ($SDCH_2$) in either *N*,*N*-dimethylformamide (DMF)/*N*,*N*-diethylformamide (DEF). The synthesized powdered MOFs were exposed to high-energy protons and alpha particles and characterized using ion-beam-induced luminescence spectroscopy (IBIL). The observed luminescence was similar to that seen in case of existing commercial scintillators. The Stokes shifts relative to the fluorescence excitation maxima for the MOFs were significantly large, minimizing an overlap between optical absorption and IBIL emission. This limited self-absorption resulting from the large Stokes shifts can lead to a new class of scintillators. These crystalline materials displayed enhanced radiation hardness and could potentially be stable for routine use with minimal concerns over radiation-induced

degradation. IBIL spectra were significantly different for MOFs with two different linkers: 4,4′-biphenyldicarboxylic acid (H_2BPDC) and 2,6-naphthalenedicarboxylic acid (H_2NDC).[83] $BPDC^{2-}$ displays a superimposable photoluminescence/IBIL emission spectra while a new 476nm IBIL emission peak was observed for NDC^{2-}. $BPDC^{2-}$ upon excitation conforms to a planar geometry inhibiting formation of a dimeric species. NDC^{2-}, on the other hand, readily forms excimer species in both ground and excited states due to intermolecular interaction.

X-ray induced scintillation was also demonstrated using MOFs with Hf/Zr as the nodes and anthracene as the connecting ligand **(Figure 5A)**[84]; high atomic numbers metal ions were chosen because of their ability to absorb X-ray irradiation. These MOFs when exposed to X-ray radiation in the 20-200keV range resulted in the ejection of fast electrons following absorption of high energy photons (**Figure 5B**). These electrons interact with the anthracene linker leading to the generation of luminescence from their excited states, which is used as a measure of ionizing radiation. Doses as low as 0.25 μGy could be sensed by these materials dispersed in aqueous media. Hf-MOF displayed enhanced radioluminescence signal due to higher X ray scattering cross section as compared to that of the Zr-MOF.

MOFs may be interesting candidates for a new class of radiation sensing materials because of their tenability. The availability of a large library of metal ions and organic linkers indicates the possibility of several combinations. Although very low doses can be sensed, linearity in the radio-therapeutic range has to be demonstrated before they could be further

used for real time dosimetry in the clinic. Factors including biocompatibility and stability/performance in biological solutions have to be studied before any potential application in vivo.

1.3 Conclusions

Several molecules and nanoscale systems are being investigated as radiation dosimeters with potential applications in fractionated radiotherapy. Some nano- and molecular scale sensors may demonstrate potential for clinical translation including for implantable applications, but additional studies on stability, sensitivity, reproducibility, toxicity, and/or biocompatibility are necessary. Most studies so far have typically been carried out with systems wherein the dosimeter does not come in direct contact with tissues and only the peripheral dose delivered is measured. Subsequent generations of dosimeters should be non-toxic, deliverable to the site of interest, be able to detect radiation doses in real time, and be able to provide a simple and quick readout. These advances have the potential to greatly improve treatment tolerance, safety and potentially, outcomes for patients undergoing radiotherapy.

In this thesis, a dosimeter based on the formation of colored dispersions of plasmonic (gold) nanoparticles from colorless solutions of gold ions upon exposure to ionizing radiation is demonstrated.

Chapter 2 POLYPEPTIDE-FACILITATED FORMATION OF BIMETALLIC PLASMONIC NANOPARTICLES IN PRESENCE OF IONIZING RADIATION

2.1 Introduction

Ionizing radiation has widespread application that ranges from medical application in the form of diagnostic imaging and cancer therapy to military uses[85-87]. A critical aspect of these applications is the level of exposure which determines the acute response of incidentally exposed organs (in therapy) or of personnel (in warfare or nuclear energy industry). A wide variety of dosimeters are available to detect radiation exposure, including one-dimensional ion-chambers and three-dimensional polymer gels[88, 89]. Portability and conformability make potential liquid-phase dosimeters attractive, although development of effective liquid dosimeters has been limited to embedding dyes in a polymer-rich matrix[90]. These systems however tend to fade over time leading to a loss of signal[91].

Engineered systems that undergo a clearly visible color change in response to ionizing radiation can be employed as rapid, portable detectors, since they do not require sophisticated secondary analyses. In particular, plasmonic nanoparticles are attractive as indicators since they demonstrate a range of colors, depending on concentration and yield[92]. We previously demonstrated that irradiating gold salt solutions (in absence of silver), together with C_2ELP molecules, resulted in the formation of gold nanoparticles[93]. In this system, high energy X-ray radiation results in the formation of both oxidizing (OH°) as well as reducing species (e^-_{aq}, H°) following radiolysis of water[94]. Reducing free radicals facilitate reduction of metal ions (M^{n+}, where n is the valency) to zero-valent metal ions

(M^0) which then nucleate and grow into nanoparticles. C_2ELP likely aids these processes by means of spontaneous metal ion reduction, nanoparticle stabilization, and nanoparticle templating due to the presence of cysteines[95, 96]. Although this approach is promising, gold nanoparticle formation was seen for doses in the 175-1000 Gy range. Here, we report that plasmonic nanoparticles can be generated from gold-silver bimetallic precursor solutions in presence of significantly lower doses (25-100 Gy), and can therefore be used as colorimetric reporters of elevated levels ionizing radiation.

2.2 Materials and Methods

Materials. Gold(III) chloride trihydrate (HAuCl4·3H2O) was purchased from Sigma-Aldrich. Isopropyl alcohol (IPA) (99.5%) was purchased from EMD. Silver Nitrate ($AgNO_3$) and dithiothreitol (DTT) were purchased from Fisher Scientific. All chemicals were used as received from the respective manufacturers without any additional purification.

Synthesis, Expression, and Purification of Cysteine containing Elastin-Like Polypeptides (ELPs). The elastin-like polypeptide used in the study, MVSACRGPG-(VG VPGVGVPGVGVPGVGVPGVGVPG)$_8$-(VGVPGVG VPGVG VPGCG VPGVG VPG)$_2$-WP, was generated using recursive directional ligation[97, 98]. This ELP contains two cysteines in the polypeptide repeat sequence and is labeled as C_2ELP. The oligonucleotide encoding the ELP was cloned in a pUC19 plasmid. Further cloning in pET25b+ expression

vector at the sfiI site was carried out. The polypeptide was expressed in Escherichia coli BLR(DE3) (Novagen), purified, lyophilized, and stored at 4°C using methods described previously[98].

Preparation of C_2ELP Samples for Irradiation with Ionizing Radiation. Lyophilized C_2ELP was dissolved in nanopure water (18.2 MΩ cm resistivity) in order to form 1 mg / mL solutions. DTT was then added to the C_2ELP solution (equal weight ratio of DTT to C_2ELP) in order to reduce the cysteines in the polypeptide chain. The solution was mixed for 1 hour under constant rotation at 4°C after which, the DTT was removed from the dissolved ELP via dialysis through a 10 kDa molecular weight cut off (MWCO) membrane. Dialysis was carried out for a maximum of 20 hours under constant rotation at 4°C. Reduced C_2ELP samples were stored at 4°C prior to use.

Sample Preparation and Irradiation with Ionizing Radiation. Samples for irradiation were comprised of $HAuCl_4$ (50 µL of 1×10^{-2} M), $AgNO_3$ (15 µL of 1×10^{-2} M), C_2ELP (200 µL of 1 mg/ml), and isopropyl alcohol (IPA) (600 µL of 0.4 M). In all cases, samples were mixed immediately prior to irradiation. All ionizing irradiation experiments were conducted at Banner-MD Anderson Cancer Center in Gilbert, AZ. A Truebeam linear accelerator was used to irradiate the samples with different doses at a dose rate of 15 Gy/minute. The radiation beam is a 6 MeV photon beam produced by the linear accelerator. The solutions were irradiated with doses of 25, 50 and 100 Gy. After irradiation, all samples

were transported back to ASU in Tempe, AZ (approximately 15 miles; 20-30 minutes travel time) and characterized at 72 h after irradiation to allow for nanoparticle formation.

Absorbance Spectroscopy. Absorbance values of the control (0 Gy) and irradiated samples were measured using a BioTek Synergy 2 plate reader in concert with Gen5 software. The absorbance spectrum was determined from 300 to 995 nm, with a step size of 5 nm, using 150 μL sample in each well of a 96-well plate. Absorbance measurements were carried out at 72 hours following X-ray irradiation. Nanopure water was used as the blank in all cases, and the presence of an absorbance peak between 500-600 nm was used as an indicator of nanoparticle formation.

Particle Size Determination. Hydrodynamic sizes of the irradiated samples were determined using dynamic light scattering (DLS), which was carried out with a DLS Particle Sizer (Corrvus Advanced Optical Instruments) in concert with a Zetasizer Nano instrument. Samples (40 μL) were pipetted into a square 1 mL cuvette and placed into the instrument for analysis.

Transmission Electron Microscopy (TEM) and Elemental Analyses (EDX). Transmission electron microscopy (TEM) visualization was carried out using a JEOL-2010F instrument. Specimen samples for TEM were prepared by casting a drop of the nanoparticle dispersion onto a carbon film on a copper mesh grid, followed by drying in

air, and air-dried samples were visualized by TEM. EDX analysis was performed on the nanoparticles using a JEOL-JEM-2000FX instrument.

2.3 Results and Discussion

In this study, we investigated polypeptide-mediated formation of bimetallic gold-silver (i.e. bimetallic) plasmonic nanoparticles as a colorimetric (visual) reporter of ionizing radiation (X-Rays). Radiation-induced hydrolysis results in the formation of free radicals which can reduce metal ions to form metal nanoparticles from their corresponding salt solutions[93] (**Figure 2.1**). Formation of bimetallic gold-silver nanoparticle dispersions is a simple, colorimetric (visual) indicator of ionizing radiation, since plasmonic nanoparticles absorb light in the visual region of the light absorption spectrum.

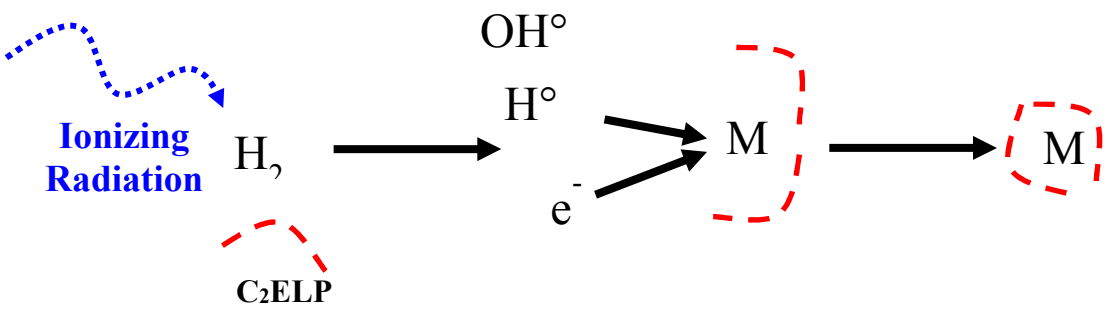

Figure 2.1 Skeleton reaction that shows radiolysis of water followed by reduction of metal salts by H* and e- resulting in the formation of zerovalent metal atoms. The metal atoms nucleate and grow to form bimetallic nanoparticles under the current conditions employed.

The reporter system investigated in the current study consists of three components, namely, isopropyl alcohol, metal salts, and a biomimetic polypeptide (C_2ELP). Isopropyl alcohol enhances metal nanoparticle yield in three ways: (1) it converts oxidizing hydroxyl radicals into isopropyl radicals which are reducing in nature and facilitate the reduction of metal ions (i.e. M^{n+}) to metal nanoparticles, (2) it scavenges oxidizing agents and therefore prevents re-oxidation of M^0 (zerovalent metal ion) to M^{n+} (metal ions), and (3) it consumes hydroxyl radicals, and reduces the reaction between hydroxyl radicals and other free radical species[99, 100]. C_2ELPs[101, 102] were employed since thiols present in cysteines can facilitate metal nanoparticle formation and / or capping[98]. In addition, amide bonds, which are an integral part of the polypeptide backbone, can also stabilize nanoparticles through N-H bonds[103].

In order to establish conditions for colorimetric detection / reporting of ionizing radiation, we investigated conditions under which spontaneous nanoparticle formation could not be observed. We first investigated varying concentrations of silver salt and C_2ELP at a fixed gold salt concentration of 0.57 mM. A silver salt concentration of 0.173 mM was deemed as an optimal condition at which spontaneous nanoparticle formation was not visually observed for a period of 72 h. Increasing the silver salt concentration beyond this condition resulted in spontaneous nanoparticle formation in the absence of radiation as seen from the characteristic spectral peaks in **Figure 2.2**.

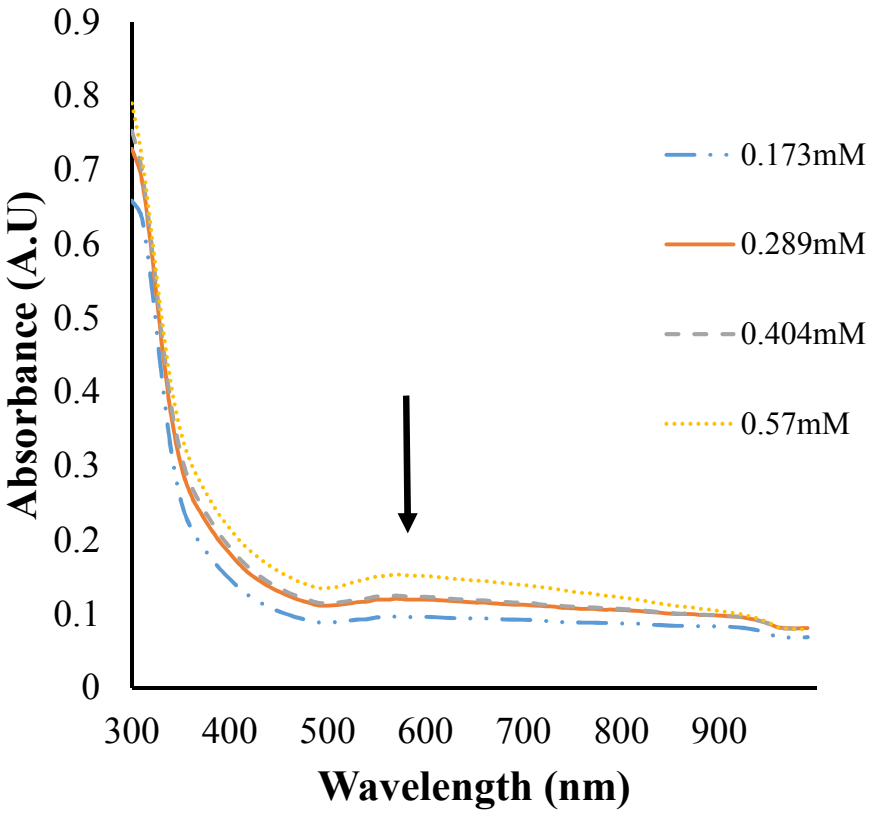

Figure 2.2 Average (n=3) absorbance spectra of C_2ELP (1 mg/ml) and gold-silver bimetallic solutions when exposed to varying concentrations of silver salt at 0 Gy at a pH 5-6. A silver salt concentration of 0.173 mM was used for further experiments due to observation of only a very weak spectral band compared to higher concentrations.

Increasing the polypeptide concentration above 1 mg / ml resulted in a concomitant increase in the dispersion color intensity indicating the formation of plasmonic nanoparticles (**Figure 2.3**). It is likely that increasing the polypeptide concentration increases the reducing activity and favors spontaneous nucleation and growth. In addition to silver salt and C_2ELP concentrations, we investigated the role of solution pH, since pH

has been shown to be an important factor determining nanoparticle synthesis[104]. **Figure 2.4** indicates that spontaneous nanoparticle formation is observed under conditions of basic pH. This is consistent with previous findings, which indicate that higher pH conditions can result in rapid reduction, likely due to the higher concentrations of OH^- ions under these conditions[105, 106]. Spontaneous nanoparticle formation was not seen under conditions of lower pH i.e. pH = 5-6. This pH condition was therefore chosen for subsequent studies.

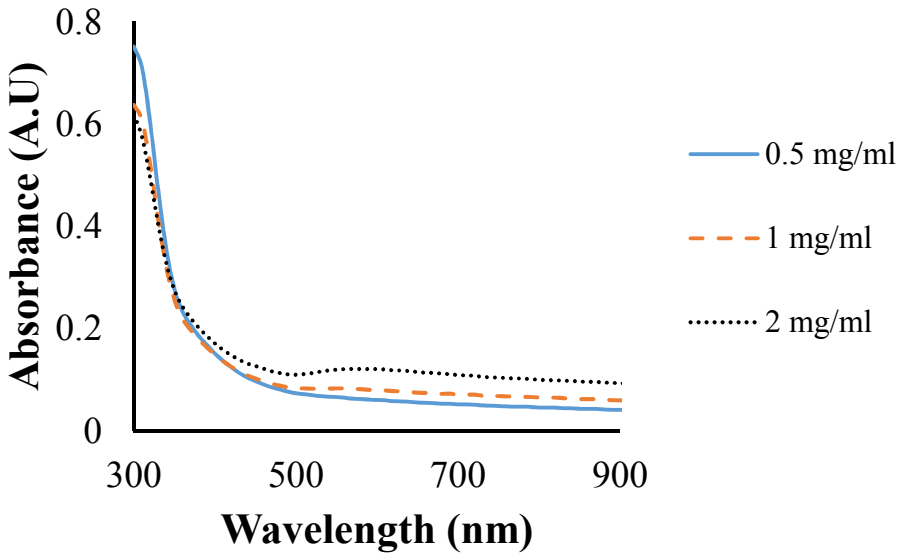

Figure 2.3 Average (n=3) absorbance spectra of C_2ELP and gold-silver bimetallic solutions when exposed to varying concentrations of C_2ELP at 0 Gy at pH 5-6. A C_2ELP concentration of 1 mg/ml was used for further experiments due to observation of a minimal spectral band compared to higher concentrations.

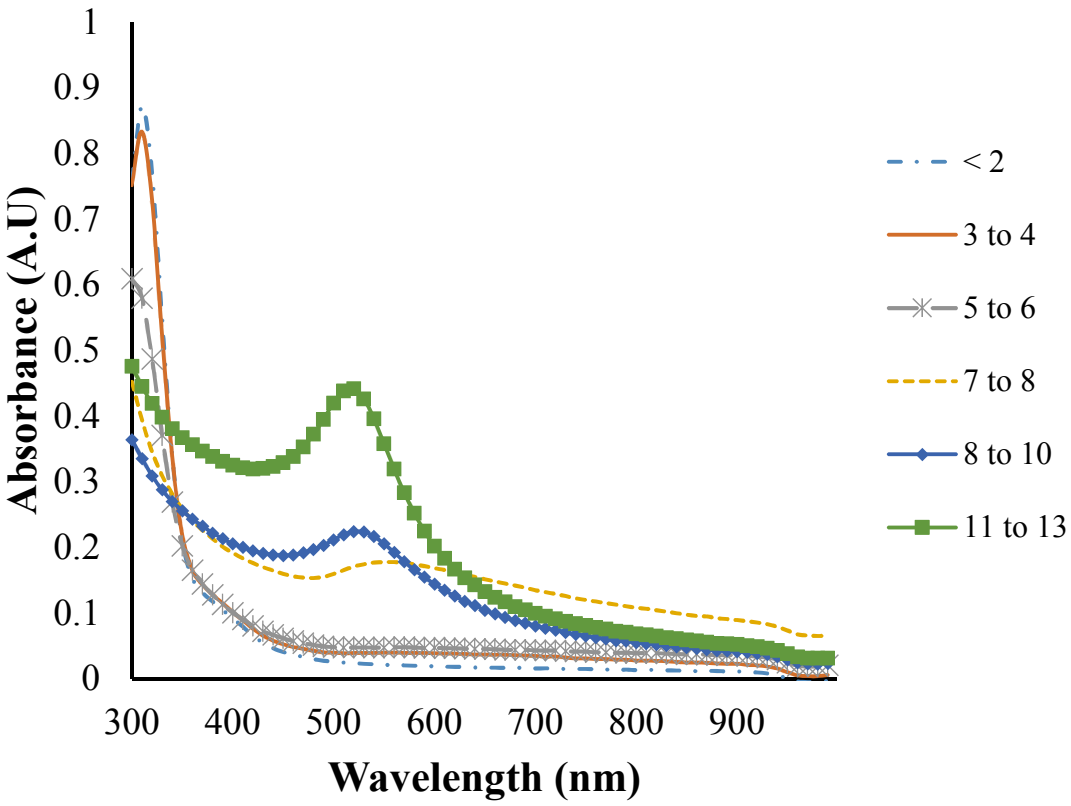

Figure 2.4 Average (n=3) absorbance spectra of C_2ELP (1 mg/ml) and gold-silver bimetallic solutions when exposed to acidic and basic pH conditions at 0 Gy (no irradiation). Absorbance spectra indicate spontaneous nanoparticle formation under conditions of basic pH, while nanoparticle formation is not seen for pH ranges of 2-6.

Following identification of operating conditions that did not result in spontaneous nanoparticle formation, the metal salt-C_2ELP solution was subjected to different doses of ionizing radiation in order to determine the minimum dose required for inducing a visible color change. No change in color was observed in samples not subjected to X-Ray radiation (**Figure 2.5A**). In addition, color change was not seen in samples irradiated with X-ray doses in the 0-20 Gy range. The minimum dose required for inducing a visual color change with the gold-silver bimetallic system was 25 Gy (**Figure 2.5 B**). Higher radiation doses of 100 Gy resulted in further intensification of the color in the liquid nanoparticle

dispersions (**Figure 2.5 C & D**), while no significant change in the intensity of color was observed for the system irradiated with a dose of 50 Gy. This is likely due to generation of higher number of reducing species at higher radiation doses (i.e. 100 Gy) which, in turn, lead to greater reduction of metal ions to their respective zerovalent metal forms. In these cases, the color change was seen three days after X-Ray irradiation. The peak absorbance value was maximum in the 100 Gy case, which is consistent with high yields that may be expected at higher radiation doses. This is also a reflection of the color intensity, which was highest for the 100 Gy case.

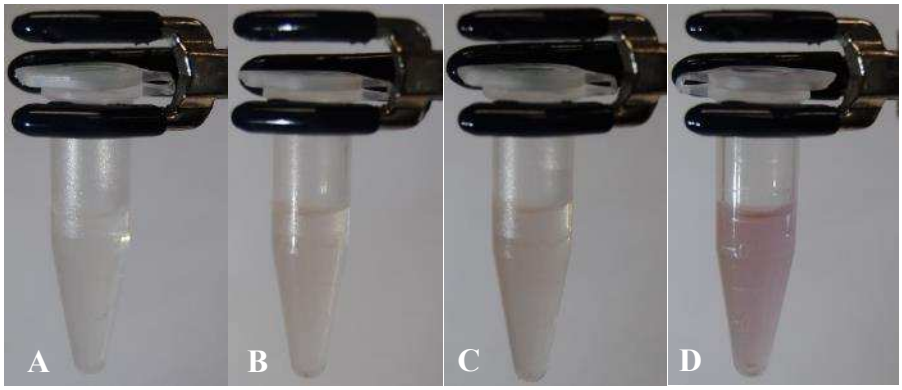

Figure 2.5 Visible, colorimetric detection of ionizing radiation as reported by the formation of plasmonic bimetallic nanoparticles. Formation of bimetallic nanoparticles was facilitated by C2ELP (1 mg/mL; pH 5-6) at different radiation doses. (A) 0 Gy, (B) 25 Gy, (C) 50 Gy and (D) 100 Gy. A visible change in color can be seen for samples irradiated with 25, 50, and 100 Gy.

Optical density is a straightforward method for detection and quantification of plasmonic nanoparticle dispersions, and is often used as a surrogate for concentration. Pure gold and silver nanoparticles demonstrate absorbance peaks at 510-570 and 400-530 nm, respectively[107, 108]. In the absence of X-ray radiation, C_2ELP molecules were not able to

reduce metal salts to the extent that a significant plasmonic peak could be observed in the absorption spectrum (**Figure 2.6A**). However, in presence of 25, 50 and 100 Gy X-ray radiation doses, absorbance peaks were seen between 500-600 nm three days after irradiation, indicating formation of plasmonic nanoparticles. These spectra are consistent with those for bimetallic gold-silver dispersions observed previously in the literature[109]. A reduction in the width of the absorption peak was observed with increasing radiation dose. This narrowing is likely an indication of lower nanoparticle polydispersity at higher radiation doses[110].

A

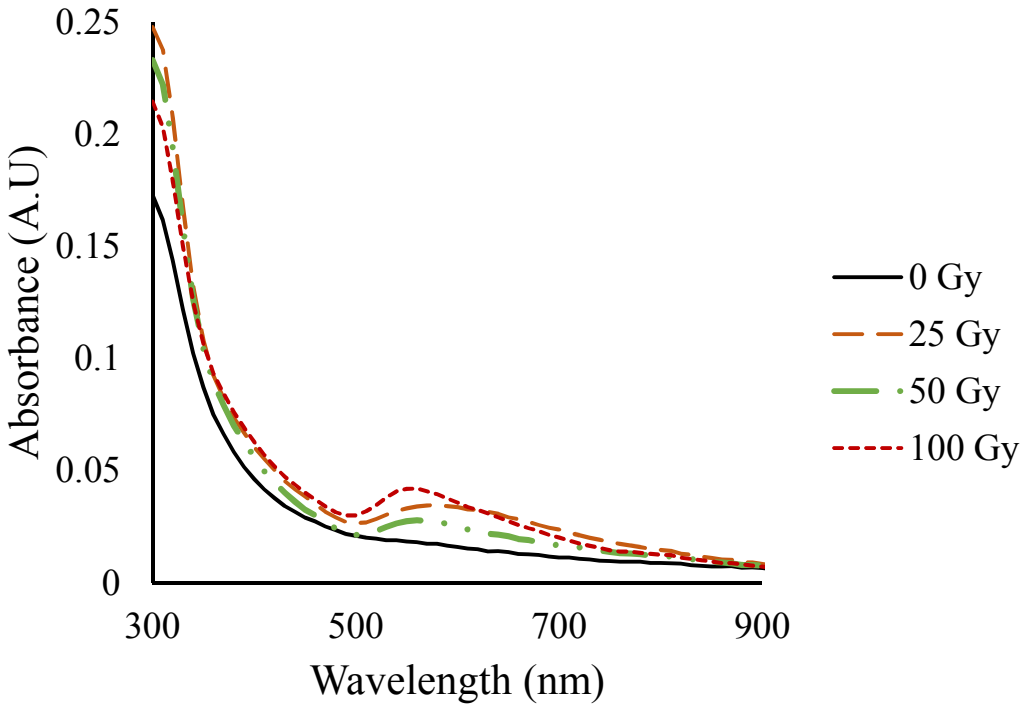

B

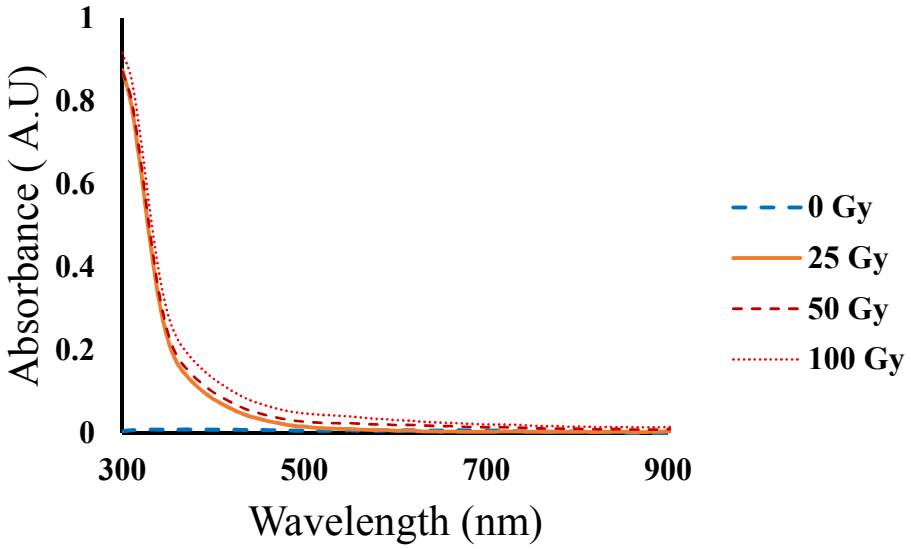

Figure 2.6 (A) Average absorbance spectra (n = 9) of C_2ELP and gold-silver bimetallic solutions in presence of C_2ELP and (B) Average absorbance spectra (n = 3) of gold-silver bimetallic solutions irradiated in absence of C_2ELP with 0 Gy (control), 25 Gy, 50 Gy, and 100 Gy. X-ray radiation indicate nanoparticle formation in case of irradiated samples in presence of C_2ELP. Absence of absorbance peak indicates no stable nanoparticles formed verifying the need for C_2ELP.

Dynamic light scattering (DLS) measurements indicated that nanoparticles with hydrodynamic diameters ranging from 80-110 nm were formed in these studies (**Figure 2.7**). Previous studies, including ours, indicate that higher radiation doses lead to the formation of smaller sized particles [93, 99, 111]. At higher radiation doses, the ratio of the unreduced metal ions to the reduced zerovalent metal is likely low, due to higher efficacy of free radical formation. The concentrations of the reduced zerovalent metal ions, and subsequently nanoclusters (nucleus for metal nanoparticle formation), tend to be higher than the unreduced metal ions in solution. Further aggregation is likely inhibited due to the presence of the capping agent. At lower doses of X-Ray radiation, the number (or concentration) of unreduced metal ions is higher than the number of metallic nuclei formed.

Thus, the unreduced ions likely tend to aggregate with the nucleus formed and result in larger sized particles on an average.

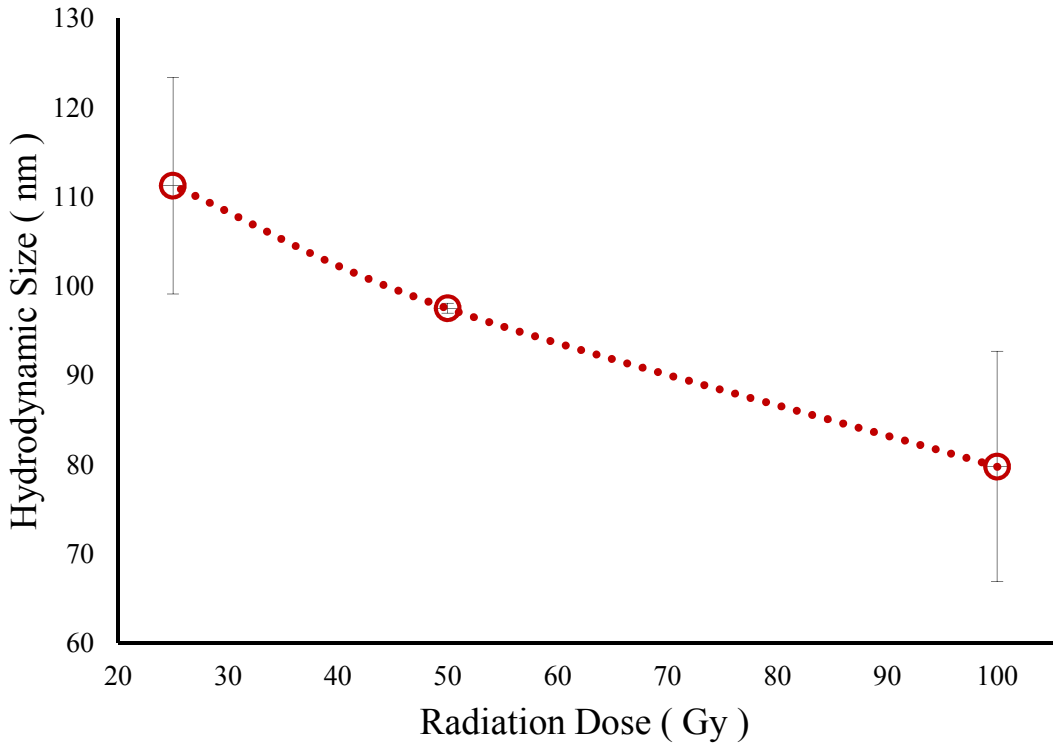

Figure 2.7 Hydrodynamic diameters, determined by dynamic light scattering (DLS), of nanoparticles formed as a function of radiation dose (n=3). Data indicate mean absorbance values from n = 3 readings ± one standard deviation. Average hydrodynamic diameter is seen to decrease modestly with increasing radiation dose. The line connecting individual data points is included for visualization alone.

X-ray irradiated and non-irradiated control samples were imaged using transmission electron microscopy (TEM) in order to visualize the bimetallic nanoparticles formed under different conditions. The core sizes of nanoparticles, as visualized using TEM, ranged from 15 to 90 nm in the different cases studied (**Figure 2.8**), while the average core sizes typically range from 10-20 nm. The control (0 Gy) did result in the formation of

nanoparticles, indicating that the C_2ELP molecules were capable of reducing metal ions and thereby templating nanoparticles in absence of radiation as seen previously[93]. This is likely due to the presence of the amide backbone in the ELP chain, along with the presence of arginine (A), which contains an amine moiety. These moieties can stabilize the nanoparticles formed due to the reduction of metal salts in the presence of tryptophan (W) residues which is known to be a powerful reducing agent for metal salts[112, 113]. However, it is important to note that neither peaks in the absorption spectrum (**Figure 2.6A**), nor significant color changes (**Figure 2.5A**) were observed in the case of C_2ELP-bimetallic metal solutions not subjected to X-Ray radiation. These observations indicate that in absence of radiation, C_2ELP did not result in high enough yields of nanoparticles to be identified visually and / or spectroscopically. Irradiating aqueous solutions of gold-silver bimetallic metal salts in presence of C_2ELP resulted in formation of plasmonic nanoparticles due to the additional reducing activity following radiolysis of water. These higher nanoparticle yields could be identified visually due to the color change (**Figure 2.5**) as well as the characteristic UV-visible absorbance spectra (**Figure 2.6**). A precipitate was visually observed when the metal salts were irradiated in absence of C_2ELP while the solution remained colorless and no peaks were seen in the the UV-Vis light absorption between 300 and 990 nm (**Figure 2.6B**). This confirms that C_2ELP is necessary as a stabilizing agent for overcoming aggregation of the metal atoms formed during radiolysis.

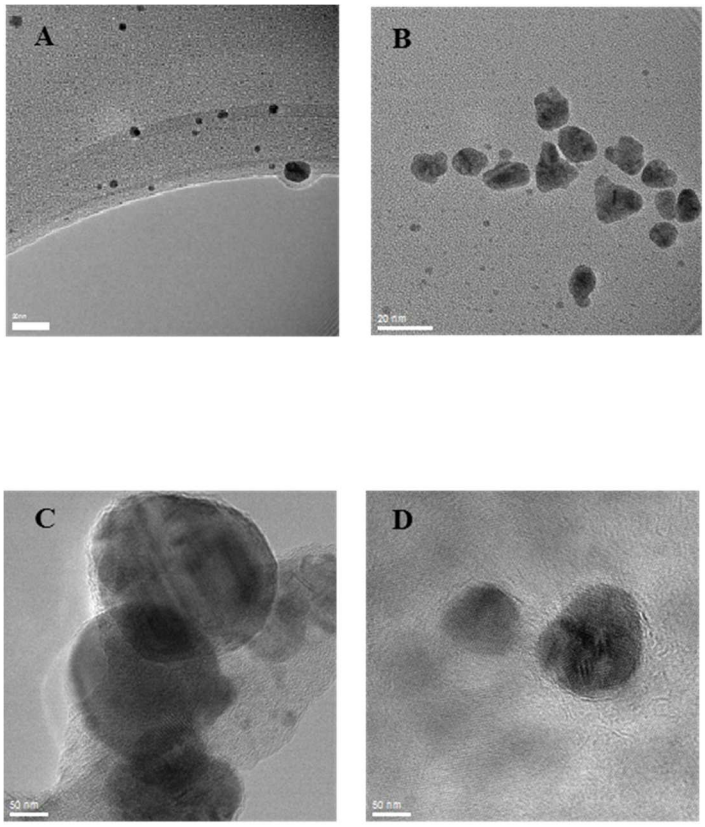

Figure 2.8 Transmission electron microscopy (TEM) images of plasmonic nanoparticles formed under irradiation. (A) control (0 Gy) and samples irradiated with (B) 25 Gy, (C) 50 Gy and (D) 100 Gy X-Ray radiation. Scale bar = 20 nm for (A) and (B), and 50 nm for (C) and (D).

Elemental analyses were carried out in order to determine the composition of the plasmonic nanoparticles formed. Heterogeneity in the elemental composition was observed among different nanoparticles investigated ($n \geq 3$ nanoparticles), and nanoparticles individually enriched in either gold or silver were seen (**Figure 2.9A-B**). The synthesis of such bimetallic clusters has been shown to proceed by a progressive reduction of metal ions during radiolysis and growth of the nanoparticles (**Figure 2.10**). During radiolysis the reducing free radicals react with gold and silver metal ions and reduce them to their zerovalent states[114]. The lesser noble metal (silver in this case) transfers electrons to the

more noble metal (gold in this case) which results in reduction of the latter from Au^{3+} to Au^{0} species. Electron transfer is made possible due to the differences in electronegativity as Au is more electronegative than Ag. The electron relay from Ag to Au is also possible between the different valence states of the gold ions (i.e. +1 and +3)[111].

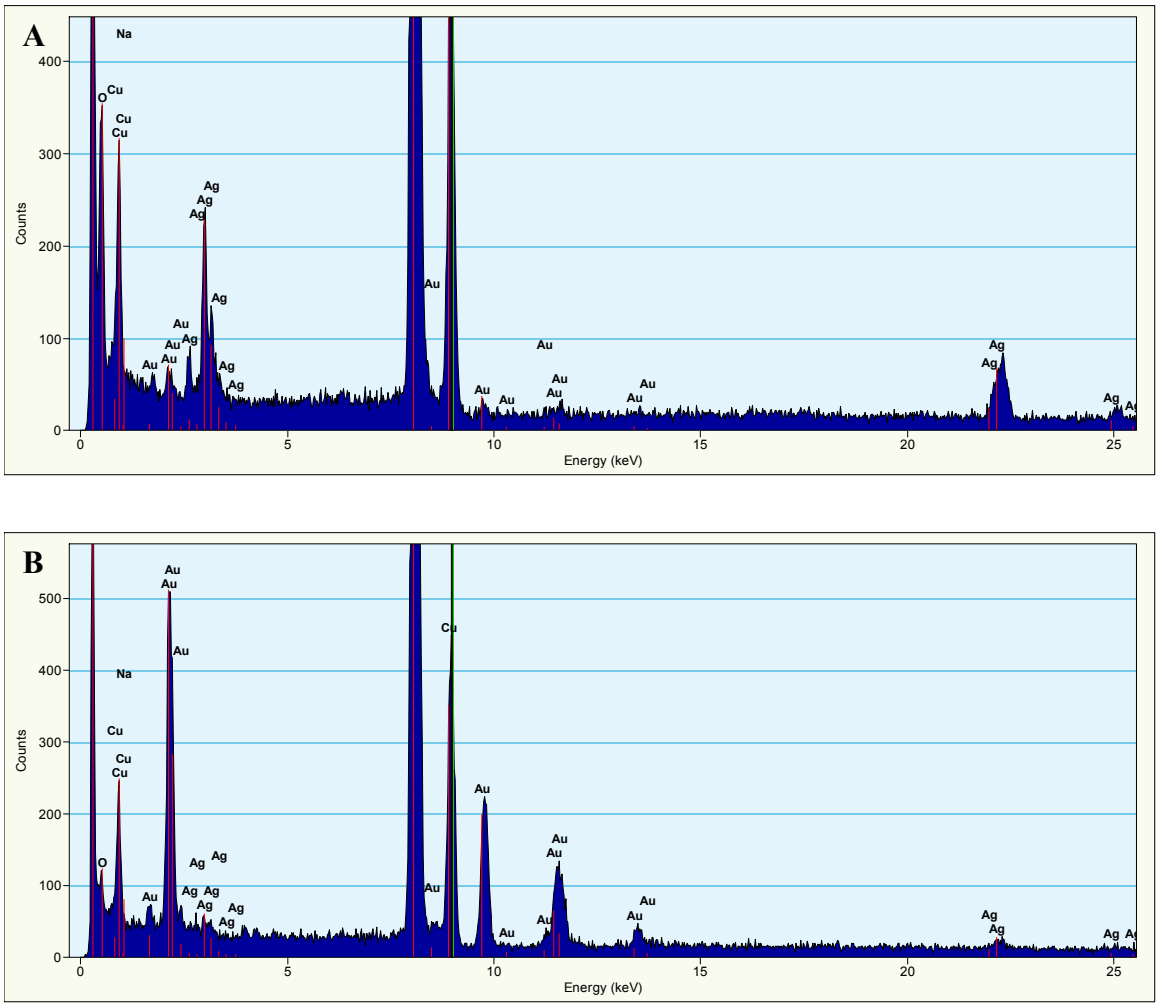

Figure 2.9 Elemental analyses of plasmonic nanoparticles (n ≥ 3) indicates presence of both gold and silver. Heterogeneity among nanoparticles is observed with some particles being enriched in silver (A) and others rich in gold (B).

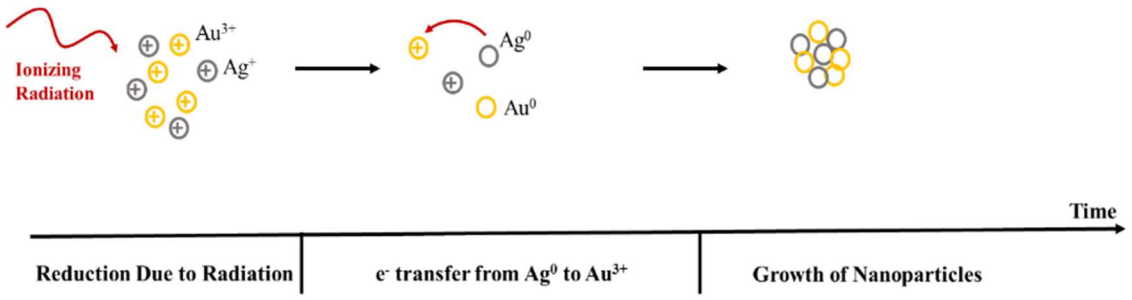

Figure 2.10 Schematic of bimetallic nanoparticle formation during radiolysis involving inter-metal electron transfer.

To further verify the need for a bimetallic system, solutions containing either silver alone or gold alone were irradiated separately (**Figure 2.11**). The maximum absorbance values were similar to the bimetallic condition (between 500-600 nm for Au salt and 400-500 nm for Ag salt). Following baseline and offset corrections (i.e. maximum absorbance at the corresponding wavelengths – absorbance at 900 nm), it was observed that the yields of the bimetallic nanoparticles were higher than those for the individual metal (Au or Ag) nanoparticles alone. This further provides support to our hypothesis that the presence of a small amount of silver ions facilitates nanoparticle formation at lower doses as those required for gold salt alone ($\geq$ 175 Gy).

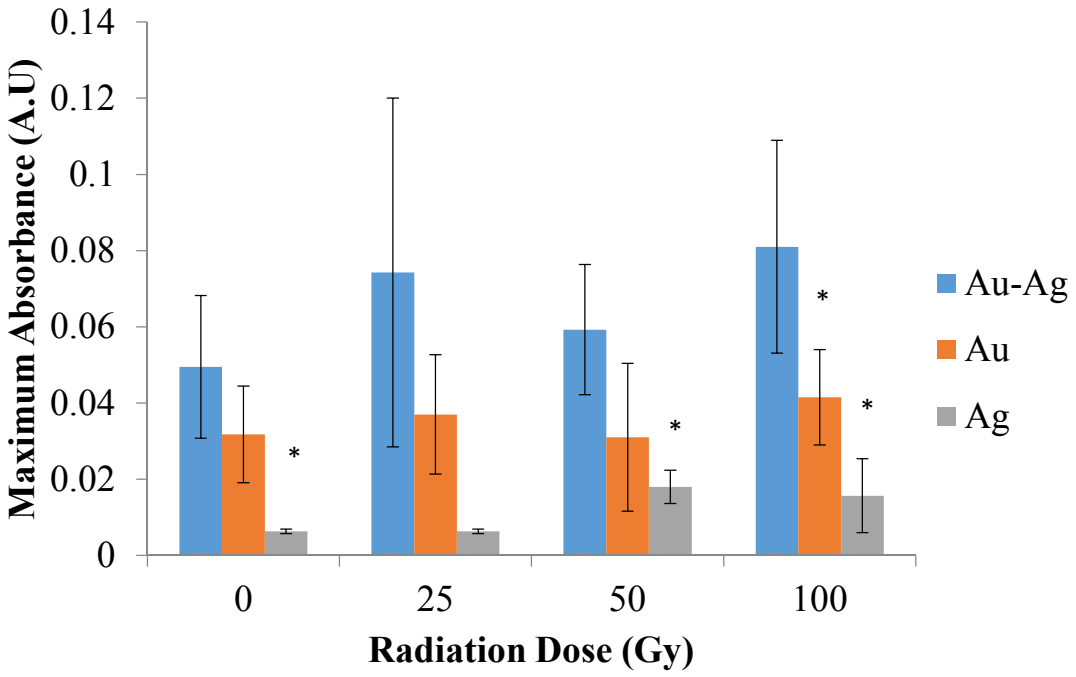

Figure 2.11 Average values of peak absorbance (n = 3) observed after C_2ELP and monometallic (Au or Ag) / bimetallic (Au and Ag) solutions were irradiated with 0 Gy (control), 25 Gy, 50 Gy, and 100 Gy X-ray radiation. Error bars indicate standard deviation. Overall increase in the average absorbance values likely indicate higher yields of bimetallic nanoparticles formed for a given radiation dose. Asterisks (*) indicate p-values < 0.05 for Au-Ag system compared to Au/Ag alone control systems, as determined using Student's t-test; p-values < 0.05 are considered statistically significant.

2.4 Conclusions

In conclusion, we report that radiation-induced nanoparticle formation from a mixture of gold-silver metal salts, scavenging agents, and cysteine-containing elastin-like polypeptides can be employed as a reporter for elevated doses of ionizing radiation, 25 Gy and higher. Even though nanoparticle formation was observed using TEM for non-irradiated (0 Gy) samples, visible color changes was observed only in case of irradiated samples, indicating a colorimetric response to radiation. Future work will involve an investigation into engineering the polypeptide, as well as optimizing operating conditions in order to further enhance the sensitivity of this simple detection system. It is anticipated

that these studies can advance the field of conformable and portable radiation detectors for various applications in healthcare, defense and space exploration.

Chapter 3 A COLORIMETRIC PLASMONIC NANOSENSOR FOR DOSIMETRY OF THERAPEUTIC LEVELS OF IONIZING RADIATION

3.1 Introduction

Radiation therapy is a common primary treatment modality for multiple malignancies, including cancers of the head and neck, breast, lung, prostate, and rectum.[115] Depending on the disease, cumulative radiation doses ranging from 20 and 70 Gy are often employed for therapeutic use. Diseased tissue and normal organ radiation sensitivities also vary.[116] In order to maximize disease treatment relative to radiation-induced side-effects, various methods of delivery including hyperfractionation (0.5-1.8 Gy), conventional fractionation (1.8-2.2 Gy), and hypofractionation (3-10 Gy)[115] have been explored. These delivery methods explore different regimes of radiation sensitivity in order to maximize tumor cell killing while optimizing treatment times.[115]

Despite obvious advantages with radiotherapy, there can be significant radiation-induced toxicity in tissues.[117] For example, radiation-induced proctitis can be of significant morbidity for patients undergoing prostate or endometrial cancer treatment. For centrally located lung cancer radiotherapy, the esophagus can be incidentally irradiated during treatments, resulting in esophagitis. In head and neck treatments, radiation of salivary gland or pharyngeal tumors can induce radiation-induced osteonecrosis. Another concern during radiotherapy is the motion of the patient as well as the natural peristalsis of internal organs. These issues highlight the importance of appropriately dosing cancerous tumors while sparing the normal tissue in order to prevent significant morbidity that arises from radiation toxicity.

Following several transformative advances since its inception in the late 19th century,[118] radiation therapy has become a complex process aimed at maximizing the dose delivered to the tumor environment while sparing normal tissue of unnecessary radiation. This has led to the development of image-guided and intensity-modulated radiation therapy.[119] The process of treatment planning requires initial simulation followed by verification of dose delivery with anthropomorphic phantoms which simulate human tissue with more or less homogeneous, polymeric materials.[120] The accuracy of the planning is determined using either anthropomorphic phantoms or 3D dosimeters.[119,121,122] During treatment, actual dose delivery can be verified with a combination of entry, exit or luminal dose measurements,[120,123,124] in a process called *in vivo* dosimetry. Administered *in vivo* doses can be measured with diodes (surface or implantable), thermoluminescent detectors (TLDs), or other scintillating detectors.[120,123,124] However, these detectors are either invasive, difficult to handle (due to fragility or sensitivity to heat and light), require separate read-out device, or measure surface doses only. TLDs are typically laborious to use and require repeated calibration, while diodes suffer from angular, energy and dose rate-dependent responses.[125] Although MOSFETs can overcome some of these limitations, they typically require highly stable power supplies.[126] In addition, these dosimeters require sophisticated and expensive fabrication processes in many cases. In light of these considerations, there is still a need for the development of robust and simple sensors in order to assist / replace existing dosimeters that can be employed during sessions of fractionated radiotherapy.[127, 128]

Unique optical properties associated with plasmonic nanoparticles[129] have led to investigation of different metal nanoparticles in imaging, hyperthermia, drug delivery, and sensing applications.[67, 130, 131] Of particular relevance to imaging and sensing is the observation that dispersions of plasmonic nanoparticles display different colors depending on the size of the particles. Metallic nanoparticles are synthesized using a wide range of wet chemistry[66, 132] and radiation[133] based techniques. Current radiation-based methods require high doses, use of complex polymers / polypeptides, scavengers and / or inert atmospheres to engender nanoparticle synthesis.[93, 134, 135] To our knowledge, none of these methods are based on dose ranges employed in fractionated radiotherapies.

In this work, we exploited lipid surfactant-templated formation of colored dispersions of gold nanoparticles from colorless metal salts as a facile, visual and quantitative indicator of therapeutic levels of ionizing radiation (X-rays) for application in radiation dosimetry. This plasmonic nanosensor can detect radiation doses as low as 0.5 Gy, and exhibit a linear response for doses relevant in therapeutic administration of fractionated radiotherapy (0.5 – 2 Gy). Modulating the concentration and chemistry of the templating lipid surfactant results in linear response in different dose ranges, which demonstrates the versatility of the plasmonic radiation nanosensor in a variety of radiotherapy applications.

3.2 Materials and Methods

Materials. Gold(III) chloride trihydrate ($HAuCl_4 \cdot 3H_2O$), trimethyloctylammonium bromide (C_8TAB) (≥ 98%), dodecyltrimethylammonium bromide ($C_{12}TAB$) (≥ 98%) and L-Ascorbic acid (AA) were purchased from Sigma-Aldrich. Cetyl trimethylammonium bromide ($C_{16}TAB$) was purchased from MP chemicals. All chemicals were used as received from the manufacturer without any additional purification.

Sample Preparation for Irradiation. First, 30μL of 0.01 M $HAuCl_4$ were mixed with 600 μL of 0.05 M $C_{x=8,12,16}TAB$. Upon addition of 30 μL (0.196 mM), 300 μL (1.96 mM), 600 μL (3.92 mM approximated as 4mM) and 900 μL (5.88 mM or ~5.9 mM) of 0.01 M L-Ascorbic acid, the solution turned colorless after shaking; the concentrations of ascorbic acid were thus varied in order to examine its effect on nanoparticle formation. Unless specifically mentioned, the volume of AA used is 900 μL. The measured pH of the precursor solution was typically between 2.9 and 3.1. Samples were prepared at Banner-MD Anderson Cancer Center, Gilbert, AZ prior to radiation.

Radiation Conditions. A Varian TrueBeam linear accelerator was used to irradiate samples at a dose rate of 15.6 Gy/min. The samples containing surfactant at a concentration of 20 mM and 10 mM were radiated at doses of 0 (control), 1.1, 3.2, 5.3, 10.5, 15.8, 26.3, 36.9 and 47.4 Gy. These are reported as 0, 1, 3, 5, 10, 16, 26, 37 and 47 Gy respectively in the article. The samples containing surfactant at a concentration 2 mM and 4 mM were irradiated with 0 (control), 0.5, 1, 1.5, 2, 2.5, 3, 5, 7.5, 10, 12.5 and 15 Gy. After irradiation

the samples were transported back to Arizona State University in Tempe, AZ (one-way travel time of approximately 20-30 minutes). At a dose rate of 15.6 Gy / min, most doses take seconds to administer to a sample, and the highest dose (47 Gy) takes a little over 3 minutes.

Absorbance Spectroscopy. Absorbance profiles of the radiated and the control samples were measured using a BioTek Synergy 2 plate reader. Absorbance values from 150 μL of sample were measured from 300 to 900 nm with a step size of 10 nm in a 96 well plate. Nanopure water (18.2 MΩcm) was used as a blank in all cases. The absorbance was corrected for offset by subtracting $A_{900\,nm}$ and the presence of a peak (or peaks) between 500 and 700 nm was used as an indicator for gold nanoparticle formation.

Determination of Critical Micellar Concentration (CMC). Pyrene (60 μL of 2 x 10^{-5}M) in acetone was added to 20 ml glass vials. Upon acetone evaporation, 2ml of C_{16}TAB of varying concentrations was added and stirred for 6 hours at room temperature. To achieve the similar conditions as the irradiation experiments, 30μL of 10mM gold salt + 600μL of the above prepared C_{16}TAB + 900μL of 10mM ascorbic acid were mixed. A fluorescence spectrophotometer with an excitation scan range of 300 – 360 nm and an emission wavelength of 390 nm was used. Ratio of I_{337}/I_{334} determined as a function of the surfactant concentration was used to calculate the CMC using pyrene as the probe based on methods described in the literature[136].

Dynamic Light Scattering (DLS) Measurements. 50 μL of the sample was transferred into a cuvette and placed into a Zetasizer Nano instrument. The software was set up to carry out measurements with autocorrelation. Thereafter, the average diameter values, along with the polydispersity index (PDI), were recorded based on the software readout.

Transmission Electron Microscopy (TEM). Samples for TEM were prepared by casting a drop of the solution onto a carbon film on a copper mesh grid. The samples were then dried in air. The above process was repeated several times to ensure good coverage. Dried samples were visualized using a CM200-FEG instrument operating at 200 kV.

Endorectal Balloon Studies. Prostate immobilization treatment (endorectal) balloon device kit was purchased from Radiadyne. The nanosensor (1.503 mL) containing 20mM C_{16}TAB was introduced into the inflatable balloon through the stem using a syringe. After irradiation with the corresponding dose, the liquid was drawn out and the absorbance was measured using a UV-visible spectrometer.

Prostate Phantom Experiments. CIRS tissue equivalent prostate phantom was aligned at the center of the prostate volume on the Philips RT CT table with CT room aligning lasers. Three radio opaque markers were placed at the isocenter of the radiation beams. The endorectal balloon was inflated to a known volume of 50 ml following insertion into the phantom. CT scan imaging was executed on the phantom with 1 mm image thickness and 1 mm spacing to total of 150 images. After scanning, they were exported to a Philips

Pinnacle treatment planning system. The prostate, rectum and the capsules were contoured and a treatment plan was generated for a 6MV radiation beam. A prescribed dose of 1 Gy to a 95% isodose encompassing the entire prostate was simulated. Pinnacle's Collapsed Cone Convolution Superposition (CCCS) algorithm was used to compute the dose to the prostate in the phantom.

3.3 Results and Discussion

Facile radiation sensors have the potential to transform treatment methods and planning in clinical radiotherapy by verifying the precise delivery of doses to the intended site of action with minimal damage to surrounding tissues. Here, we report studies on a simple colorimetric, liquid-phase plasmonic nanosensor that can detect therapeutic levels of ionizing radiation. X-rays, in concert with templating lipid micelles, induced the formation of colored dispersions of gold nanoparticles from a colorless gold salt solution, thereby resulting in a visible indicator of ionizing radiation.

Several molecular design considerations were employed in order to develop the plasmonic nanosensor for detecting therapeutic doses (broadly 0.5 -10 Gy) of ionizing radiation. The basic working principle behind the plasmonic nanosensor involves reduction of colorless gold ions to gold nanoparticles (colored) by generating zerovalent (Au(0)) ions in order to facilitate nanoparticle nucleation and growth. Gold ions typically exist in a trivalent state (Au(III)) in metal salts, and we first sought to convert these ions to monovalent gold ions (Au(I)). This is because the reduction of Au(I) to Au(0) is thermodynamically favored over

the reduction of Au(III) to Au(0) due to the higher standard reduction potential of the former.[137] Au(I) has an electronic configuration of $4f^{14}5d^{10}$ and requires a single electron for conversion (reduction) to Au(0),[138] which then grow to form nanoparticles.

In the current plasmonic nanosensor, the electron transfer required for reducing Au(I) to Au(0) is facilitated by splitting water into free radicals following exposure to ionizing radiation (X-rays). Water splitting by ionizing radiation generates three key free radicals, two of which, e^- and H·, are reducing, and the other (˙OH·) is oxidizing in nature.[93] Ascorbic acid is an antioxidant and is capable of removing the oxidizing OH· radicals, which can inhibit nanoparticle formation. Finally, C_xTAB (x=8, 12, 16) surfactants were employed for their ability to template gold nanoparticles.[139] Taken together, a colorless metal salt precursor solution consisting of a mixture of auric chloride ($HAuCl_4$), L-ascorbic acid (AA) and cetyl (C_{16}), dodecyl (C_{12}), or octyl (C_8) trimethylammonium bromide ($C_{x;\ x=16/12/8}TAB$) surfactant molecules (**Figure 3.1**; please see the Experimental Section for more details),[140, 141] form the key constituents of the novel plasmonic nanosensor for detecting ionizing radiation as described in the following sections.

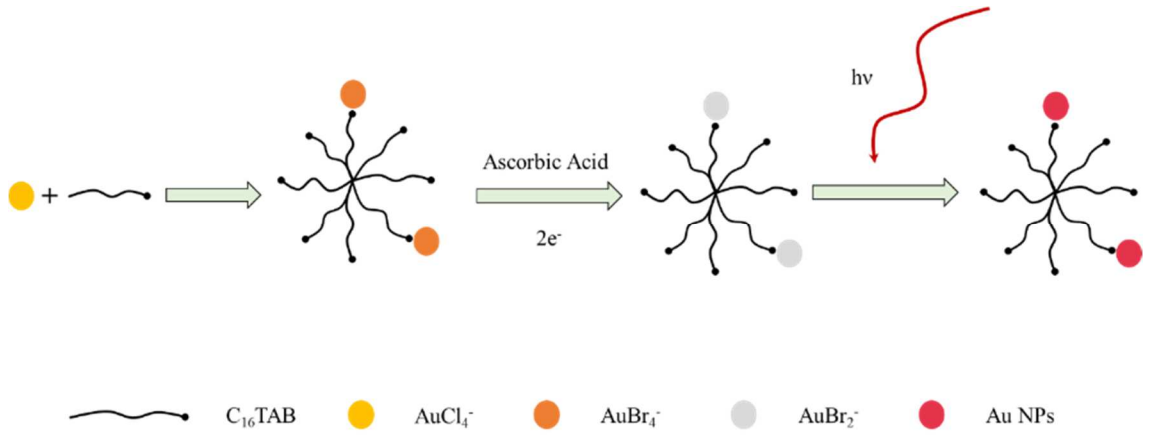

Figure 3.1 Schematic depicting the reaction progress after addition of various components in the plasmonic nanosensor for ionizing radiation. The concept for this figure was adapted from [142]. $HAuCl_4$ salt solution is yellow in color, but changes to orange upon addition of C_xTAB. Addition to ascorbic acid results in the formation of a colorless solution forming the precursor solution for the plasmonic nanosensor. Irradiation with ionizing radiation (*e.g.* X-rays shown as hν) results in the formation of colored dispersions of gold nanoparticle. The color of gold nanoparticle dispersions (AuNPs) can vary in color depending on the size of the nanoparticles.

C_xTAB and $HAuCl_4$ (gold salt) were first mixed leading to the formation of $Au^{III}Br_4^-$. $HAuCl_4$ (Au(III)) shows a prominent light absorption peak at 340 nm, which shifts to 400 nm after addition of $C_{16}TAB$, likely due to the exchange of a weaker chloride ion by a stronger bromide ion (**Figures 3.2 A and B, Figure 3.1**).[138] The shift in the absorption peak can also be seen visually as a color change from yellow to orange. Ascorbic acid reduces Au(III) to Au(I) in a two-electron, step-reduction reaction,[138] and addition of the acid to an orange-colored solution of $HAuCl_4$ and $C_{16}TAB$ renders it colorless with no observable peaks between 300 and 999 nm (**Figure 3.2 C, Figure 3.1**). This mixture of C_xTAB, ascorbic acid, and $HAuCl_4$ is employed as the precursor solution of the plasmonic radiation nanosensor. It has been shown that addition of up to 5 molar equivalent excess ascorbic acid does not result in the formation of zerovalent gold or Au(0) species, which can be partly attributed to the lower oxidation potential of the acid in presence of

C_{16}TAB.[143] However, a characteristic peak in the range of 500-600 nm corresponding to gold nanoparticles is observed if ascorbic acid is directly reacted with the gold salt in the absence of C_{16}TAB (**Figure 3.2 D**),[138] indicating spontaneous formation of nanoparticles in absence of the lipid surfactant under the conditions employed.

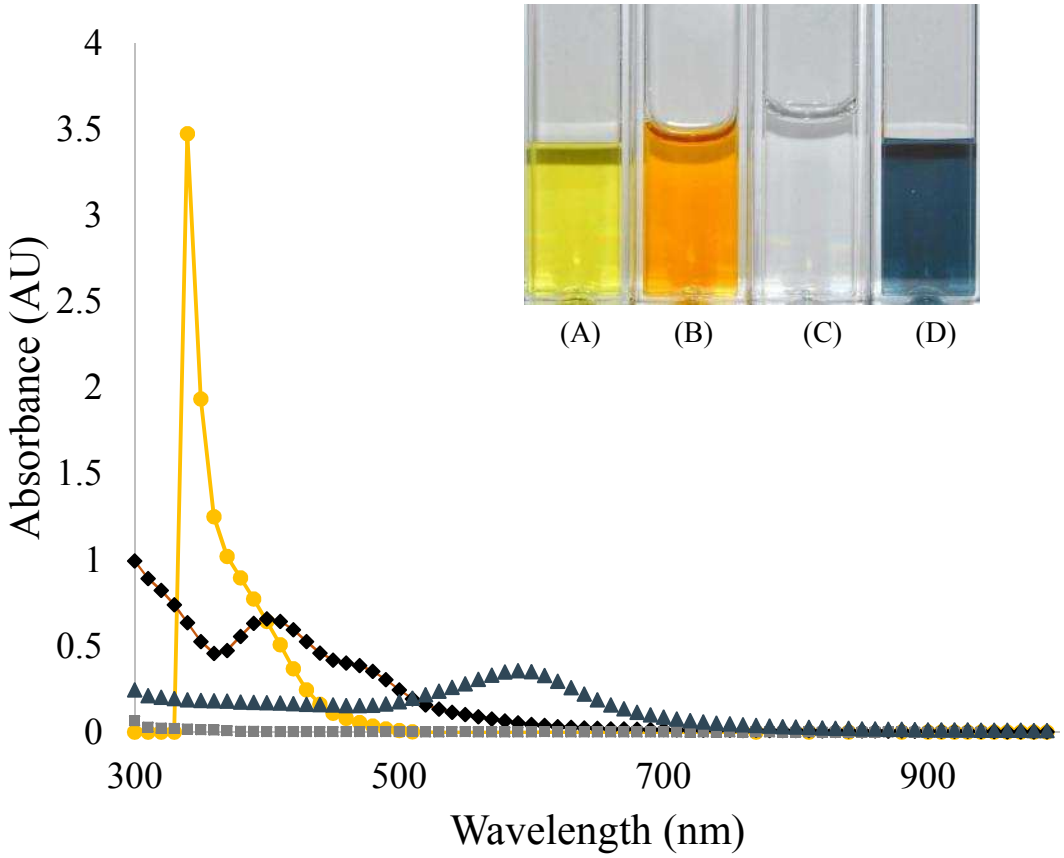

Figure 3.2 UV-Visible spectral profiles of (A) $HAuCl_4$ (Circles) (B) $HAuCl_4$ + C_{16}TAB (Diamonds), (C) $HAuCl_4$ + C_{16}TAB + Ascorbic Acid (Squares) and (D) $HAuCl_4$ + Ascorbic Acid (AA) (Triangles).

We next optimized the concentration of ascorbic acid (AA) in the presence of the surfactant (C_{16}TAB) and gold salt employed in the precursor solution for the plasmonic nanosensor; the maximal dose of 47 Gy was delivered in order to study the effect of ascorbic acid on nanoparticle formation (**Figure 3.3**). A marked increase in nanoparticle formation is

observed when excess AA is used, and the effect saturates at 600 µL of 0.01 M (4 mM AA) (**Figure 3.3**). Although saturation was observed when 4 mM AA were used, we used ~5.9 mM AA for all subsequent experiments in order to ensure adequate quenching of $OH^{\cdot}$ radicals which can reduce the yield of nanoparticles generated. Control experiments with (1) gold salt ($HAuCl_4$) alone, (2) gold salt + $C_{16}TAB$ and (3) gold salt + $C_{12}TAB$ were also carried out in presence of different X-ray doses, but in absence of ascorbic acid. Absorbance profiles of the samples were measured after 7 hours, and the absence of peaks from 500-900 nm indicated the absence of plasmonic (gold) nanoparticles (**Figure 3.4**).

A

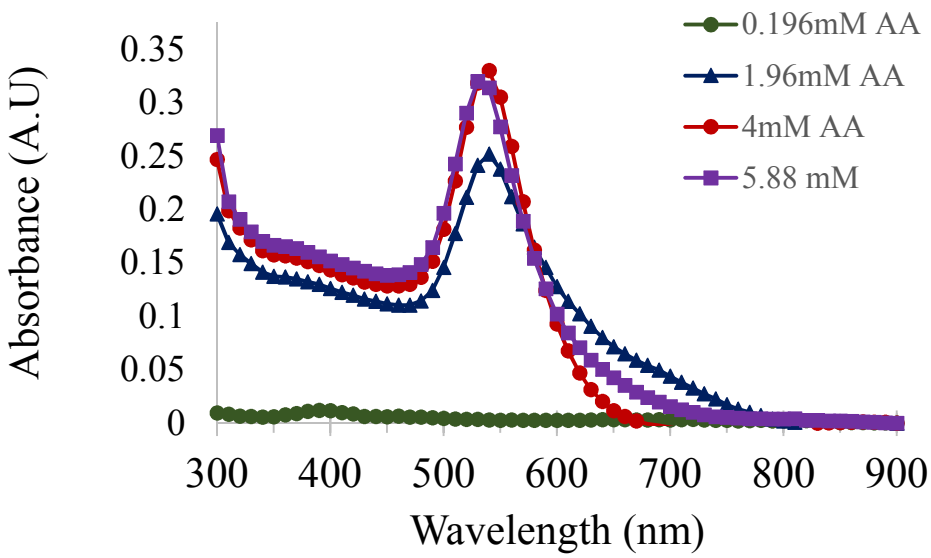

B

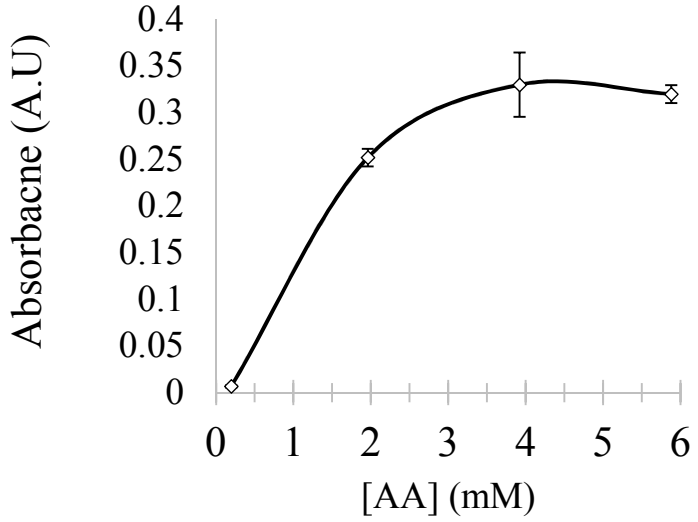

Figure 3.3 (A) UV-Vis spectra of varying ascorbic acid volumes along with gold and C_{16}TAB irradiated at 47 Gy. (B) Maximum absorbance values of samples containing varying concentrations of ascorbic acid. A significant increase in the absorbance peak intensity is observed at ~ 520 nm when the amount of ascorbic acid is increased, indicating an increase in the formation of gold nanoparticles.

A

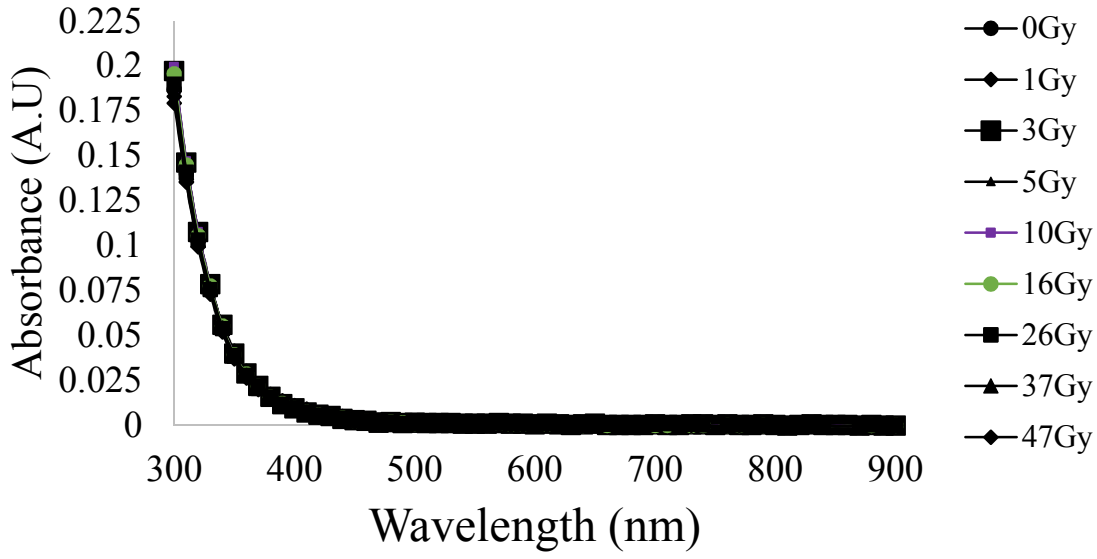

B

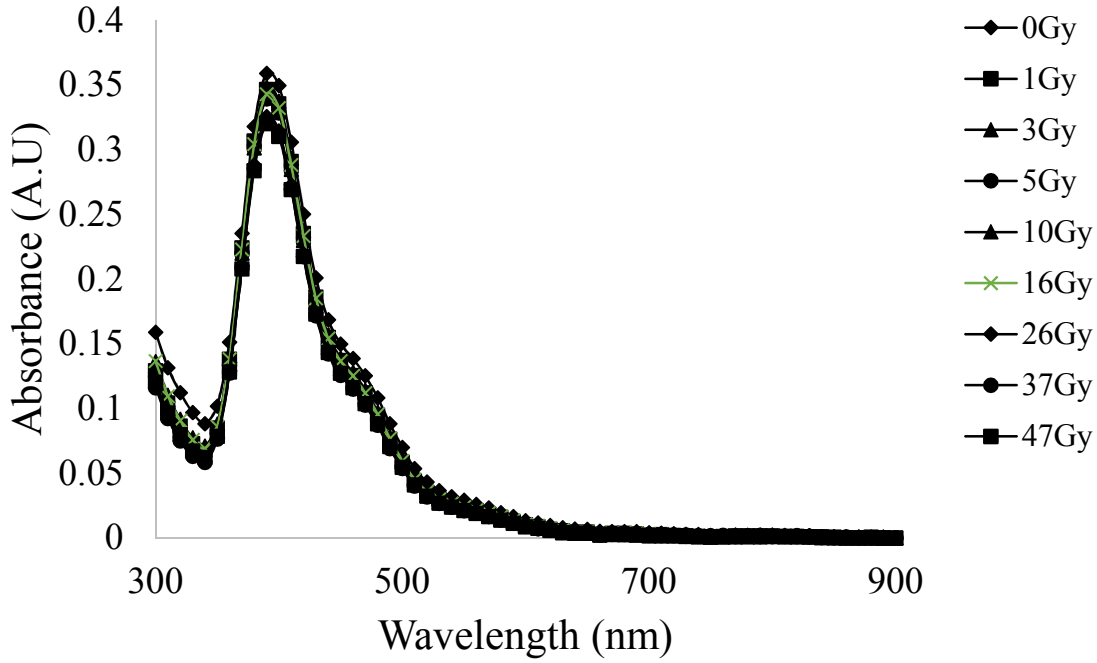
0.4
0.35
0.3
0.25
0.2
0.15
0.1
0.05
0
Absorbance (A.U)
300
500
700
900
Wavelength (nm)
0Gy
1Gy
3Gy
5Gy
10Gy
16Gy
26Gy
37Gy
47Gy

C

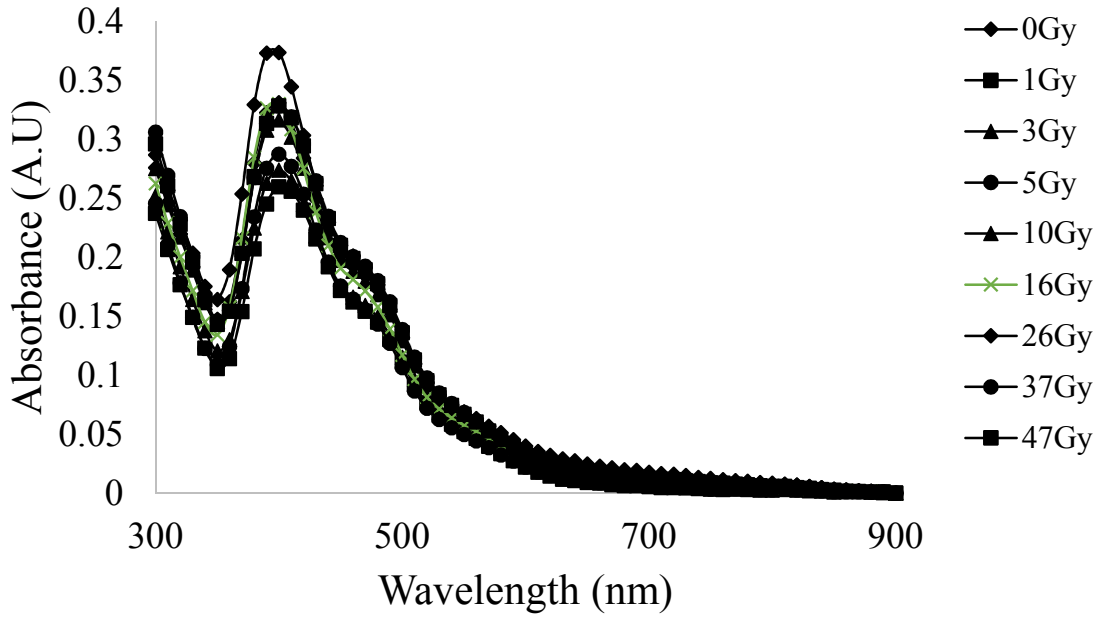

Figure 3.4 Absorbance spectra of (A) gold salt (0.196 mM) (B) gold salt (0.196 mM) + C_{16}TAB (20 mM) (C) gold salt (0.196 mM) + C_{12}TAB (20 mM). Nanoparticle formation is not observed in the absence of ascorbic acid signifying its importance in the plasmonic nanosensor system.

Next, we investigated the efficacy of three cationic surfactants, C_8TAB, C_{12}TAB, and C_{16}TAB, for inducing nanoparticle formation in presence of different doses of ionizing radiation (**Figure 3.5**). All three surfactants have trimethyl ammonium moieties as the head group and bromide as the counter ions; only the lipid chain length was varied as C_8, C_{12}, and C_{16} in these molecules and a concentration of 20 mM was employed for each lipid. As stated previously, a large number of e^-_{aq} and $H^{\cdot}$ radicals are generated following exposure of the solution to X-rays which facilitate the conversion of Au^+ ions to their zerovalent Au^0 state.[99] The Au^0 species act as seeds upon which further nucleation and coalescence occurs.

This, in turn, leads to an increase in size and eventual formation of nanoparticles, which are stabilized by surfactant molecules. Formation of these plasmonic nanoparticles imparts a burgundy / maroon color to the dispersion; the intensity of the color increases with an increase in radiation dose applied (**Figure 3.6**).

A

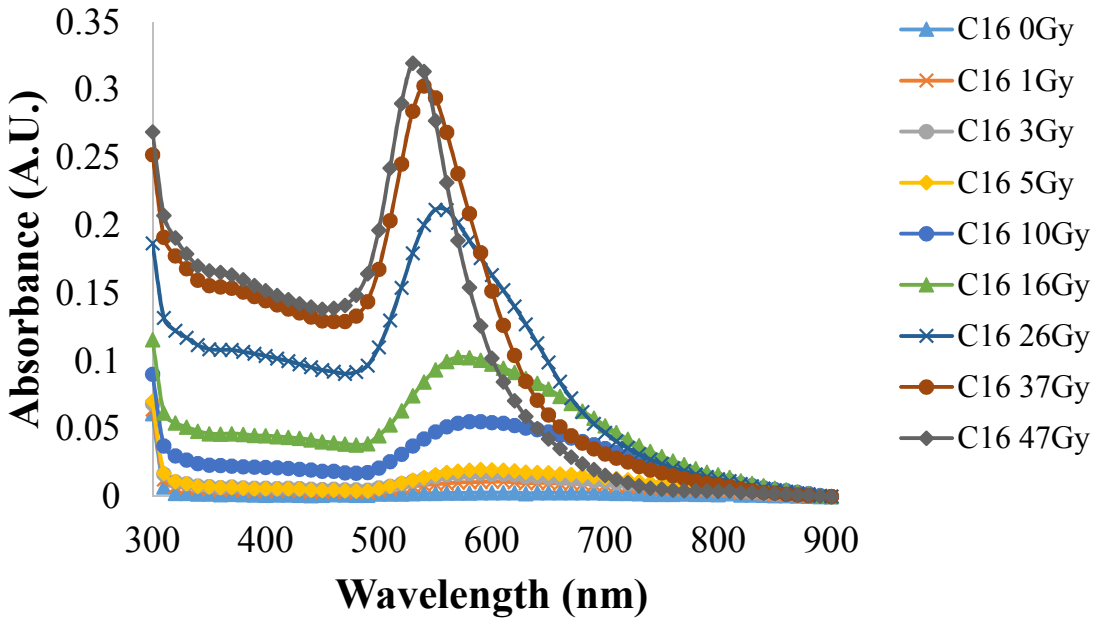

B

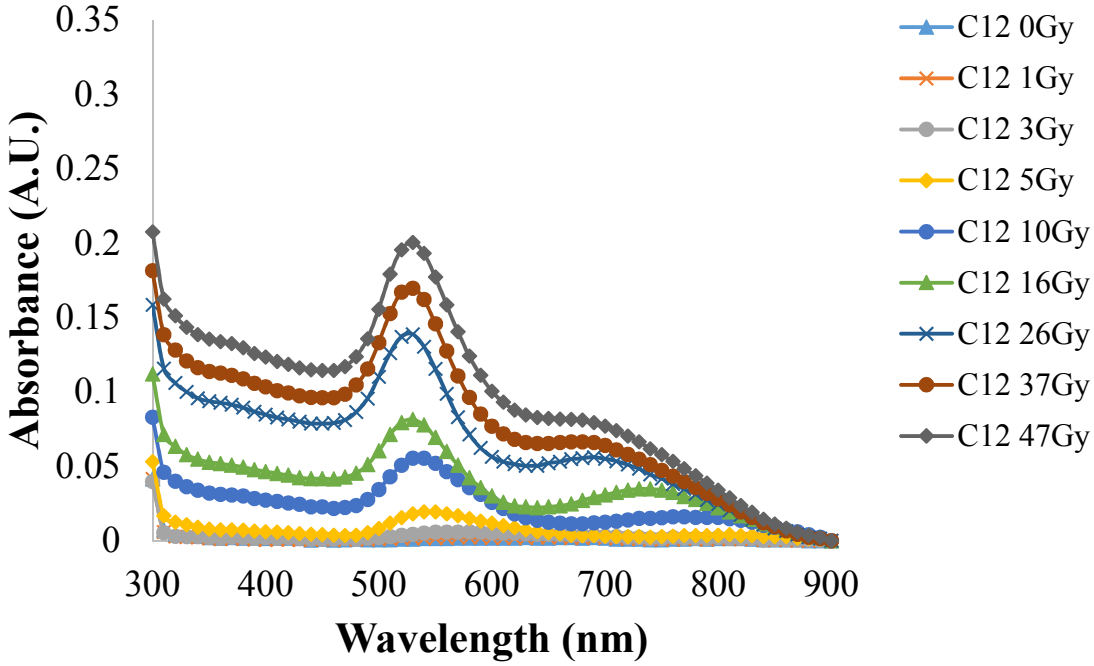
0.35
0.3
0.25
0.2
0.15
0.1
0.05
0
Absorbance (A.U.)
300
400
500
600
700
800
900
Wavelength (nm)
C12 0Gy
C12 1Gy
C12 3Gy
C12 5Gy
C12 10Gy
C12 16Gy
C12 26Gy
C12 37Gy
C12 47Gy

C

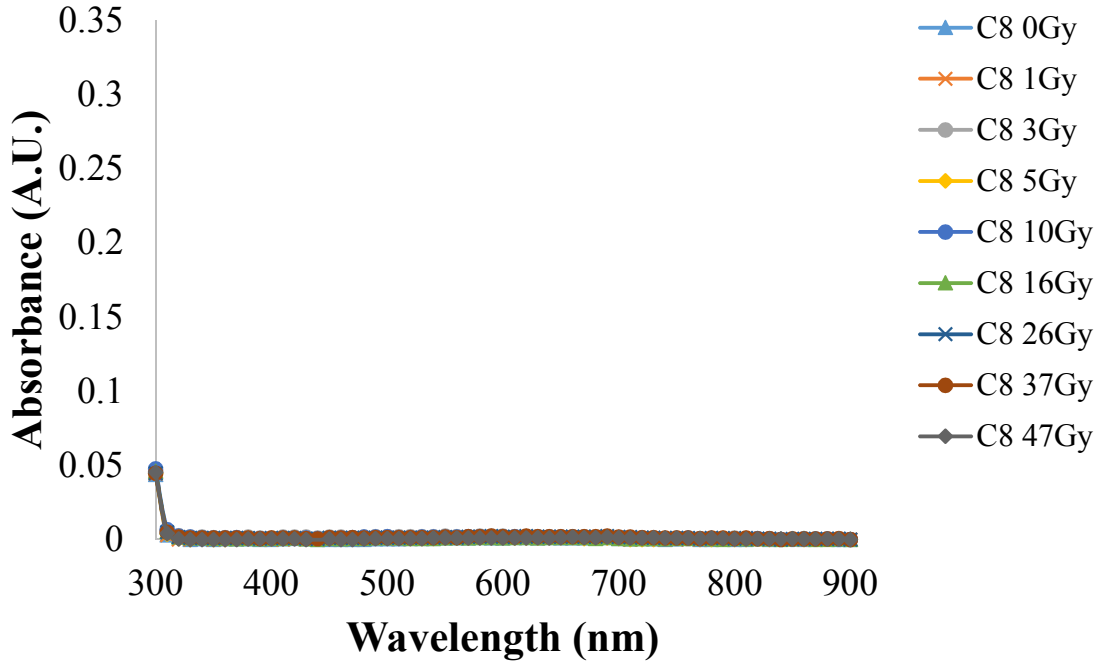

Figure 3.5 UV-Vis absorption spectra of the control (0 Gy) and X-ray irradiated samples containing (A) C_{16}TAB, (B) C_{12}TAB and (C) C_8TAB after 7 hours. The concentration of each lipid surfactant was 20 mM.

A

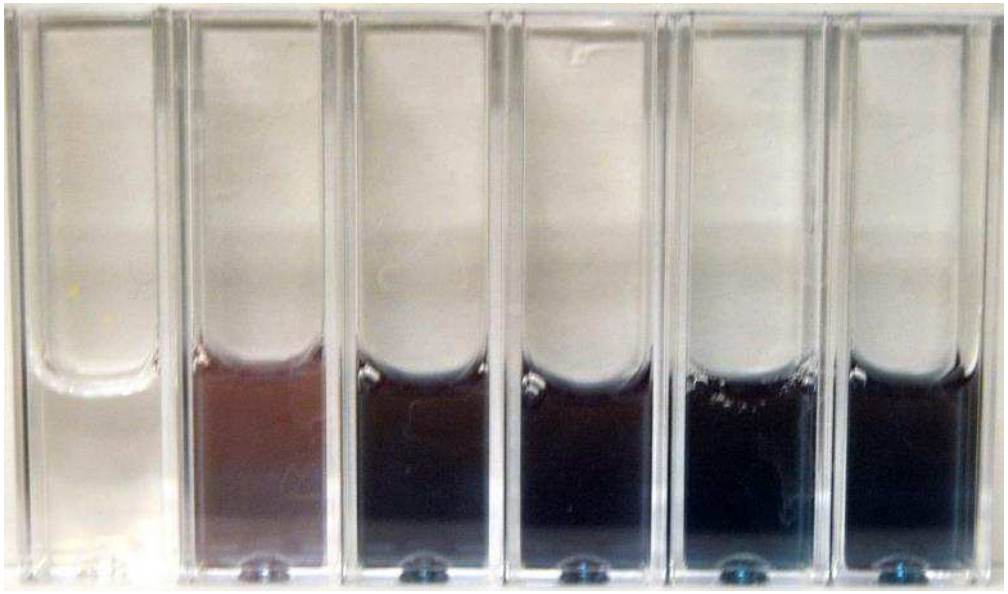

0 0.5 1 1.5 2 2.5

B

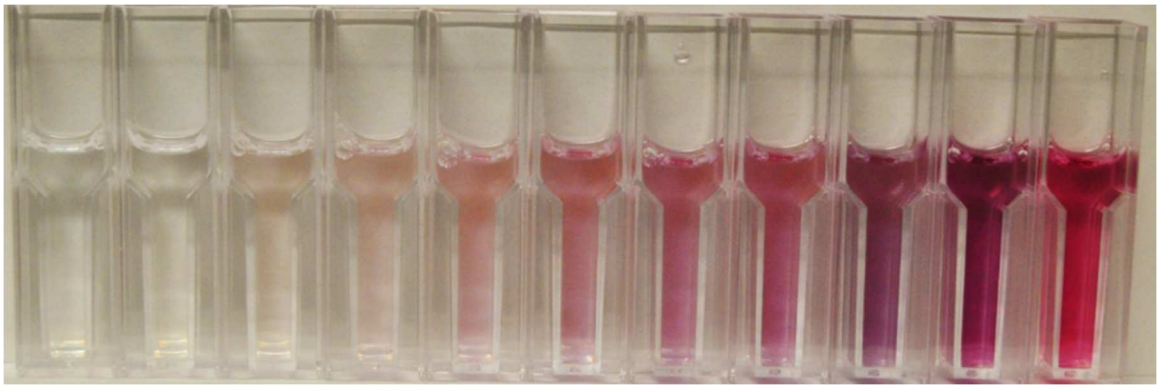

0 1 3 5 7.5 10 12.5 15 26 37 47

C

0 1 3 5 10 16 26 37 47

D

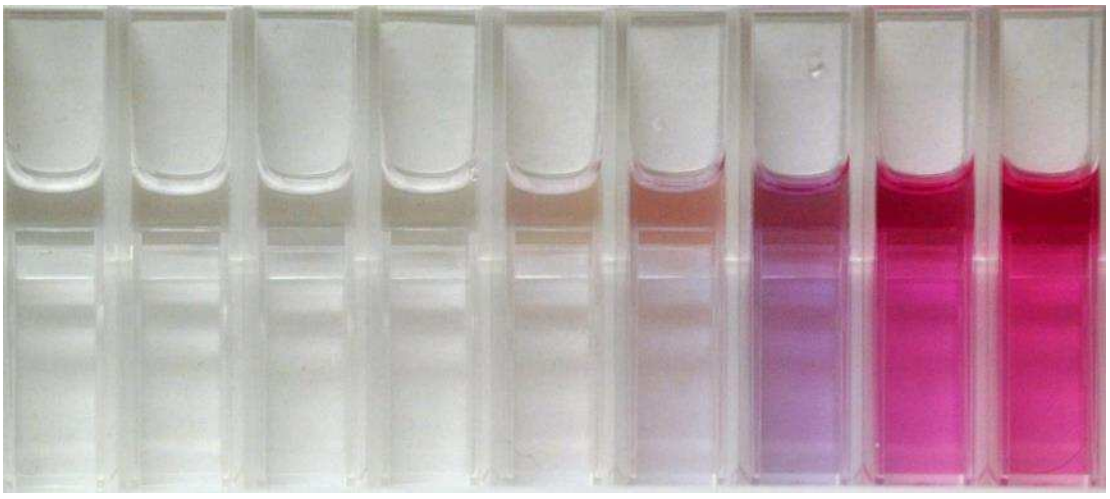

0 1 3 5 10 16 26 37 47

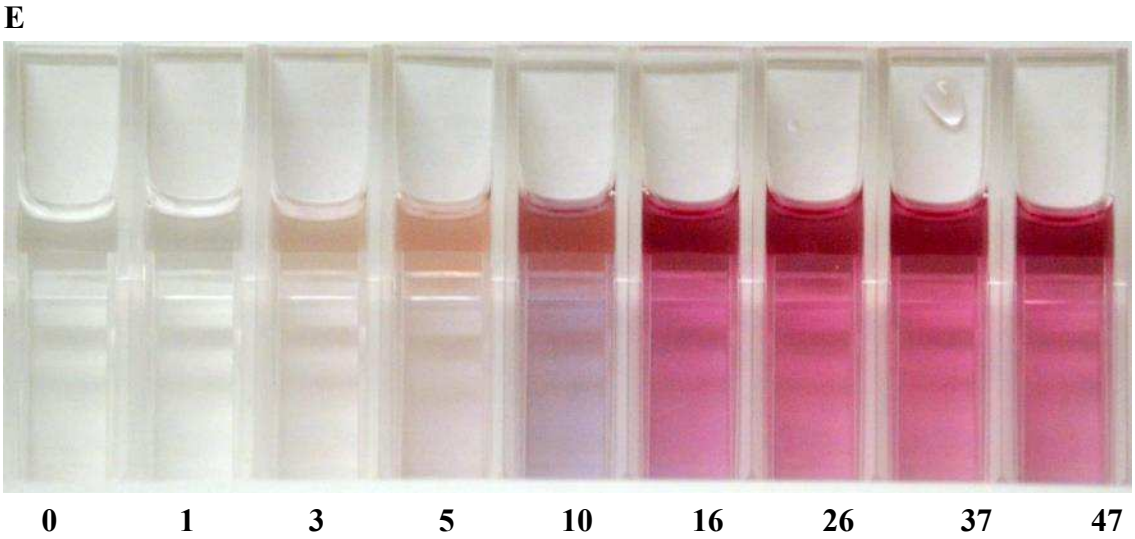

Figure 3.6 Optical images of samples containing different C_{16}TAB and C_{12}TAB concentrations irradiated with a range of X-ray doses (Gy) (A) 2 mM C_{16}TAB, (B) 4mM C_{16}TAB, (C) 10mM C_{16}TAB, (D) 20mM C_{16}TAB and (E) 20mM C_{12}TAB 2 hours post X-ray irradiation. The corresponding X-ray radiation dose leading to the observed visual color change is indicated below each sample in Gray (Gy).

Nanoparticle formation was seen as early as 1 h following irradiation in many cases, although 2 h were required for samples irradiated with lower doses (1, 3 and 5 Gy) (**Figure 3.7**). No significant differences in absorbance intensity were observed thereafter until a period of 7 hours, which was the maximum duration investigated in these cases. Nanoparticle formation was observed at radiation doses as low as 1 Gy, which is well within the range of doses employed for radiotherapy.[144] While C_{16}TAB or C_{12}TAB were effective at templating nanoparticle formation even at low doses (1-5 Gy), C_8TAB did not show any propensity for templating nanoparticle formation even at the highest radiation dose (47 Gy) employed. C_{12}TAB-templated gold nanoparticles exhibited unique spectral profiles under ionizing radiation; two spectral peaks - one between 500 and 550 nm and

another between 650 and 800 nm - were seen (**Figure 3.5 B**). This is in contrast to C_{16}TAB which exhibited only a single peak between 500 and 600 nm (**Figure 3.5 A)**. The linear response of absorbance due to nanoparticle formation, seen between 5-37 Gy, was significantly more pronounced for C_{16}TAB than that for C_{12}TAB (**Figure 3.8**). Although nanoparticle formation was seen in the 1-5 Gy range, the absorbance of the dispersions under these conditions did not fall in the linear range (5-37 Gy), which indicated that the nanosensor was not sensitive at these lower doses. Given these findings, we focused our subsequent studies mainly on the C_{16}TAB lipid surfactant in order to further optimize the nanosensor.

A

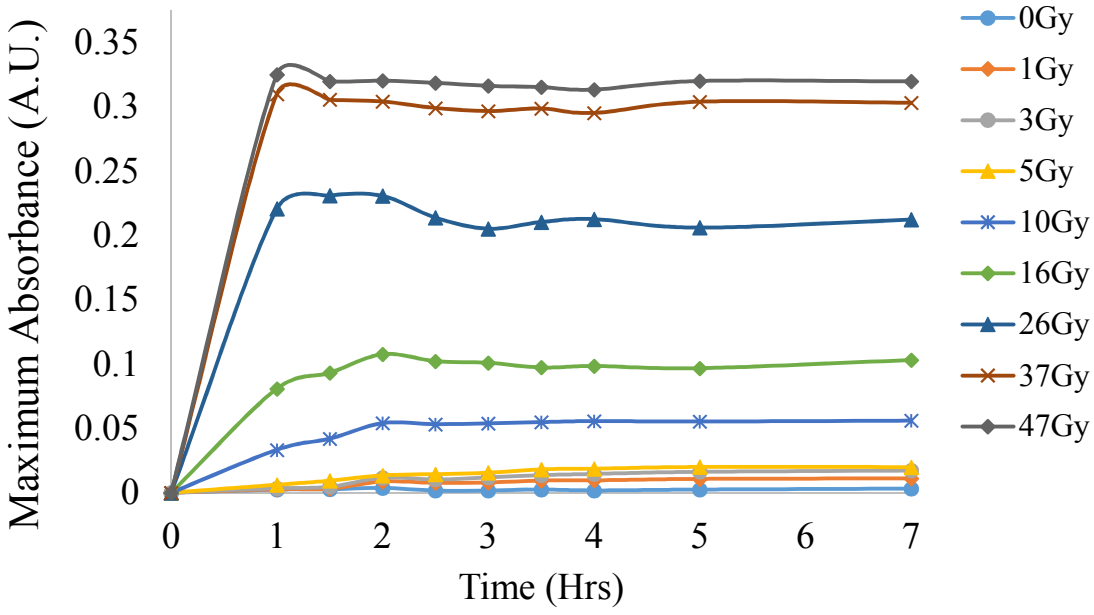

B

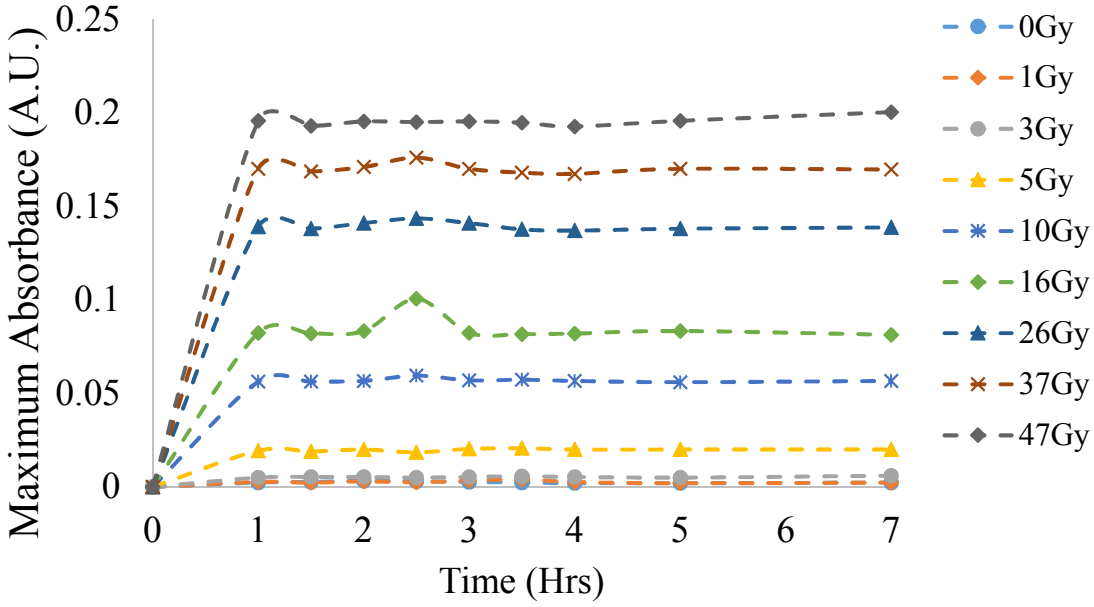

C

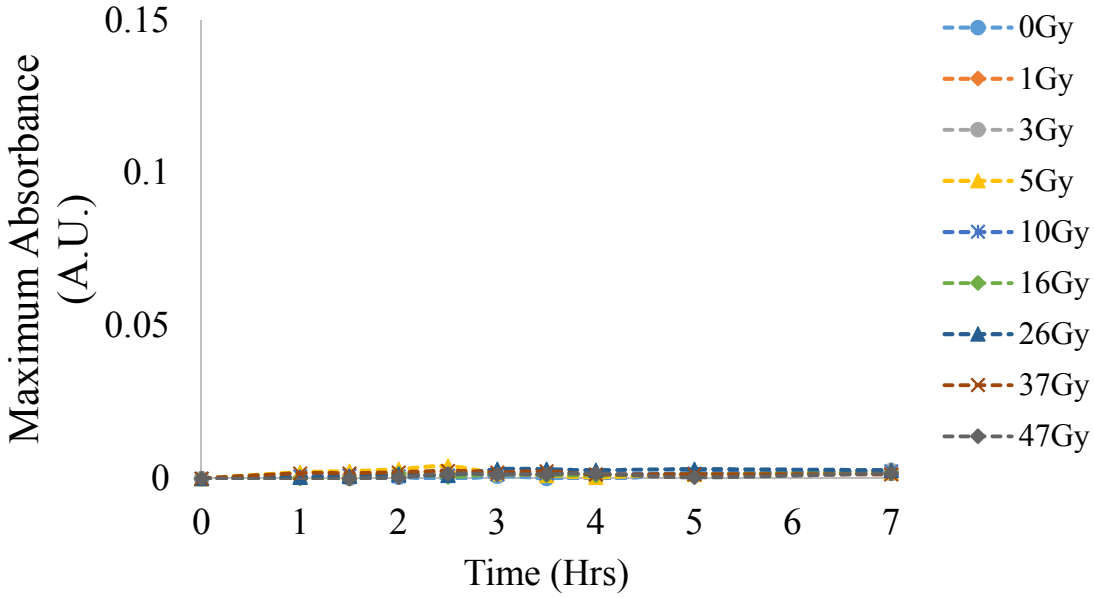

Figure 3.7 Kinetics of gold nanoparticle formation following exposure to different doses of ionizing radiation (0-47 Gy) for (A) C_{16}TAB, (B) C_{12}TAB and (C) C_8TAB. Maximum (peak) absorbance values, typically between 450 nm and 650 nm, are plotted as a function of time following irradiation. The maximal value is reached at 1 h in most cases, but requires up to 2 h for lower doses. The value remains unchanged over a period of 7 h.

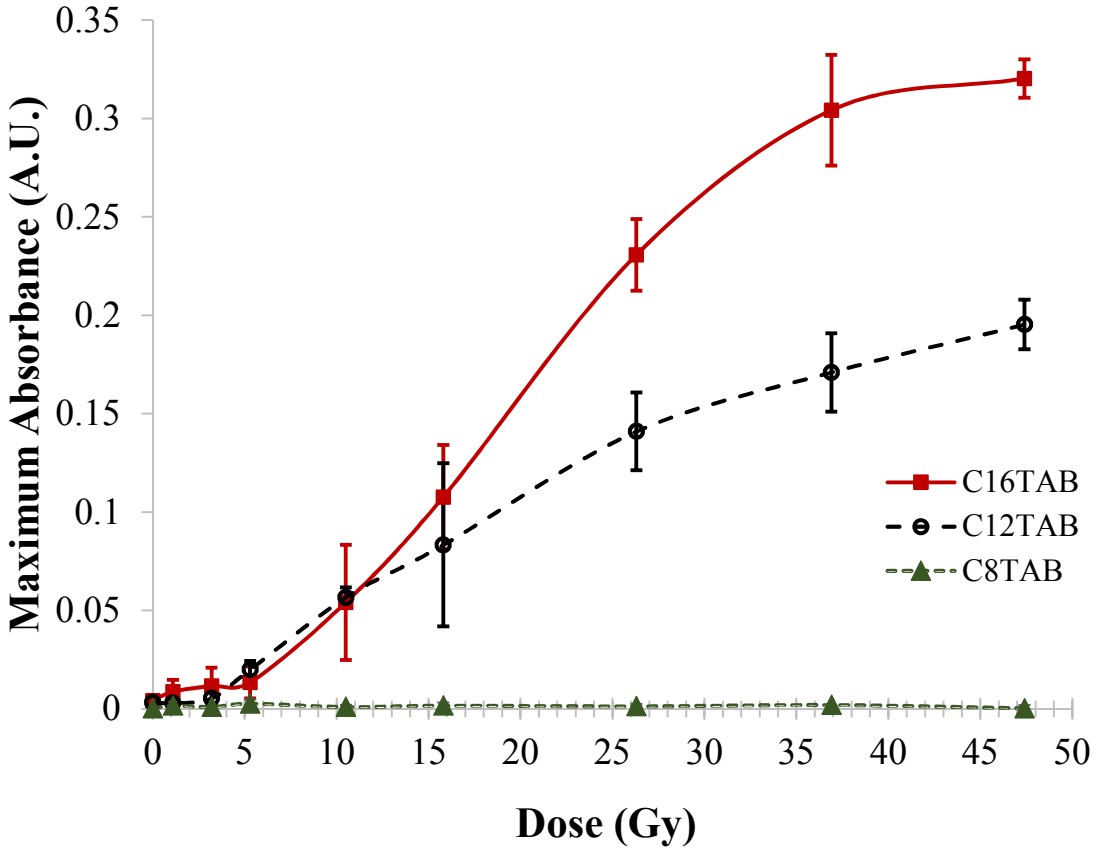

Figure 3.8 Maximum absorbance vs. radiation dose (Gy) after 2 hours of X-ray irradiation. C_{16}TAB (red filled squares, solid line) and C_{12}TAB (orange open circles, dotted line) surfactants. C_8TAB (green triangles, dotted line) does not show any response to radiation. The lipid concentration was 20 mM in all cases.

The critical micelle concentration (CMC) of C_{16}TAB is reported to be approximately 1 mM.[145] Using the pyrene fluorescence assay, we determined the CMC of C_{16}TAB in the nanosensor precursor solution (*i.e.* gold salt and ascorbic acid in deionized water) to be ~0.39 mM, which was slightly lower than ~0.88 mM determined in deionized (DI) water (**Figure 3.9**). Pre-micellar aggregates are thought to exist when C_{16}TAB concentration is lower than 7.4 mM, while stable micelles are observed at higher concentrations of the lipid

surfactant.[146] It has been previously suggested that smaller, pre-micellar aggregates can facilitate enhanced catalytic activity of Fe(III) and promote oxidation of sulphanilic acid compared to fully matured micelles, likely due to the increased ratio of the reactant species to the surfactant molecules.[147] We therefore hypothesized that increasing the ratio of the metallic species (Au^{+}) to the aggregate (pre-micellar / micellar) $C_{16}TAB$ species will lead to greater propensity for nanoparticle formation upon exposure to ionizing radiation and therefore increased sensitivity of the resulting nanosensor at lower radiation doses. Based on the assumption that the number of aggregate species increases with lipid concentration,[146] we next investigated different concentrations of $C_{16}TAB$ (0.7 mM, 2 mM, 4 mM and 10 mM) in the nanosensor, while keeping the concentrations of gold ions and ascorbic acid constant.

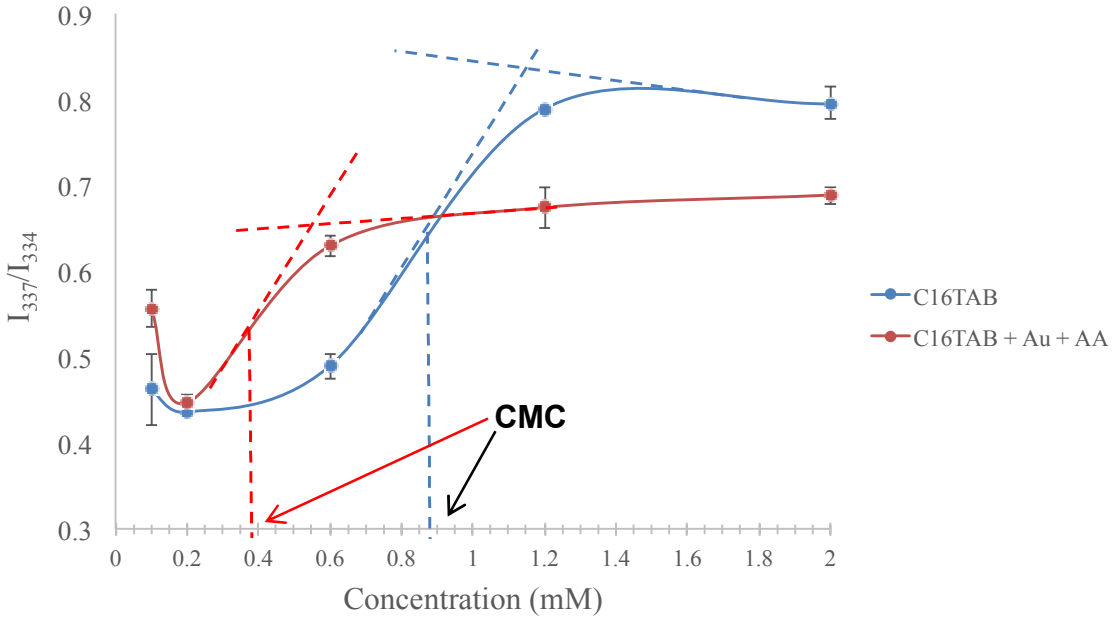

Figure 3.9 Determination of the critical micelle concentration (CMC) value for C_{16}TAB in the nanosensor precursor solution ('C_{16}TAB + Au + AA' in the legend) and DI Water ('C_{16}TAB' in the legend) using the pyrene fluorescence assay. The intensity ratio of I_{337}/I_{334} was plotted as a function of the lipid surfactant concentration and the CMC value was determined from the mid-point as shown in the figure. The dashed lines are for visualization alone. n = 2 independent experiments. Spontaneous nanoparticle formation was seen with the nanosensor precursor solution at 0.1 mM resulting in increased fluorescence intensity at this condition. As seen in the figure, the CMC of C_{16}TAB was ~0.88 mM and that for C_{16}TAB in the nanosensor precursor solution was ~0.39 mM.

Use of C_{16}TAB concentrations below its CMC in the nanosensor precursor solution resulted in spontaneous formation of gold nanoparticles in absence of ionizing radiation; gold nanoparticle formation can be seen from the characteristic absorbance peak of the dispersion in **Figures 3.9 and 3.10**. However, the propensity for spontaneous nanoparticle formation is significantly reduced or lost at concentrations well above the CMC. A distinct color change can be observed for radiation doses as low as 0.5 Gy at a C_{16}TAB concentration of 2mM, which is above the CMC of the lipid surfactant (**Figures 3.6A** and **3.11**). A linear response was observed for radiation doses ranging from 0.5 to 2 Gy under these conditions (**Figure 3.12**). As the concentration of C_{16}TAB increases (4, 10, 20 mM), the radiation dose required to template nanoparticle formation also increases (**Figures 3.6** and **3.11**). Furthermore, the color of the nanoparticle dispersion formed is significantly different in cases of 2mM C_{16}TAB (blue-violet) compared to that observed in cases of 4 mM (bluish-red), 10 mM (red / pink) and 20 mM (burgundy / maroon) C_{16}TAB, likely indicating different sizes of nanoparticles formed under these conditions. An increase in color intensity is observed with increasing radiation dose (**Figures 3.5 and 3.6)**, which allows for dose quantification using absorbance measurements. While it is most desired that the nanosensor is sensitive to therapeutic doses used in conventional and

hyperfractionated radiotherapy (~0.5-2.0 Gy) as seen in the case of 2mM C_{16}TAB, results with different concentrations of the lipid surfactant indicate that the response of the plasmonic nanosensor can be tuned by simply modifying the concentration of the lipid surfactant. Such visual colorimetric sensors possess significant advantages of convenience and likely, cost, over those that employ fluorescence changes or electron spin resonance measurements for detecting ionizing radiation.

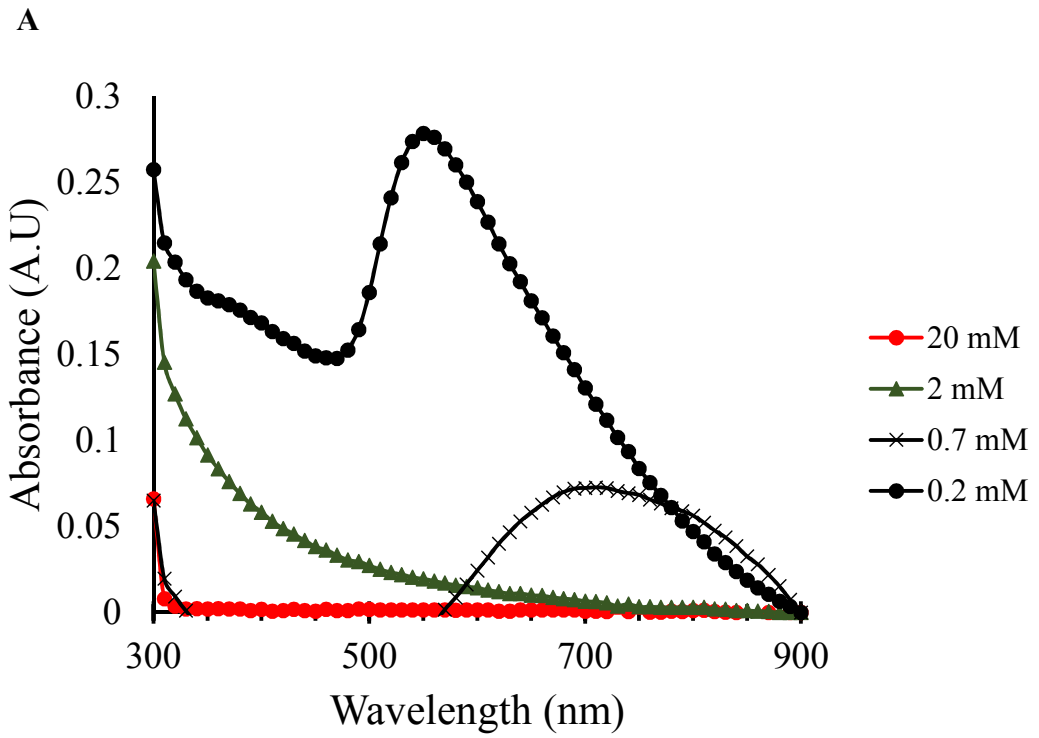

B

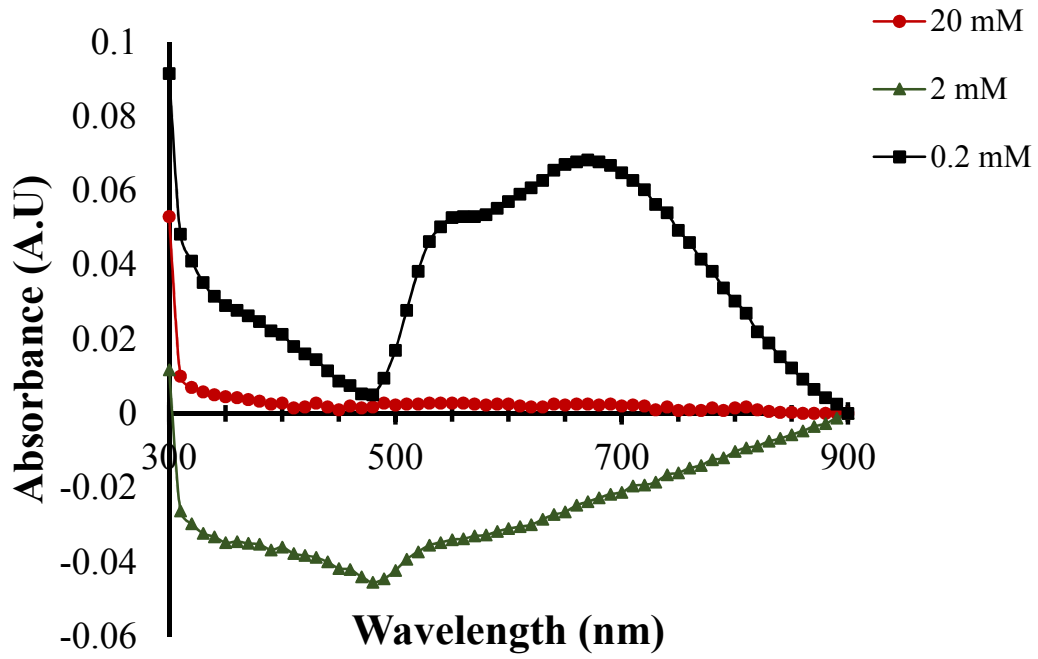
20 mM
2 mM
0.2 mM
0.1
0.08
0.06
0.04
0.02
0
-0.02
-0.04
-0.06
300
500
700
900
Absorbance (A.U)
Wavelength (nm)

C

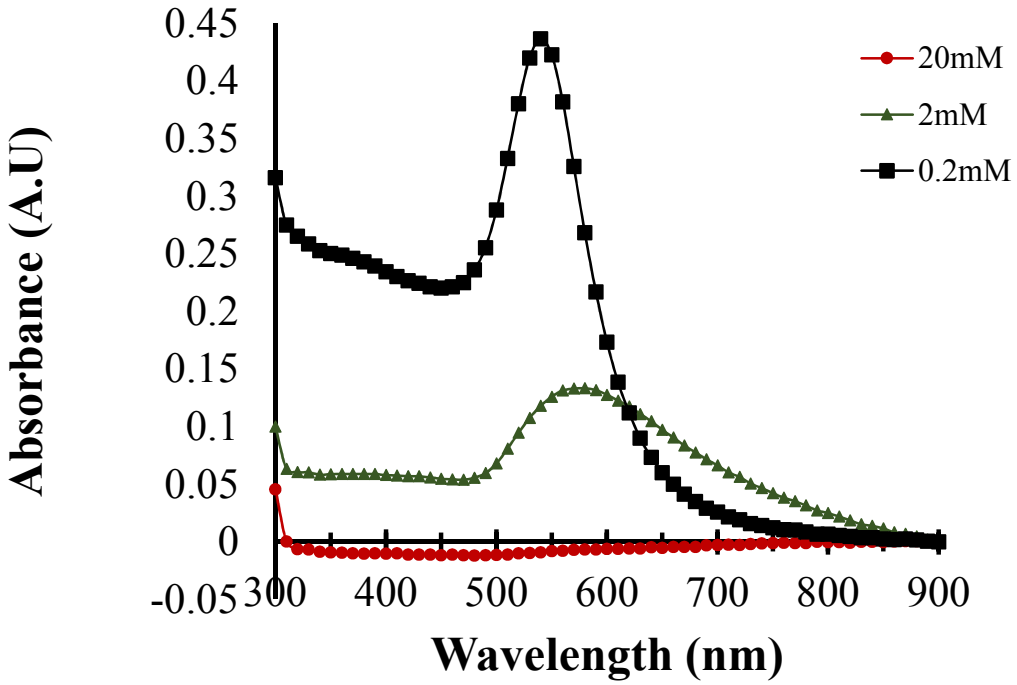
20mM
2mM
0.2mM
0.45
0.4
0.35
0.3
0.25
0.2
0.15
0.1
0.05
0
-0.05
300
400
500
600
700
800
900
Absorbance (A.U)
Wavelength (nm)

Figure 3.10 Absorbance spectra of precursor monovalent gold salt solutions under conditions of no radiation (i.e. 0 Gy) in presence of different concentrations of (A) C_{16}TAB and (B) C_{12}TAB (C) C_8TAB recorded after 10 minutes of incubation. Spontaneous nanoparticle formation was seen at 0.2 mM for all lipid surfactants, as indicated by the characteristic absorbance peak of gold nanoparticles at ~520 nm. In contrast, no nanoparticle formation was observed at a lipid concentration of 20 mM for up to 7 h.

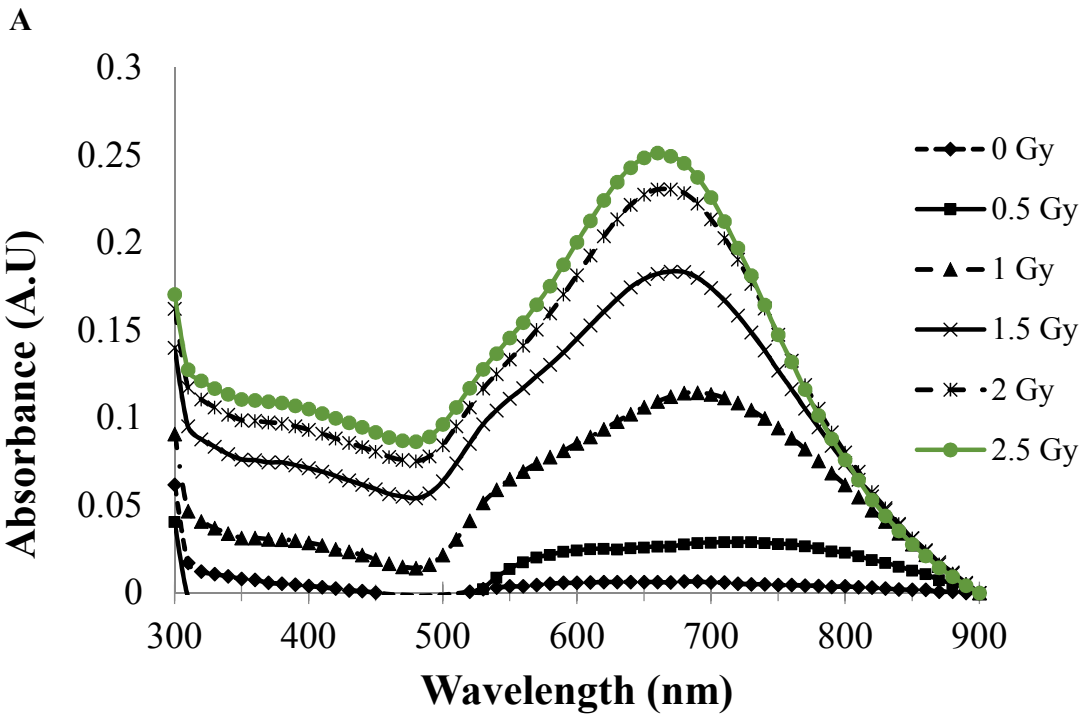

B

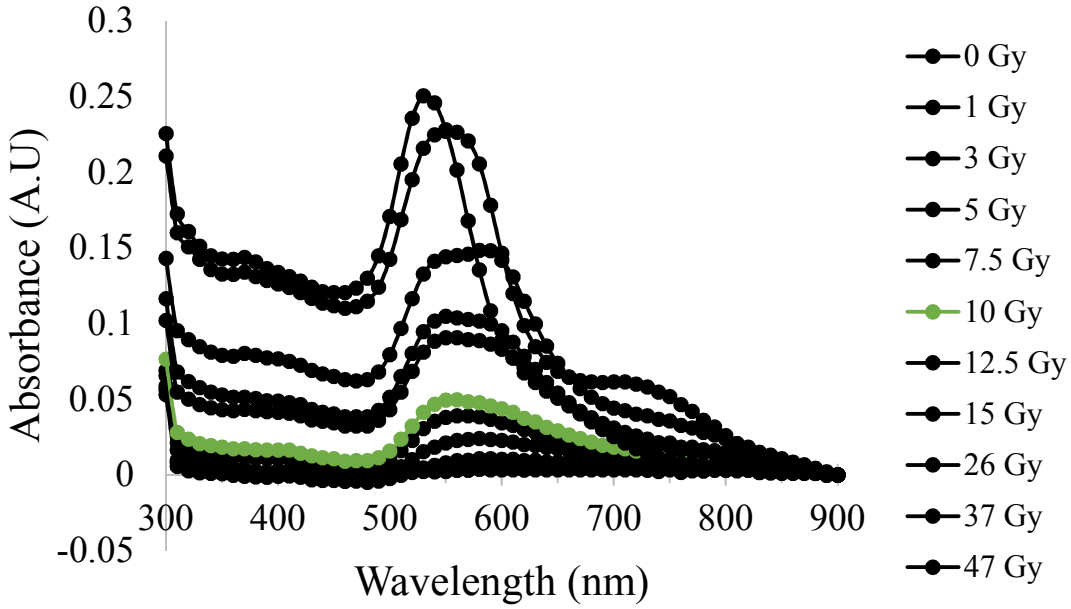
0.3
0.25
0.2
0.15
0.1
0.05
0
-0.05
Absorbance (A.U)
300
400
500
600
700
800
900
Wavelength (nm)
0 Gy
1 Gy
3 Gy
5 Gy
7.5 Gy
10 Gy
12.5 Gy
15 Gy
26 Gy
37 Gy
47 Gy

C

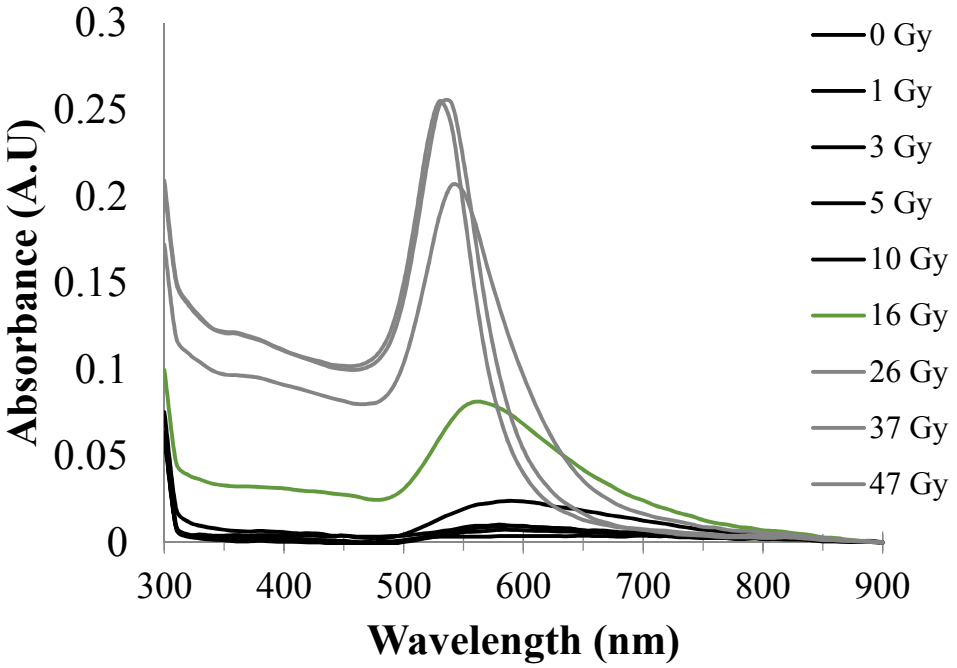
0.3
0.25
0.2
0.15
0.1
0.05
0
Absorbance (A.U)
300
400
500
600
700
800
900
Wavelength (nm)
0 Gy
1 Gy
3 Gy
5 Gy
10 Gy
16 Gy
26 Gy
37 Gy
47 Gy

D

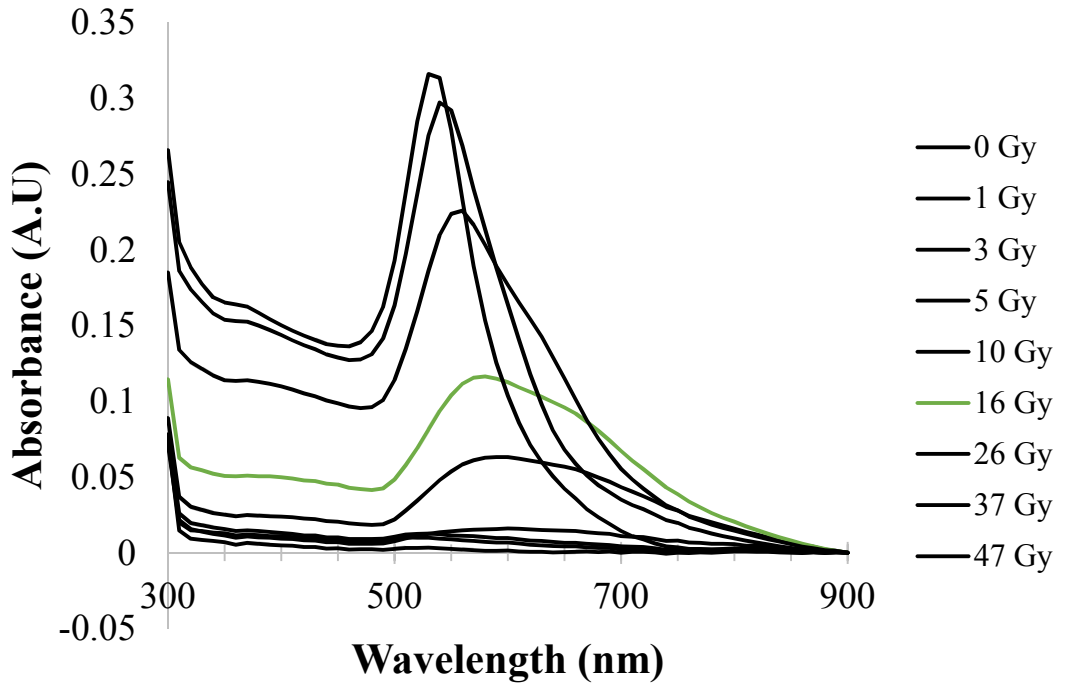

Figure 3.11 Maximum absorbance vs. wavelength for different concentrations of C_{16}TAB after a duration of 2 hours post irradiation with different doses of X-rays. (A) 2mM (B) 4mM (C) 10mM (D) 20mM C_{16}TAB.

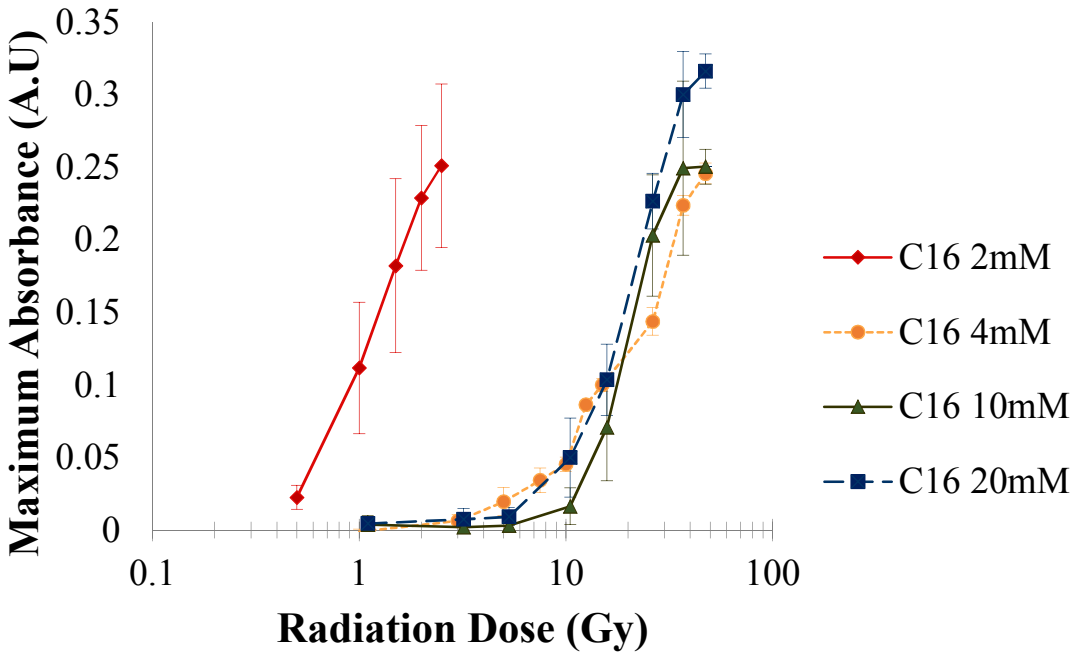

Figure 3.12 Maximum absorbance vs. radiation dose for varying concentrations of C_{16}TAB 2 hours post X-ray irradiation. Red filled diamonds, solid line: 2 mM C_{16}TAB, Orange filled circles, dashed line: 4 mM C_{16}TAB, Green filled triangles, solid line: 10 mM C_{16}TAB, and Blue filled squares, dashed line: 20mM C_{16}TAB.

Free radicals generated upon radiolysis of water are thought to be localized in finite volumes called spurs.[148] These spurs can expand, diffuse, and simultaneously, react, leading to the formation of molecular products. These highly reactive free radicals have very short lifetimes of $\sim 10^{-7} - 10^{-6}$ s at 25°C.[148] Reaction volumes consisting of nanoscale features can facilitate enhanced reaction kinetics and ensure efficient utilization of these free radicals for the formation of nanoparticles.[149] In case of the current plasmonic nanosensor, this was achieved by the use of amphiphilic molecules that self-assemble into micelles above their respective critical micellar concentrations (CMCs). A strong interaction is possible between the positively charged head group of the lipid surfactant micelles and the negatively charged $AuCl_4^-$ ions (**Figure 3.1**).[150] This interaction can lead

to incorporation of $AuCl_4^-$ ions in the water-rich Stern layer leading to the formation of a 'nanoreactor'.[149, 150] However, spontaneous formation of nanoparticles (*i.e.* in absence of ionizing radiation) was seen when concentrations of C_{16}TAB were lower than the CMC (**Figure 3.10**). We hypothesize that spontaneous nanoparticle formation observed at lower concentrations of the surfactant is likely due to negligible steric hindrance between the surfactant and ascorbic acid;[22] absence of these barriers results in nanoparticle growth which can be observed spectroscopically.[151] It is only when the concentrations of C_{12}TAB and C_{16}TAB are higher than the CMC, that no spontaneous formation of gold nanoparticles is seen in the precursor solution, and ionizing radiation is required to induce nanoparticle formation. Of the three lipid surfactants, only the concentration of C_8TAB was significantly below its CMC value (130 mM),[152] while the concentrations employed were significantly higher than the CMCs of C_{12}TAB (CMC ~15 mM[145]) and C_{16}TAB (CMC ~1 mM[145]). In the case of C_8TAB, there is an absence of these "nanoreactors", which may explain lack of nanoparticle formation under these conditions. The self-assembly of C_{12}TAB and C_{16}TAB lipid surfactants to nanoscale micelles above their respective CMCs is therefore key for the functioning of the plasmonic nanosensor.

Key features of gold nanoparticle absorbance spectra include the shape of the surface plasmon resonance band and the position of the maximal (peak) absorption wavelength. While C_{16}TAB-templated nanoparticles showed a single maximal absorption peak (at ca. 520 nm), C_{12}TAB-templated nanoparticles showed two peaks: one at ca. 520 nm (visual region) and another at ca. 700 nm (near infrared or NIR region; **Figure 3.5 B**), particularly at higher doses of ionizing radiation. The width of the spectral profiles at lower doses

signifies a somewhat polydisperse population of the nanoparticles (**Figures 3.5 A, B and 11**)[153]. The absorbance peaks are red-shifted with decreasing radiation doses, suggesting an increase in particle size under these conditions compared to those obtained at higher doses.

Nanoparticles formed in presence and absence of ionizing radiation were further characterized for their hydrodynamic diameters and morphology using dynamic light scattering (**Figure 3.13**) and transmission electron microscopy (TEM; **Figure 3.14, 3.15 and 3.16**), respectively. TEM images indicated that a mixture of spherical and rod-shaped nanoparticles was observed at the higher radiation doses (47 Gy) in case of C_{12}TAB as the templating surfactant (**Figure 3.14 D**). This can explain the absorption spectral profile with peaks in both, the visual and near infrared range of the spectrum in case of nanoparticles templated using 20 mM C_{12}TAB (**Figure 3.5 B**). A significant decrease in the near infrared absorption peak is observed at lower X-ray doses. Although the spectral profile indicates formation of gold nanospheres, we observed an ensemble of unique anisotropic (dendritic and nanowire) structures (**Figure 3.15**). Such structures were not observed at similar X-ray doses when 20 mM C_{16}TAB was used as the templating surfactant. A strong interaction energy (U) between C_{12}TAB and Au (111) has been previously described[154]. This strong affinity for the Au (111) crystal plane is thought to favor slower desorption of the surfactant along Au (111) leading to growth along other available crystal planes. This can allow for the formation of rod-shaped and other anisotropic nanostructures. Although C_{16}TAB has been used to synthesize nanowires and nanorods previously, these methods typically involve the use of additional chemicals including NaOH or $AgNO_3$.[102,155] In the current

case, it is likely that the gold nanoparticles aggregate more rapidly in situ due to the strong hydrophobic nature of the long of C_{16}TAB chains, leading to the formation of quasi-spherical nanoparticles and not anisotropic nanostructures.[154]

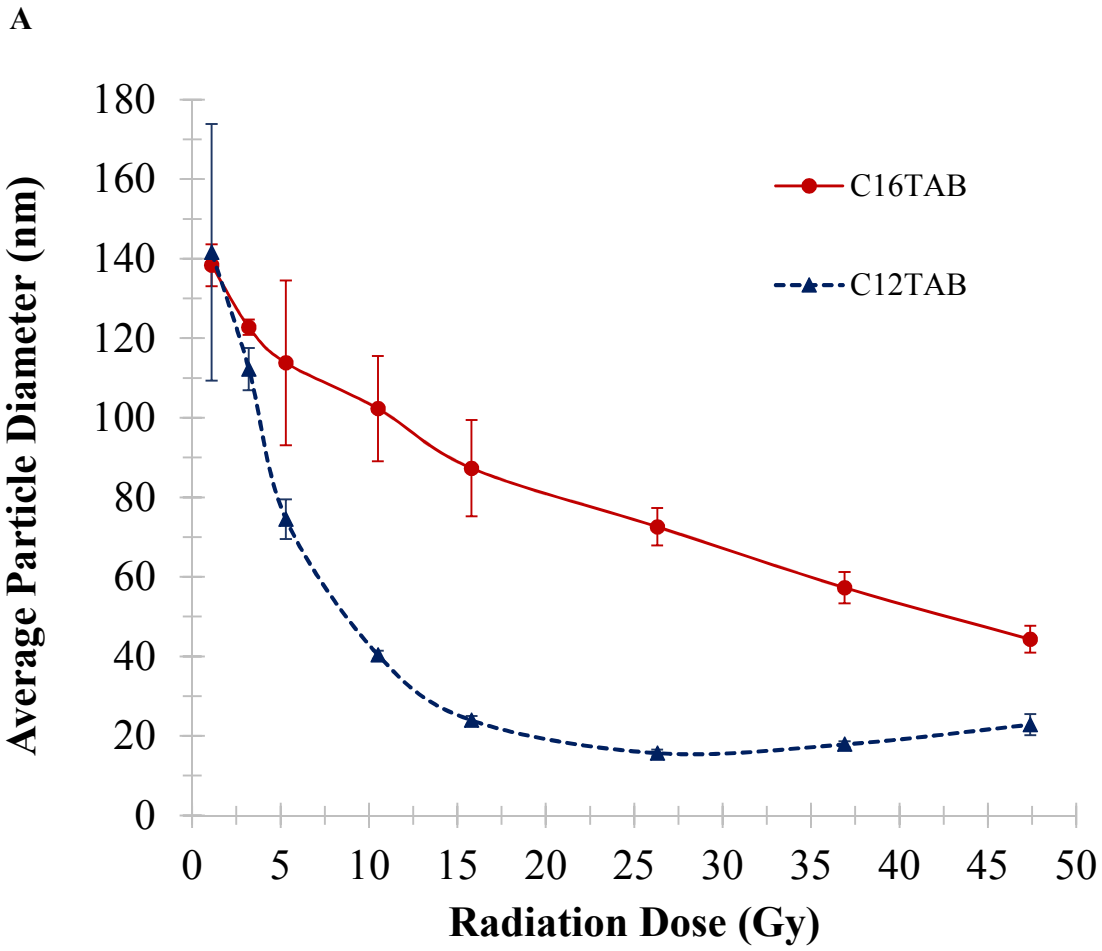

B

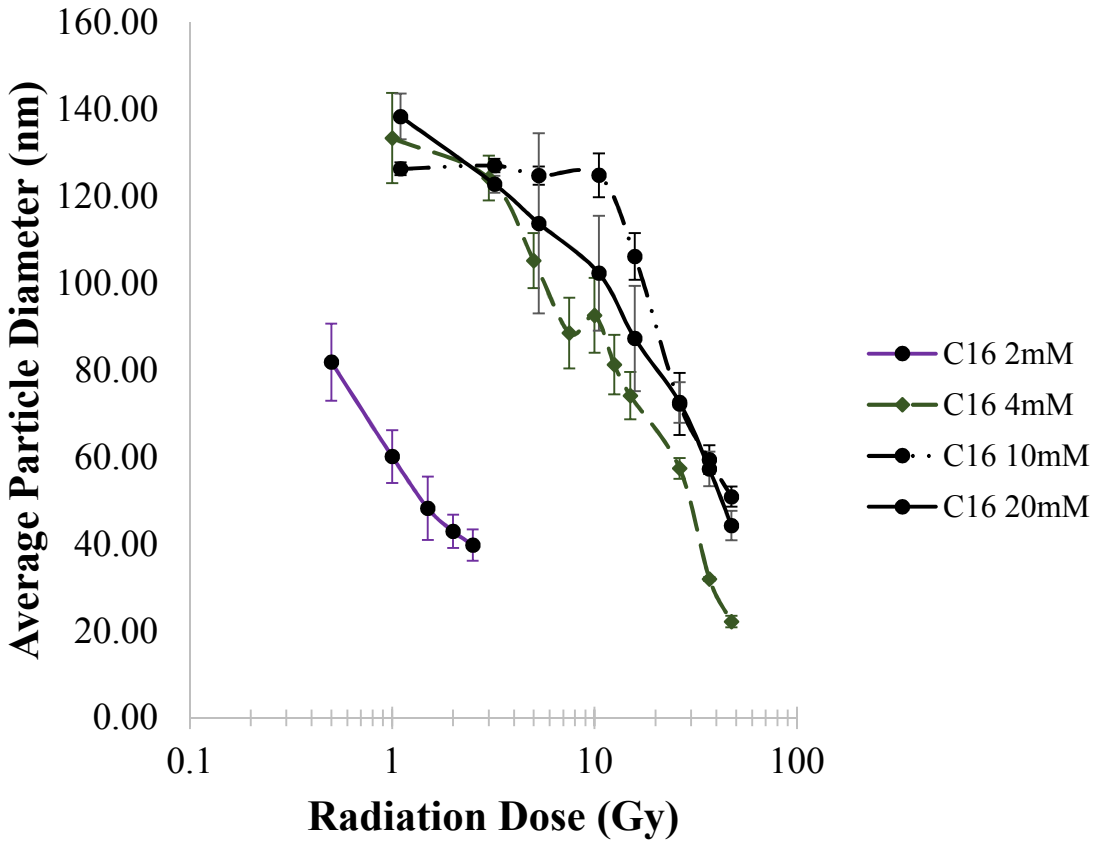

Figure 3.13 (A) Nanoparticle hydrodynamic diameter vs. radiation dose evaluated using dynamic light scattering. An increase in average particle diameter is observed with a decrease in radiation dose for both 20 mM C_{16}TAB (red circles) and 20 mM C_{12}TAB (blue triangles). (B) Hydrodynamic diameter vs. radiation dose for different concentrations of C_{16}TAB (plotted on a $\log_{10}$ scale on the X-axis). An increase in average particle diameter is observed with a decrease in radiation dose for all four different concentration of C_{16}TAB employed. Blue circles: 2mM; green diamonds: 4mM; orange circles: 10mM and yellow circles: 20mM C_{16}TAB.

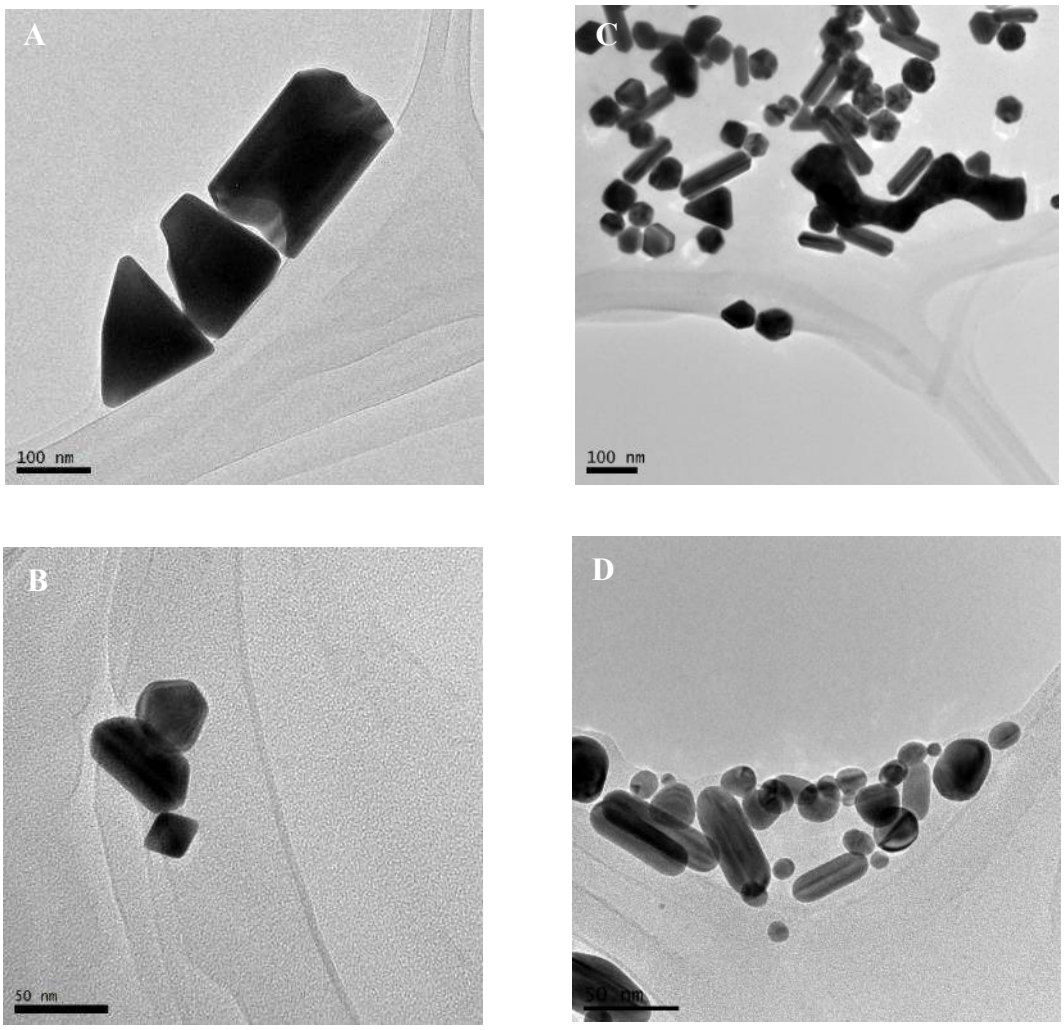

Figure 3.14 Transmission Electron Microscopy (TEM) images of nanoparticles after exposure to ionizing (X-ray) radiation using two different lipid surfactants, 20 mM C_{16}TAB (left) and 20 mM C_{12}TAB (right). (A) 1 Gy, (B) 47 Gy, (C) 5 Gy and (D) 47 Gy.

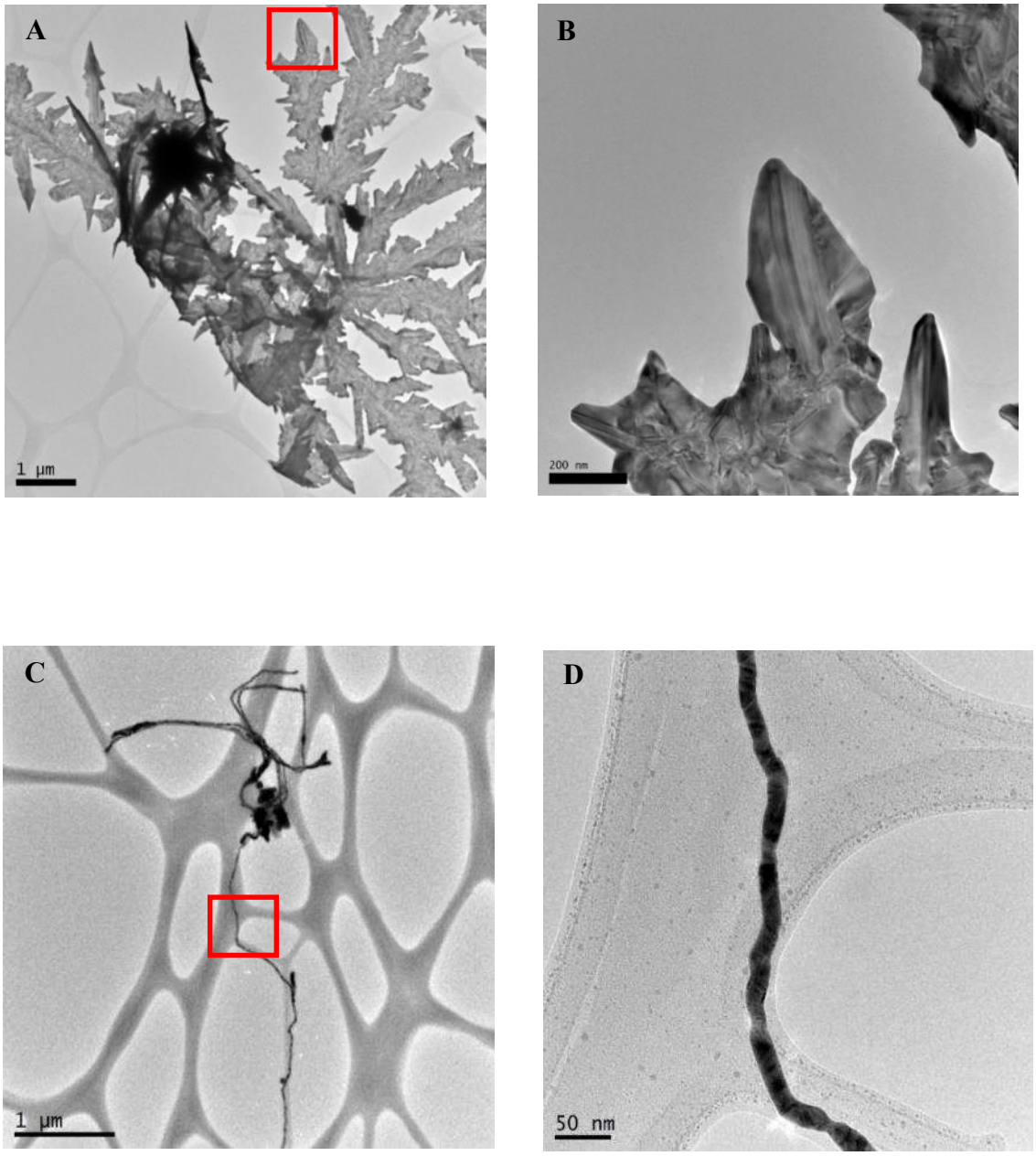

Figure 3.15 Transmission electron microscopy (TEM) images of anisotropic nanostructures (A) dendritic and (C) nanowire-like structures formed in case of C_{12}TAB at 5 Gy X-ray radiation dose. Images on the right show magnified images of the highlighted regions inside red box from Figures (A) and (C).

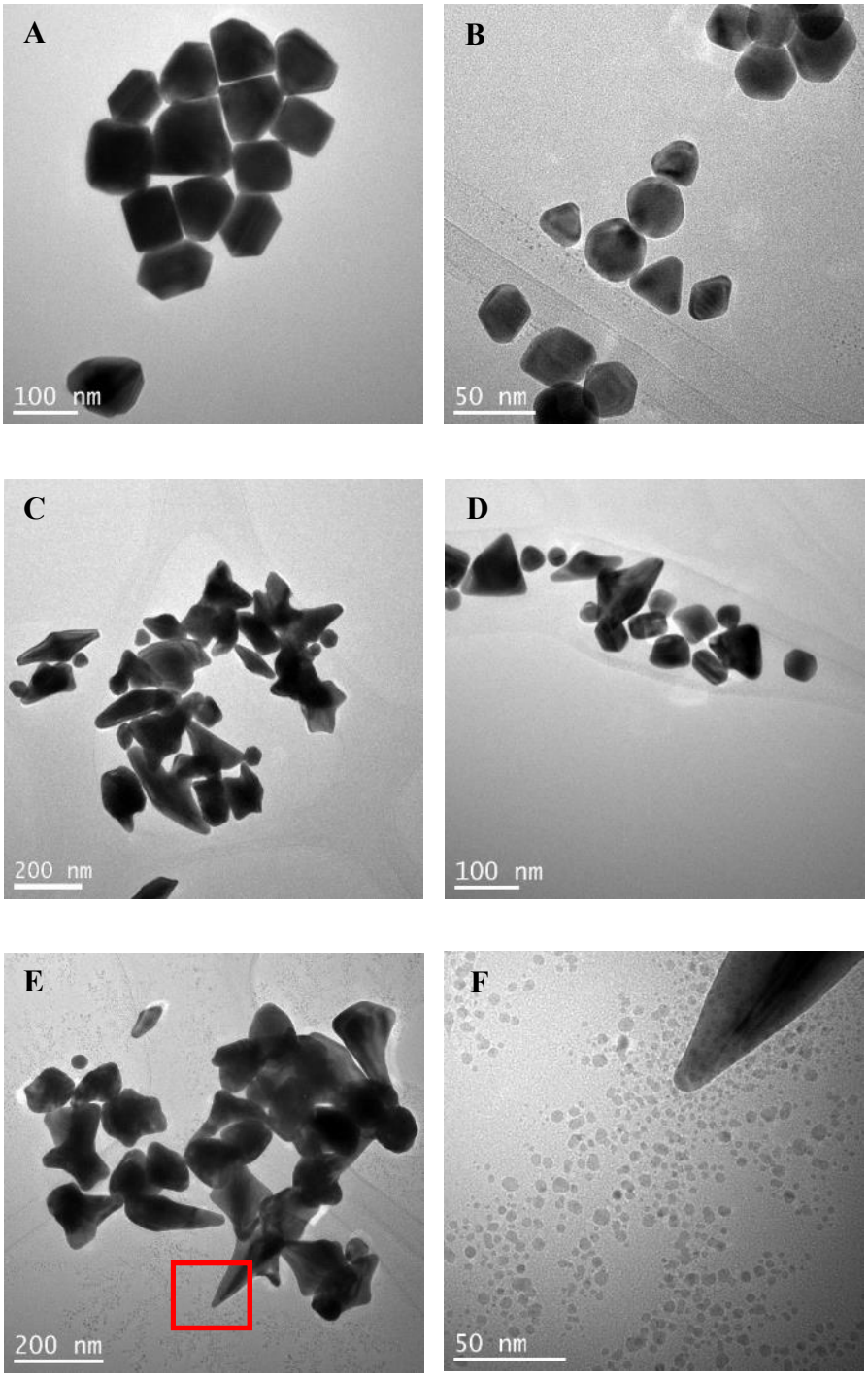
A
100 nm
B
50 nm
C
200 nm
D
100 nm
E
200 nm
F
50 nm

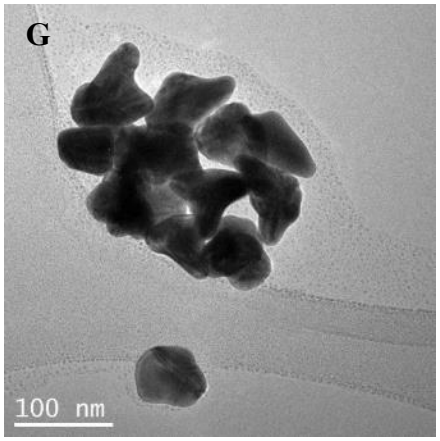

Figure 3.16 Transmission Electron Microscopy (TEM) images of gold nanoparticles formed after exposure to ionizing (X-ray) radiation using the following conditions of C_{16}TAB. (A) 10 mM and 5 Gy, (B) 10 mM and 47 Gy, (C) 4 mM and 5 Gy, (D) 4 mM and 15 Gy, (E) 2 mM and 0.5 Gy, (F) Magnified image of highlighted area of E showing smaller particles, and (G) 2 mM and 2.5 Gy.

TEM images indicated a reduction in the size of the metal nanoparticles with increasing radiation dose. Dynamic light scattering (DLS) studies on irradiated samples (**Figure 3.13 and Table 3.1**) also indicated a decrease in nanoparticle hydrodynamic diameters with increases in X-ray dose, which is in good agreement with information from TEM images. High radiation doses generate a larger number of free radicals in comparison to lower radiation doses, which can lead to the reaction with and therefore, consumption of a higher number of metal ions. This leads to the formation of a higher concentration of zerovalent gold species in comparison to samples irradiated at lower doses. These unstable Au(0) seeds grow and can be capped by the cationic lipid surfactant resulting in smaller sized nanoparticles.[99] In contrast, at lower doses of ionizing radiation, the ratio of concentration of Au(0) to Au(I) is likely smaller. It is possible that unreacted metal ions coalesce with the smaller population of gold seeds and in turn lead to the formation of nanoparticles with larger diameters.[99]

Surfactant	Dose	Average Diameter (nm)	Standard Deviation Diameter (nm)	Average Polydispersity Index(PDI)
C_{16} 20mM	1 Gy	138.4	5.3	0.2
	3 Gy	122.8	1.9	0.2
	5 Gy	121.1	20.7	0.3
	10 Gy	102.3	13.2	0.2
	16 Gy	88.5	12.1	0.2
	26 Gy	72.6	4.7	0.2
	37 Gy	57.3	4.0	0.3
	47 Gy	45.5	3.4	0.3
C_{16} 2mM	0.5 Gy	81.9	8.9	0.3
	1 Gy	60.2	6.1	0.3
	1.5 Gy	48.2	7.3	0.4
	2 Gy	42.9	3.8	0.4
	2.5 Gy	39.8	3.6	0.4
C_{16} 4mM	1 Gy	133.4	10.4	0.2
	3 Gy	124.2	5.2	0.2
	5 Gy	105.3	6.3	0.2
	7.5 Gy	88.6	8.1	0.3
	10 Gy	92.6	8.6	0.3
	12.5 Gy	81.3	6.9	0.3
	15 Gy	74.2	5.5	0.3
	26 Gy	57.4	2.4	0.3
	37 Gy	32.0	0.4	0.5
	47 Gy	22.1	1.3	0.6
C_{16} 10mM	1 Gy	126.4	1.5	0.2
	3 Gy	127.1	1.6	0.2
	5 Gy	124.8	2.1	0.2
	10 Gy	124.9	5.0	0.2
	16 Gy	106.2	5.4	0.2
	26 Gy	72.2	7.1	0.2
	37 Gy	59.4	3.3	0.3
	47 Gy	50.9	2.3	0.2
C_{12} 20mM	1 Gy	141.6	32.2	0.5
	3 Gy	112.2	5.3	0.2
	5 Gy	75.2	5.0	0.3
	10 Gy	40.4	1.0	0.5
	16 Gy	23.9	1.1	0.6
	26 Gy	15.7	0.8	0.6
	37 Gy	17.9	0.7	0.6
	47 Gy	21.6	2.7	0.6

Table 3.1 Average hydrodynamic diameters of gold nanoparticles formed after irradiation along with their corresponding polydispersity indices.

We next investigated the translational potential of our plasmonic nanosensor for detecting X-ray radiation under conditions that simulate those employed in human prostate radiotherapy in the clinic. While radiotherapy is common in the treatment of prostate cancer patients, exposure of normal tissues (*e.g.* underlying rectal wall) to radiation is a cause for concern. Information on the dose delivered during a particular stage of a fractionated radiotherapy regimen can help plan the subsequent stage in order to achieve better patient outcomes. However, to our knowledge, there is no available method for determining the actual dose received by the rectal wall during prostate radiotherapy. Endorectal balloons are typically used for holding the prostate in place and for protecting the rectal wall during radiotherapy treatments in humans.[156] We therefore used the endorectal balloon as means to administer the plasmonic nanosensor, and used this set-up to determine the dose received at different points along the rectal wall. In all cases, the efficacy of the plasmonic nanosensor was evaluated in endorectal balloons *ex vivo*; no studies on human patients were carried out.

We first incorporated 1.5 ml of the precursor solution (20 mM $C_{16}TAB$ + AA + $HAuCl_4$) into endorectal balloons as shown in **Figure 3.17A** in order to investigate the efficacy of the plasmonic sensor using this potential method of delivery. The nanosensor precursor solution was subjected to two relatively high, but clinically relevant doses of 7.9 and 10.5 Gy (n=3). These relatively high doses were used in order to establish proof-of-concept efficacy of the nanosensor in the endorectal balloon. The absorbance of the plasmonic nanosensor, which changes color inside the balloon itself (light pink color seen in **Figure 3.17B** for a balloon subjected to a radiation dose of 10.5 Gy), was employed to determine

the radiation dose delivered to the balloon. A calibration curve between 5 and 37 Gy from the plot between maximum absorbance and radiation dose after 7 hours was employed to determine the radiation dose delivered. Doses of ~8.5 ± 1.7 Gy and ~7.9 ± 2.0 Gy were calculated from the calibration curve for delivered doses of 10.5 Gy and 7.9 Gy, respectively (**Table 3.2**). Due to the nonlinearity of the curve below 5.3 Gy, the control (0 Gy) showed a value ~4.4 ± 0.41 Gy (n = 3) when the calibration equation was employed, indicating that the operating region of the plasmonic nanosensor, with a CTAB concentration of 20 mM, is between 5 Gy and 37 Gy and is not reliable for lower doses of radiation for CTAB concentrations of 20 mM.

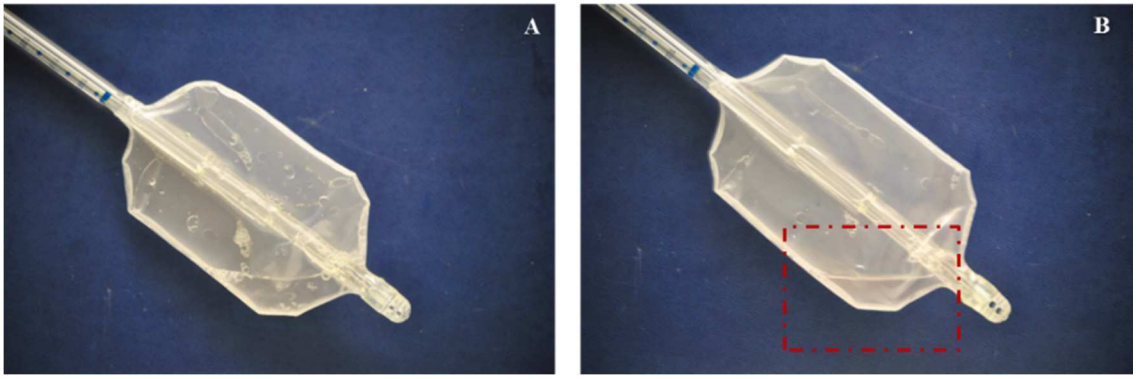

Figure 3.17 (A) An endorectal balloon with precursor solution not subjected to irradiation with X-rays (B) Endorectal balloon post irradiation with 10.5 Gy X-rays. The dashed rectangle shows a light pink colored dispersion following exposure to X-ray radiation.

Delivered Dose (Gy)	**Measured Absorbance (A.U)**	**Calculated Dose from the calibration curve**	**Average Radiation Dose Delivered ± S.D**

		(Gy)	(Gy)
0	0.003, 0.002, 0.009	4.19, 4.09, 4.85	4.38 ± 0.41
7.9	0.05, 0.015, 0.045	9.30, 5.50, 8.76	7.85 ± 2.05
10.5	0.061, 0.035, 0.032	10.50, 7.67, 7.35	8.51 ± 1.73

Table 3.2 Absorbance values measured 7 hours following exposure of endorectal balloons with the plasmonic nanosensor (20 mM C_{16}TAB concentration) following exposure to different doses of ionizing radiation. The calibration equation used was Absorbance = 0.0092*Dose - 0.0356. The 0 Gy data point is outside the linear range (5 – 37 Gy) of the plasmonic nanosensor.

Based on the above findings, we next investigated the detection efficacy of the plasmonic nanosensor in an anthropomorphic phantom that is employed to simulate prostate radiotherapy treatments in the clinic. In these studies, 200 µL of the precursor solution (C 4) uge tubes, which were then ta en they were aligned along the st o AB (2 mM) in these studies, si t which are directly relevant to p al balloon placed under the si ra ent plan described in the E n ent plan was designed such th al y (dark blue line in **Figure 3.** he ine in **Figure 3.18B**). Thus, tw m of the balloon just below th sule 3) outside the balloon was su oyed in order to obtain spatial in e tissue phantom.

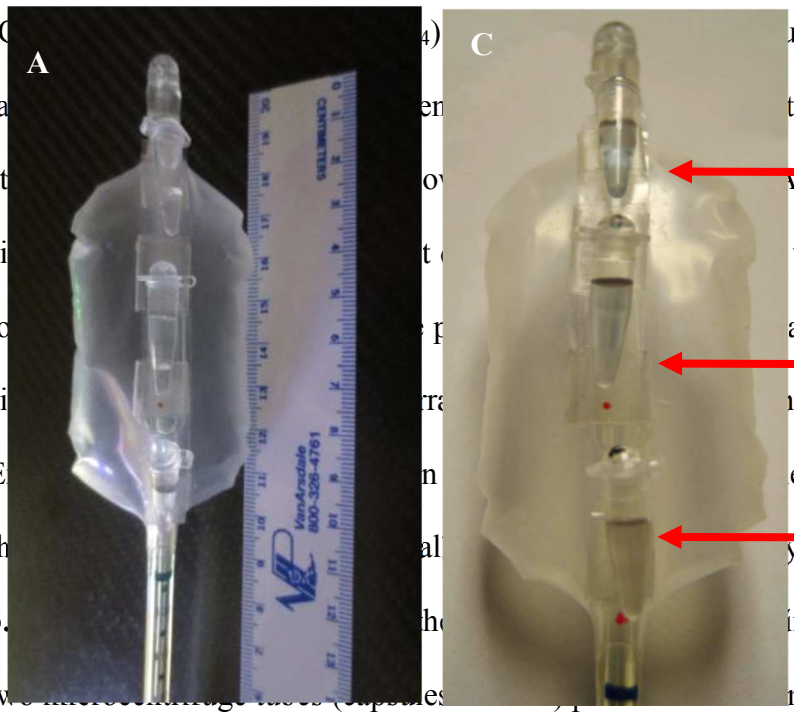

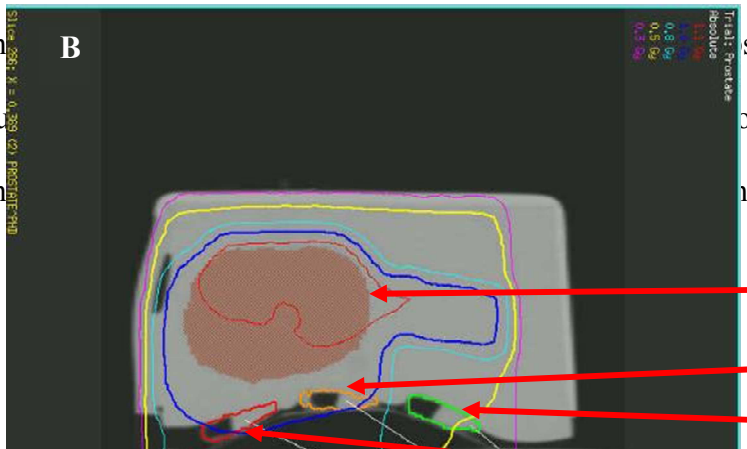

1 Gy

(capsule 2)

Figure 3.18 (A) Digital image showing the nanoscale precursor solution (200 μL) in microcentrifuge tubes placed along the stem outside of an endorectal balloon. (B). X-Ray contrast image of the phantom which shows the dose treatment plan, prostate tissue, the endorectal balloon, and the microcentrifuge tube / nanosensor location below the prostate tissue and on the endorectal balloon. (C). Digital image of the plasmonic nanosensor 2 h following treatment with X-rays in the prostate phantom.

Capsule No. (Actual Dose Delivered in Gy)	Measured Absorbance (A.U)	Calculated Dose from the calibration curve (Gy)	Average Radiation Dose Delivered ± S.D (Gy)
1 (1)	0.12, 0.138, 0.154	1.09, 1.20, 1.30	1.20 ±0.11
2 (1)	0.105, 0.154, 0.137	1.00, 1.30, 1.20	1.17± 0.16
3 (0.5)	0.016, 0.03, 0.025	0.44, 0.53, 0.50	0.49 ± 0.04

Table 3.3 X-ray Radiation dose determined using the plasmonic nanosensor placed on an endorectal balloon in a prostate phantom as shown in **Figure 3.18**. The absorbance was determined 2 h after radiation exposure using the equation Absorbance = 0.1597*Dose – 0.0542. The linear range for this condition ranged from 0.5 Gy to 1.5 Gy. A C_{16}TAB concentration of 2mM was used in these studies.

Optical images (**Figure 3.18C**) clearly indicate the formation of blue-violet colored dispersions for capsules 1 and 2, while a dispersion of lighter intensity can be seen in capsule 3. The absorbance of the dispersions were measured 2 h following exposure to radiation, and a calibration curve was employed to estimate the radiation dose as indicated by the radiation sensor. **Table 3.3** shows a comparison of the actual dose delivered and the dose estimated from the calibration of the plasmonic nanosensor. Data from the plasmonic nanosensor indicates that capsules 1 and 2 received doses of ~1.2 ± 0.1 Gy (actual dose = 1 Gy) and ~1.2 ± 0.2 Gy (actual dose = 1 Gy), respectively, while capsule 3 received a dose of ~0.5 ± 0.04 Gy (actual dose = 0.5 Gy) (**Table 3.3**). These are excellent estimates of the actual doses received by the capsules in the tissue phantom, and more importantly, can be employed to obtain spatial information on the radiation dose delivered to the rectal wall

below the prostate. Taken together, our results indicate the utility of the plasmonic nanosensor as a simple detection system in simulated clinical settings. These results demonstrate a potential clinical application of the plasmonic nanosensor in prostate cancer radiotherapy. It is very likely that different formulation methods and / or fabricated devices will be necessary in translating this technology to different clinical applications.

3.4 Conclusions

We have demonstrated a simple, versatile and powerful nanosensor platform for dosimetry of therapeutically relevant doses of ionizing radiation for potential use in cancer radiotherapy. This is a unique method since it (1) is easy to formulate and visualize due to the colorimetric response, and (2) does not need expensive equipment for detection. While a 'yes / no' determination may be made simply by observation using the naked eye, only an absorbance spectrophotometer is required for quantifying the radiation dose. A visible color change also ensures the ease of detecting the radiation dose with the naked eye. It was found that both, C_{12}TAB and C_{16}TAB were able to function as templating molecules in the plasmonic nanosensor at concentrations above their critical micelle concentration (CMC), while spontaneous nanoparticle formation was observed at lipid surfactant concentrations below the CMC. The toxicity of C_{16}TAB can be a limitation, although appropriate formulation and administration methods (*e.g.* endorectal balloons) may obviate these concerns to some extent.[157] We were able to enhance the sensitivity of the nanosensor to lower radiation doses by modifying the concentration of C_{16}TAB, thus making this a highly versatile platform for a variety of applications. Furthermore, these observations suggest that interplay between surfactant chemistry and aggregation state determine the

extent of nanoparticle formation by lipid-based surfactant molecules. Nanoparticles formed during the radiation sensing operation were characterized by UV-Vis spectroscopy, dynamic light scattering and transmission electron microscopy in order to obtain detailed information on particle size and morphology. Different nanostructures, including spheres, rods, and dendrites were obtained depending on the cationic surfactant employed. Finally, we demonstrated the utility of the current technology in translational applications; the plasmonic nanosensor was able to detect the delivered radiation dose with satisfactory accuracy when placed in an endorectal balloon *ex vivo*. The plasmonic nanosensor was able to detect doses as low as 0.5 Gy, and was able to report on the spatial distribution of radiation dose delivered in the vicinity of the rectal wall when investigated using an endorectal balloon placed in the prostate phantom. The translational application of such a dosimeter can help therapists with treatment planning and potentially enhance selectivity and efficacy of treatment leading to improved patient outcomes. Future work will involve investigations into engineering new generations of templating molecules that improve the sensitivity of detection with lower potential toxicities, formulation methods for improving the versatility of this technology, and appropriate pre-clinical models in order to facilitate translation of this technology in clinical radiotherapy applications.

Chapter 4 DETECTION OF THERAPEUTIC LEVELS OF IONIZING RADIATION USING PLASMONIC NANOSENSOR GELS

4.1 Introduction

Radiotherapy and chemotherapy are among the most widely administered treatment modalities in cancer[158]. Radiotherapy is typically administered in fractions of 2 Gy dose / day leading to a cumulative dose of 20-70 Gy over the course of the treatment; 1 Gy is 1 joule of energy absorbed by a mass of 1 kg. Clinical radiotherapy utilizes advanced methods including image-guided delivery, intensity-modulated radiation therapy (IMRT), stereotactic radiosurgery (SRS) and stereotactic body radiotherapy (SBRT)[159]. Treatment planning in these approaches involves numerous processes and individuals, which can increase the probability of error[127]. The ability to determine the actual dose delivered to target disease sites and / or adjoining healthy tissue can lead to significant reduction in error and may show correlations with response and morbidity leading to more effective treatment planning.

Current dosimeters include semiconductor diodes and thermoluminescent dosimeters (TLDs)[160]. TLD operation is time consuming and requires a specialist operator, and semiconductor diodes are energy and dose rate dependent. Currently available dosimeters cannot be molded into different shapes that can conform to tissues during clinical radiotherapy. Polymer gel dosimeters were developed in order to overcome these limitations, and have been explored in IMRT and SRS treatments. However, a key limitation in using polymer gel based dosimeters is the use of magnetic resonance imaging (MRI) for determining the delivered dose, which makes their routine use very challenging.

Taking these factors into consideration, there is a strong requirement for the development of a simple gel-based dosimeter which can detect therapeutic doses of ionizing radiation. In particular, advances in molecular and nanoscale systems can lead to simple and effective approaches for detecting therapeutic doses of ionizing radiation[161].

Gold nanoparticles have attracted great interest in biomedical diagnostics and chemical sensing owing to unique optical properties associated with the size and shape of these nanoparticles[66, 67]. We recently developed a liquid-phase sensor that is based on the formation of gold nanoparticles from a colorless metal salt solution upon exposure to therapeutic levels of ionizing radiation[162]. Although this is a powerful and simple approach for detecting ionizing radiation, a liquid-phase system has limitations in cases where detecting doses over a two-dimensional surface area may be necessary. In the current study, we report a simple colorimetric gel-based plasmonic nanosensor that can detect ionizing radiation in the dose range that is conventionally employed in fractionated clinical radiotherapy (i.e. 0.5 - 10 Gy). In this system, gold nanoparticles are generated in translucent gels upon irradiation with ionizing (X-ray) radiation levels employed in fractionated radiotherapy. Formation of gold nanoparticles renders color to the originally colorless and translucent gel, which facilitates visual detection as well as quantitative colorimetric dose determination. To our knowledge, these colorimetric gel-based plasmonic nanosensors are first of their kind, and can potentially be translated to clinical use in radiotherapy.

4.2 Materials and Methods

Materials. Gold(III) chloride trihydrate ($HAuCl_4.3H_2O$), dodecyltrimethylammonium bromide ($C_{12}TAB$) (≥98%) and L-ascorbic acid (AA) were purchased from Sigma-Aldrich. Cetyltrimethylammonium bromide ($C_{16}TAB$) was purchased from MP chemicals. All chemicals were used as received from the manufacturer without additional purification. MilliQ water, at a resistivity of 18.2 MΩ.cm, was used as solvent for all experiments.

Hydrogel Preparation for Irradiation. $C_{x=12,16}TAB$ (600 μL of 50 mM solution in MilliQ water) was mixed with 30 μL of 10 mM $HAuCl_4$ in MilliQ water. Different amounts of agarose were dissolved in DI water and heated until a clear solution of 5%, 7.5% or 10% w/v agarose were formed. Liquid agarose (500 μL) was then mixed with the gold-surfactant mixture. This liquid mixture (650 μL) was allowed to set in prefabricated molds, which results in agarose discs of ~1.5 cm diameter. Ascorbic acid (650 μL of 10 mM in MilliQ water) was allowed to diffuse into the gel for 10 minutes leading to the formation of the hydrogel nanosensor precursor. These translucent hydrogel discs were used subsequently for irradiation studies.

X-Ray Irradiation. A Varian Truebeam linear accelerator radiation therapy system at the Banner-M.D. Anderson Cancer Center in Gilbert, AZ (one-way travel time of approximately 20 min from ASU) delivering a 6 MV photon beam was used to irradiate the translucent hydrogel at a dose rate of 15.6 Gy/min. The samples are irradiated at doses of 0, 1, 2, 3, 5, 7.5 and 10 Gy.

Nanosensor Gel Dosimetry in an Anthropomorphic Thorax Phantom. All phantom experiments were carried out at the Banner-M.D. Anderson Cancer Center in Gilbert, AZ (one-way travel time of approximately 20 min from ASU). A CIRS tissue equivalent thorax phantom was aligned on a Philips RT CT table with CT room aligning lasers. A total of 150 CT scan images were acquired with a 1 mm image thickness and 1 mm image spacing which were then exported to a Philips Pinnacle treatment planning system. The thorax phantom was then contoured and a treatment plan was generated for a 6 MV radiation beam. Pinnacle's Collapsed Cone Convolution Superposition (CCCS) algorithm was used to calculate the dose in the thorax phantom. A 3 Gy dose was delivered to the skin of the phantom while a 2 Gy dose was delivered to the second mediastinum (6 cm from the top) of the thorax phantom. Post irradiation analyses (e.g. absorbance) were performed at Arizona State University in Tempe, AZ. A calibration curve was developed for doses ranging from 0-3 Gy by irradiating the gel nanosensor samples at 100 cm source-to-surface distance or SSD with a standard uniform beam.

Absorbance Spectroscopy. A BioTek Synergy 2 plate reader was used to determine the absorbance profiles of the irradiated and control samples. Absorbance values of gel samples in a 24 well plate were measured from 300 to 990 nm with a step size of 10 nm. Nanopure water was used as blank for the study. The characteristic plasmonic absorption peak between 500-600 nm was used as an indicator of gold nanoparticle formation. This absorbance value was offset by subtracting absorbance value at 990 nm (A_{990}) from the peak (maximum) value. A curve was plotted with the maximum values obtained against

their corresponding doses for C_{12}TAB and C_{16}TAB for nanosensor gel samples. To maintain consistency a different calibration curve was generated for the phantom studies since the source to surface distance (SSD) was different for this set up compared to gels not used in the phantom. The calibration equations obtained were subsequently used to calculate the dose delivered in the phantom.

Scanning Electron Microscopy. Following X-ray irradiation, the gel nanosensor samples were dried by exposing them to air at room temperature. The gel was sputter-coated with a thin film of gold-palladium prior to microscopy. SEM analyses were carried out in an XL 30 Environmental instrument in order to visualize the presence of gold nanoparticles in the agarose hydrogel.

Image Processing. All images were acquired using a Canon EOS 1100D camera under suitable lighting. The images were cropped to the desired size in the Fotor Photo Editor application. No further editing was carried out on the pictures reported in this article.

Statistical Analyses. All irradiation experiments were carried out a minimum of three times independently unless otherwise stated. The results are expressed as mean ± one standard deviation. These calculations were carried out using Microsoft Excel.

4.3 Results and Discussion

The working principle of the agarose gel-based nanosensor is based on the reduction of gold ions to gold nanoparticles following exposure to ionizing radiation (**Figure 4.1**). Agarose gels containing gold ions are colorless and translucent, and the gel changes color to maroon due to the formation of gold nanoparticles upon exposure to therapeutic levels of ionizing (X-ray) radiation. Zerovalent gold ions Au(0) generated in this process ultimately lead to nanoparticle nucleation and growth[163]. Originally existing in a trivalent state Au(III) in metal salts, the gold salt was first reduced to its monovalent Au(I) form using ascorbic acid. This was carried out in order to increase the thermodynamic favorability towards the formation of Au(0) species, because the reduction potential of Au(I) is higher than that of Au(III); only one electron is required to reduce Au(I) to Au(0)[137, 138]. Irradiation with ionizing radiation (X-rays) engenders splitting of water molecules in the gel, which, in turn, leads to the formation of ionizing radicals. Radiation-induced free radicals, e^- and $H\cdot$, are reducing in nature, and $OH\cdot$ is an oxidizing agent. These $OH\cdot$ radicals impede nanoparticle formation but can be removed by ascorbic acid, which acts as an antioxidant[134].

A

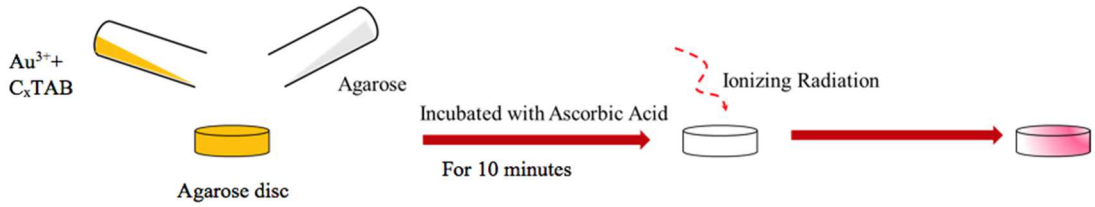

B

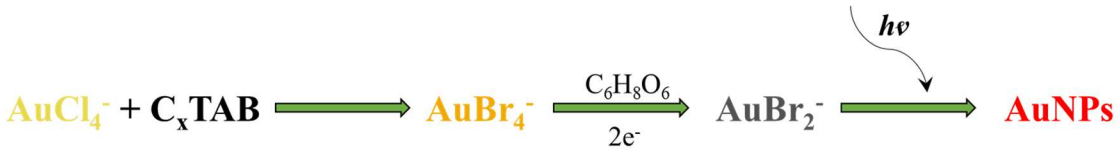

Figure 4.1 (A) Schematic of the hydrogel nanosensors for the detection of therapeutic levels of ionizing radiation (e.g. X-rays). A mixture of 10 mM $HAuCl_4$ and 50 mM C_xTAB (x=12, 16) is mixed with liquid agarose and allowed to set in a circular mold to form a disc (16 mm in diameter and 3 mm in thickness). Ascorbic acid (10 mM) is allowed to diffuse into the gel from the top for 10 minutes immediately prior to subjecting the disc to different doses of ionizing radiation. Irradiation of this colorless hydrogel with ionizing radiation (X-rays) results in the formation of gold nanoparticles in the hydrogel, which results in a visible change in color of the gel from colorless to maroon. (B) Chemical reactions involved in the current hydrogel-based nanosensor. $HAuCl_4$ solution, which is yellow in color, changes to orange upon addition of the surfactant (C_xTAB). Subsequent addition of ascorbic acid ($C_6H_8O_6$) led to reduction of Au(III) to Au(I), which renders the gel colorless and translucent. Irradiation with ionizing radiation (X-rays) results in the formation of gold nanoparticles (AuNPs), which render a burgundy color to the gel due to the plasmonic properties of these nanoparticles.

In addition to the gel and gold ions, we employed $C_{x\ (x=12,16)}TAB$ surfactants in this study in order to facilitate the formation of gold nanoparticles[139]. The agarose polysaccharide contains functional moieties which can simultaneously assist in reduction of gold salt and templating of gold nanoparticles[164]. Altogether, a colorless metal salt precursor solution comprising of a mixture of auric chloride ($HAuCl_4$), L-ascorbic acid (AA) and cetyl (C_{16}) or dodecyl (C_{12}) trimethylammonium bromide ($C_{x;\ x=16,\ 12}TAB$) surfactant molecules and agarose[140, 141], form the key constituents of the novel gel based plasmonic nanosensor for detecting therapeutic levels of ionizing radiation. Key factors which influenced our current selection of the agarose hydrogel include (1) low toxicity / biocompatibility, (2) water solubility of the gel constituent material, (3) ease of generation, and (4) ease of mechanical property modulation. Agarose-based hydrogels have been investigated as scaffolds for

regenerating damaged tissues or as platforms for controlled drug release owing to their low toxicities[165, 166].

We first carried out several control experiments in order to investigate the suitability of the current agarose-based plasmonic nanosensor system. Wang *et.al* demonstrated that mixing $HAuCl_4$ with heated agarose[164] induced the spontaneous formation of gold nanoparticles. However, in absence of ionizing radiation, we did not observe the formation of a red / maroon-colored hydrogel (**Figure 4.2A**); a concomitant absorbance peak between 500-600 nm, which is indicative of gold nanoparticles, was also not seen (**Figure 4.3A**). Formation of an intense yellow-colored liquid was seen when a mixture of $HAuCl_4$ and C_xTAB (x = 12 or 16) was mixed with heated agarose, likely due to the replacement of chloride ions by bromide ions from C_xTAB (**Figure 4.2B and C**)[138, 167]. This ligand transfer leads to a new absorbance peak at ~370 nm (**Figures 4.3B and C**), and subsequent cooling led to the formation of pale yellow-colored gels. Addition of ascorbic acid to this gel formulation reduces the gold salt from Au(III) to Au(I)[168] rendering the gel colorless (**Figures 4.2D and E**), which is consistent with previous observations[138, 162]; the loss in color is also indicated by the loss or absence of peaks in the UV-vis spectrum (**Figure 4.3D and E**). This colorless formulation is used as the plasmonic nanosensor gel in all subsequent radiation detection studies. In the absence of ionizing radiation, this precursor gel (i.e. agarose containing ascorbic acid, $HAuCl_4$ and C_xTAB) remained colorless due to minimal, if any, formation of gold nanoparticles; no absorbance peak was seen at ca. 520 nm. In the absence of C_xTAB surfactant molecules, direct addition of ascorbic acid to agarose gels containing $HAuCl_4$ resulted in the spontaneous formation of gold nanoparticles[169]. In the

absence of ascorbic acid, irradiation of agarose gels containing C_xTAB and $HAuCl_4$ with X-rays did not induce a change in the yellow color of the gels (**Figure 4.4**), although a small peak at 520 nm was observed in case of 10% agarose (**Figure 4.5 A**). Taken together, these results indicate that all components i.e. agarose, $HAuCl_4$, C_xTAB, and ascorbic acid (AA) are necessary to form the colorless precursor gel formulation of the plasmonic radiation nanosensor.

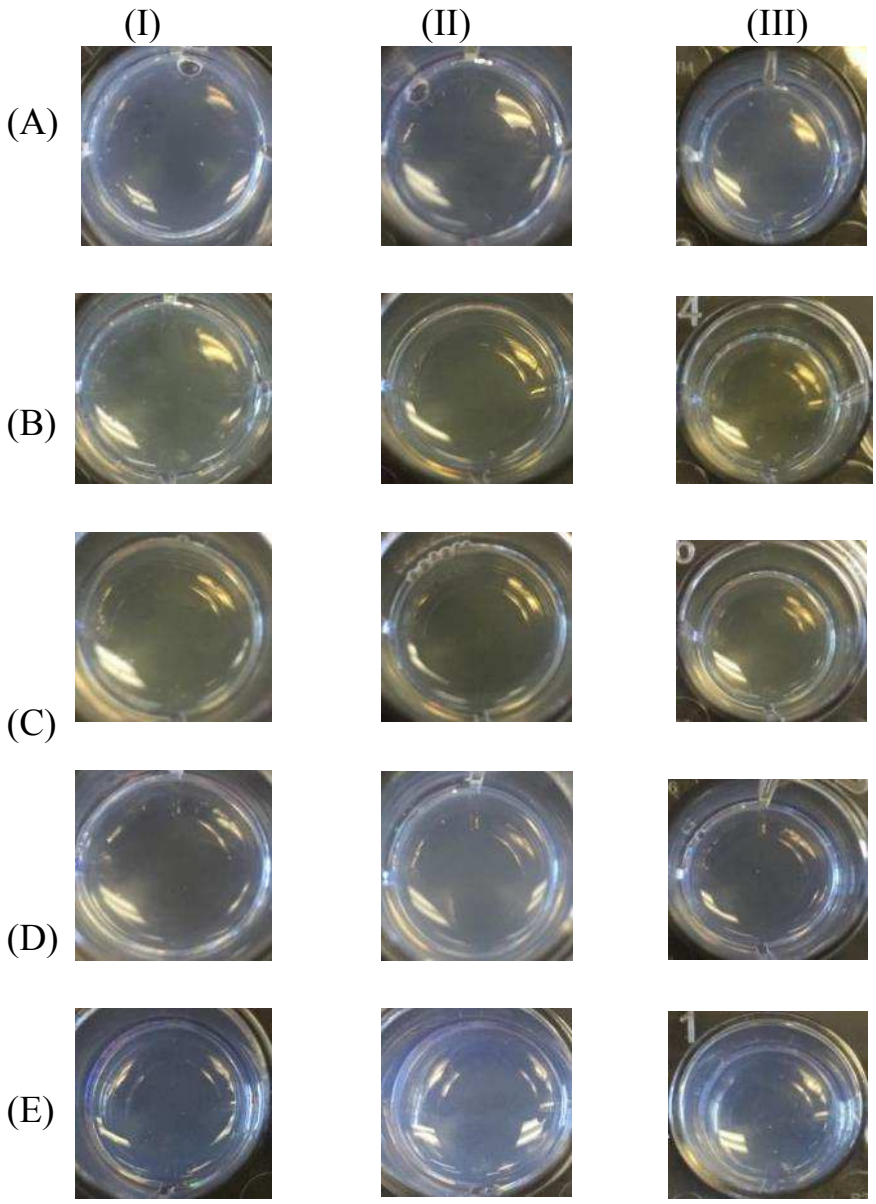

Figure 4.2 Images of the precursor nanosensor agarose gels not subjected to X-rays. Images were acquired 1 hr following formulation. (A) Agarose gels containing only 10mM $HAuCl_4$, (B) Agarose gel formulated with 10 mM $HAuCl_4$ and 50 mM $C_{12}TAB$ (no ascorbic acid), (C) Agarose gel formulated with 10 mM $HAuCl_4$ and 50 mM $C_{16}TAB$ (no ascorbic acid) (D) Agarose gel formulated with 10 mM $HAuCl_4$, 50 mM $C_{12}TAB$ and 10 mM ascorbic acid, (E) Agarose gel formulated with 10 mM $HAuCl_4$, 50 mM $C_{16}TAB$ and 10 mM Ascorbic Acid. Columns (I), (II) and (III) correspond to 5%, 7.5% and 10% (w/v) agarose respectively.

(A)

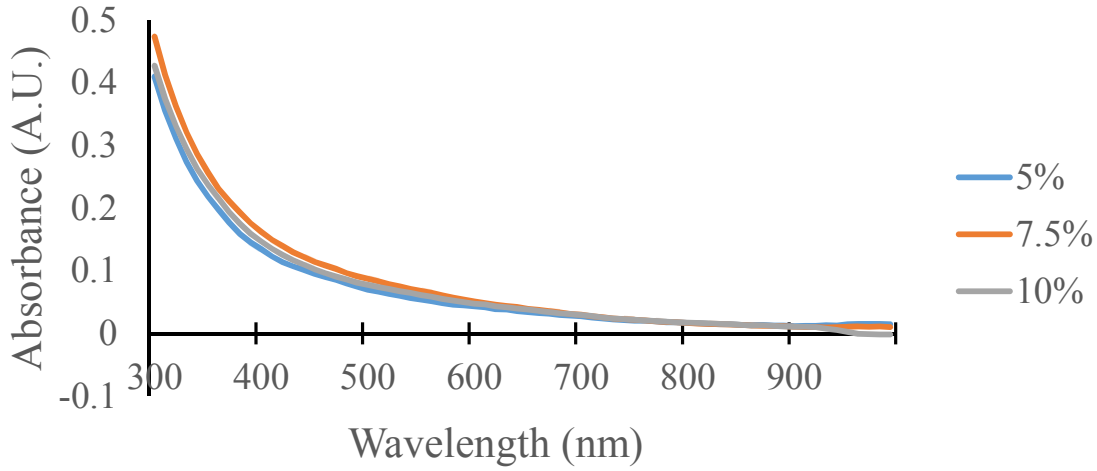

(B)

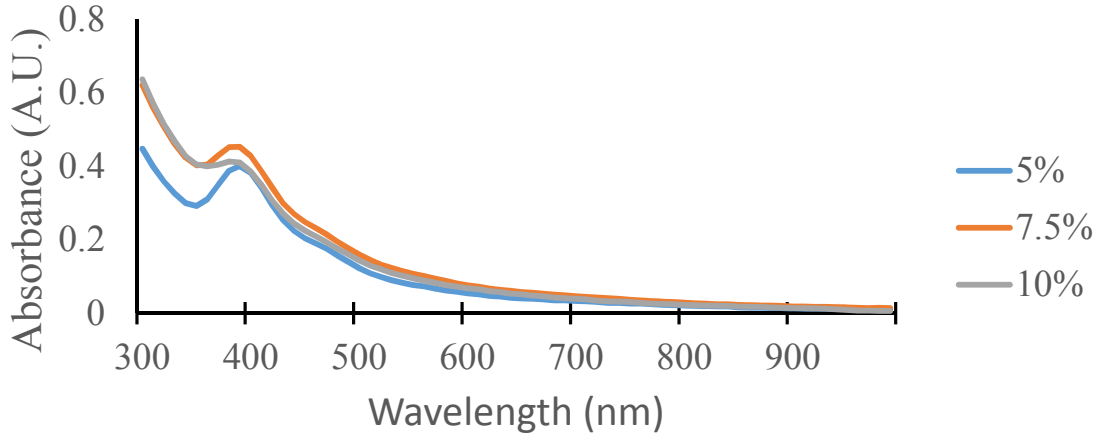

(C)

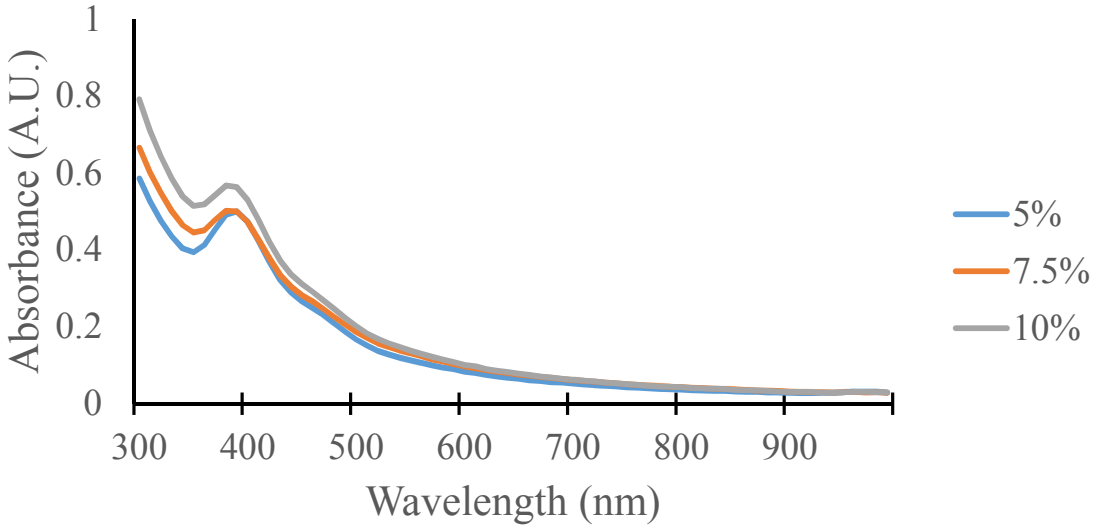
Absorbance (A.U.)
1
0.8
0.6
0.4
0.2
0
300
400
500
600
700
800
900
Wavelength (nm)
5%
7.5%
10%

(D)

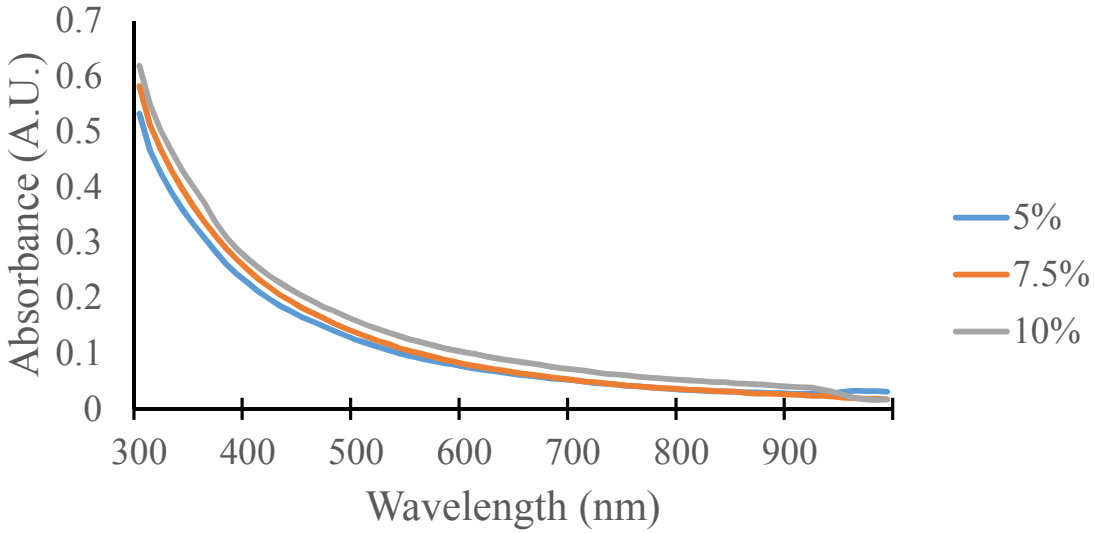
Absorbance (A.U.)
0.7
0.6
0.5
0.4
0.3
0.2
0.1
0
300
400
500
600
700
800
900
Wavelength (nm)
5%
7.5%
10%

(E)

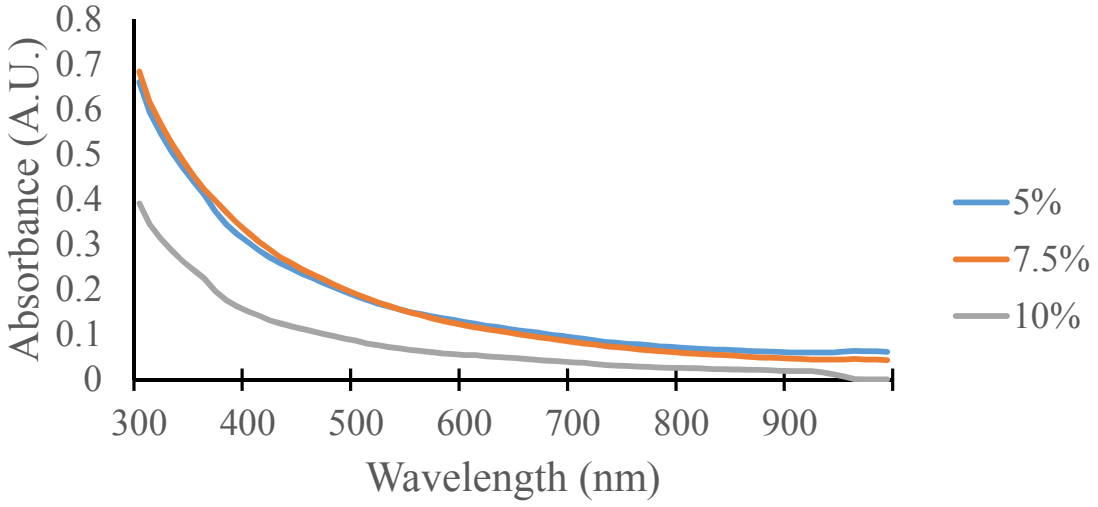

Figure 4.3 Absorbance spectra of agarose gels containing (A) 10 mM Au^{3+} (i.e. $HAuCl_4$), (B) 10 mM Au^{3+} + 50 mM $C_{16}TAB$, (C) 10 mM Au^{3+} + 50 mM $C_{12}TAB$, (D) 10 mM Au + $C_{16}TAB$ + 10 mM ascorbic acid (AA), and (E) 10 mM Au^{3+} + 50 mM $C_{12}TAB$ + 10 mM AA. These spectra were acquired 1h following preparation of the individual gel formulations.

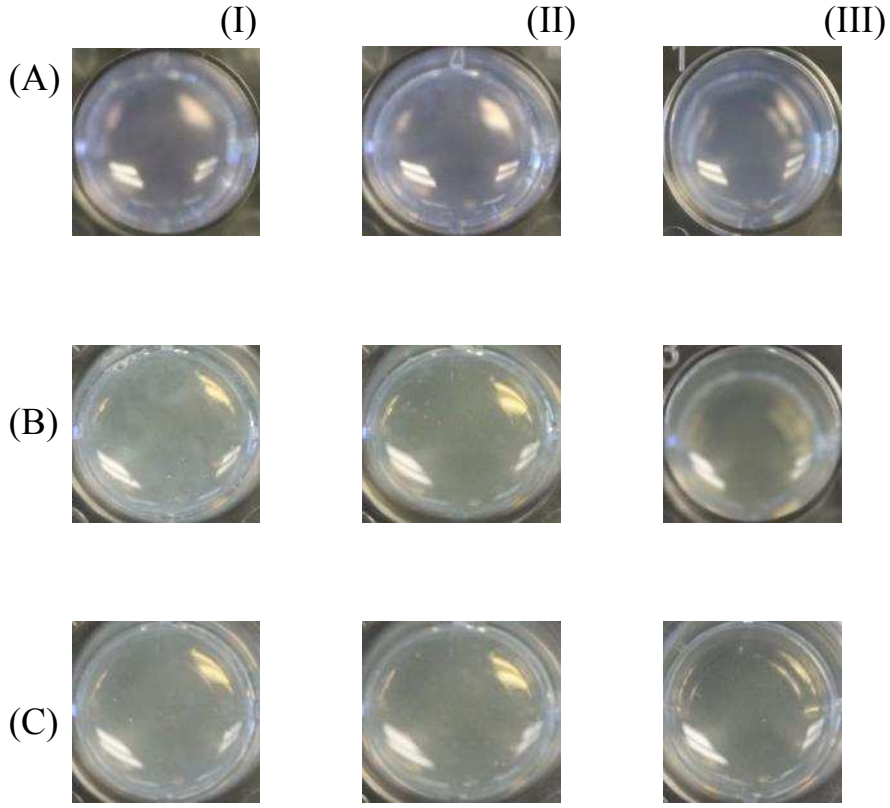

Figure 4.4 Images of control agarose gels acquired after 1hr and 2 Gy radiation; ascorbic acid was not used in these formulations (A) agarose gels consisting of only 10 mM $HAuCl_4$, (B) agarose gel formulated with 10 mM $HAuCl_4$ and 50 mM $C_{12}TAB$, (C) agarose gel formulated with 10 mM $HAuCl_4$ and 50 mM $C_{16}TAB$. Columns (I), (II) and (III) correspond to 5%, 7.5% and 10% (w/v) agarose respectively.

(A)

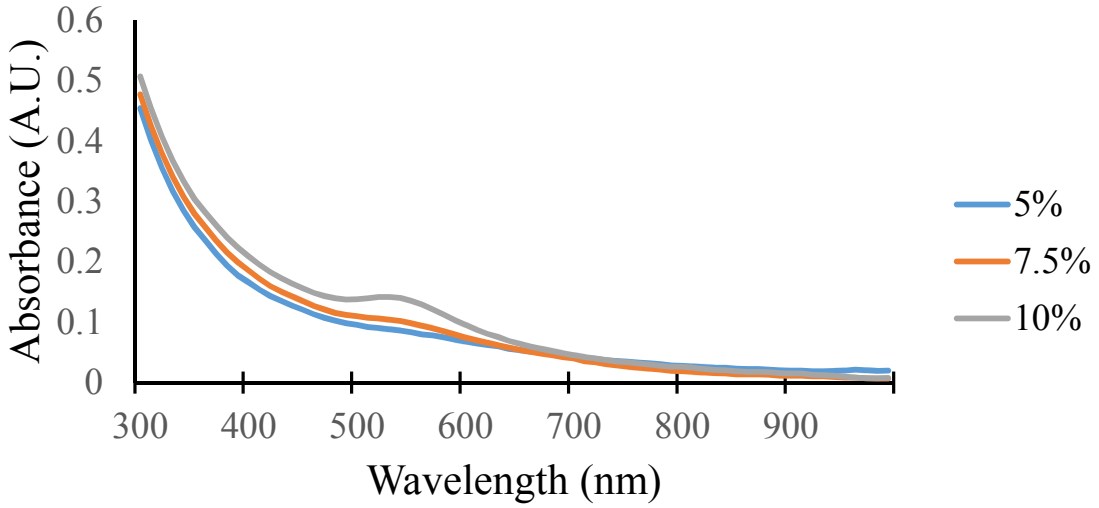

(B)

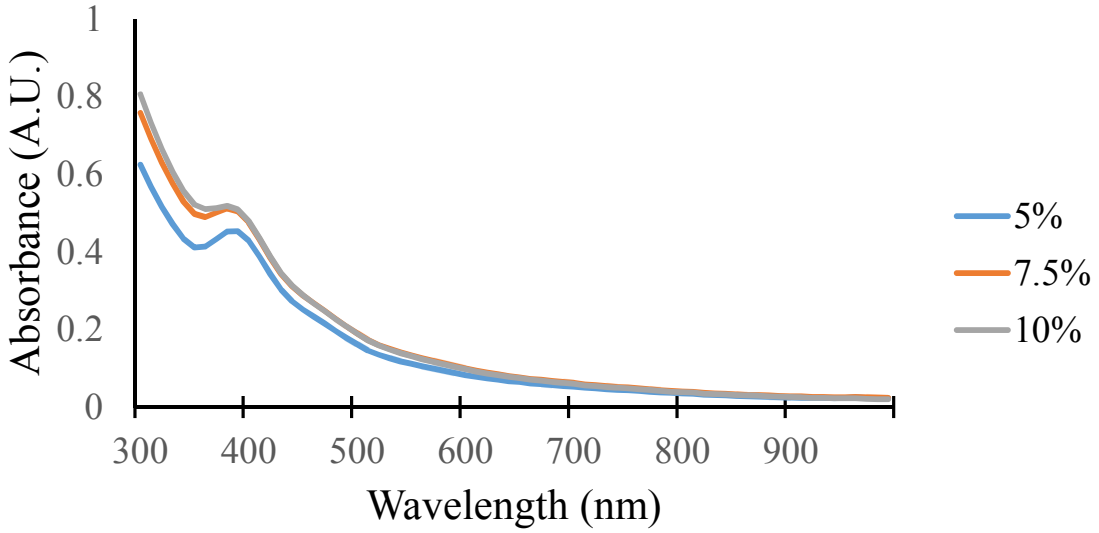

(C)

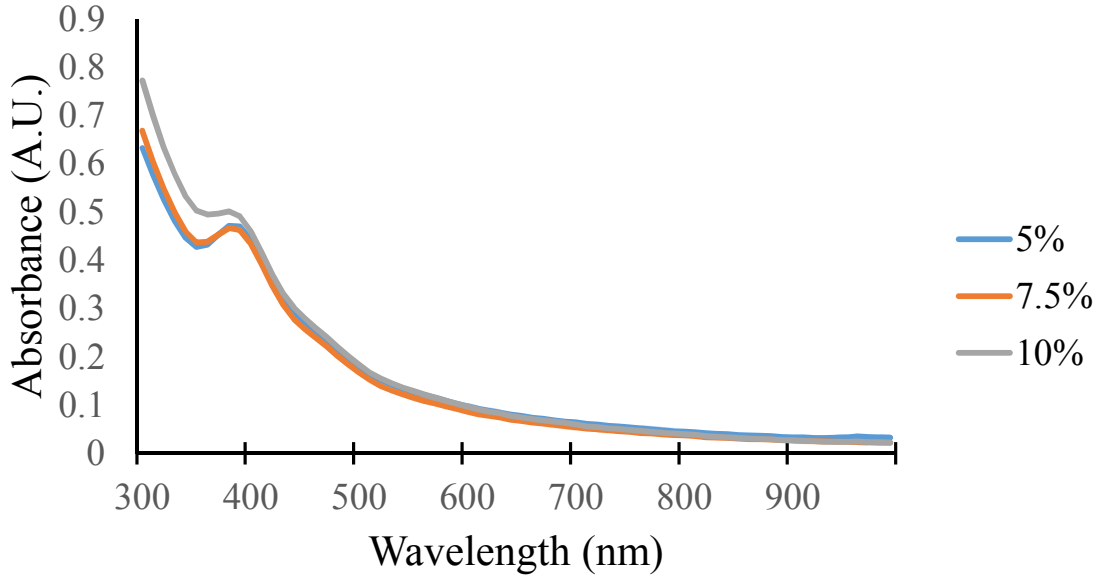

Figure 4.5 Absorbance spectra of different control formulations irradiated with 2 Gy X-ray dose dose (A) 10 mM Au^{3+} (i.e. $HAuCl_4$) (B) 10 mM Au^{3+} + 50 mM $C_{16}TAB$ (C) 10 mM Au^{3+} + 50 mM $C_{12}TAB$. The spectra were acquired 1hr following irradiation. Note: ascorbic acid was not used in these control gel formulations.

Irradiation of the precursor gel formulation with different doses of ionizing radiation resulted in the formation of gold nanoparticles, which rendered a maroon color to the gel (**Figure 4.6**). Exposure of hydrogel to ionizing radiation results in the formation of e^-_{aq} and $H^{\cdot}$ radicals upon water splitting, which facilitates the reduction of monovalent gold Au(I) ions to its zerovalent Au(0) state[170]. Further nucleation and coalescence of the Au(0) species (seeds) leads to the formation of gold nanoparticles[171]; the gold nanoparticles are likely stabilized by the C_xTAB surfactant molecules present in the gel[172]. The intensity of the maroon color depends on the concentration of gold nanoparticles in the gel, which, in turn, is dependent on the radiation dose delivered to the gel. This increase in color intensity is eventually a direct result of the increase in the number of free radicals generated at higher

radiation doses[173], which can reach a saturation level at a particular dose beyond which the colorimetric response stays invariant.

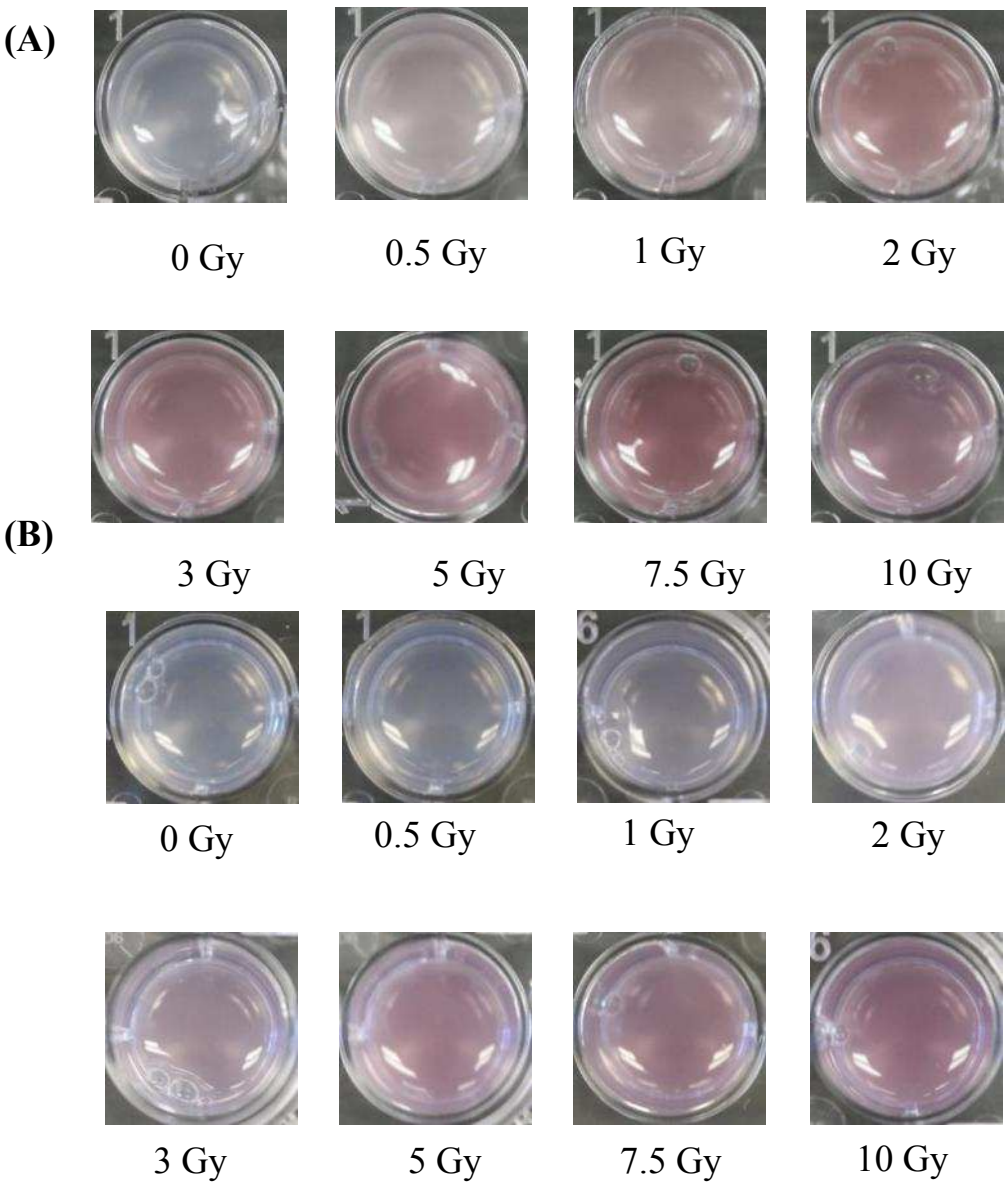

Figure 4.6 Images of 5% (w/v) agarose gel containing (A) 50 mM C_{12}TAB and (B) 50 mM C_{16}TAB surfactants following exposure to different doses of ionizing (X-ray) radiation. Formation of gold nanoparticles renders a maroon color to the gel. Images were acquired 1 h after subjecting the gels to X-ray irradiation. All samples contain 10 mM $HAuCl_4$ and 10 mM ascorbic acid.

The color change of gels, from colorless to maroon, was visible to the naked eye as early as 10 minutes following exposure X-rays (**Figures 4.6, 4.7 and 4.8**), although lower doses (0.5 and 1 Gy) required 15-20 mins for a visible change in color. The change in color was quantified using UV-vis absorbance spectroscopy 1 h following irradiation, since this was the earliest when we could determine absorbance due to travel time between the radiation center and ASU (absorbance analysis). A characteristic spectral peak in the range of 500-600 nm (**Figure 4.9 and 4.10**) was indicative of gold nanoparticle formation in the gel. No significant difference in the absorbance intensity was observed over a period of four hours once the color was formed (**Figure 4.11**). Longer durations were not investigated, but we do not anticipate fading or bleaching since the colorimetric response is based on formation of nanoparticles, which are more stable than dyes. Formation of nanoparticles in the gel was further verified using field-emission scanning electron microscopy (**Figure 4.12)**. Image analysis indicated that the average size of gold nanoparticles formed in the gel was ~ 35 nm.

(A)

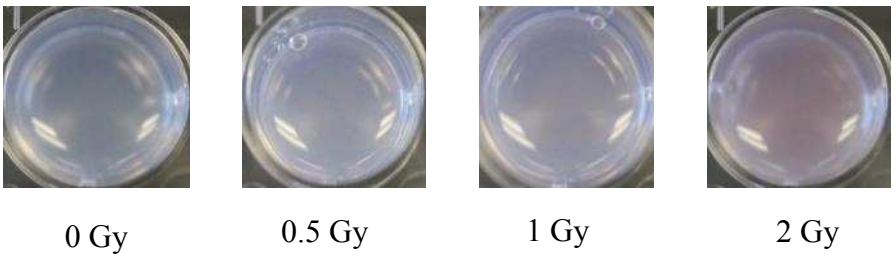

0 Gy 0.5 Gy 1 Gy 2 Gy

3 Gy 5 Gy 7.5 Gy 10 Gy

(B)

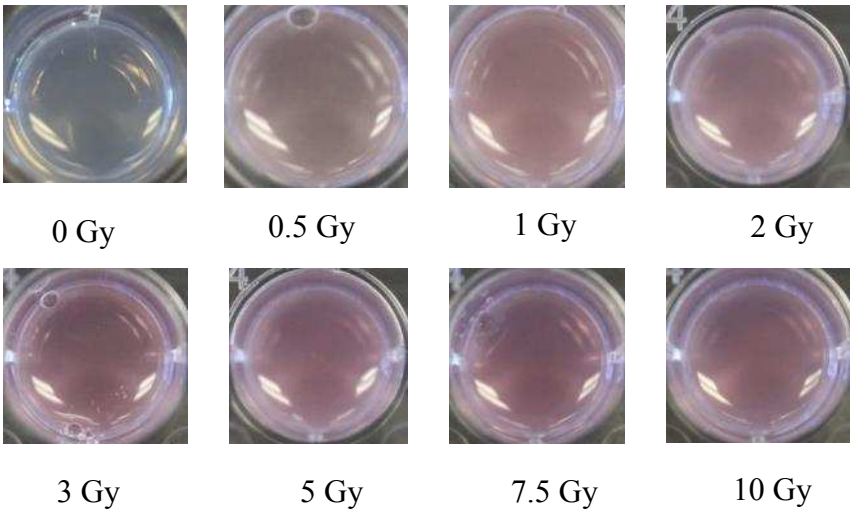

Figure 4.7 Images of 7.5% (w/v) agarose nanosensor gel with (A) C_{16}TAB and (B) C_{12}TAB following irradiation with different radiation doses. Images were acquired 1 h after irradiation.

(A)

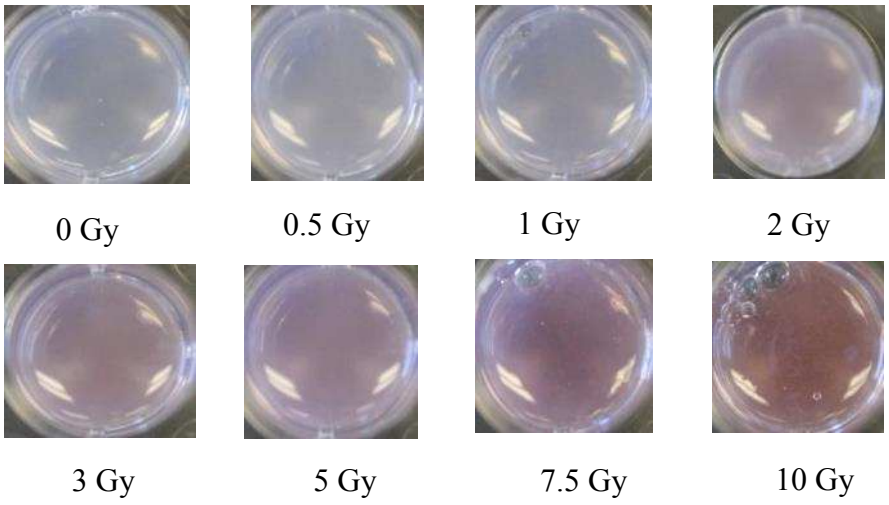

(B)

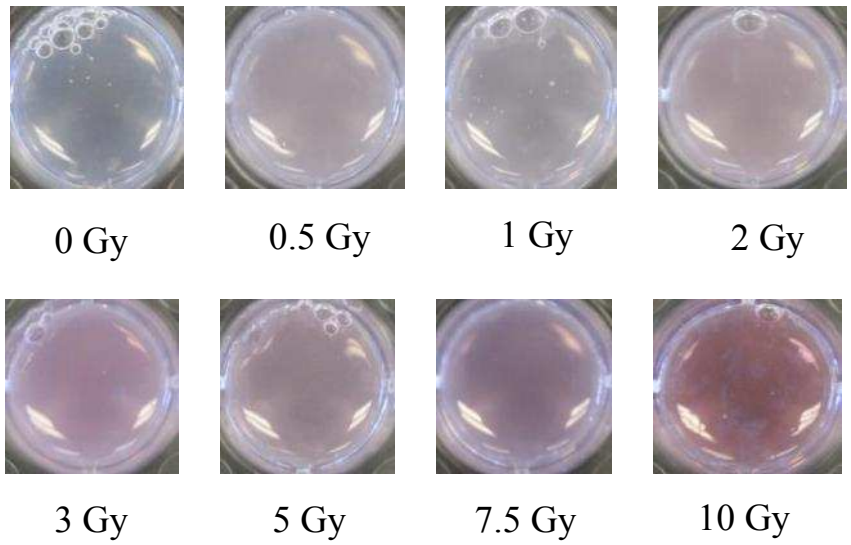

Figure 4.8 Images of 10% (w/v) agarose nanosensor gel containing (A) C16TAB and (B) C12TAB following irradiation with different radiation doses. Images were acquired 1 h after irradiation.

(A)

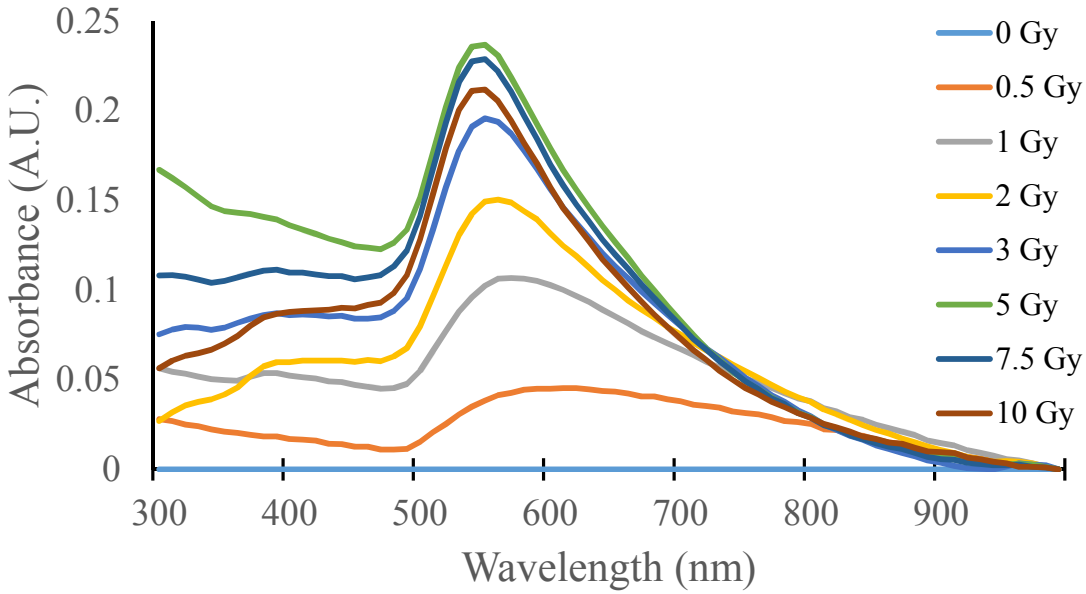

(B)

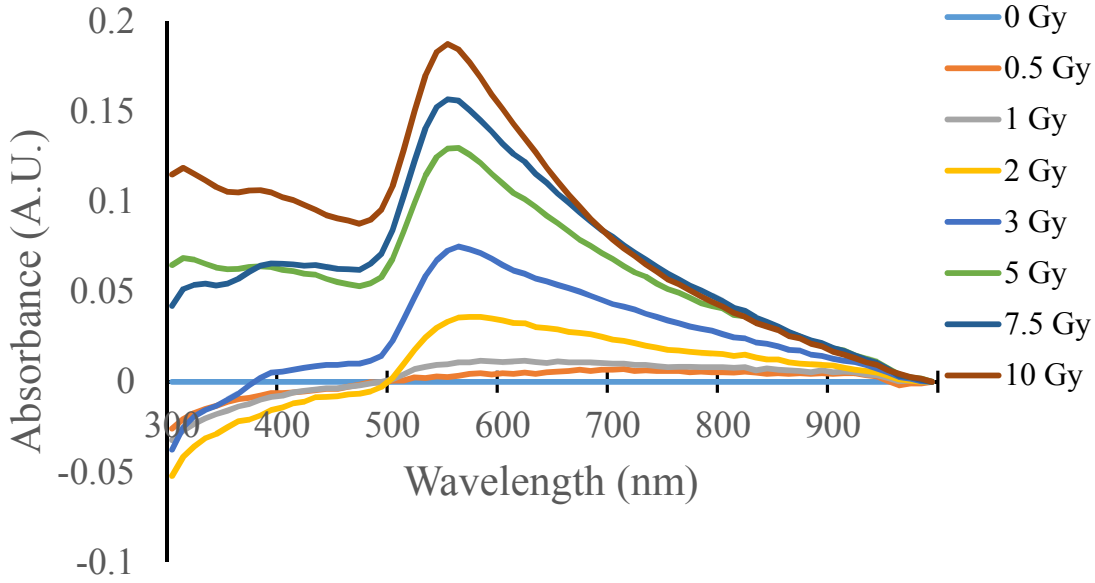

Figure 4.9 Absorbance spectra of 5% (w/v) agarose nanosensor gels containing **(A)** C_{12}TAB and **(B)** C_{16}TAB irradiated with different X-ray doses. Characteristic absorbance peaks between 500 – 600 nm wavelength are indicative of gold nanoparticle formation.

(A)

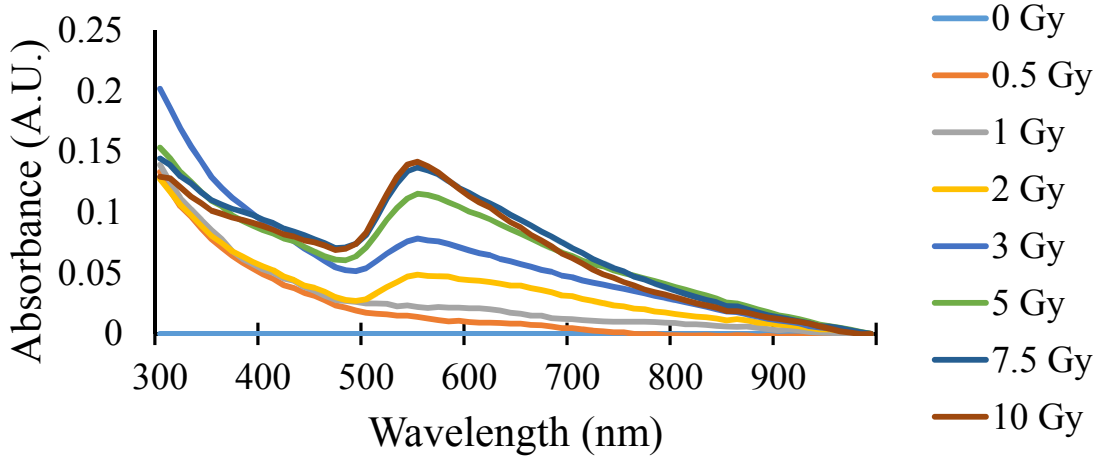

(B)

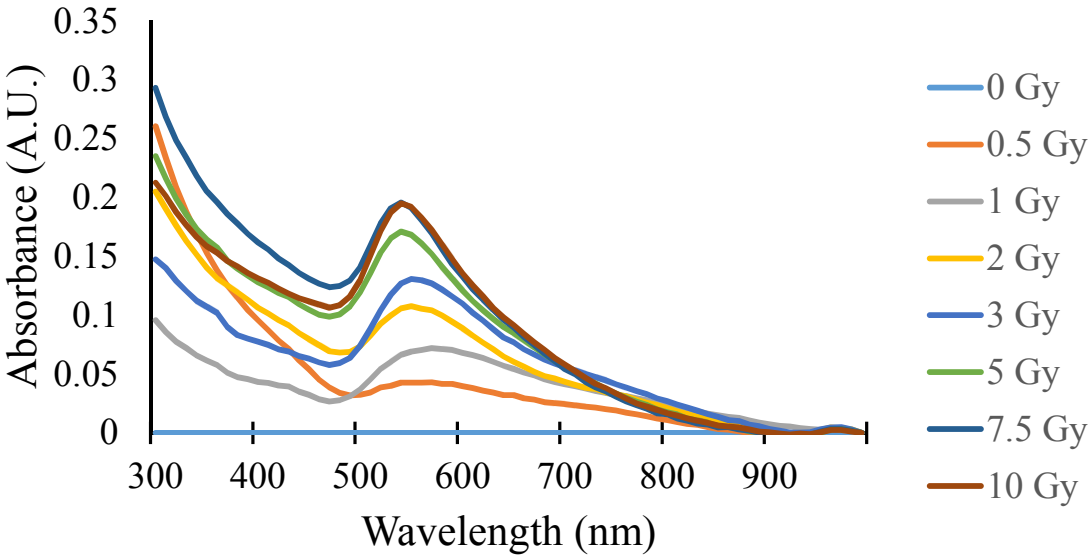
0.35
0.3
0.25
0.2
0.15
0.1
0.05
0
Absorbance (A.U.)
300
400
500
600
700
800
900
Wavelength (nm)
0 Gy
0.5 Gy
1 Gy
2 Gy
3 Gy
5 Gy
7.5 Gy
10 Gy

(C)

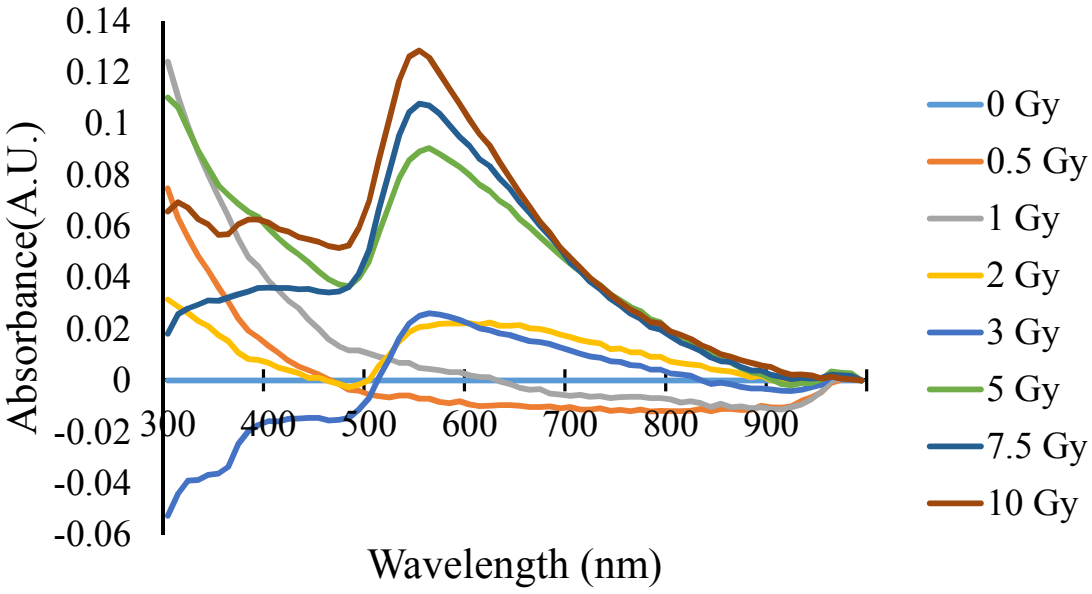
0.14
0.12
0.1
0.08
0.06
0.04
0.02
0
-0.02
-0.04
-0.06
Absorbance(A.U.)
300
400
500
600
700
800
900
Wavelength (nm)
0 Gy
0.5 Gy
1 Gy
2 Gy
3 Gy
5 Gy
7.5 Gy
10 Gy

(D)

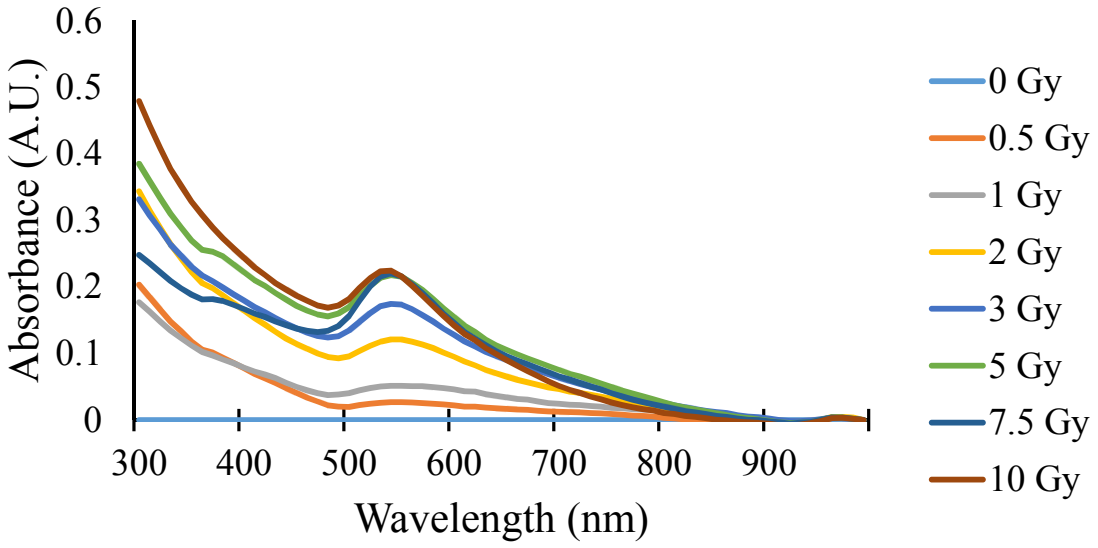

Figure 4.10 Absorbance spectra of **(A)** 10 mM $HAuCl_4$ + 50 mM $C_{16}TAB$ + 7.5% (w/v) agarose + 10 mM ascorbic acid **(B)** 10 mM $HAuCl_4$ + 50 mM $C_{12}TAB$ + 7.5% (w/v) agarose + 10 mM ascorbic acid **(C)** 10 mM $HAuCl_4$ + 50 mM $C_{16}TAB$ + 10% (w/v) agarose + 10 mM ascorbic acid **(D)** 10 mM $HAuCl_4$ + 50 mM $C_{12}TAB$ + 10% (w/v) agarose + 10 mM ascorbic acid, subjected to various doses of X-ray radiation.

(A)

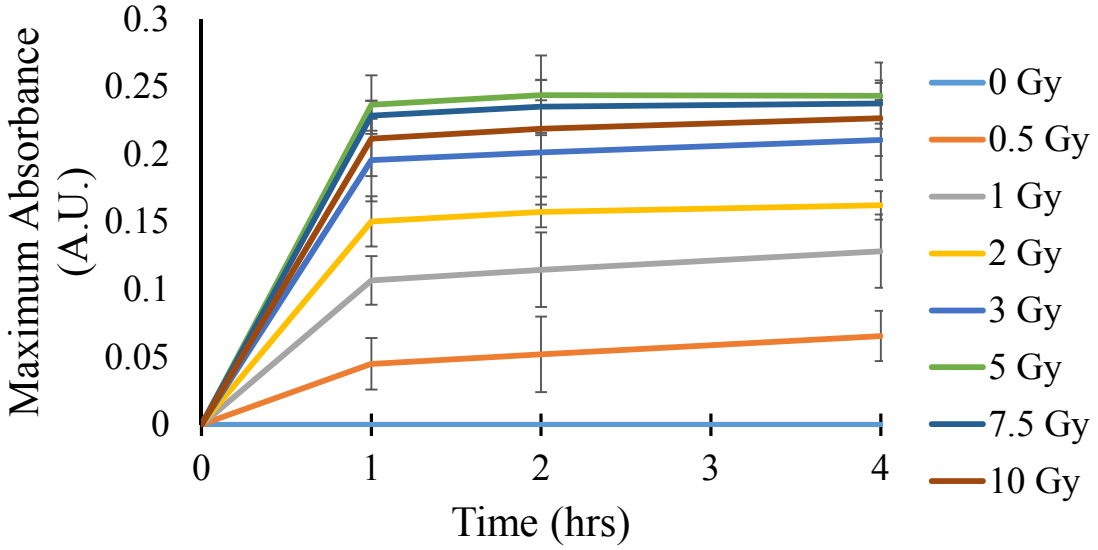

(B)

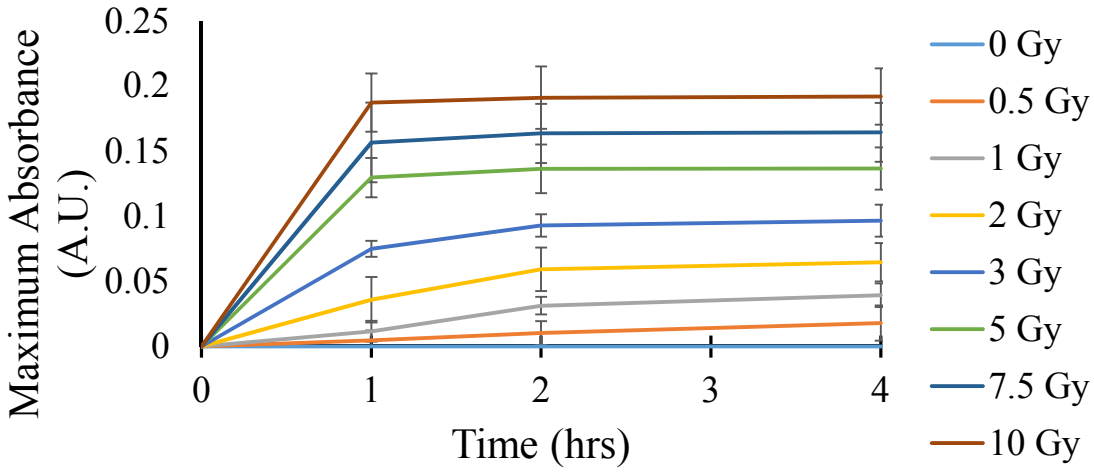

Figure 4.11 Kinetics of gold nanoparticle formation in 5% (w/v) agarose nanosensor gels with **(A)** C_{12}TAB and **(B)** C_{16}TAB following irradiation with different doses of X-rays. Absorbance spectra of the gels were acquired from 300 – 900 nm and the peak value of the absorbance (typically ca. 530 nm) at every time point was used to generate this plot. Earliest determination of the absorbance values was at 1 h due to travel time between the Banner-M.D. Anderson Cancer Center (radiation treatment) and ASU (absorbance analyses).

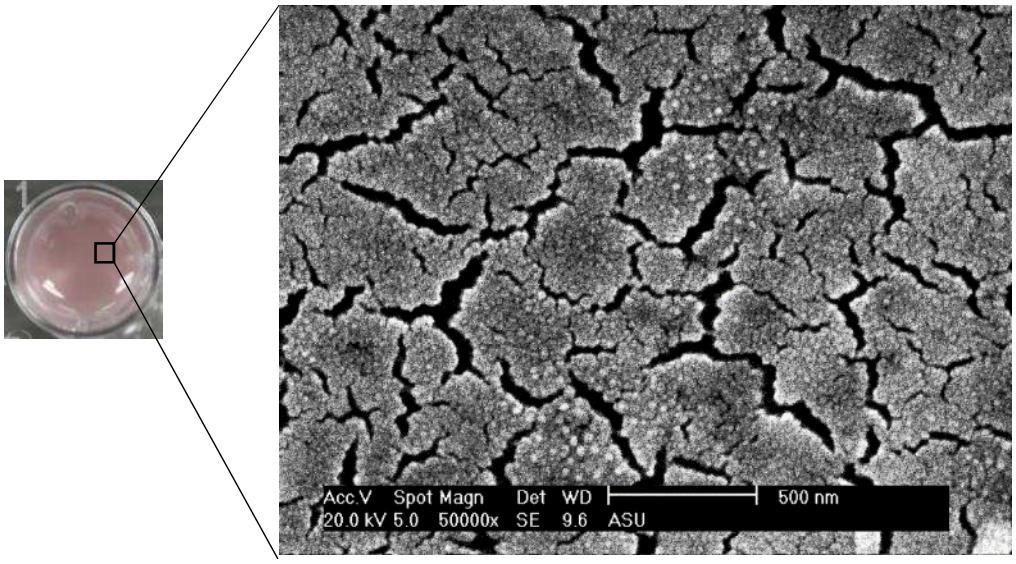

Figure 4.12 SEM image showing gold nanoparticles formed in a 5% (w/v) agarose nanosensor with C_{12}TAB as surfactant post 2 Gy irradiation. Note the location of the SEM in the gel inset is approximate.

Both C_{12}TAB and C_{16}TAB surfactant species were successful in facilitating the formation of gold nanoparticles in the therapeutic radiotherapy dose range, although C_{12}TAB demonstrated a higher efficacy for the formation of nanoparticles at lower doses (e.g. 0.5 Gy). Following reduction of gold ions to zerovalent gold, nanoparticle growth occurs due to collisions among Au(0) seeds or between Au(0) seeds and unreacted Au^{3+} ions; surfactant molecules eventually cap the nanoparticles formed. We hypothesize that C_{12}TAB possesses a higher diffusion coefficient compared to C_{16}TAB due to its smaller size. This, in turn, is likely responsible for its effective transport through the gel network, which facilitates nanoparticle formation at lower doses. Increasing the agarose content (w/v ratio) can limit the diffusion of molecules and nanoparticles through the gel matrix. Indeed, a decrease in the intensity of the maroon color formed was seen following 1 Gy irradiation when 10% agarose was used as compared to 5% agarose (**Figures 4.6B and 4.8B**). The absorbance value decreased from 0.1066 to 0.04, indicating that increasing the agarose concentration decreased nanoparticle yields likely as a result of diffusion limited growth. We also observed that the size of the nanosensor gel did not significantly influence the qualitative colorimetric response; gels formulated in 96 well plates (~7 mm in diameter and ~3 mm in thickness) also demonstrated a characteristic linear response to those formulated above (i.e. gels generated in 24 well plates, ~1.5 cm in diameter and ~3 mm in thickness) despite their smaller diameters (**Figures 4.13A and 4.13B**).

(A)

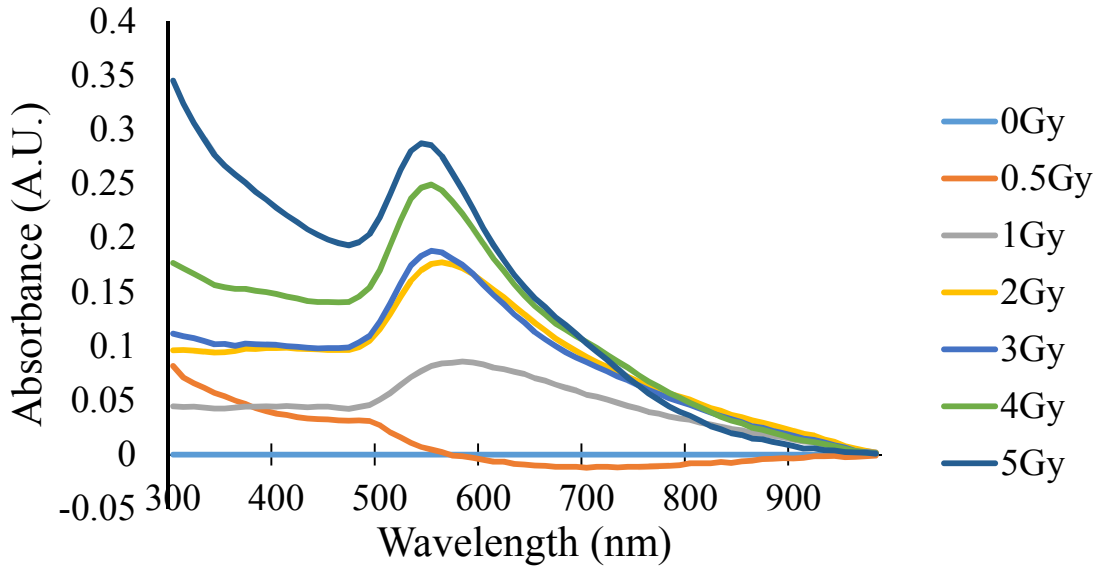

(B)

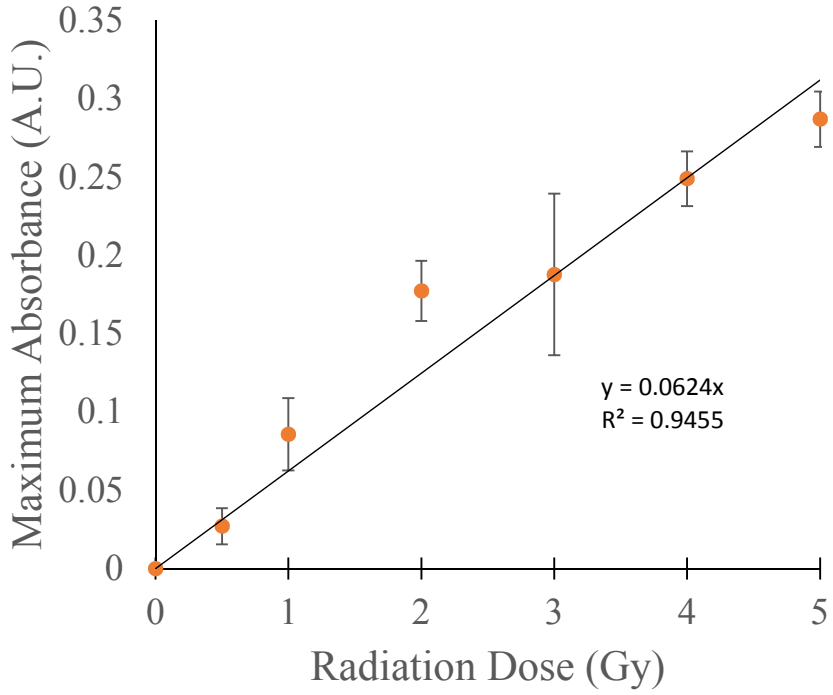

Figure 4.13 Efficacy of nanosensor gels formulated in 96 well plates, which led to gels with smaller dimensions. **(A)** Absorbance spectra of 5% (w/v) agarose nanosensor gels containing C_{12}TAB. **(B)** Calibration of maximum absorbance vs. radiation dose 1hr post radiation.

Following irradiation, nanosensor gels were investigated using UV-spectroscopy in order to obtain a quantitative correlation between nanoparticle formation and the delivered radiation dose. The maximum absorbance value was plotted as a function of X-ray radiation dose ranging from 0.5-10 Gy (**Figures 4.14, 4.15 and 4.16**), which is used for conventional and hypo fractionated radiotherapy in the clinic. As seen in **Figure 4.14,** the C_{12}TAB surfactant was more effective at templating the formation of gold nanoparticles compared to C_{16}TAB; a more intense maroon color of the nanosensor gels was seen in the case of C_{12}TAB compared to that obtained using C_{16}TAB. A linear range of gel absorbance was obtained between X-ray doses of 0 – 3 Gy using C_{12}TAB as the templating surfactant and a calibration curve was generated (**Figures 4.17A**). This is very much within the dose range used in conventional fractionated radiotherapy in the clinic. Higher radiation doses did not enhance gold nanoparticle formation as seen by the invariant absorbance at doses $\geq$ 5 Gy. The efficacy of the nanosensor gel was determined by delivering an actual dose of 1.5 Gy (not used for generating the calibration curve). The color change at 1h was quantified using absorbance analysis, and use of the calibration curve resulted in a dose estimation of 1.61 ± 0.16 Gy for the actually delivered dose of 1.5 Gy, which indicates the utility of this approach for dosimetry in fractionated radiotherapy. Clinically available NanoDots OSLDs™ resulted in a final dose of 1.63 ± 0.007 Gy (n=3). Clinical error percentages for dosimeters are approximately 3.9% for MOSFETs and 5.1% for TLDs[174], respectively. Our colormetric gel nanosensor has an error of 7%, which is comparable to that observed with NanoDots OSLDs™ and are in the range of those reported for MOSFETs and TLDs, which can be more cumbersome to use.

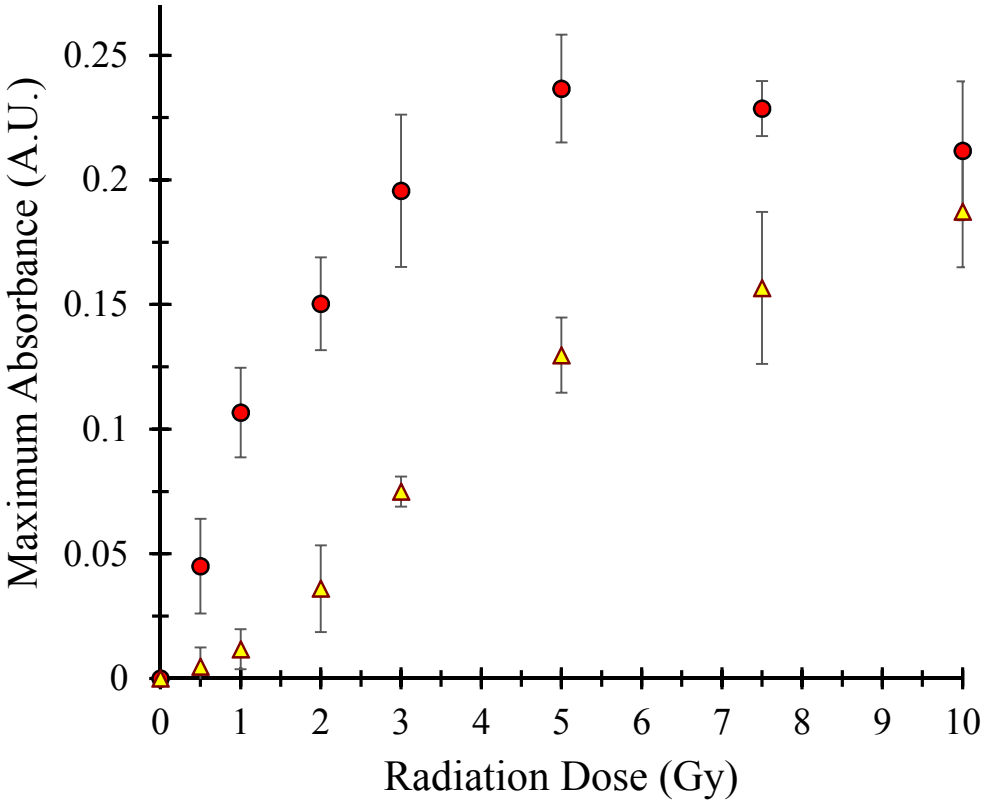

Figure 4.14 Absorbance response of the plasmonic nanosensor gel following irradiation with X-rays; maximum absorbance vs. radiation dose 1h post X-ray irradiation is shown in the plot. Circles indicate the nanosensor response for C_{12}TAB, and triangles indicate the response for C_{16}TAB formulated with 10 mM $HAuCl_4$ in a 5% (w/v) agarose gel.

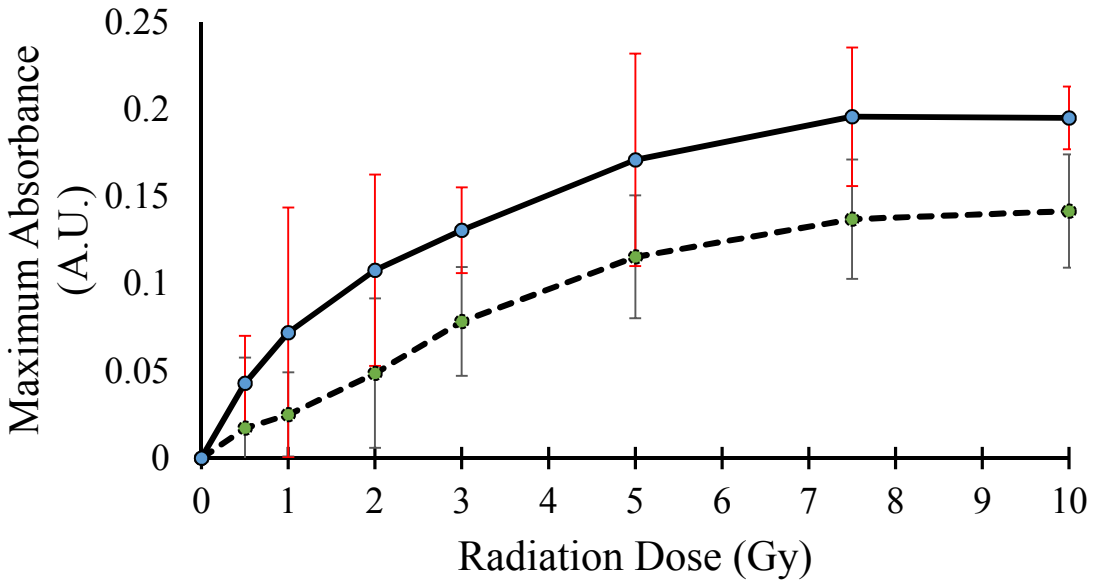

Figure 4.15 Absorbance response of the plasmonic nanosensor gel following irradiation with X-rays. Maximum absorbance vs. radiation dose 1h post irradiation is shown in the plot. Solid line indicates response with C_{12}TAB and dashed line indicates the response with C_{16}TAB for **7.5%** (w/v) agarose gel.

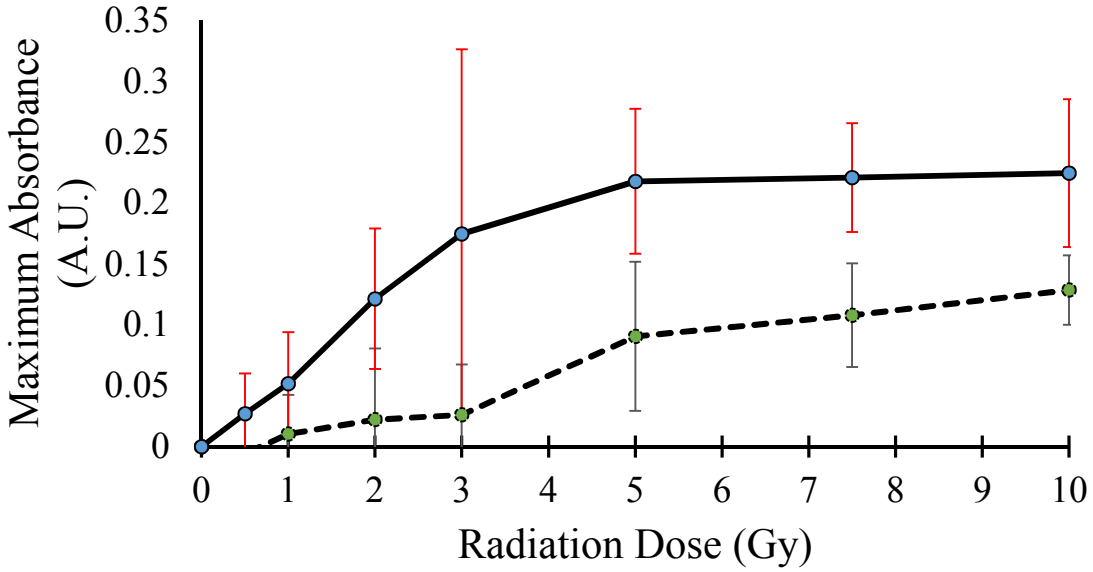

Figure 4.16 Absorbance response of the plasmonic nanosensor gel following irradiation with X-rays. Maximum absorbance vs. radiation dose 1h post irradiation is shown in the plot. Solid line indicates response with C_{12}TAB and dashed line indicates the response with C_{16}TAB for **10%** (w/v) agarose gel.

A

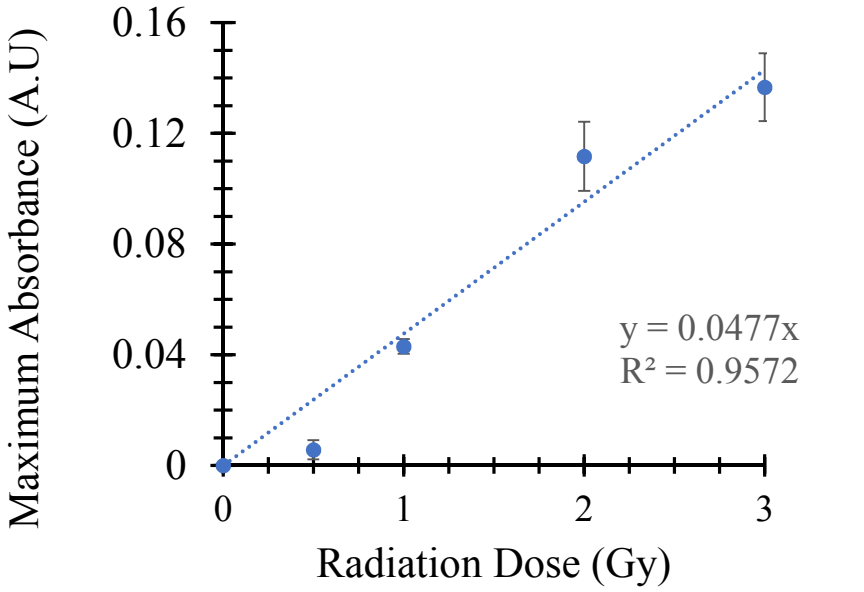

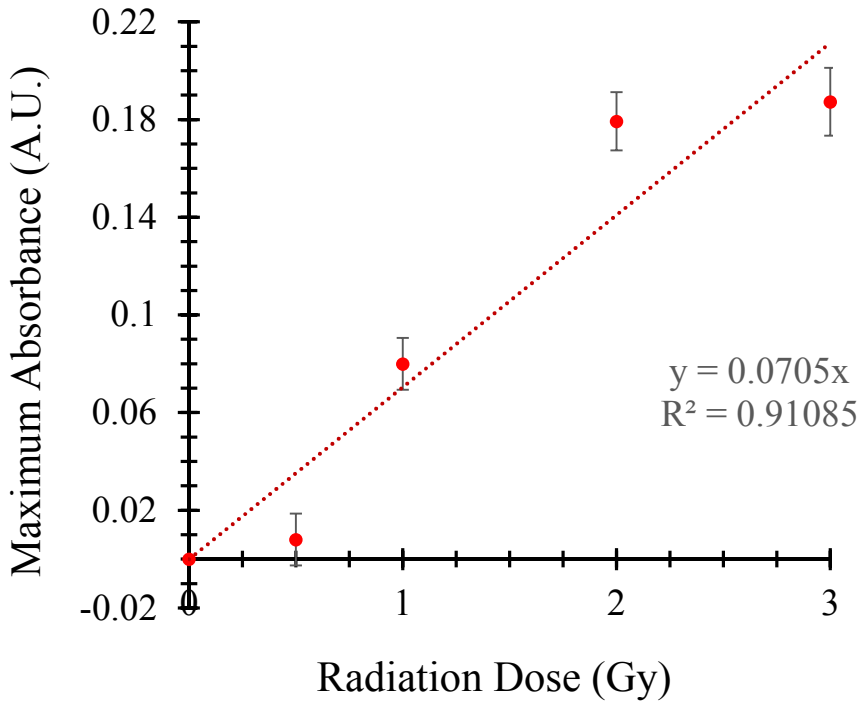

Figure 4.17 (A) Calibration curve of gel absorbance vs. radiation dose (0 – 3 Gy). This curve used for nanosensor gel-based dosimetry of fractionated radiotherapy doses in absence of an anthropomorphic thorax phantom. **(B)** Calibration curve of gel absorbance vs. radiation dose (0 – 3 Gy). This curve used for nanosensor gel-based dosimetry of fractionated radiotherapy doses at the isocenter (100 cm SSD) delivered to the anthropomorphic thorax phantom.

Radiation dosimeters for *in vivo* / *ex vivo* applications should exhibit energy independence, dose rate independence, and minimal attenuation of the incoming ionizing radiation energy[175]. The nanosensor gel showed no significant differences in the optical response (i.e. color change / absorbance) when different dose rates and energies were employed (**Figure 4.18A**). This can be expected since the minimum energy required to ionize water is ≈11 eV[176], which is substantially lower than the energy delivered in these systems. Sources that deliver energy above the required minimum photon energy can ionize water molecules leading to formation of free radicals that can reduce metal ions to nanoparticles. Decreasing the dose rate to 1 Gy/min from 6 Gy/min also did not significantly affect the final absorbance of the nanosensor gel, likely because they both generate approximately the same number of free radicals. Radiolysis products are a function of radiation type (α , β and γ radiation) and independent of dose rate since the energy deposited remains constant irrespective of the rate at which the dose is being generated[173]. The reduction of metal ions by the hydrated electron is completed in a short time (order of 10^{-7} – 10^{-6} s) compared to the longer time scales of nucleation and crystal growth of the nanoparticles (order of minutes)[148]. We hypothesize that since the metal ions reduced by the hydrated electrons are similar in both cases, the final concentration of nanoparticles is independent of dose rate. The relatively low concentration of heavy metal ions (Au^{3+}) in the agarose hydrogel does not alter the incident radiation dose of 1 Gy (**Figure 4.18B**), which is another key requirement of an effective dosimeter. Our results demonstrate that the response of the nanosensor gel is independent of the dose rate delivered and does not attenuate the dose delivered (i.e. no absorption of the incoming energy), all of which are desirable characteristics for *in vivo* / *ex vivo* dosimetry.

(A)

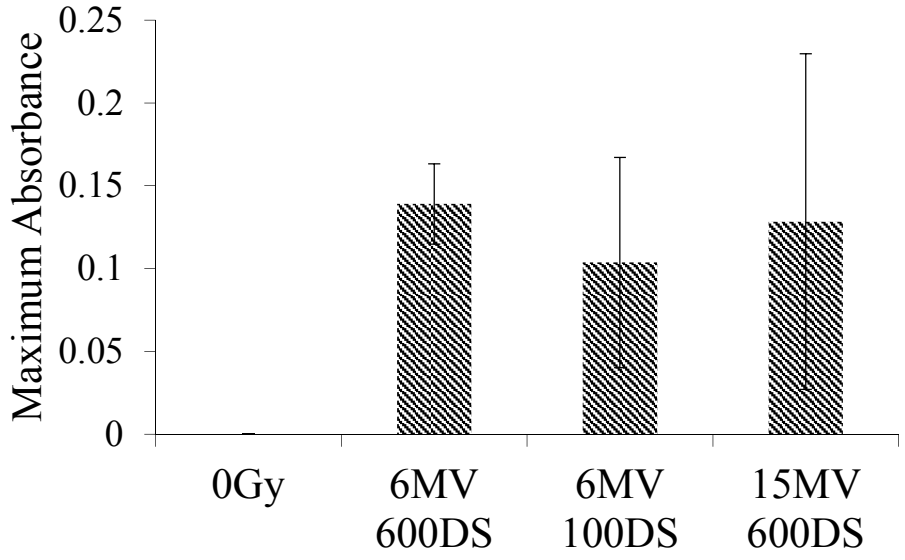

(B)

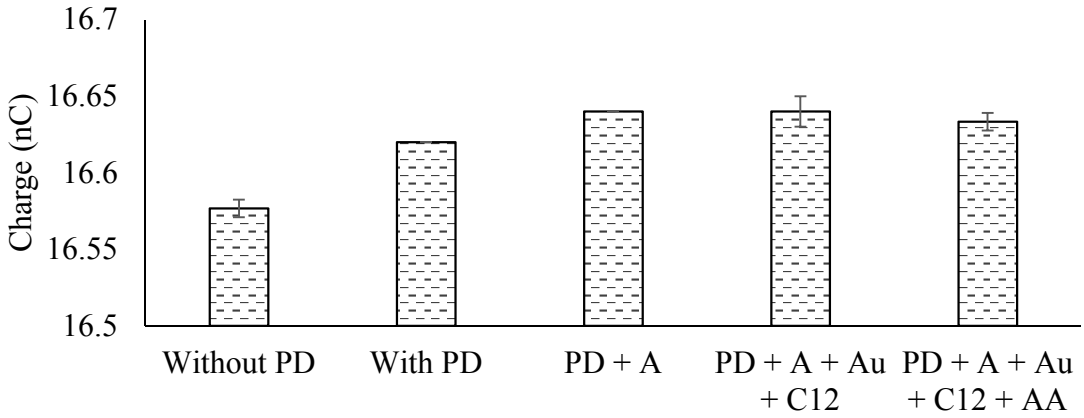

Figure 4.18 (A). Maximum absorbance of the agarose nanosensor gels irradiated with 2 Gy at different dose rates and energy (6 MV and 15 MV). No significant differences in absorbance were observed under these conditions employed indicating dose rate and energy independence of the nanosensor gel system (DS indicates the dose rate in Monitor Units/min) (B). Ion chamber dosimeter is placed below the agarose hydrogel (A) molded to the shape of a 4 inch petri dish (PD) to measure heavy metal (Au) induced radiation attenuation. Even in the presence of heavy metal (Au) and ascorbic acid (AA) there is no significant dose attenuation observed.

We further investigated the translational capabilities of the nanosensor gel using an anthropomorphic thorax phantom (**Figure 4.19A**) which allows the determination of

radiation dose at the skin and mediastinum. The lower half of the mediastinum was subjected to a dose of 2 Gy while the skin was irradiated with 3 Gy as shown by the treatment plan in **Figure 4.19B**. Hydrogel discs containing C_{12}TAB as surfactant were formulated into similar shapes and sizes as those used for calibration (carried out outside the phantom), and placed at the site in the phantom in order to monitor the radiation dose delivered. A linear curve between 0 Gy and 3 Gy was used to quantify the radiation dose delivered to the phantom. Based on the calibration **(Figure 4.17 B)**, a dose of 2.15 ± 0.18 Gy was estimated for a delivered dose of 2 Gy, and a dose of 3.27 ± 0.35 Gy was estimated for the 3 Gy delivered to the skin. The distinct visual color change, coupled with a simple quantitative measurement (UV-Vis absorbance), indicates the potential of this approach for detecting clinically relevant radiotherapy doses.

(A)

(B)

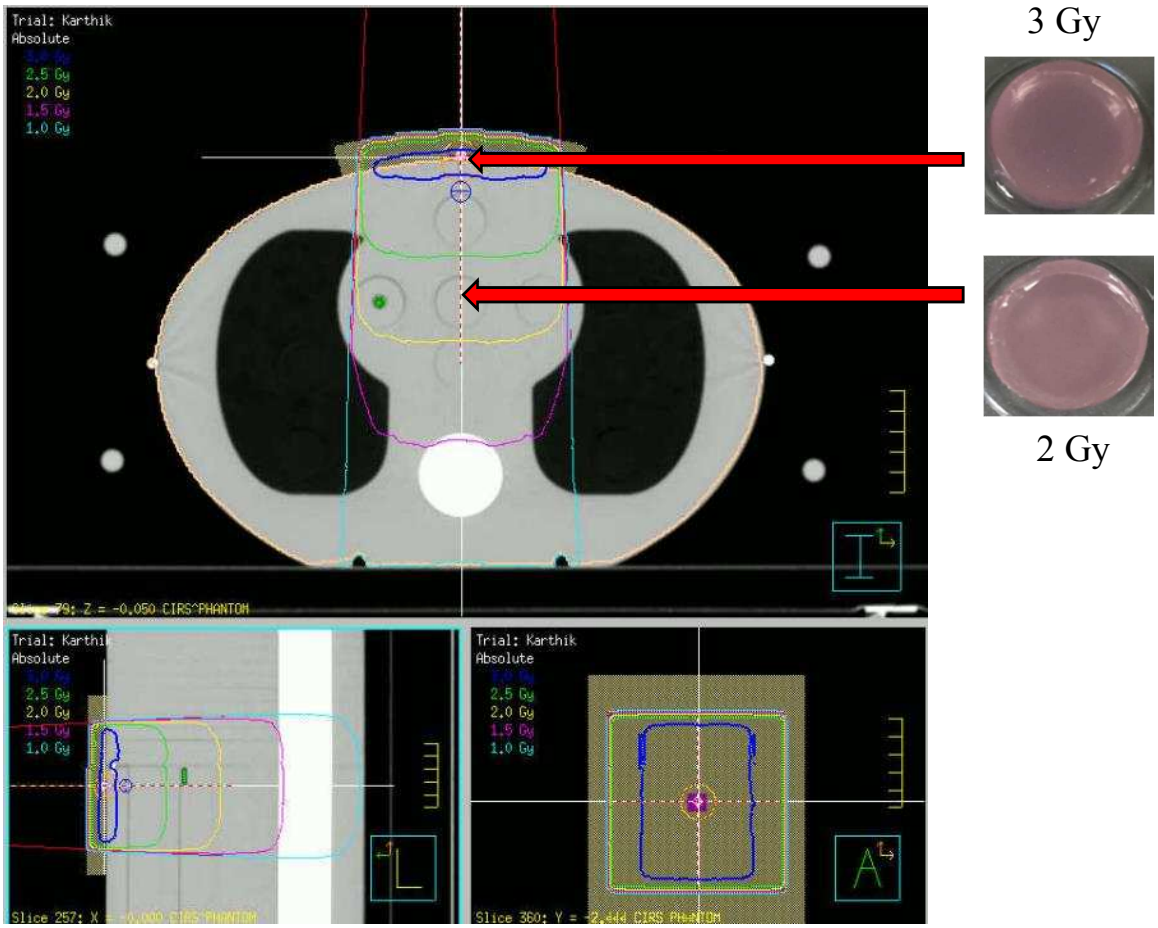

Figure 4.19 (A) Image of the anthropomorphic thorax phantom used in the current radiation dosimetry studies (B) An X-ray computed tomography (CT) scan image of the thorax phantom used in the experiments, showing the radiation dose treatment plan. The inside of the phantom is irradiated with a 2 Gy dose while the skin was irradiated with 3 Gy dose.

Delivered Dose (Gy)	Average radiation Dose Delivered ± one S.D. (Gy) Gel Nanosensor (n=3)
3	3.27 ± 0.35
2	2.15 ± 0.18

Table 4.1 The table indicates the dose delivered according to the treatment plan and the radiation dose estimated by the gel based plasmonic nanosensor.

4.4 Conclusions

To our knowledge, this is the first demonstration of a colorimetric gel dosimeter for detecting therapeutically relevant doses of ionizing radiation currently employed in individual fractions in fractionated radiotherapy. The nanosensor gel was able to detect doses as low as 0.5 Gy, demonstrated a linear response in the range of 0 – 3 Gy, and was effective when placed in an anthropomorphic thorax phantom, all of which indicate the suitability of this approach in detecting radiation doses delivered during an individual fraction (typically 2 Gy) in fractionated radiotherapy. Use of hydrogels can facilitate adaptation to different anatomical shapes (e.g. skin, breast, etc.), and the ease of detection and quantification of this approach can facilitate easy translation to clinical use. Although agarose was used as a model for biocompatible hydrogels, several gel systems, including poly(lactic-co-glycolic acid) or PLGA, could also be investigated for this application. Ascorbic acid is an FDA-approved GRAS (generally recognized as safe) compound. One potential concern of the current gel nanosensor system is the toxicity of C_{16}TAB and

C_{12}TAB as templating surfactants, especially at higher concentrations. However, this can be mitigated by the use of lower concentrations and more effective formulation methods (e.g. secondary containment in a device)[177]. However, further biocompatibility studies using animal (e.g. mouse) models will be necessary to determine this. In addition, identification of biocompatible templating molecules can further obviate potential toxicity concerns. We anticipate that these new developments will accelerate the translation of nanosensor gels for detecting radiation doses in the clinic.

Chapter 5 HYDROGEL NANOSENSORS FOR COLORIMETRIC DETECTION AND DOSIMETRY IN PROTON BEAM THERAPY

5.1 Introduction

Radiation therapy is one of the primary treatment modalities employed for the ablation of various tumors in a clinical setting[178]. Ideally, one can enhance therapeutic outcomes of ionizing radiation by maximizing the sparing of the volume of healthy tissues that otherwise get exposed to XRT. At present, most external beam radiotherapy (EBRT) is administered using high-energy photons (e.g. X-rays), which characteristically deliver exit doses. This results in the delivery of significant amounts of radiation to normal tissues lying either adjacent or towards the distal end of the target (e.g. tumor). This can lead to side effects, including radiation-induced toxicity, in healthy tissues.

Proton beam therapy is an alternate form of radiation therapy in which particles (protons), instead of high-energy photons, are delivered to the tumor, potentially leading to greater control and precision over dose deposition at the disease site[179]. This can lead to decreased damage to the surrounding tissue and cause fewer side effects post radiation treatment. This is primarily due to the unique dose deposition characteristics of protons known as the Bragg peak[180]. As the protons enter a patient's body they lose their kinetic energy following collisions with electrons in tissues. As the protons slow down, their interaction cross section with electrons increases steadily until it reaches a sharp maximum shortly before the protons come to rest. This sharp maximum gives rise to the dosimetric Bragg peak[181] of maximal dose at the target site.

Radiation doses are typically delivered in fractions of 2 Gy dose/day (conventional fractionated radiotherapy) leading to a cumulative dose in the range of 20 - 70 Gy for the entire treatment course (1 Gy = 1 Joule energy absorbed by 1 kg mass). Typically, patients are treated daily once a day, 5 days per week, and over a period of 8-9 weeks. Following the development of sophisticated imaging techniques and beam delivery modalities, hypofractionated proton beam therapy in which, higher doses are delivered per treatment fraction (e.g. 4 Gy dose/day), has also found increased application in the treatment of cancer. This modality of treatment has been employed for aggressive tumor sites including in the liver, prostate and lung where high radiation doses are required in order to allow for a high rate of local control with minimal toxicity to the surrounding tissue[182-184].

The complexity of precisely delivering radiation doses to tumor sites has increased dramatically over the last decade. The rapid development of these advances has led to some imbalance in the development of verification technologies (dosimeters) for detecting potential sources of error during treatment. Clearly, detection of excess or deficient radiation levels delivered to patients will lead to improved safety and efficacy of the treatment[185]. Solid-state dosimeters, including p-type semiconductor diodes and diamond detectors, are among those employed in the clinic[186]. These detectors require specialized equipment for reading output (i.e. radiation dose), exhibit energy dependence, can require expensive fabrication processes, and do not conform to human anatomical features. These difficulties partially motivated the use of radiochromic films in clinical settings. The response of these films to radiation is typically measured at up to 24 hours post irradiation until relative stability of response is achieved[187]. A faster response is required to determine

the delivered radiation dose in order to administer any modifications to the treatment plan in order to ensure the safety of the patient. Polymer gel dosimeters require the use of sophisticated and expensive visualization modalities including magnetic resonance imaging (MRI)[161, 186], which limits their practical use in the clinic. There is a need for a novel dosimeter that can overcome these limitations, demonstrate a rapid and robust performance (e.g. response time less than 24 hours), result in safe and effective monitoring radiation doses in proton therapy, potentially leading to improved patient outcomes.

Gold nanoparticles have been used in a wide range of applications including catalysis, imaging, diagnostics and molecular delivery[66, 67, 188]. Of particular relevance, colorimetric assays using gold nanoparticles have been employed as sensors for the detection of analytes including toxic metal ions and biological enzymes[189, 190]. Gold nanoparticles are easy to synthesize, inert, functionalizable, and demonstrate tunable size and shape dependent properties (including colorimetric responses)[191], all of which make them attractive for sensor development.

Advances in molecular and nanoscale systems offer new options for effective radiation dosimetry[192]. Ionizing radiation causes formation of free radicals in water following hydrolysis. We employed this phenomenon in concert with effective templating molecules (e.g. aliphatic surfactants) in order to engender the formation of plasmonic (gold and gold-silver) nanoparticles from their respective metal ion formulations[93, 162, 193-195]. The formation of plasmonic nanoparticles in liquid or gel formulations is accompanied by a visible color change which is distinct from the original metal ion formulation, which is

colorless. Here, we report, for the first time, a colorimetric approach for the rapid detection of therapeutic levels (0-3 Gy_{RBE}) of proton irradiation (Relative Biological Effectiveness or RBE is defined as the ratio of doses required to reach the same level of biological effectiveness when comparing two ionizing radiation treatment modalities)[196]. The extent of the color intensity depends on the dose of protons delivered to the gel and can be used for quantitative dose determination. To our knowledge, this is the first colorimetric nanosensor for detecting and predicting proton doses and has high potential for translation to clinical proton beam radiotherapy.

5.2 Materials and Methods

Materials. Gold(III) chloride trihydrate ($HAuCl4.3H_2O$), decyltrimethylammonium bromide ($C_{10}TAB$) (≥98.0%; non-aqueous titration grade), dodoceyltrimethylammonium bromide ($C_{12}TAB$) (≥98%), myristyltrimethylammonium bromide ($C_{14}TAB$) (≥99%), L-ascorbic acid and agarose were purchased from Sigma-Aldrich. Cetyltrimethylammonium bromide ($C_{16}TAB$) was procured from MP Chemicals. The chemicals received from the vendors were not purified further. MilliQ water (18.2 MΩ.cm) was used as solvent for all experiments.

Preparation of the Precursor Hydrogel. $HAuCl_4$ (30 µL of 10 mM solution) was mixed with 600 µL of 50 mM solution of $C_{x=10,12,14,16}TAB$ aliphatic surfactants, and 100 µL of the above mixture were discarded. Heated aqueous agarose (500 µL of 5% v (ml) /w (mg)) was added to the gold-surfactant solution. 24 well plates (diameter ~16 mm) were used to set the liquid mixture (200µL, 400µL and 650 µL) and form gels with a thickness of ~1, 2 and 3 mm respectively. 10mM ascorbic acid (200µL for a 1mm gel, 400µL for a 2mm gel

and 650 μL for a 3mm gel) was allowed to diffuse into the gel for 10 minutes, resulting in the formation of translucent gel discs. These discs were used for irradiation studies as precursor hydrogels.

Proton Beam Irradiation. All CT simulations of the phantom based setup and proton beam irradiations were conducted at the Proton Beam Therapy Center at Mayo Clinic Hospital, Phoenix, AZ. CT simulations were performed using the SOMATOM Definition AS (Siemens Healthcare, Erlangen, Germany), and spot-scanning based proton treatment plans were created using the Eclipse (Varian Medical Systems, Palo Alto, CA) treatment planning system (version PCS 13.7) (TPS). Proton irradiations were delivered using the PROBEAT-V Proton Beam Therapy System (Hitachi, Ltd., Tokyo, Japan). Proton beam therapy doses are customarily prescribed and reported in relative biological effectiveness (RBE) - weighted absorbed dose (D_{RBE}). In this work, in order to obtain physical dose D_RBE values may simply be divided by a constant factor of 1.1.

Gel samples were placed in the inner wells of a 24-well plate, which was placed on the table with 5 cm-thick acrylic blocks placed above and below it. A CT simulation of the phantom was performed with slice thicknesses of 2 mm. A single Field Uniform Dose based treatment plan was designed in order to deliver 0.5 Gy_{RBE} uniformly across the central wells. The treatment was optimized such that the 99% of the dose reporting reference volume received 100% of the dose. In order to deliver larger doses to these gel samples, sequential treatment plans were generated by simply scaling the doses to higher D_{RBE} levels: 0.5, 1.0, 1.5, 2.0, 3.0, 4.0 and 5.0 Gy_{RBE}. These doses delivered to our samples

were validated with another reference film dosimeter. A piece of Gafchromic EBT3 film (Ashland, Bridgewater, NJ) was placed directly below the well plate during irradiation of the gel with 2.0 Gy_{RBE}. Reference dosimetry using these calibrated gafchromic films matched the TPS calculated doses to within +/- 2.5%. While the irradiation times ranged between 41 seconds for the 0.5 Gy_{RBE} dose and 86 seconds for the 5.0 Gy_{RBE} dose, dose rate dependence of these dosimeters has not been investigated in this particular study.

Plasmonic Gel Dosimetry on an Anthropomorphic Child Phantom. A CT simulation, using a slice thickness of 1 mm and a pitch of 1.0, was performed on an ATOM 704 anthropomorphic phantom (CIRS Inc., Norfolk, VA), which models a 1-year-old infant. Three radio-opaque markers were placed at isocenter, and two more were placed at the head and foot to ensure a reproducible setup. A plan was created whereby a posterior-anterior field was used to deliver a prescription D_{RBE} of 1.8 Gy_{RBE} to a target encompassing the spine. The phantom was irradiated with gel samples placed on the table at various points beneath it, providing a measurement of the skin dose to the phantom.

Absorbance Spectroscopy. Following irradiation with different proton doses, the absorbance spectra of the gel samples were measured for wavelengths ranging from 300 to 990 nm with a step size of 10 nm using a BioTek Synergy 2 plate reader. All absorbance measurements were carried out at 2 hours following irradiation, because the travel time from the Mayo Clinic to ASU can vary. However, the color change was seen as early as 15 minutes post irradiation in most cases. The absorbance values obtained were offset by subtracting the wavelength at 990 nm. The peak between 500-600 nm was used as an

indicator for the formation of gold nanoparticles. A maximum absorbance value between 500-600 nm vs. proton dose was plotted for all surfactants.

Compression Testing. Force under compression for failure was recorded using a TA.XT Plus Texture Analyzer (Texture Technologies Corp., Hamilton, MA) equipped with Exponent (Stable Microsystems) software. The hydrogels were placed between the stationary plate and the moving accessory (TA-8; 1/4" spherical ball). The accessory movement speed used was 2mm/sec and a trigger force of 0.049N was set. The maximum compressive force force required was measured through the force vs distance curve generated.

Image Processing. A Canon EOS 1100D camera was used to acquire all gel images. The Fotor Photo Editor application was used to crop the images to the desired size, but no further editing was carried out. All pictures reported in this article were acquired for visualization alone and not used for quantification of the dose response, which was carried out using absorbance analysis.

Transmission Electron Microscopy. The irradiated sample was kept at room temperature overnight for air drying. The dried sample was soaked in epoxy resin. Thin slices of the cured epoxy-containing sample were sectioned using an ultramicrotome. These thin samples were imaged using a Philips CM 12 Transmission electron microscope.

Statistical Analyses. All experiments were carried out in triplicate unless otherwise stated. Statistical analysis calculations were carried out using Microsoft Excel and data are expressed as the mean of these independent experiments ± one standard deviation.

5.3 Results and Discussion

The ability to detect proton doses administered to tissues can have significant implications for improving treatment outcomes in cancer radiotherapy. To this end, a robust nanosensor that can reliably detect doses at the intended target and / or at nearby tissues can enhance the efficacy of radiotherapy, which can lead to improved patient outcomes. Here, we report our studies on a gel-based colorimetric nanosensor that can detect doses employed for fractionated proton radiotherapy in the clinic. The nanosensor works on the principle that exposure of a precursor hydrogel to high-energy radiation (e.g. photons) or particles (e.g. protons) results in the formation of free radicals upon hydrolysis (water splitting), which, in turn, reduce the encapsulated gold ions to gold nanoparticles within the gel matrix **(Figure 5.1)**[162, 193]. The plasmonic properties of these gold nanoparticles renders a color (typically maroon) to the gel. The intensity of the color is governed by amount nanoparticles formed, which, in turn, is dependent on the dose of protons absorbed.

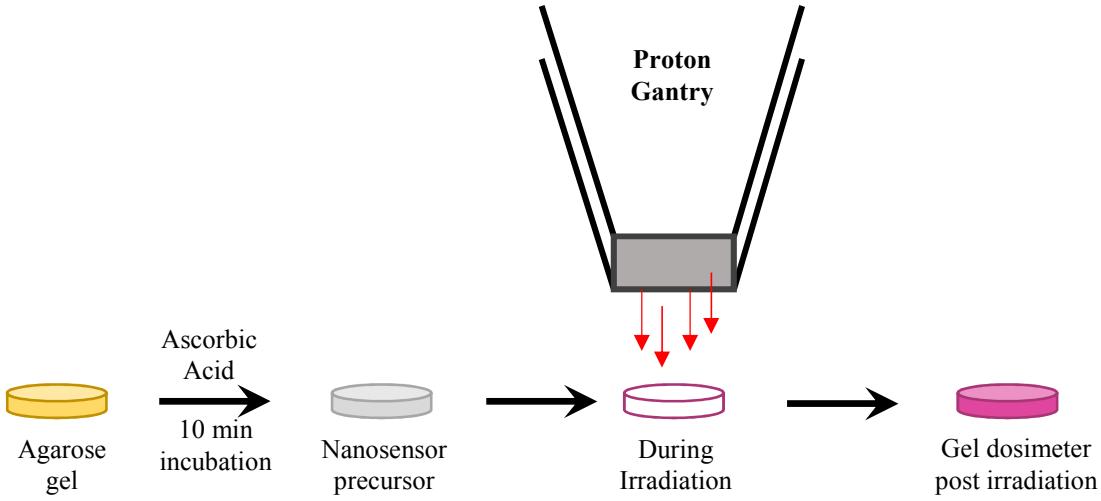

Figure 5.1 Schematic of nanosensor gel dosimeters for proton beam therapy. Cylindrical hydrogel discs, 16 mm diameter and 3 mm height, are formulated with 10 mM $HAuCl_4$, 50 mM C_xTAB (x=10, 12, 14 or 16) and 5% (w/v) agarose. Just prior to irradiation, 10 mM ascorbic acid is added from the top and allowed to diffuse into the gel for 10 minutes. A characteristic maroon color is seen post irradiation due to formation of gold nanoparticles within the gel matrix.

Initially, gold exists as trivalent Au(III) ions along with the cationic surfactant molecules within the heated agarose solution. These Au(III) metal ions are first reduced to monovalent Au(I) ions using ascorbic acid as the reducing agent[194]. The reduction potential of Au(I) is higher than that of Au(III), which increases the thermodynamic favorability of zerovalent gold ion or Au(0) formation[138, 197]. These Au(0) ions are thought to nucleate and grow to form gold nanoparticles; the cationic surfactant used in the formulation (C_xTAB; x=10, 12, 14, or 16) likely stabilizes the gold nanoparticles formed and may also play a role in templating the nanoparticles.

Irradiation of Au(I)-containing agarose gels with high-energy proton particles can facilitate splitting of water molecules in the hydrogel, which, in turn, can result in the formation of e-, H· and OH· free radicals[198]. Of these, e^- and H· are reducing in nature and help reduce Au(I) ions to zerovalent Au(0) ions. Ascorbic acid, an antioxidant, is thought to help quench the oxidizing OH· radicals formed in the process[199], which can further enhance the efficacy of nanoparticle formation. The agarose hydrogels are initially translucent and colorless prior to irradiation, but change color to maroon once exposed to protons due to formation of gold nanoparticles within the matrix, resulting in a visible indicator of proton therapy doses. Surfactants of different chain lengths ($C_{x,\ \text{where}\ x=10,\ 12,\ 14,\ \text{or}\ 16}$TAB) were employed to facilitate the formation of gold nanoparticles. Water solubility, biocompatibility and ease in formulation of hydrogels were the key factors influencing the selection of agarose as the gel matrix in these studies.

We fabricated agarose gels with thicknesses of 1, 2 or 3 mm loaded with C_{12}TAB and C_{14}TAB surfactants and investigated them for a colorimetric response following irradiation with protons (2 Gy). An increase in the absorbance was observed with an increase in the gel thickness following irradiation **(Figure 5.2)**. It was observed that the 1mm and 2mm thick gels formed a higher meniscus curvature making the gels non-homogenous. This led to the formation of a non homogenous distribution of gold nanoparticles in the gel, which could even be visually observed **(Figures 5.3A, 5.3B, 5.4A and 5.4B)**. However, the distribution of gold nanoparticles was visually homogeneous in gels that were ~3 mm in thickness **(Figures 5.6A and 5.6B)**. Absorbance values, used to quantify gold nanoparticle formation, were similar at different points along the diameter, which further indicated a

uniform distribution of nanoparticles formed in the 3 mm thick agarose matrix (**Figure 5.5).** This uniform distribution of nanoparticles and the ease of handling of the 3 mm hydrogels made this formulation an excellent choice for further radiation experiments.

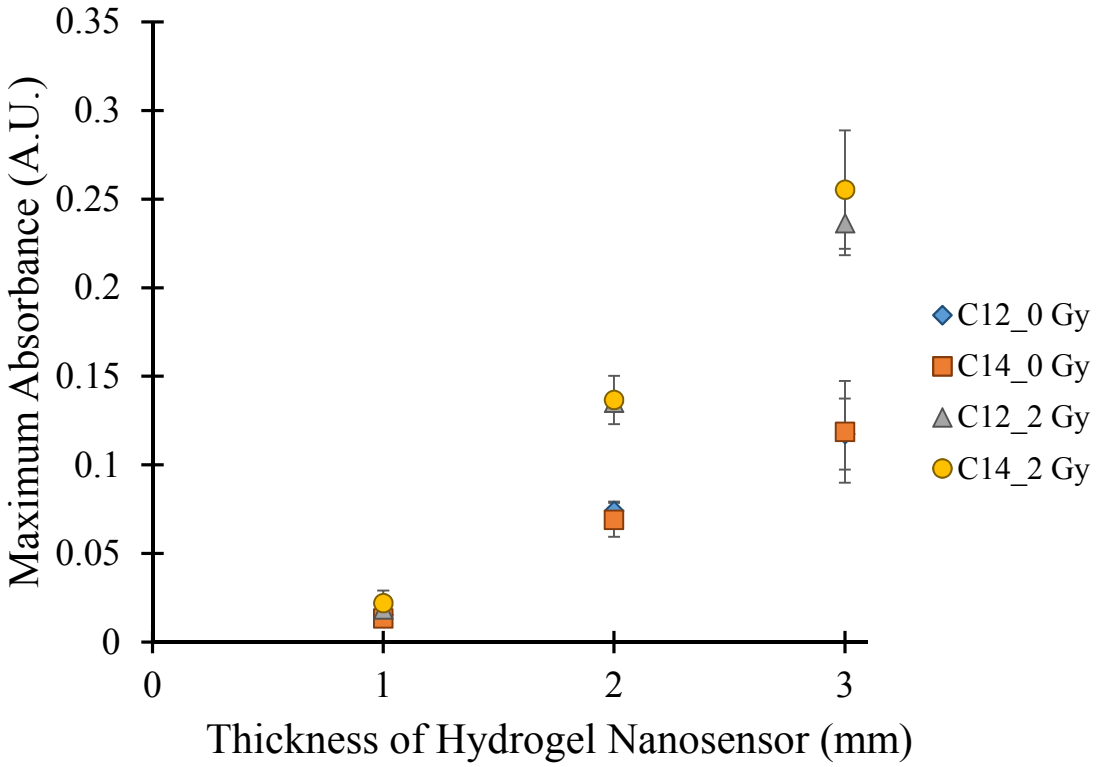

Figure 5.2 Absorbance spectra of the hydrogel nanosensor following irradiation with proton beam therapy. A plot depicting maximum absorbance vs radiation dose 2 hours post irradiation is shown. Gels containing 50 mM C_{12}TAB surfactant irradiated with 0 Gy_{RBE} (depicted by blue diamonds) and 2 Gy_{RBE} (depicted by grey triangles), and 50 mM C_{14}TAB surfactant irradiated with 0 Gy_{RBE} (depicted by orange squares) and 2 Gy_{RBE} (depicted by yellow circles) with varying thickness are shown in the plot. In the figure, Gy_{RBE} is denoted as only as Gy.

(A)

$C_{12}TAB$ $C_{14}TAB$

(B)

$C_{12}TAB$ $C_{14}TAB$

Figure 5.3 Images of nanosensor gel of thickness 1 mm containing $C_{12}TAB$ or $C_{14}TAB$ surfactants. **(A)** Control gels irradiated with 0 Gy_{RBE} **(B)** nanosensor gels irradiated with 2 Gy_{RBE} radiation dose using proton beams. All gels contain 10 mM $HAuCl_4$ and 10 mM ascorbic acid. All images were taken 2 hours after irradiation of gels with protons.

(A)

$C_{12}TAB$ $C_{14}TAB$

(B)

$C_{12}TAB$ $C_{14}TAB$

Figure 5.4 Images of nanosensor gel of thickness 2mm containing $C_{12}TAB$ or $C_{14}TAB$ surfactants. (A) Control gels irradiated with with 0 Gy_{RBE} and (B) nanosensor gels irradiatied with 2 Gy_{RBE} radiation dose using proton beams. All gels contain 10 mM $HAuCl_4$ and 10 mM ascorbic acid. All images were taken 2 hours after irradiation of gels with protons.

(A)

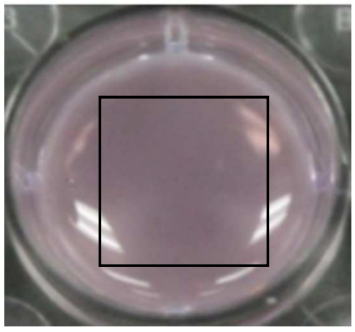

0.109	0.104	0.103	0.108
0.106	0.102	0.1	0.105
0.105	0.1	0.099	0.104
0.108	0.103	0.105	0.105

(B)

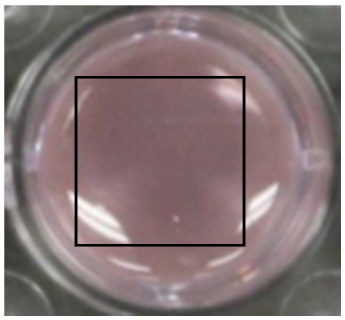

0.196	0.173	0.167	0.18
0.175	0.163	0.161	0.168
0.172	0.164	0.162	0.168
0.178	0.167	0.167	0.175

Figure 5.5 Absorbance values of 3mm Agarose gels at different locations on the hydrogel measured 2 hours post irradiation. Gels containing **(A)** C_{12}TAB and **(B)** C_{14}TAB surfactants were irradiated with 2 Gy_{RBE} radiation dose using proton beams. All gels contain 10 mM $HAuCl_4$ and 10 mM ascorbic acid.

(A)

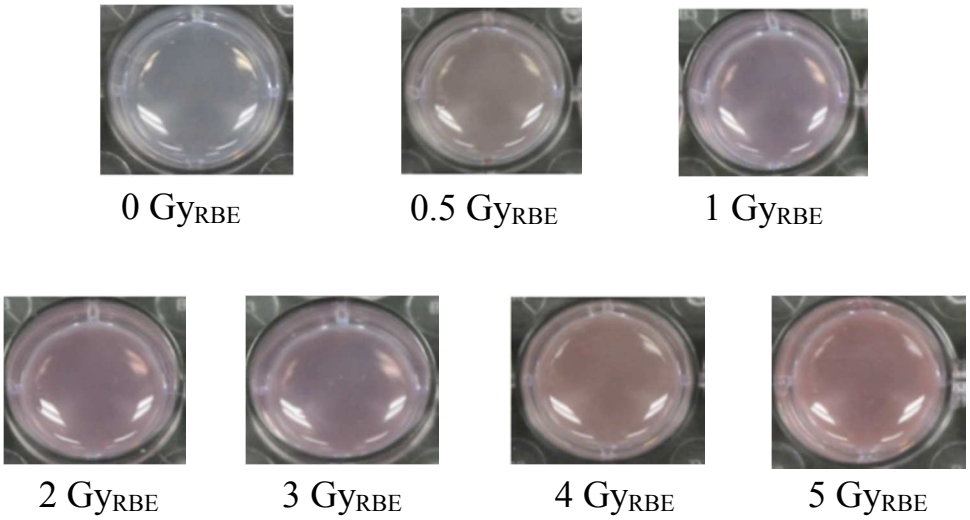

(B)

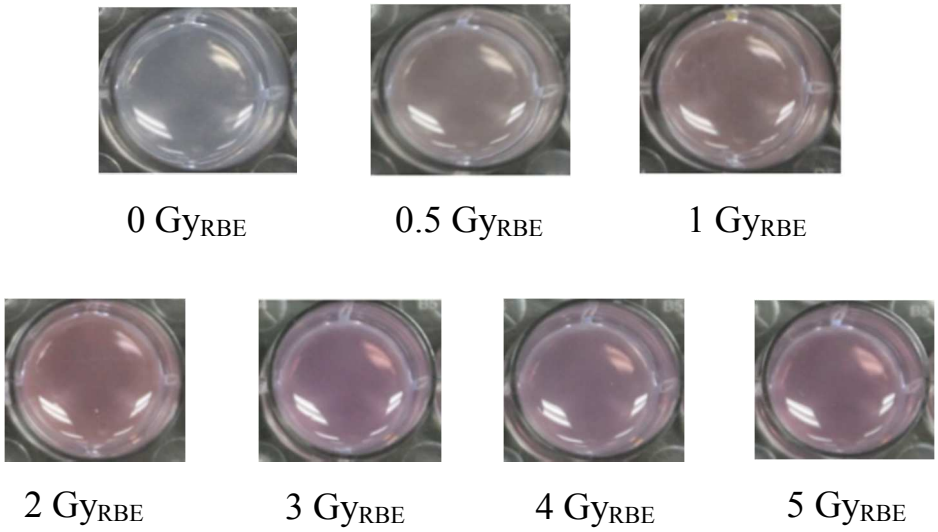

Figure 5.6 Images of nanosensor gels containing (A) 50 mM C_{12}TAB and (B) 50 mM C_{14}TAB surfactants, irradiated with different doses of proton beams as indicated. All gels contain 10 mM $HAuCl_4$ and 10 mM ascorbic acid. All images were taken 2 hours after irradiation of gels with protons.

A number of control experiments were carried out in order to investigate the performance of the gel nanosensor system. An intense yellow color of the hydrogel was observed

following the mixture of $HAuCl_4$ and C_xTAB (x=10,12,14 or 16) with heated agarose. The observed color is caused by the ligand exchange of Cl^- in $AuCl_4^-$ to Br^- present in C_xTAB[138]. It is likely that $AuBr_4^-$ exists as stable CTA-$AuBr_4^-$ metallomicelles within the agarose matrix[138]. Ascorbic acid reduces $AuBr_4^-$ to $AuBr_2^-$, which indicates conversion of gold ions from the trivalent Au(III) state to the monovalent Au(I) state[200]. Ascorbic acid is a weak reducing agent and thus, only partial reduction of the gold (from Au(III) to Au(I)) is likely possible in the presence of a high concentration of the surfactant. This is because the oxidation potential of the ascorbic acid reduces in micellar environments[201]. The yellow-colored hydrogels turn colorless once ascorbic acid is added to the hydrogel, which is the precursor hydrogel used in all proton irradiation studies. We suggest that the presence of micelles in our hydrogel system leads to enhanced shielding between Au^+ ions and ascorbic acid, which retards spontaneous nanoparticle formation.

Irradiation of ~3 mm agarose hydrogels containing $HAuCl_4$ and C_xTAB with protons but in the absence of ascorbic acid did not induce any color change to the hydrogel **(Figure 5.7)**. Similarly, irradiation of gels containing a mixture of $HAuCl_4$ and agarose alone (no ascorbic acid or C_xTAB) did not result in a change in color **(Figure 5.7)**. These results indicate that all components - $HAuCl_4$, C_xTAB, ascorbic acid and agarose - play a key role in the formulation of the plasmonic hydrogel based nanosensor for detecting proton doses. Interestingly, we observed that $C_{10}TAB$ shows a slight development of color, which indicates spontaneous nanoparticle formation even in absence of radiation. $C_{10}TAB$ (CMC ~65mM) does not form micelles at concentrations employed (~25mM) in the current

system[202]. This likely leads to low steric hindrance and allows for spontaneous nanoparticle formation, which can be visually observed (**Figure 5.8**).

(A)

(B)

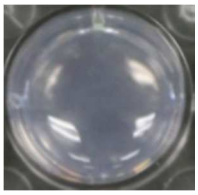

Figure 5.7 Images of controls of agarose gels acquired 2 hours post a 2 Gy_{RBE} radiation dose containing **(A)** 10 mM $HAuCl_4$ and 50 mM $C_{x=10,12,14\&16}TAB$ surfactant (From left to right), but no ascorbic acid **(B)** only 10 mM $HAuCl_4$, and no $C_{x=10,12,14\&16}TAB$ or ascorbic acid. No change in color was observed post irradiation.

(A)

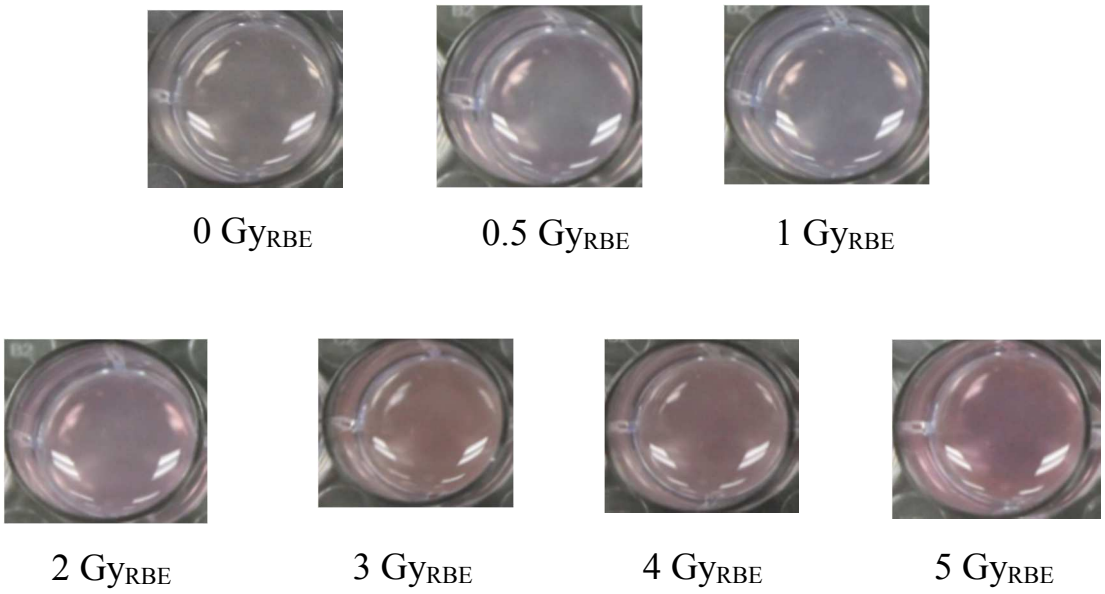

(B)

Figure 5.8 Images of nanosensor gel samples composed of (A) 50 mM C_{10}TAB and (B) 50 mM C_{16}TAB surfactants. All gels contain 10 mM $HAuCl_4$ and 10 mM ascorbic acid. All images were taken 2 hours after irradiation of samples with protons.

All surfactants employed were able to facilitate and template the formation of gold nanoparticles when exposed to the therapeutic doses of proton irradiation (0-5 Gy_{RBE}). A characteristic maroon color of gold nanoparticles was visible post irradiation in the hydrogels **(Figures 5.6A, 5.6B, 5.8A and 5.8B)**. The time necessary for the development of the color development was dependent on the nature of surfactant used. C_{12}TAB-loaded agarose demonstrated the color change as early as ~5 min, but C_{14}TAB-loaded hydrogel demonstrated a color change in ~10 minutes following irradiation with a 2 Gy_{RBE} dose, which is conventionally employed in fractionated radiotherapy **(Figures 5.9)**. Low doses (0.5 Gy_{RBE} or 1 Gy_{RBE}) irradiation required longer times (~15 minutes) for the development of the maroon color. Formation of gold nanoparticles was further visualized using transmission electron microscopy (TEM; **Figure 5.10**); non-homogenous particle distribution was observed with particles ranging from 20-100 nm in diameter / longest dimension.

(A)

C_{12}TAB C_{14}TAB

(B)

C_{12}TAB C_{14}TAB

(C)

C_{12}TAB C_{14}TAB

(D)

C_{12}TAB C_{14}TAB

Figure 5.9 Images of nanosensor gels formulated with 50 mM C_{12}TAB and C_{14}TAB surfactants. Gels were irradiated with a 2 Gy_{RBE} dose of proton beams, and images were taken at **(A)** t = 0 mins, **(B)** t = 5 mins, **(C)** t = 10 mins and **(D)** t = 15 mins post irradiation. All gels contain 10 mM $HAuCl_4$ and 10 mM ascorbic acid. Images are representative from n= 3 experiment.

(A) **(B)**

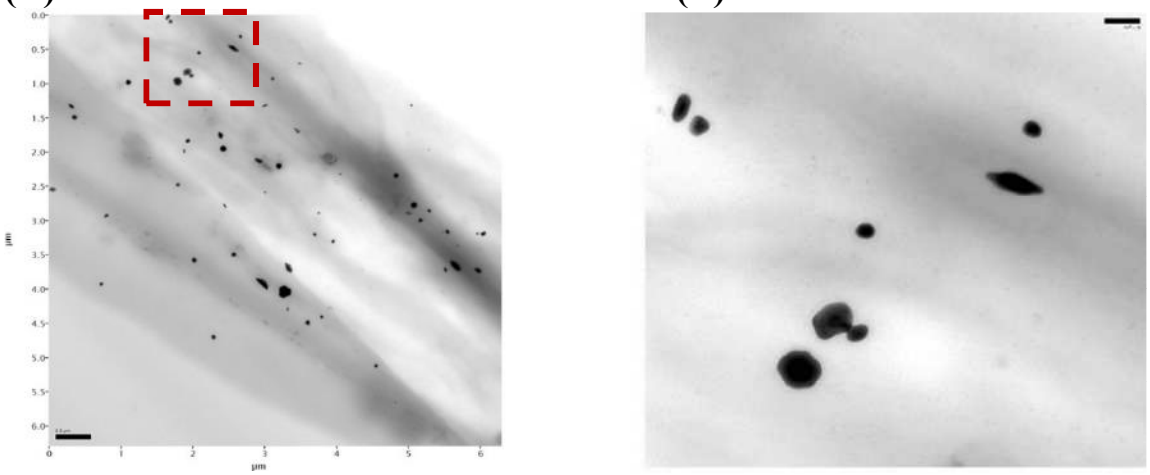

Figure 5.10 Transmission Electron Microscopy (TEM) micrographs of gold nanoparticles generated within the nanosensor gel formulated with C_{12}TAB as surfactant and irradiated with 2Gy_{RBE} proton radiation dose. (A) Low-magnification image depicting presence of gold nanoparticles in the dried hydrogel. Scale bar = 0.5µm (B) High-magnification image of the highlighted region in Figure A. Scale bar = 0.1µm

The increase in color intensity of the nanosensor gel is directly dependent on the formation of gold nanoparticles upon irradiation, which depends on the generation of free radicals. Increases in proton dose results in an increase in the formation of free radicals. Thus, absorbance of the hydrogel is an indicator of the dose delivered to the gel. Consequently, absorbance of the hydrogels was quantified using UV-vis spectroscopy 2 hours post irradiation with protons **(Figure 5.11)** in order to quantify the colorimetric response of the nanosensor gels. A characteristic spectral peak corresponding to the presence of gold nanoparticles was observed at ~520nm. Once the change in gel changed color occurred, no further change in color was observed for up to 4 hours, indicating stability of the generated nanoparticles over time (**Figure 5.12**). We monitored visual and spectroscopic changes in the control hydrogel (0 Gy_{RBE}) and the hydrogel irradiated with 2 Gy_{RBE} for a longer duration **(Figure 5.13 and 5.14)**. It was observed that no significant changes in the absorbance signal was noticeable even after one week. Gold nanoparticles are known to be stable and we do not anticipate change in the color of the gel over longer durations, although it is unlikely that the nanosensor gels will be used for longer studies because the turnaround between two fractionated radiotherapy sessions is ~24 h. We also determined the mechanical integrity (hardness) of pristine agarose hydrogel and compared it to the nanosensor hydrogels pre and post proton irradiation (2 Gy_{RBE}) **(Figure 5.15)**. The hardness of the different gels was studied by measuring the maximum force required to indent the hydrogel which was quantified from the force vs distance plot obtained. All samples were compared to pure agarose using unpaired two-tailed t-test. The p-values obtained were greater than 0.05 indicating no significant changes in the hardness of the nanosensor gels compared to that of agarose. These results indicate that proton treatment

and concomitant nanoparticle formation do not have a significant effect on the mechanical integrity of the gels.

(A)

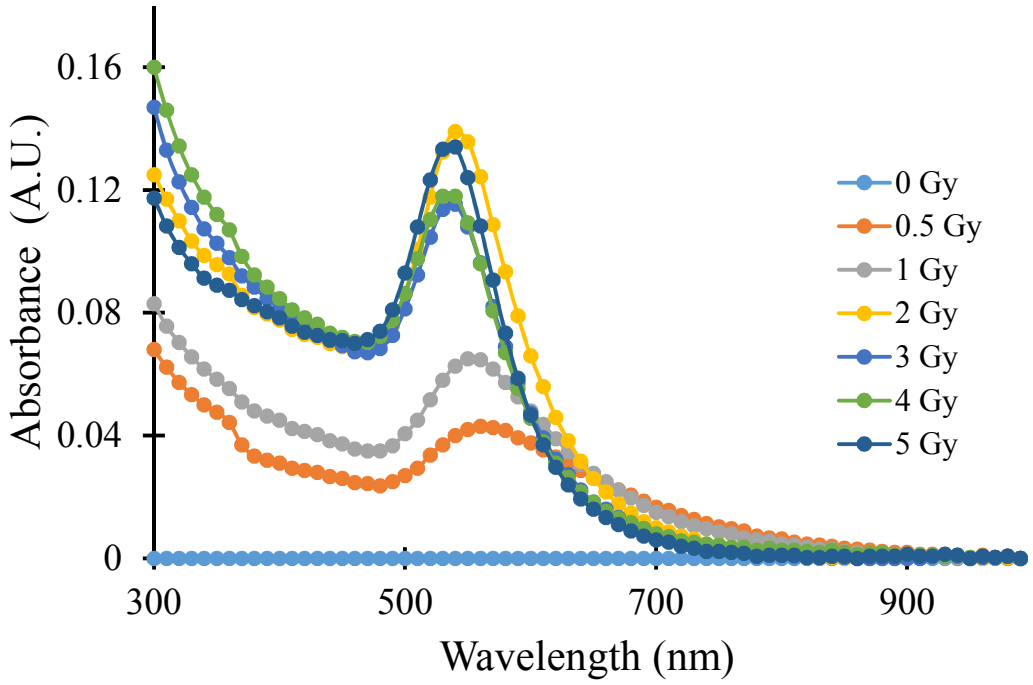

(B)

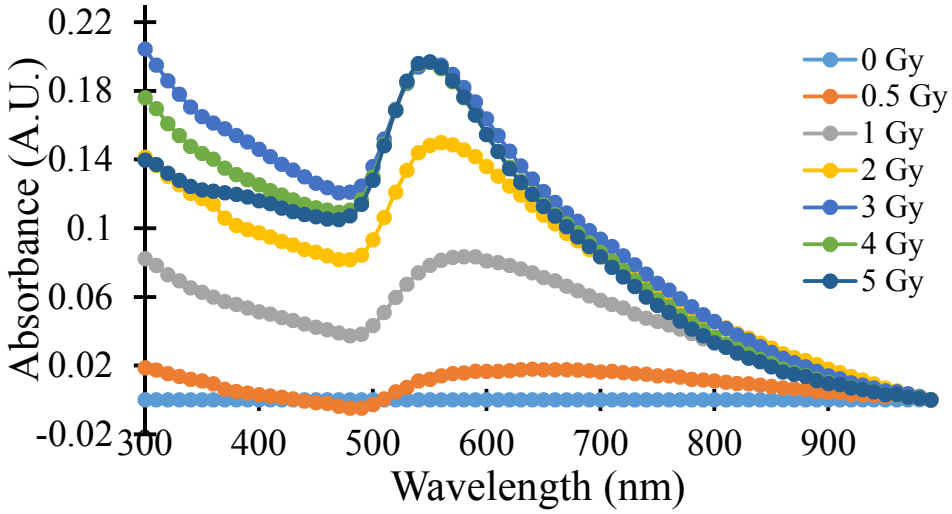

(C)

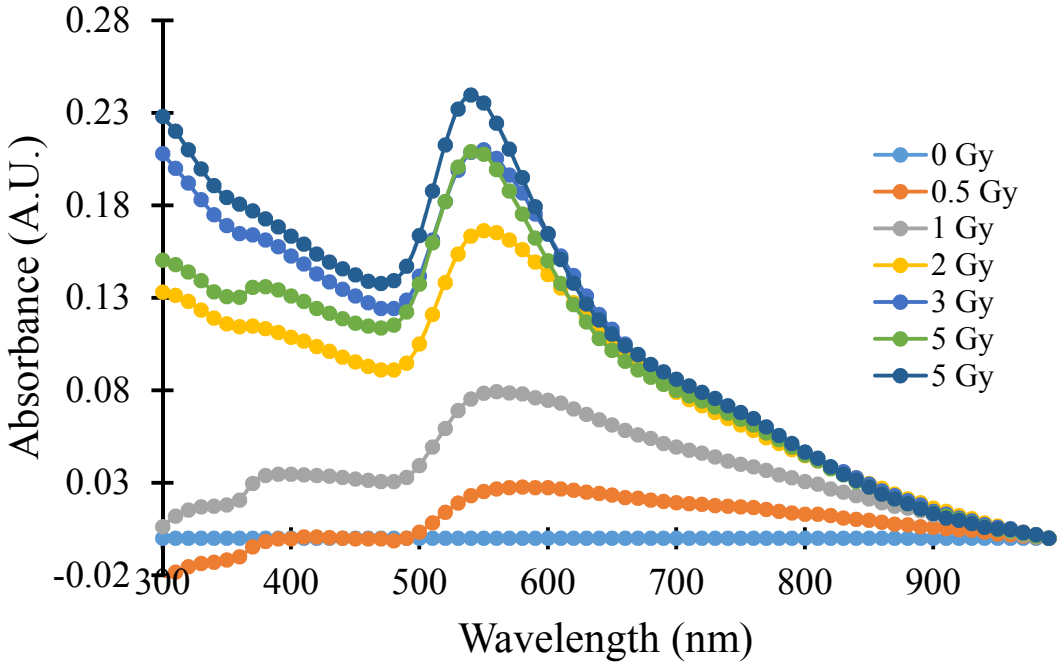

(D)

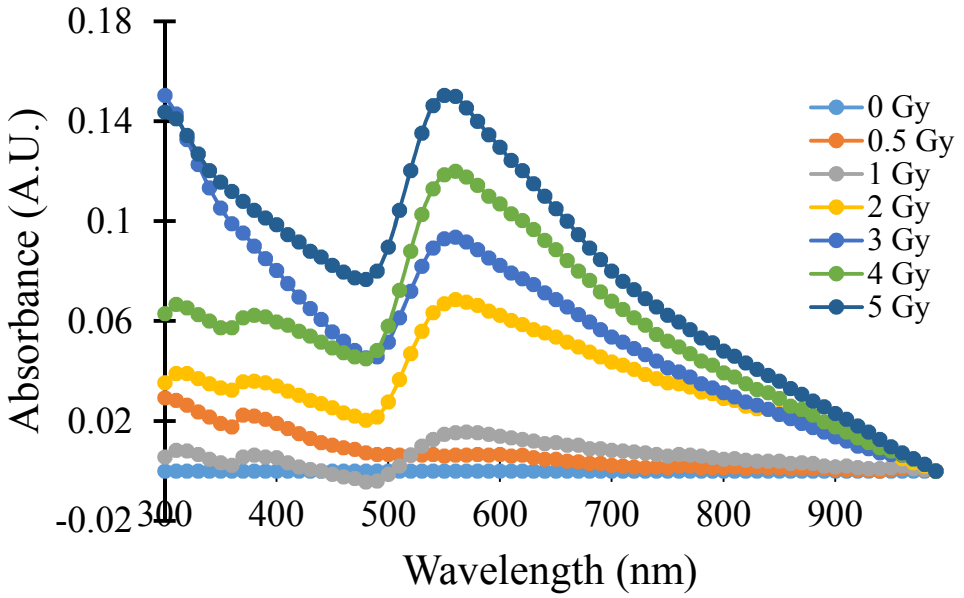

Figure 5.11 Absorbance spectra of nanosensor gels containing **(A)** C_{10}TAB, **(B)** C_{12}TAB, **(C)** C_{14}TAB and **(D)** C_{16}TAB as surfactants post irradiation with proton beams at different doses. Gold nanoparticle formation is indicated by a characteristic peak between 500 – 600 nm. In the figure, Gy_{RBE} is denoted as Gy.

(A)

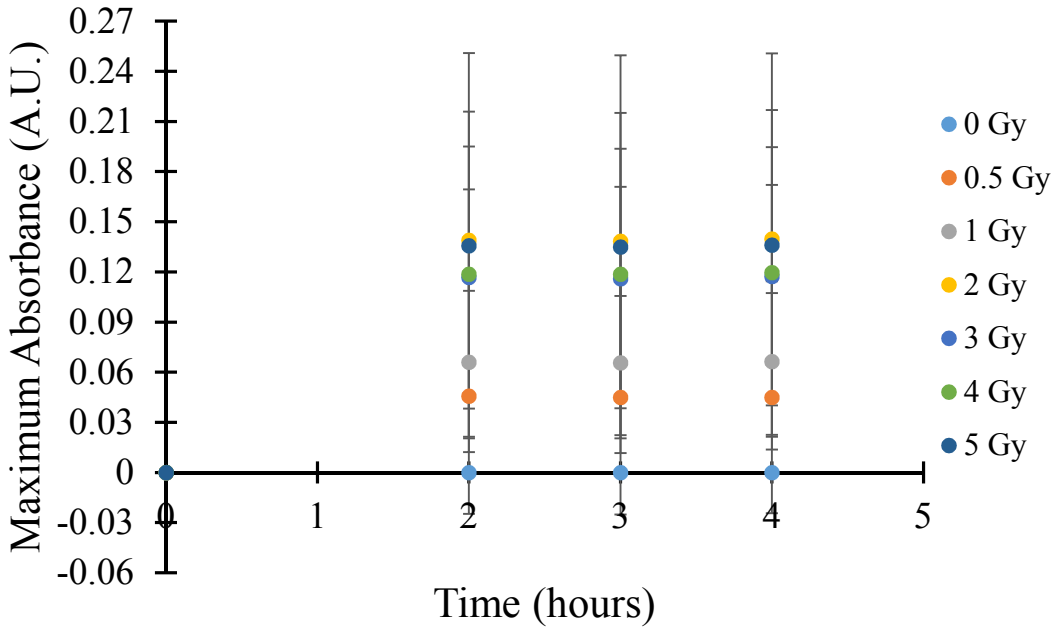
Maximum Absorbance (A.U.)
0.27
0.24
0.21
0.18
0.15
0.12
0.09
0.06
0.03
0
-0.03
-0.06
0
1
2
3
4
5
Time (hours)
0 Gy
0.5 Gy
1 Gy
2 Gy
3 Gy
4 Gy
5 Gy

(B)

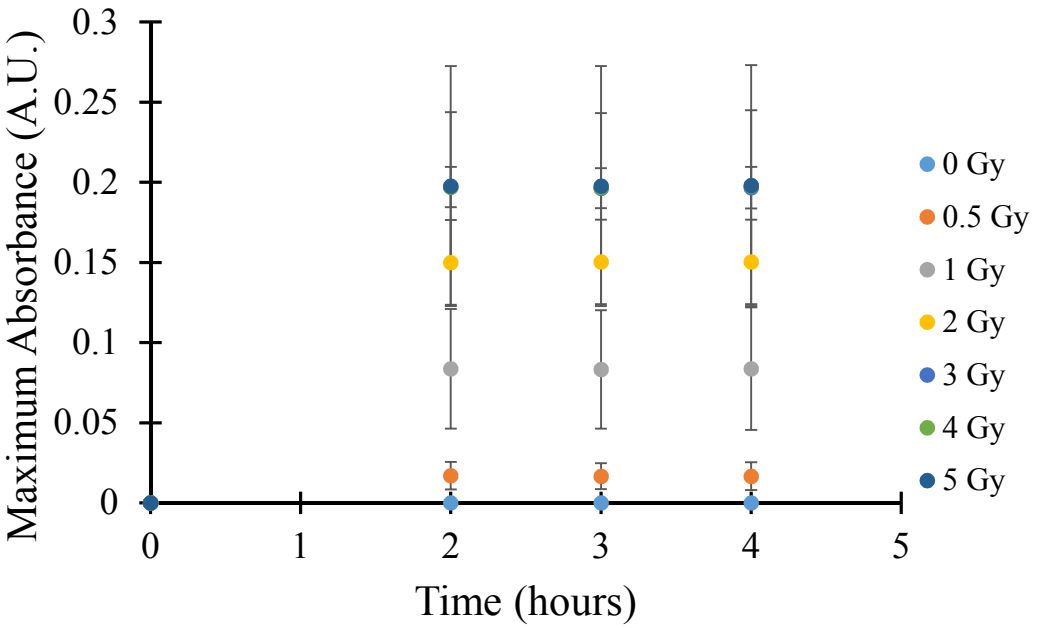
Maximum Absorbance (A.U.)
0.3
0.25
0.2
0.15
0.1
0.05
0
0
1
2
3
4
5
Time (hours)
0 Gy
0.5 Gy
1 Gy
2 Gy
3 Gy
4 Gy
5 Gy

(C)

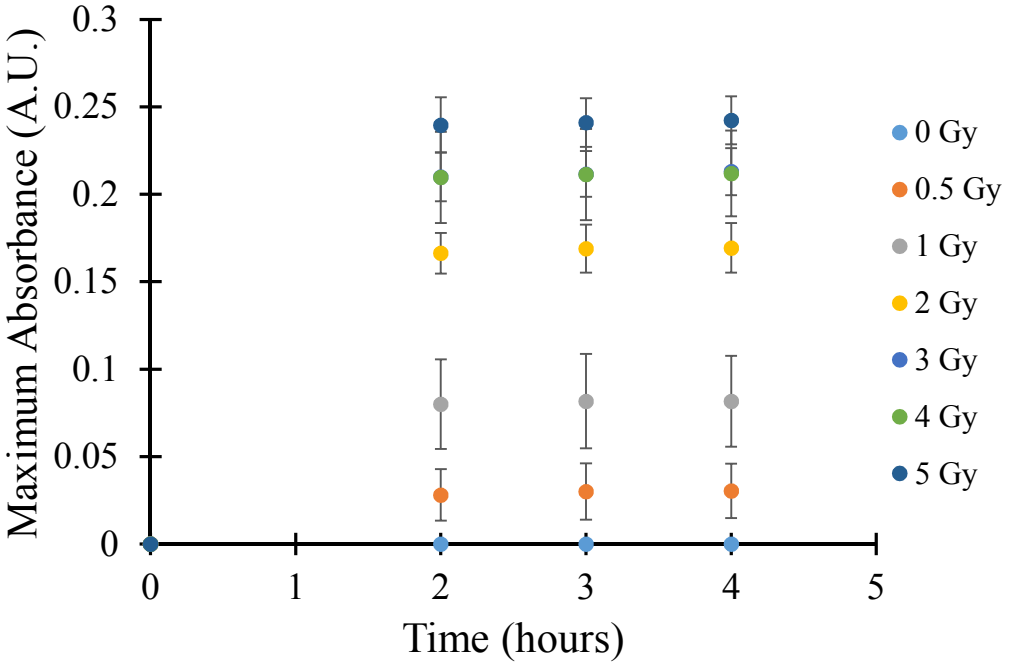
Maximum Absorbance (A.U.)
0.3
0.25
0.2
0.15
0.1
0.05
0
0
1
2
3
4
5
Time (hours)
0 Gy
0.5 Gy
1 Gy
2 Gy
3 Gy
4 Gy
5 Gy

(D)

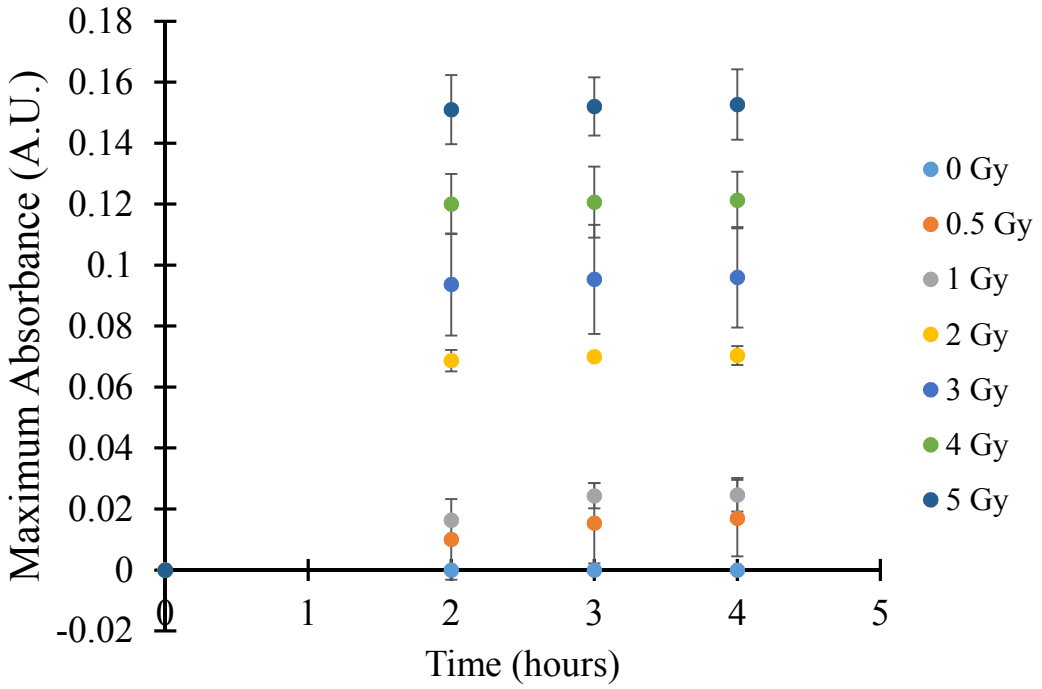

Figure 5.12 Absorbance of gold nanoparticles formed in agarose hydrogels formulated with **(A)** C_{10}TAB, **(B)** C_{12}TAB, **(C)** C_{14}TAB and **(D)** C_{16}TAB following irradiation with different proton doses. Absorbance spectra were measured 2 hours post irradiation with the maximum absorbance (typically at a wavelength between 500 – 600 nm) plotted against time to generate the plot. In the figure, Gy_{RBE} is denoted as Gy.

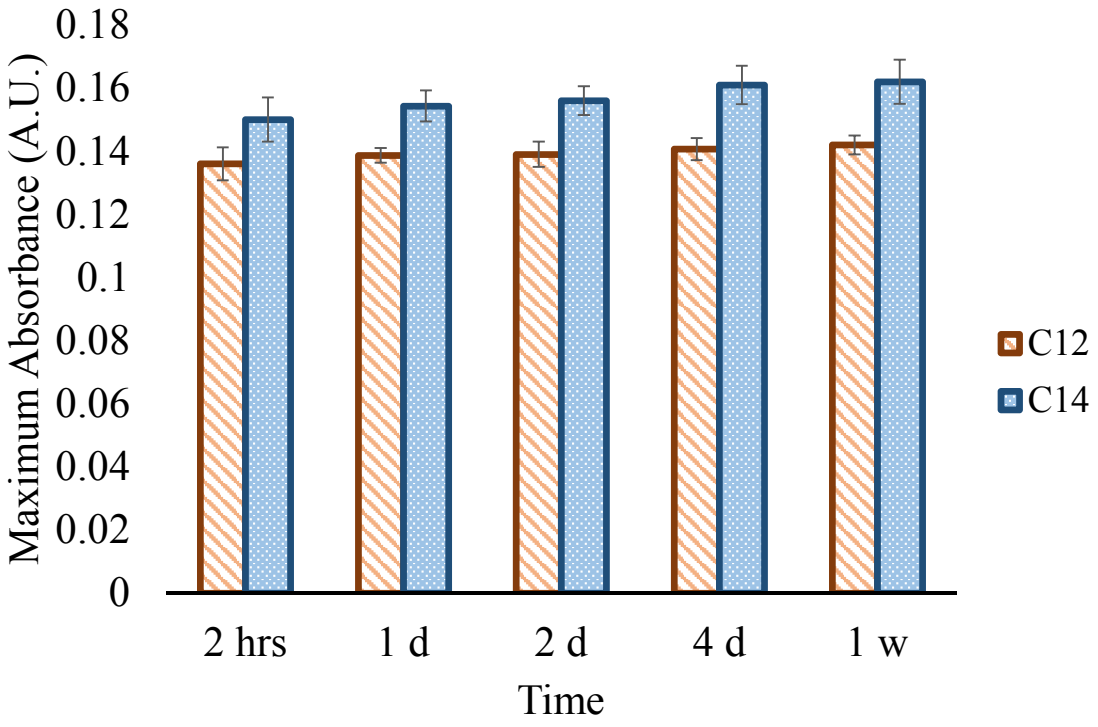

Figure 5.13 The stability of the colorimetric response of the hydrogel nanosensor was studied for up to one-week (1 w) post irradiation of the gel samples with protons. Absorbance spectra of C_{12}TAB- or C_{14}TAB-loaded nanosensor gels irradiated with 0 Gy_{RBE} and 2 Gy_{RBE} were acquired at the indicated time points. Unpaired T-test was performed using the function T.TEST in MS Excel for each time point and the absorbance value was compared to the absorbance value at 2 h. The p-values were found to be greater than 0.05 and hence the change in the absorbance was considered to be insignificant, indicating stability of the colorimetric response of the nanosensor gels. N = 3 independent experiments.

(A)

(i) (ii)

(B)

(i) (ii)

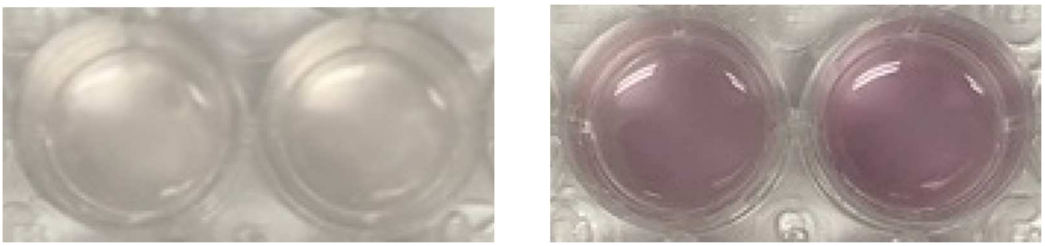

(C)

(i) (ii)

Figure 5.14 Images of nanosensor gels containing irradiated with (i) 0 Gy_{RBE} (control) and (ii) 2 Gy_{RBE}. In each image, C_{12}TAB-loaded gels are on the left and C_{14}TAB-loaded gels are on the right. Images were obtained after (A) 2 hours (B) 1 day and (C) 1 week post irradiation with protons (or not in case of the control or Gy_{RBE} images). Representative images from n=3 independent experiments.

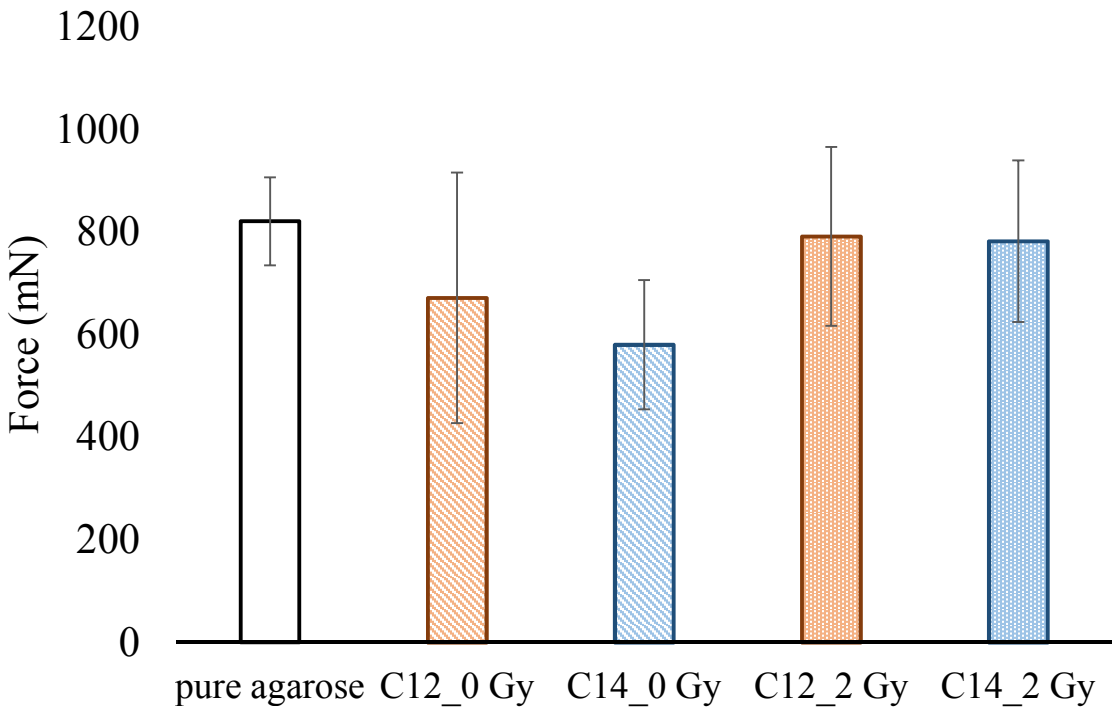

Figure 5.15 Material hardness of the nanosensor gels was measured using a TA.XT Texture Analyzer. The above plot shows the maximum force required by each gel sample to completely indent the nanosensor. All the samples were compared to pure agarose using unpaired 2-tailed t-test, indicating no significant changes in the hardness of the gel.

A correlation between the administered proton radiation dose and maximum absorbance at 2 h was plotted between 0 - 5 Gy_{RBE} **(Figure 5.16 and 5.17)**, which is a range commonly used in conventional fractionated proton beam therapy. It is desirable to have a sensor that functions in the conventional therapeutic range (1-2 Gy). However, recent developments in radiotherapy require a sensor that can also be adapted with ease to detect higher radiation doses typically used in hypofractionated regimes (i.e. > 2Gy / fraction). The range of the gel nanosensor can be tuned by simply modifying the concentration of the surfactant C_{12}TAB **(Figure 5.18A, 5.18B, 5.19A and 5.19B)**. Such ease in modulating the sensitivity of the nanosensor offers a significant advantage over existing conventional dosimeters.

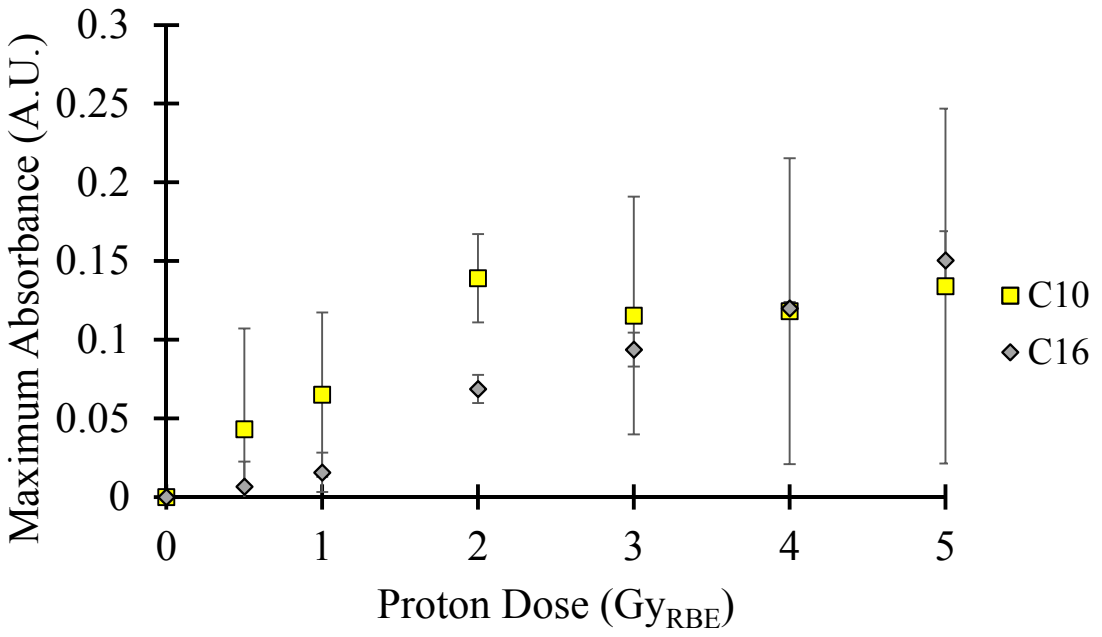

Figure 5.16 Absorbance spectra of the nanosensor gel following irradiation with proton beams. A plot depicting maximum absorbance vs radiation dose 2 hours post irradiation is shown. **(A)** yellow squares represent C_{10}TAB surfactant-loaded gels and while **(B)** grey diamonds representing C_{16}TAB with 10 mM $HAuCl_4$ and 10 mM ascorbic acid with 5% agarose is shown in the plot.

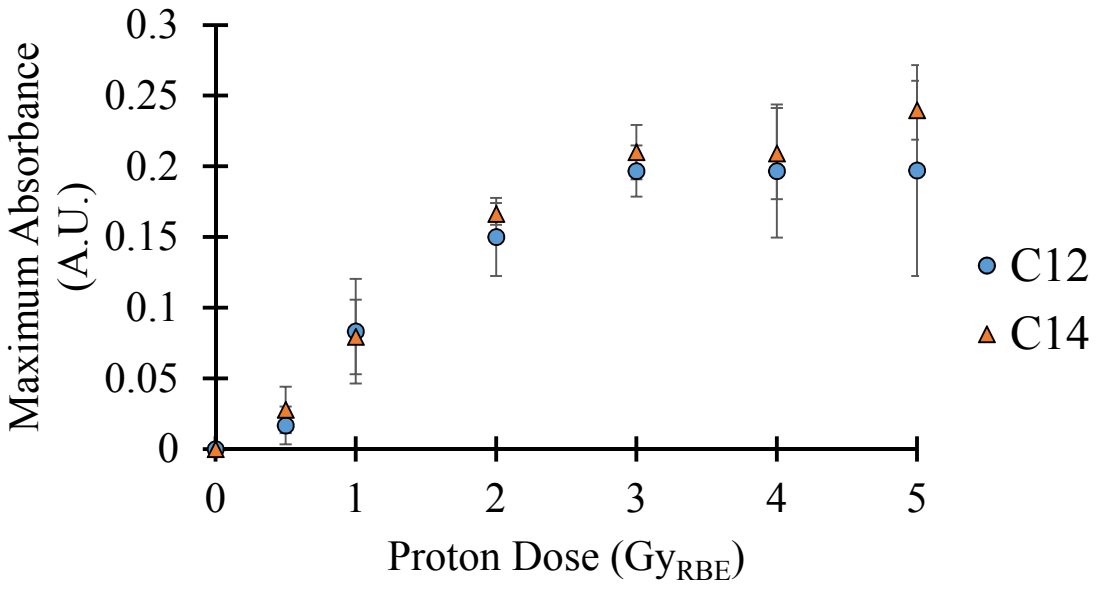

Figure 5.17 Absorbance spectra of the nanosensor gel following irradiation with proton beams. A plot depicting maximum absorbance vs radiation dose 2 hours post irradiation is shown. **(A)** blue circles represent C_{12}TAB surfactant-loaded nanosensor gels and **(B)** orange triangles represent C_{14}TAB-loaded nanosensor gels. Agarose gels (5%) were formulated with 10 mM $HAuCl_4$ and 10 mM ascorbic acid in all cases.

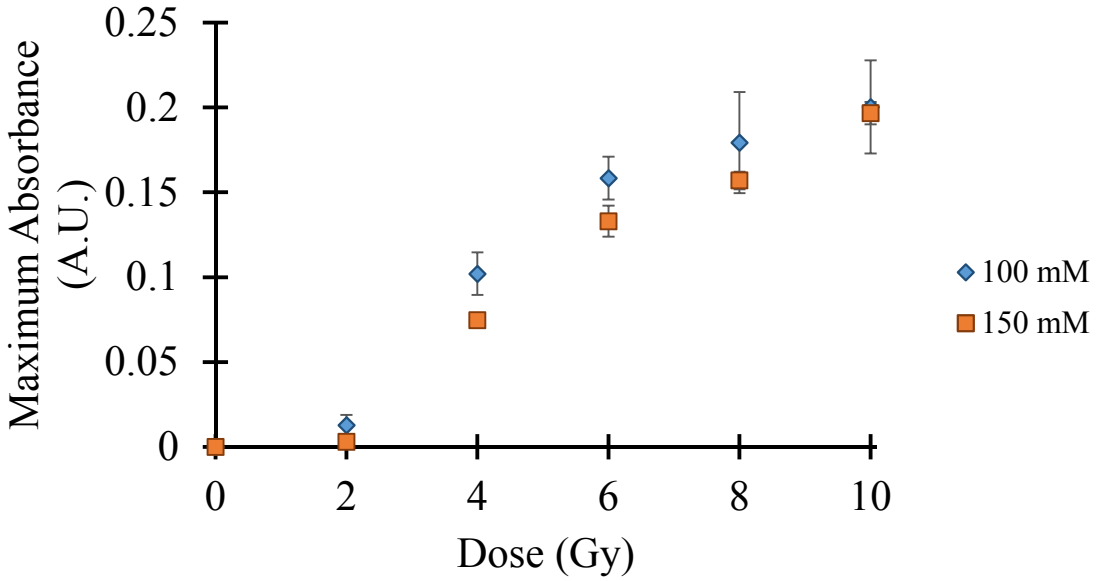

Figure 5.18 Absorbance spectra of the nanosensor gel following irradiation with proton beam therapy. A plot depicting maximum absorbance vs radiation dose 2 hours post irradiation is shown. C_{12}TAB gels formulated with concentrations (A) 100 mM depicted with blue diamonds (B) 150 mM depicted with orange squares with 10 mM $HAuCl_4$ and 10 mM ascorbic acid with 5% agarose is shown in the plot.

(A)

(B)

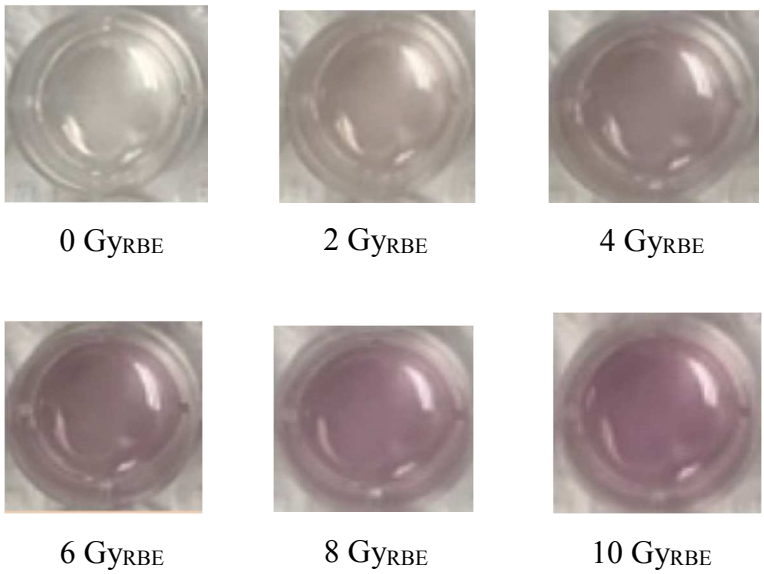

Figure 5.19 Images of nanosensor gels containing (A) 100 mM and (B) 150 mM C_{12}TAB surfactant irradiated with different doses of proton beams as indicated. All gels contain 10 mM $HAuCl_4$ and 10 mM ascorbic acid. All images were taken 2 hours after irradiation of gels with protons.

Reaction volumes on the nanoscale can enhance reaction rates of e^-_{aq} generated upon radiolysis with $[AuBr_2]^-$ ions attached to the head group of the micelle. It has been previously reported that the efficiency of charge transfer was enhanced in presence of cationic micelles (hexadecyltrimethylammonium bromide or CTAB micelles and a mixture of CTAB and cetylpyridinium or CP micelles) compared to anionic micelles[203]. It was hypothesized that hydrated electrons were more easily transported in the solvent, possibly due to the favorable attractive force between this negatively charged species and cationic micelles[204]. This attractive force can lead to an increased probability of capture of hydrated electrons by the micelle and reaction with $[AuBr_2]^-$. When these electrons interact with an empty site (i.e. no Au^+ is present), an electron hopping / migration mechanism can facilitate intermicellar reaction between Au^+ ions and hydrated electrons leading to the formation of Au^0 atoms[205].

Compared to C_{10}TAB and C_{16}TAB, C_{12}TAB and C_{14}TAB showed higher efficacies of nanoparticle formation, as indicated by the maximum absorbance determined for a given radiation dose. In our current formulation, C_{10}TAB does not form micelles based on the concentration used. In the absence of micelles, hydrated electrons are not influenced by the positive field and hence recombine and participate in secondary chemical reactions before reacting with Au^+ ions. This leads to a reduced yield of Au^0 atoms which, in turn, results in low yields of gold nanoparticles in case of C_{10}TAB compared to C_xTAB (x=12, 14). The other three surfactant C_xTAB (x=12, 14, 16) do form micelles under the formulation conditions employed in the current study. There are three possible outcomes for the decay of radiation-generated hydrated electrons as shown schematically in **Figures 5.20A-C**. The

electron is attracted towards the micelle but reacts with other generated free radicals (H· and OH·) to form secondary products like hydrogen before reaching the micelle / gold ions[206]. The second possibility is that the electron reaches an empty site of the micelle and undergoes migration/hopping to reduce the gold ion present in the nearby Au^{1+} occupied site. The third and final decay mechanism involves direct interaction of the electron with a gold ion in the micelle resulting in the conversion of Au^{1+} to Au^{0}. We hypothesize that the maximum reduction occurs when a micelle of sufficient charge is present with the optimal aggregation number of the surfactants leading to micelle formation.

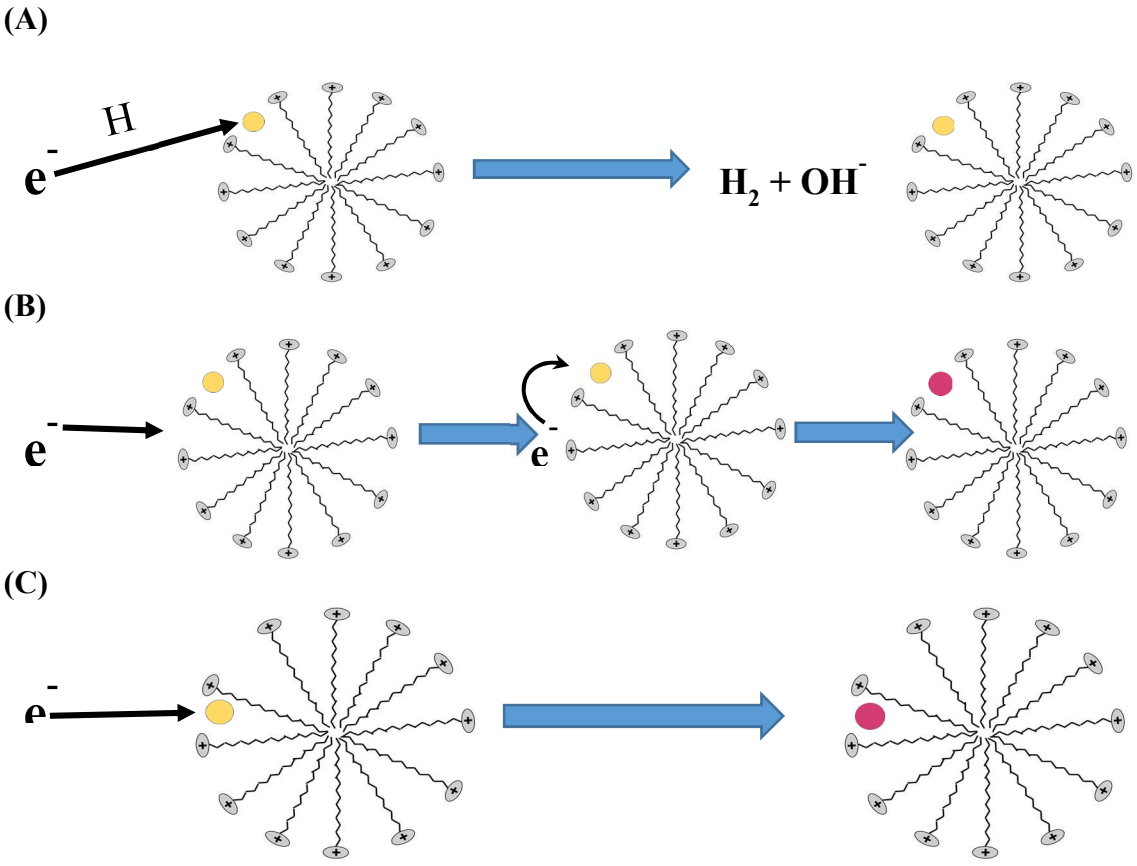

Figure 5.20 Three possible scenarios of the decay of generated hydrated electron post irradiation with protons. **(A)** Formation of peroxides and other secondary products, **(B)** Electron hopping from an empty micellar site of the generated hydrated electron to reduce a nearby Au(I) ion, and **(C)** Direct reduction by the generated electron of Au(I) ion to Au(0).

C_{16}TAB has a stronger positive electrostatic field compared to the other surfactants employed in the study due to the higher aggregation number of monomers required to form a self-assembled micelle[207]. Due to the high aggregation number of C_{16}TAB (90)[208], the probability of a hydrated electron directly reducing an $[AuBr_2]^-$ ion is lower when compared to that with C_{12}TAB and C_{14}TAB. The availability of hydrated electron migration/hopping for reducing Au^+ ions is also significantly reduced under the influence of a strong electrostatic field[203]. This can result in lower yields of zerovalent Au^0 ions, which, in turn, is responsible for lower yields of gold nanoparticles. Experimentally, this is indicated by the lower absorbance values seen in case of C_{16}TAB compared to C_{12}TAB or C_{14}TAB under similar irradiation conditions. We suggest that C_{12}TAB and C_{14}TAB with aggregation numbers 55 and 75 respectively[208], form micellar nanostructures with surface charge characteristics that are optimal for facilitating the formation of gold nanoparticles in gels in a dose-dependent manner following proton irradiation.

We next evaluated the predictive ability of our nanosensor with C_{12}TAB or C_{14}TAB formulated in the agarose gel, leading to their functions as potential dosimeters. A linear correlation between gold nanoparticle absorbance and radiation dose was found in the range of 0 – 3 Gy_{RBE} for both C_{12}TAB and C_{14}TAB **(Figure 5.21**). The calibration curve with C_{12}TAB had a correlation of y=0.069x, while that with C_{14}TAB was y=0.074x, where y is the absorbance and x is the dose in Gy_{RBE}. A test dose of 1.5 Gy_{RBE} was delivered to the gel to investigate the predictive ability of the nanosensor gels. The color change of this test gel was quantified 2 hours post irradiation using the respective calibrations, which

indicated a dose of 1.8 ± 0.44 Gy_{RBE} for the C_{12}TAB gels and 2.1 ± 0.1 Gy_{RBE} for the C_{14}TAB surfactant gels, indicating better predictive ability of the C_{12}TAB gels.

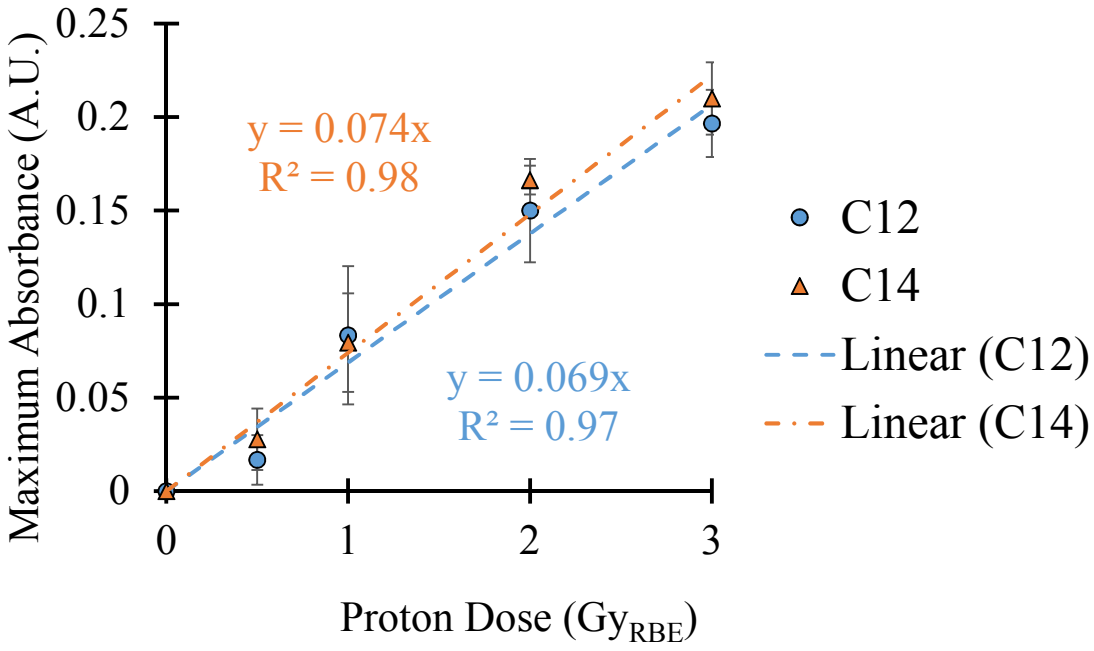

Figure 5.21 Calibration curve for C_{12}TAB (blue dotted line) and C_{14}TAB (orange dotted line) using maximum absorbance vs proton dose from 0 - 3 Gy_{RBE}, 2 h post irradiation.

A simple homogenous phantom, e.g. a cube or cylinder, is not adequate for verifying the accuracy of the delivered radiation dose.[209] A system that mimics human anatomy as closely as possible is therefore necessary for more accurately predicting the efficacy of radiotherapy in the clinic. We used an anthropomorphic child phantom for investigating the translational potential of the plasmonic nanosensor hydrogel for proton irradiation **(Figure 5.22A)**. Gels formulated with C_{12}TAB or C_{14}TAB surfactants were employed in the phantom studies, because of the better calibration curves obtained with these surfactants compared to the other surfactants. The gels were placed within the defined field under the

spine of the phantom **(Figure 5.22B)** and subjected to a dose of 1.8 Gy_{RBE}; the respective calibration curves from 0-3 Gy_{RBE} were used for estimation of the dose delivered. A prediction of 1.6 ± 0.2 Gy_{RBE} was made using the calibration curve for C_{12}TAB, and a prediction of 1.4 ± 0.4 Gy_{RBE} was made using the calibration curve for C_{14}TAB calibration curve, respectively. Our nanosensor hydrogel with C_{12}TAB surfactant shows an 11% error to the true value of the dose delivered (i.e. 1.8 Gy_{RBE}). Clinically used MOSFETs have an error percentage of ± 5% which is comparable to our current system[210]. The performance of the sensor can further be improved by fine tuning several key processes during fabrication including like preserving uniformity of gel pore size. Pore sizes and distributions in hydrogels have been previously shown to control the *in situ* growth of gold nanoparticles[211]. A control over pore size can be employed to exert better control over nanoparticle reduction and growth kinetics which can lead to consistent nanoparticle sizes following radiation. The clearly visible color change, simple detection technique using absorbance spectroscopy, and the ability to quantitatively predict doses demonstrates the potential of the hydrogel nanosensor for dosimetry in fractionated proton beam radiotherapy in the clinic.

(A)

(B)

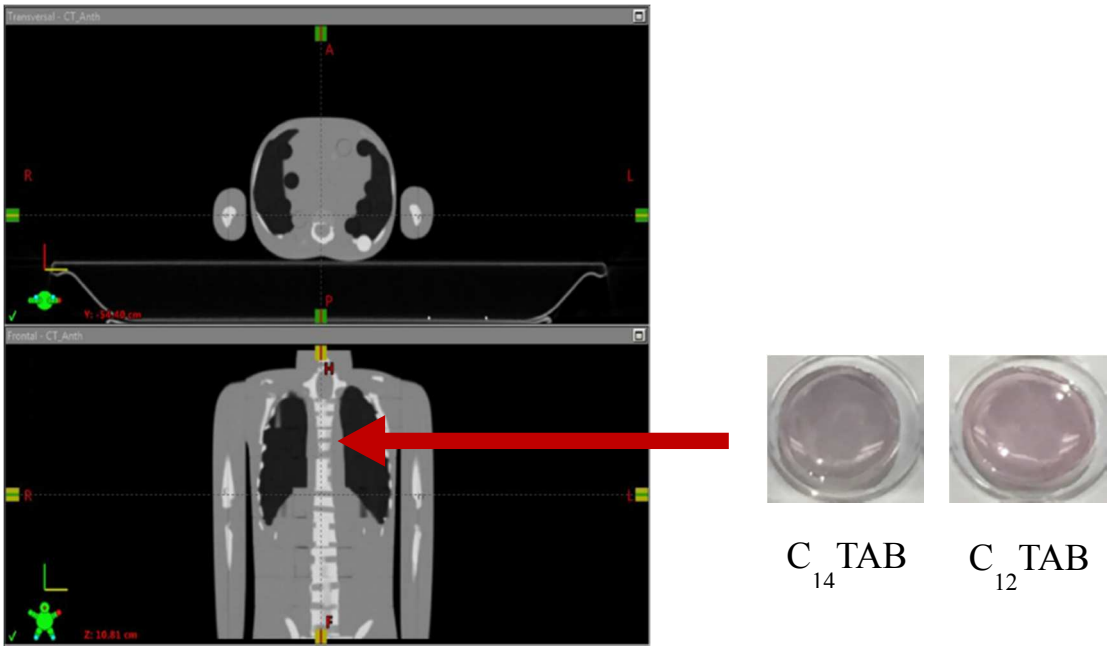

Figure 5.22 (A) Evaluation of the predictive ability of hydrogel nanosensors using an anthropomorphic child phantom placed on the irradiation table and subjected to proton therapy. **(B)** an X-ray computed tomography (CT) scan image of the phantom used in the experiments. The spinal cord of the phantom is irradiated with 1.8 Gy_{RBE}.

Surfactant	Actual Dose Delivered (Gy_{RBE})	Average Dose Delivered ± one S.D. (Gy_{RBE})
$C_{12}TAB$	1.8	1.6 ± 0.2
$C_{14}TAB$	1.8	1.4 ± 0.4

Table 5.1 The table indicates the dose delivered to each of the surfactants employed in the experiments and the average dose calculated using the $C_{12}TAB$ and $C_{14}TAB$-based hydrogel nanosensors.

5.4 Conclusions

To our knowledge, we have developed the first gel-based colorimetric nanosensor for detecting and predicting radiation dose delivered in proton beam therapy. The hydrogel nanosensor was able to detect doses as low as 0.5 Gy_{RBE} and showed a robust linear calibration between a dose range of 0-3 Gy_{RBE}. The gel nanosensor was able to predict the dose delivered to an anthropomorphic child phantom with significant accuracy, indicating promise for translation to the clinic. In addition to the simple, visible, stable and quantifiable nature of the readout, the hydrogel system can be contoured for patient personalized treatments. Agarose and ascorbic acid are generally regarded as safe, and $C_{16}TAB$ is used in antibacterial formulations used on skin[212]. Although the surfactants used in the formulation of the gels can be toxic at elevated concentrations, use of secondary containment devices or eventual replacement of the surfactant with biocompatible templating molecules will alleviate these concerns. The development of a new generation of cationic surfactants that allow for precise control of nanoparticle size and yields can lead

to sensors with improved prediction abilities. We believe that this one-of-a-kind nanosensor holds high promise for translation to clinical proton beam therapy.

Chapter 6 ELECTRON BEAM DOSIMETRY USING PLASMONIC HYDROGEL NANOSENSOR

6.1 Introduction

Radiotherapy is a frequently employed technique for the treatment of cancer.[213, 214] Significant advancements in the control over the gantry rotation and the introduction of multileaf collimators have facilitated the improvements in treatment efficacy.[215] This progress has given rise to development of novel radiation delivery techniques like intensity modulated radiotherapy (IMRT), image guided radiotherapy (IGRT), stereotactic radiotherapy and radiosurgery (SRS) and conformal radiotherapy. Currently, high energy photons are the primary source of radiation in clinical settings. But when administered to a tumor site there exists a large exit dose outside the target volume resulting in radiation-induced toxicity.[216, 217] To overcome this, high energy charged particles (electrons) are employed in clinical radiotherapy[218]. Electron beams have an inherent property of depositing their maximum dose at the required depth beyond which there is a sharp radiation dose fall off[219]. The high dose gradients result in radiation dose sparing of the healthy tissue from undesirable radiation damage. This mandates the use of electron beam radiotherapy over high energy photons for skin malignancies. Characteristics such as uniform dose deposition, altering dose depth by mere change in beam energy and ease in treatment planning make it a viable option for treatment of cancerous lesions.

Precise measurements of the delivered dose are critical for patient safety and treatment efficacy. Although there have been rapid advancements in the techniques involved in

electron beam treatment, there is a lack in the development in dosimeters to keep up with improved techniques. Conventionally used dosimeters include thermoluminescent dosimeters (TLDs), radiochromic films and semiconductor diodes have significant drawbacks. Measurements using TLDs are very time consuming and labor intensive making its routine operation very cumbersome[220]. Semiconductor diodes with their accurate readout are limited due to its dose rate dependence which limits their periodic operation.[221] Radiochromic films lack the ability to conform and adapt onto patient specific anatomy making them prone to positional instability and causing dose inconsistency with the delivered and predicted dose.[222, 223] There is still a need for a dosimeter that can detect doses in the therapeutic window while addressing all the above challenges.

Recent advancements in molecular and nanoscale systems could play a key role in the development of a dosimeter for the detection of therapeutic levels of ionizing radiation.[224] Gold nanoparticles with their unique optical and physiochemical properties have found application in diagnostics, imaging and drug delivery.[224-228] Taking advantage of the inherent property of gold nanoparticles, we recently designed a liquid based colorimetric sensor dependent on the formation of gold nanoparticles from its colorless precursor salt solution upon irradiation[162]. We further formulated the next generation colorimetric sensor by developing a hydrogel-based sensor to facilitate easy handling and minimize application concerns[229, 230]. In this study, we extend the applicability of the hydrogel nanosensor to the detection of high energy electrons employed clinically. The system consists of a cationic surfactant stabilized gold nanoparticles generated upon exposure to high energy electrons rendering a change in color to pink/maroon to the hydrogel. The intensity of color increases

with increasing irradiation and is used as a measure to quantify the delivered radiation dose. Finally, the ability of the hydrogel nanosensor to capture topographical dose profiles using a fixing agent post irradiation is reported. To the best of our knowledge, this colorimetric nanosensor for electron beam dosimetry is the first of its kind which could have potential translational applications in clinical settings.

6.2 Materials and Methods

Materials. Molecular biology grade agarose, L-ascorbic acid (AA), dodoceyltrimethylammonium bromide (C_{12}TAB) (≥98%), L-glutathione reduced (≥98%), gold(III) chloride trihydrate ($HAuCl_4.3H_2O$) and myristyltrimethylammonium bromide(C_{14}TAB)(≥99%) were acquired from Sigma-Aldrich. Cetyltrimethylammonium bromide(C_{16}TAB) was obtained from MP Chemicals. Sodium dodecylsulfate was obtained from Bio-Rad Laboratories while Tween 20 was purchased from Fisher Scientific. The chemicals were employed in the study with no further processing or purification. The solvent employed in the study was MilliQ water (18.2 MΩ.cm).

Hydrogel Nanosensor Preparation. To fabricate a hydrogel with a diameter of ~1.5 cm and thickness of 3 mm, a 24 well plate is used as a mold. Briefly, 600 µL of a 50 mM stock solution of C_xTAB (x = 12,14,16) was prepared and mixed with 30 µL of 10 mM $HAuCl_4$ in a 1.7 mL microcentrifuge tubes. From this mixture, 100 µL was removed prior to the addition of heated 2% liquid agarose (500 µL). From this mixture, 650 µL was removed

and poured into the molds of the well plate and allowed to set as gels prior to irradiation experiments. The gels were then incubated in 10 mM Ascorbic Acid (650μL) for 10 minute resulting in translucent hydrogels.

To fabricate a hydrogel with a diameter of ~3.5 cm and thickness of 3 mm, a 6 well plate is used as a mold. Briefly, 1.63mL of a 75 mM stock solution of C_{14}TAB was prepared and mixed with 81.6 μL of 10 mM $HAuCl_4$ in a 15 mL microcentrifuge tubes. From this mixture, 272 μL was removed prior to the addition of heated 2% liquid agarose (1.44 ml). This mixture (2.88mL) was poured into the molds of the well plate and allowed to set as gels prior to irradiation experiments. The gels were then incubated in 10 mM Ascorbic Acid (2.88 ml) for 10 minutes resulting in translucent hydrogels.

X-ray irradiation. All experiments were conducted at the Banner-MD Anderson Cancer Center in Gilbert. The energy and dose rate of the beam were set at 6 MeV and 600 MU/min unless otherwise mentioned. A standard field size of 10 cm x 10 cm was maintained throughout the study. For spatial dose deposition, only half the gel was placed in the irradiation field. Post irradiation, further analysis was carried out at Arizona State University in Tempe, AZ (approximate travel time of 30 minutes).

Post-processing of Hydrogel Nanosensor. Glutathione was used as a post processing agent to quench nanoparticle formation. Glutathione was added from the top of the gel, 30 minutes post irradiation and incubated for 10 minutes. The volumes used for incubation

were 650 μL for a hydrogel nanosensor with a diameter of 1.5cm and 2.88 mL for a hydrogel nanosensor with a diameter of 3.5cm. The residual glutathione from the surface of the hydrogel nanosensor was discarded and used for further quantification.

Absorbance Spectroscopy. The absorbance spectra for all samples was obtained using a BioTek Synergy™ 2 plate reader. Absorbance values were measured from 300 nm to 990 nm with a step size of 10 nm. MilliQ water was used as blank for all experiments. Although the change in color is observable 15 minutes post irradiation, due to the travel time between Banner M.D Anderson Cancer Center, Gilbert and Arizona State University, Tempe measurements were quantified 2 hours post irradiation. To normalize the absorbance spectra for further analysis, the absorbance at 990nm was subtracted from the absorbance of all wavelengths. Absorbance at 540 nm wavelength was plotted as a function of radiation dose to generate the calibration curve which is used to determine unknown radiation doses.

Topographical Mapping of Hydrogel Nanosensor. A 1536 well plate set up in a BioTek Synergy™ 2 plate reader having a grid size of ≈2mm x 2mm was used. Absorbance values at 540 nm and 990 nm were measured along the entire gel surface, leading to a dose map of the gel surface. The final absorbance was calculated by subtracting the absorbance values of water and 990 nm wavelength from the absorbance value at 540 nm wavelength. The calibration curve was used to predict the delivered dose to each cell of the grid corresponding to its topographical dose map over the gel surface.

Transmission Electron Microscopy (TEM). The gels were dissolved in 1,2-propane diol (a chaotropic agent) by gently heating at 80 °C for 15 mins. The resultant liquefied hot mixture was centrifuged at 4000 rpm for 10 mins and supernatant agarose-propane diol mixture was discarded carefully to isolate the gold nanoparticles pellet. The pellet was further dispersed in deionized water. The samples were prepared for imaging by casting a drop of this mixture onto a carbon film onto a TEM grid. The samples were dried overnight in air. A CM200-FEG instrument operating at 200 kV in the LeRoy Eyring Center for Solid State Sciences at ASU was used for imaging of gold nanoparticles in the irradiated gels.

Hydrogel Nanosensor Dosimetry in Anthropomorphic Thorax Phantom. The anthropomorphic phantom was positioned on the radiotherapy table and aligned using guiding lasers. The hydrogel nanosensor was positioned in the middle of a 10cm x 10cm radiation field. A 1.3 cm tissue-equivalent bolus was placed on top of the hydrogel nanosensor. Each hydrogel nanosensor received a radiation dose of 2.5 Gy.

Image Acquisition. All images were acquired using a HPLaserJet 3390. Furthermore, images were cropped to the required size and no further editing or post processing of the images was carried out.

Statistical Analysis. All experiments were performed in quintuples unless otherwise specified. Data analysis for all independent experiments was performed using Microsoft Excel. Data reported in the manuscript are represented as mean ± one standard deviation.

6.3 Results and Discussion

Electron beam therapy is frequently used for the treatment of superficial layers (epidermis and dermis) of malignant skin lesions[231]. Fractionated electron beam therapy involves delivering a cumulative dose of 20-70 Gy in fractions of 1-2 Gy per session over a course of several weeks[232]. There is a need to ensure precise and accurate delivery of radiation to patients. Current dosimetry devices are complex to fabricate and cumbersome to operate thereby limiting its routine use. There is still a critical need for the development of facile dosimeters that are robust, easy to fabricate and operate to ensure patient safety during radiotherapy.

The principle behind the hydrogel nanosensor is the reduction of gold salt to gold nanoparticles following exposure to high energy electrons. Gold ($HAuCl_4$), present natively in its trivalent state Au(III) is thermodynamically unfavorable to reduce as compared to Au(I)[137]. To carry out the conversion of Au(III) to Au(I) and retain it in its monovalent state without undergoing further reduction, a room temperature reaction using ascorbic acid (Vitamin C) was carried out in the presence of three distinctly charged (cationic, anionic and non-ionic) surfactants. In the presence of sodium dodecylsulfate (anionic) and Tween-20 (non-ionic surfactant), the addition of ascorbic acid results in the development of a pink/purple color and a characteristic peak between 500 and 600nm in the UV-Visible spectra suggesting spontaneous formation of gold nanoparticles (**Figure 6.1**). Interestingly, in the presence of the cationic surfactant, no spontaneous nanoparticle formation is observed with lack of color developed (transparent) and the absence of the

characteristic peak in the UV-Visible spectra (**Figure 6.1**). The presence of a transparent solution has been attributed to the formation of Au(I) ions[138]. We hypothesize the favorable electrostatic interaction between the negatively charged tetrachloroaurate ions and positively charged cationic surfactant leads to enhanced shielding of Au(III) to ascorbic acid thereby inhibiting spontaneous gold nanoparticle formation. Based on this rationale, we employed cationic surfactants for our studies.

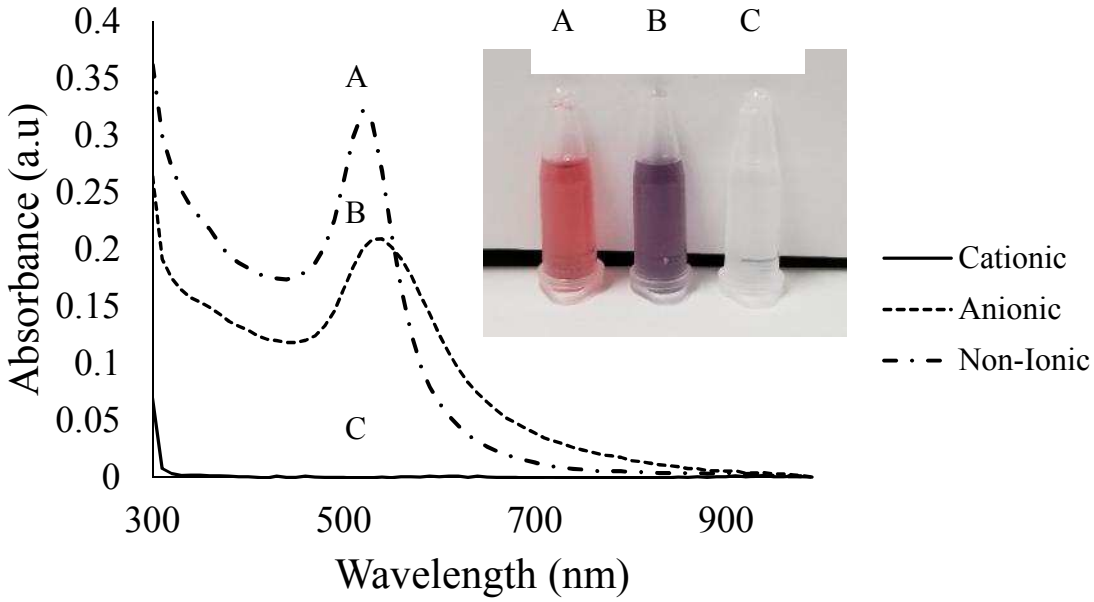

Figure 6.1 UV-Visible spectra and digital images illustrating the presence and absence of spontaneous gold nanoparticle formation with three distinctly charged surfactants. Both anionic and non-ionic surfactants display spontaneous nanoparticle formation (<2mins) with the presence of a spectral peak between 500-600nm while in the presence of cationic surfactants no such spectral peaks are observed. The inset displays the presence of a pink and purple colored dispersion which are characteristic of gold nanoparticles when anionic and non-ionic surfactant are employed while a colorless solution is seen when cationic surfactant is employed indicating no spontaneous nanoparticle formation. The surfactants used are C_{16}TAB (cationic), SDS (Anionic) and Tween 20 (Non-ionic) at a concentration of 20mM. The final gold and ascorbic acid concentrations were 0.2mM and 4mM respectively.

High energy electrons employed in the study for irradiation could be involved in both direct and indirect mechanisms of reduction of Au(I) to Au(0). Exposure to ionizing radiation

involves generation of reactive free radicals including hydrated electrons (e^-_{aq}), hydrogen free radicals ($H^\cdot$) and hydroxyl free radicals ($OH^\cdot$) through the splitting of water[233]. The generation of reducing species including e^-_{aq} and $H^\cdot$ play a vital role in the reduction of Au(I) to Au(0). Although $OH^\cdot$ is an oxidizing agent and can impede nanoparticle formation through dissolution of Au(0), the presence of ascorbic acid (anti-oxidant) could potentially minimize these unfavorable side reactions[234]. High energy electrons irradiation could also be potentially involved in direct reduction of Au(I) to Au(0). To facilitate easy handling and concerns during application, we have further incorporated the gold salt, cationic surfactant and ascorbic acid in an agarose hydrogel. Agarose based hydrogels have acquired lot of attention as controlled drug release platforms and as scaffolds for regenerative tissues due to their low toxicity[235]. The selection criteria for agarose as the hydrogel base for our nanosensor was based on the following parameters: its biocompatibility, ease in modulation of mechanical properties by mere change in concentration and ease in generation of the gel[235].

Hydrogel nanosensors with a diameter of ≈ 1.5cm and ≈ 3mm thickness were fabricated with three different cationic surfactants (C_xTAB) with varying chain lengths (x = 12, 14 and 16) and their response to therapeutic levels of high energy electrons irradiation (0-5Gy) were determined. In all cases exposure to high energy electrons rendered a maroon color to the hydrogel due to the formation of gold nanoparticles while the non-irradiated control remained colorless **(Figure 6.2)**. For any given cationic surfactant, increasing levels of exposed high energy electrons resulted in a deepening of the maroon color developed in the hydrogel nanosensor. Exposure of hydrogel nanosensor to increasing levels of high

energy electrons resulted in a direct increase in the number of reducing species, which, in turn, led to a higher probability of reduction of Au(I) to Au(0). Further nucleation and growth of Au(0) results in the formation of gold nanoparticles imparting the characteristic color (maroon) to the hydrogel.

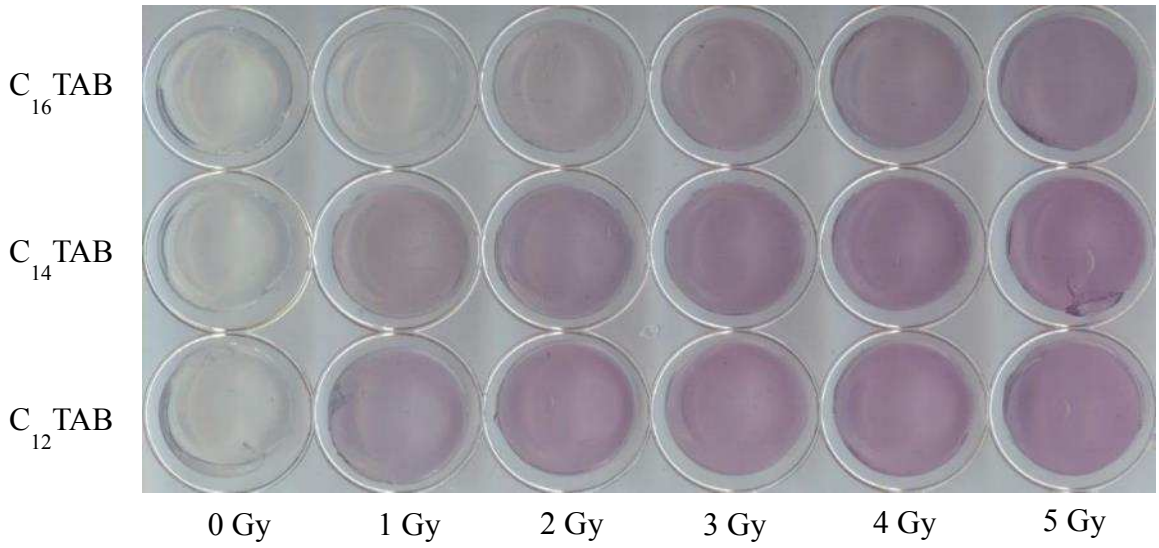

Figure 6.2 Image of hydrogel nanosensor contain (top) 50 mM C_{16}TAB, (middle) 50 mM C_{14}TAB and (bottom) 50 mM C_{12}TAB surfactants, irradiated with different doses of electron beam as indicated. All gels contain 10 mM HAuCl4, ascorbic acid. All images were taken 2 hours post irradiation with electrons. No L-glutathione was added to hydrogels post irradiation.

The change in color from colorless to maroon for C_{12}TAB loaded hydrogels were observed ≈5 minutes post irradiation, while the color change for C_{14}TAB and C_{16}TAB surfactant employed hydrogels were seen ~10 minutes and ~15 minutes post irradiation respectively. Interestingly, we observe that the varying the chain length of the surfactant affects the sensitivity of the hydrogel nanosensor to high energy electrons. Specifically, for a fixed radiation dose of 1 Gy decreasing the chain length of the cationic surfactant resulted in an increase in the developed color in the hydrogel nanosenosor. At the surfactant

concentrations employed in the study (final concentration ≈20mM), the cationic surfactants in the study form micelles.[145] Gold nanoparticle growth is governed by the frequency of collisions between cationic micelles containing $AuBr^{2-}$ and with the radiation generated zerovalent Au(0) atoms before they are stabilized by the cationic surfactant in the hydrogel nanosensor.[236] We hypothesize that decreasing chain length results in increasing diffusion coefficients of the micelles.[237] This increased mobility could potentially result in an increased frequency of collision involving cationic surfactant loaded $AuBr^{2-}$ and radiation generated Au(0) resulting in higher yields of gold nanoparticles with decreasing order of cationic chain length.

The hydrogel nanosensors were further quantified using UV-Visible spectroscopy 2-hour post irradiation **(Figure 6.3)**. A characteristic spectral peak between 500 and 600nm indicative of gold nanoparticles is observed.[238] On further analysis, a clear increase in absorbance at 540nm is observed with increasing levels of high energy electrons (**Figure 6.4**). This trend corroborates the increase in intensity of pink/maroon that is seen with the naked eye. To further visualize the presence of gold nanoparticles, the irradiated hydrogel nanosensor was characterized using transmission electron microscopy **(Figure 6.5)**. A non-homogenous particle distribution was observed with an average particle size ≈ 54 ± 17nm. Although both C_{12}TAB and C_{14}TAB surfactant containing hydrogels were capable of nanoparticle formation, C_{14}TAB was employed for all further experiments.

A

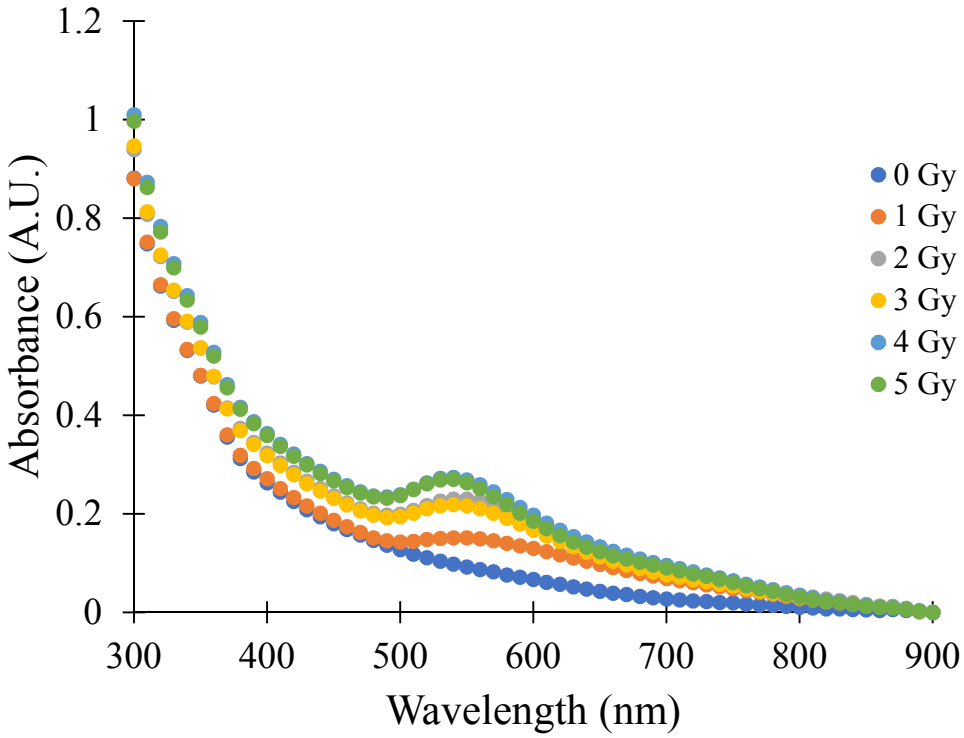
1.2
1
0.8
0.6
0.4
0.2
0
Absorbance (A.U.)
300
400
500
600
700
800
900
Wavelength (nm)
0 Gy
1 Gy
2 Gy
3 Gy
4 Gy
5 Gy

B

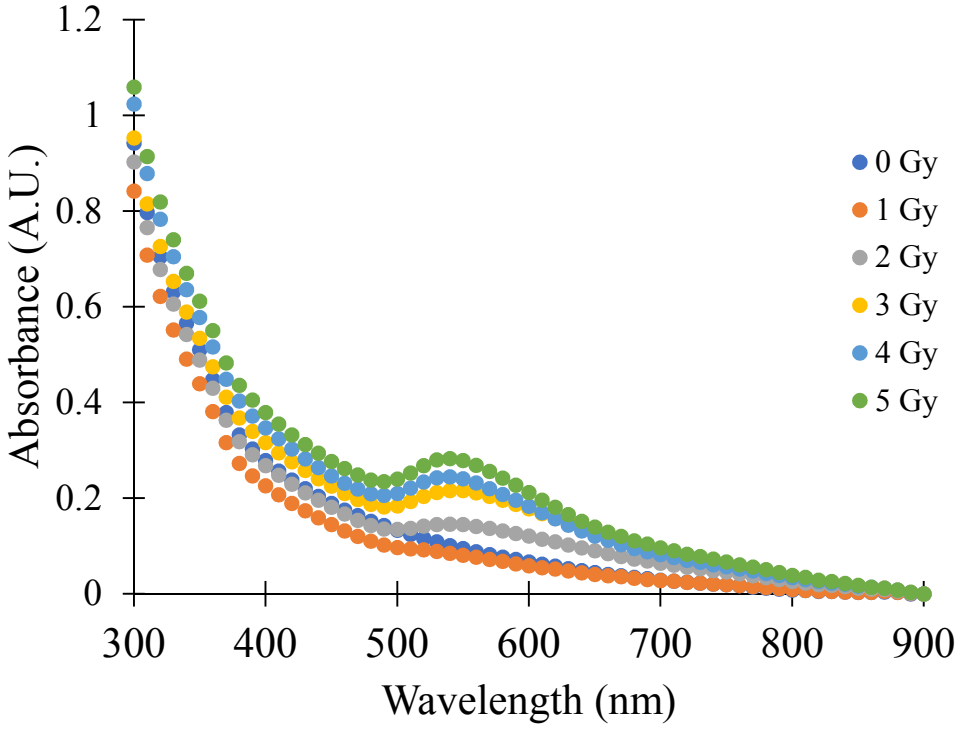
1.2
1
0.8
0.6
0.4
0.2
0
Absorbance (A.U.)
300
400
500
600
700
800
900
Wavelength (nm)
0 Gy
1 Gy
2 Gy
3 Gy
4 Gy
5 Gy

C

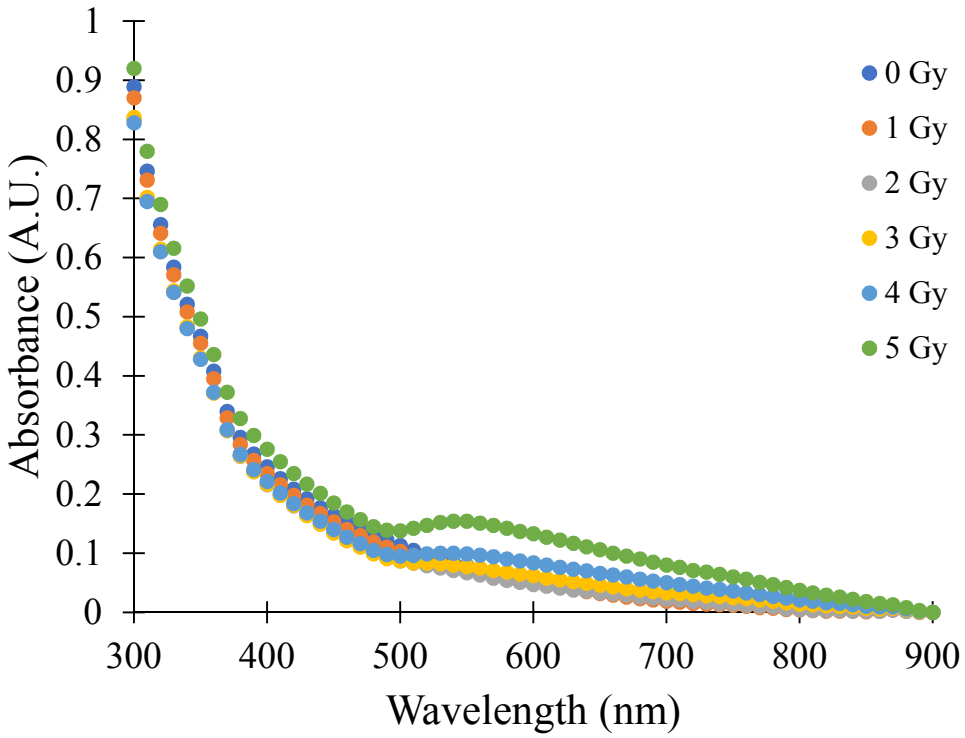

Figure 6.3 Absorbance spectra of hydrogel nanosensor containing 50 mM **(A)** C_{12}TAB, **(B)** C_{14}TAB and **(C)** C_{16}TAB as surfactant post irradiation as a function of radiation dose. Appearance of the characteristic peak between 500-600nm is indicative of gold nanoparticle formation. Absorbance of the hydrogel nanosensor was measured 2 hours post irradiation.

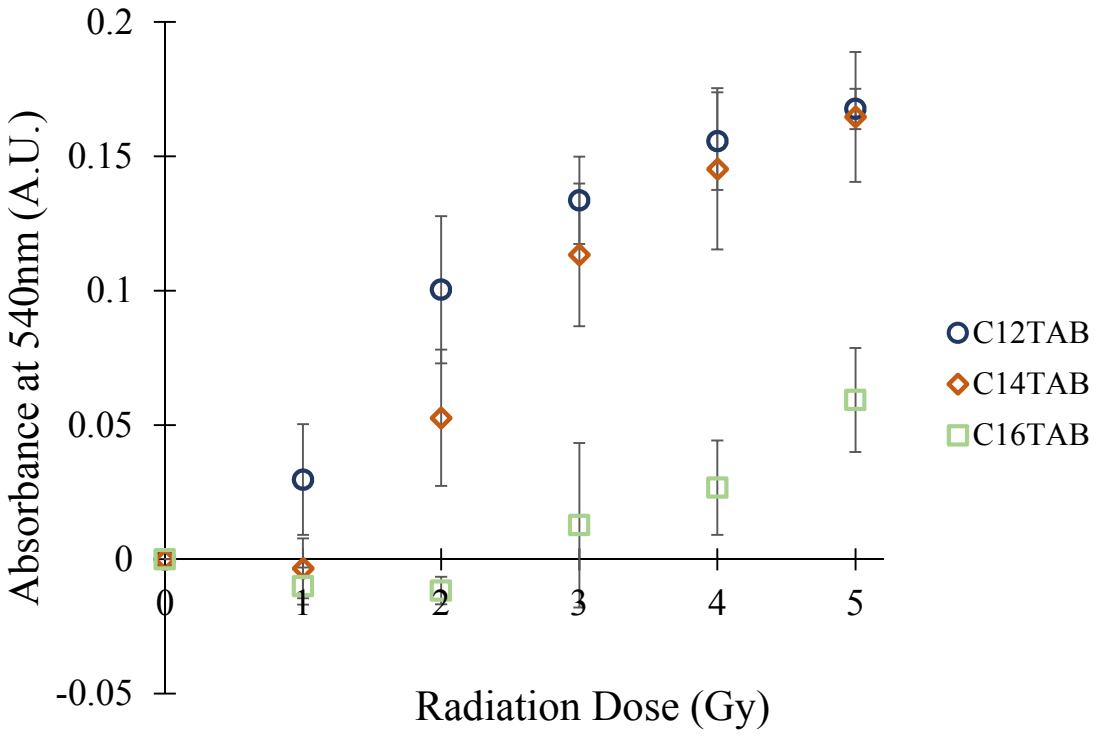

Figure 6.4 Absorbance at 540nm as a function of radiation dose. The formulation of the hydrogel nanosensor with 50mM C_{12}TAB (Blue Circle), 50mM C_{14}TAB (Orange Diamond) and 50mM C_{16}TAB (Green Squares). Absorbance at 540nm was measured 2 hours post irradiation.

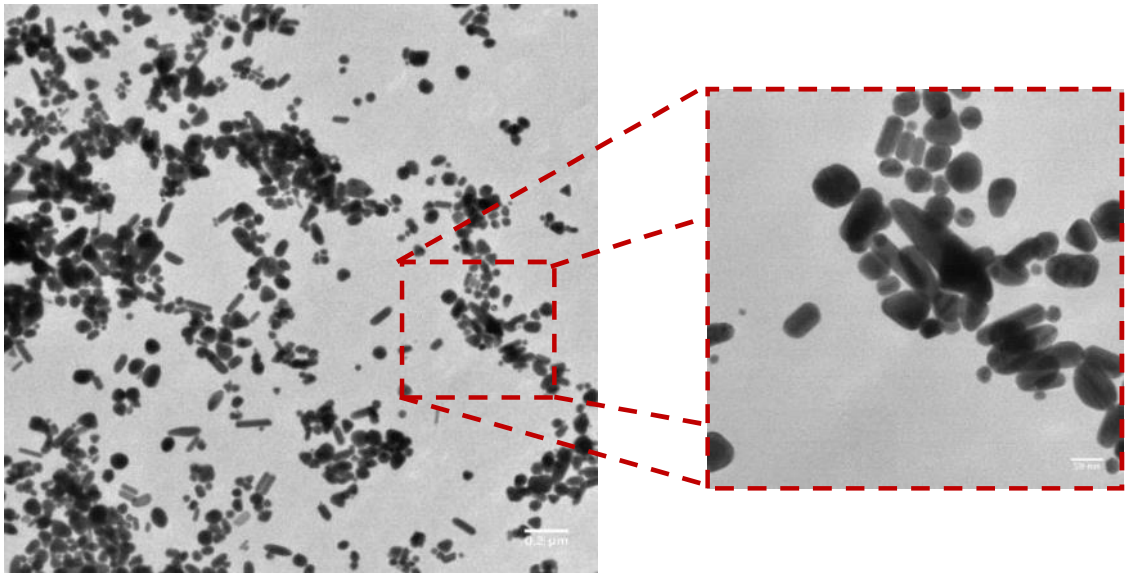

Figure 6.5 Transmission Electron Microscopy (TEM) micrographs of gold nanoparticles with $C_{14}TAB$ as surfactant irradiated with a 4 Gy electron beam dose. (Left) Low magnification image depicting the presence of gold nanoparticles in the dried hydrogel. (Right) High magnification image of the highlighted region (Dashed Red Box).

Clinical radiotherapy involves radiation field sizes larger than $1cm^2$.[239] In order to adapt to larger field sizes, hydrogel nanosensors of ≈ 3.5 cm diameter and ≈ 3 mm thickness were fabricated with a final concentration of 30mM $C_{14}TAB$ surfactant. These hydrogel nanosensors were further investigated to determine their ability to preserve topographical radiation information by irradiating one-half of the hydrogel nanosensor with a dose of 3Gy. We observe a change in color to pink/maroon in one half of the hydrogel nanosensor. However, observation of these hydrogel nanosensors over longer durations displayed a "bleed-over" of the color to the non-irradiated regions (**Figure 6.6**). We attribute this phenomenon to additional growth of nanoparticles in the non-irradiated regions due to collisions between unreacted $AuBr^{2-}$ ions in the non-irradiated region with radiation

generated gold nanoparticles in the irradiated region. To inhibit this "bleed-over" phenomena, we hypothesized that the addition of a quenching agent to complex/react with the unreacted $AuBr^{2-}$ will be required to prevent further nucleation and growth in the non-irradiated regions. Gold-thiol bond has been demonstrated to be similar to the gold-gold bond, and in light of this we reasoned the addition of glutathione (thiol containing tripeptide) would complex/react with unreacted $AuBr^{2-}$ ions.[240] Indeed, incubation with glutathione for 10 minutes (30 minutes post radiation) led to the complete arrest of the "bleed-over" phenomena. Based on this observation, , further studies were conducted with the post addition of glutathione.

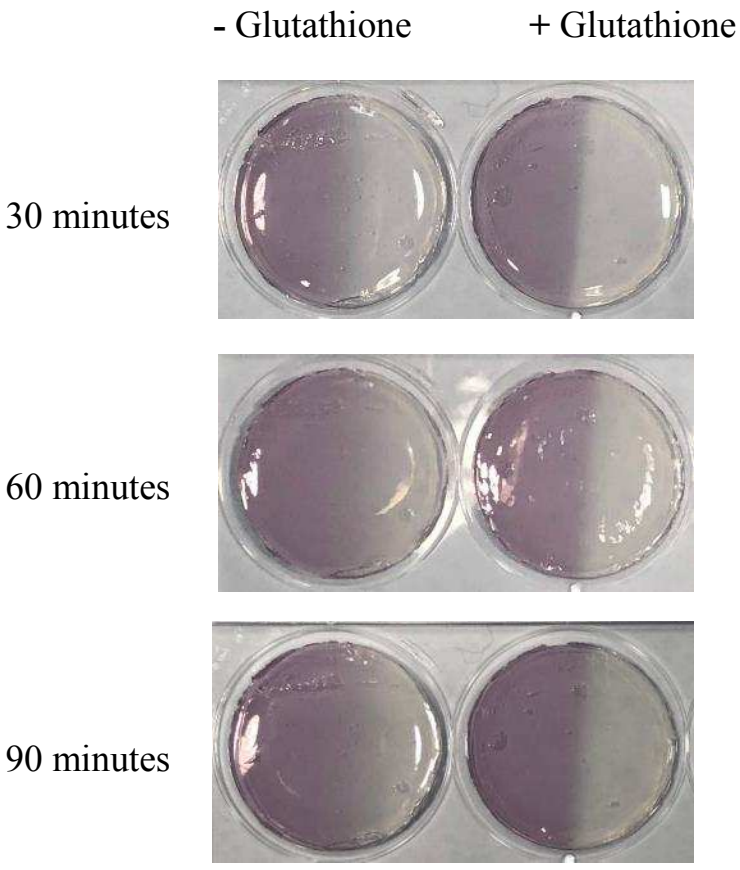

Figure 6.6 Images of the hydrogel nanosensor incubated with no glutathione (Left) and with 25mM glutathione for 10 minutes (30 minutes post-irradiation). Topographical dose profile is maintained upon incubation with glutathione.

Prior to quantifying the topographical dose profile delivered to the hydrogel nanosensor, the hydrogel nanosensors were exposed to various levels of therapeutically relevant high energy electrons (**Figure 6.7**). The absorbance value at 540 nm wavelength is plotted against its corresponding administered dose to generate the calibration curve which will be used to determine unknown radiation doses (**Figure 6.8**). While the response saturated beyond 5 Gy, a linear trend with an equation y=0.03x (y is the absorbance at 540nm and x is the dose in Gy) is observed between 0 – 5 Gy. Three unknown pilot doses were employed to verify the efficacy of the hydrogel nanosensor(**Table 6.1**). These results demonstrate the ability of the hydrogel nanosensor to predict the delivered radiation dose. The spatial dose distribution capability of the nanosensor was tested by irradiating half of the hydrogel nanosensor with a 3 Gy radiation dose (**Figure 6.9**). Upon completion of the irradiation, a visual appearance of maroon/pink is observed in the irradiated region while the non-irradiated regions remains transparent. Glutathione is added 30 minutes post-irradiation to preserve the topographical dose profile. The absorbance at 540nm is measured in finite grids of ≈2mm x 2mm along the diameter of the hydrogel nanosensor and is used to predict the delivered radiation dose. The line profile predicted along the diameter of the hydrogel nanosensor is in agreement with delivered radiation dose fall-off profile. These results taken together indicate the potential of the hydrogel nanosensor to qualitatively and quantitatively determine topographical dose profiles.

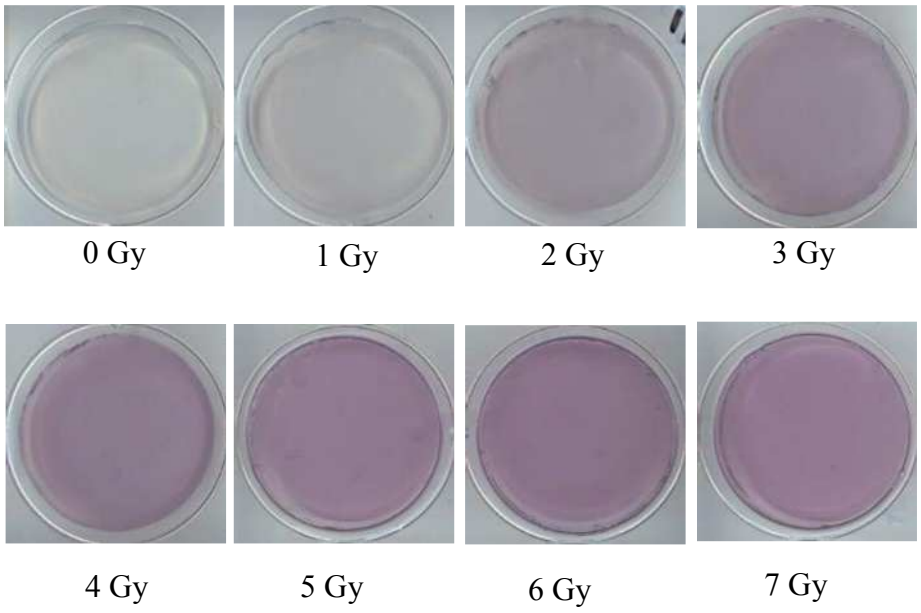

Figure 6.7 Images of hydrogel nanosensor irradiated with different doses of electron beam irradiation. The hydrogel nanosensor contains 10 mM $HAuCl_4$, 75 mM $C_{14}TAB$, 2% (w/v) agarose and incubation with 10 mM ascorbic acid for 10 minutes. Hydrogel nanosensor was further incubated with glutathione (25mM) for 10 minutes 30 minutes post irradiation. All images were taken 2 hours post irradiation.

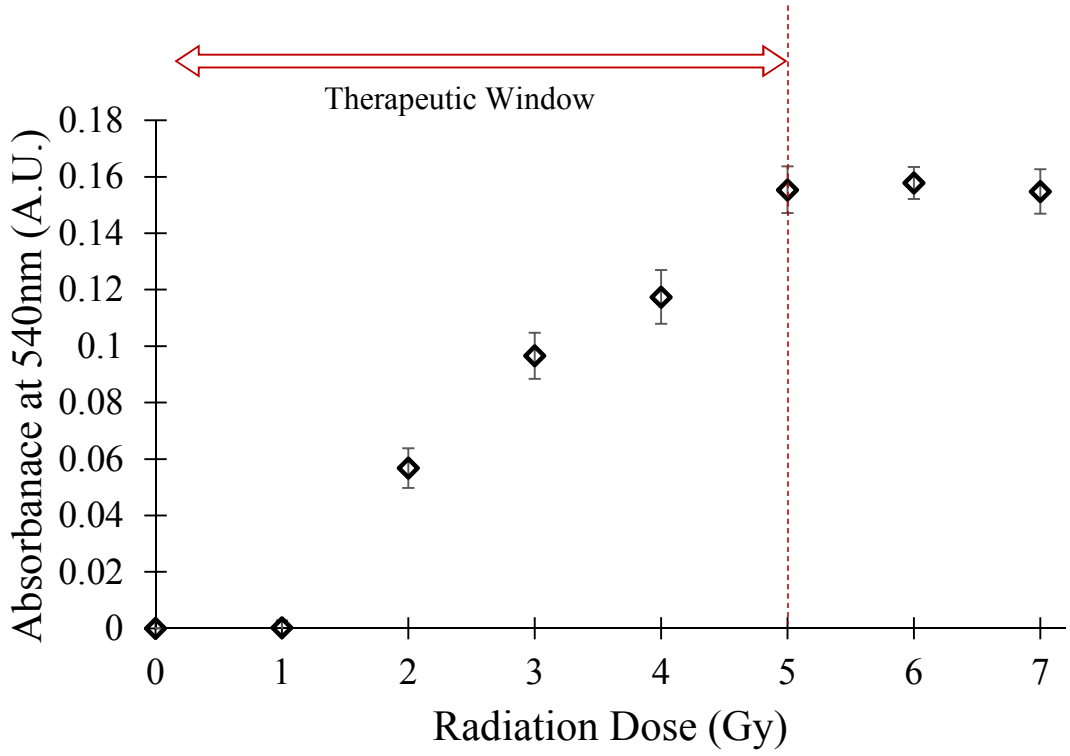

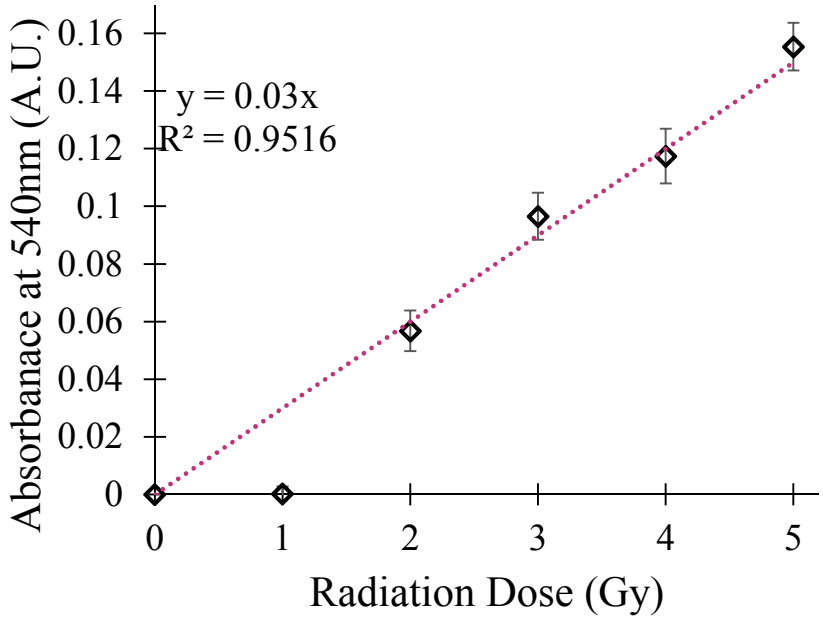

Figure 6.8 (A) Absorbance at 540nm as a function of radiation dose. The linear range in the therapeutic window of the hydrogel nanosensor (0-5 Gy) is indicated. **(B)** Calibration curve for C_{14}TAB using absorbance at 540nm as a function of radiation dose between 0 and 5 Gy. The hydrogel nanosensor contained C_{14}TAB at a concentration of 75mM. Absorbance of the hydrogel nanosensor was measured 2 hours post irradiation.

Delivered Radiation Gy	Predicted Radiation Gy	Error %
1.5	1.23 ± 0.21	18
2.8	2.85 ± 0.29	1.8
4.5	4.0 ± 0.24	11

Table 6.1 Table indicating the efficacy of the hydrogel nanosensor in predicting the dose delivered. Error percentages range between 2 to 20%.

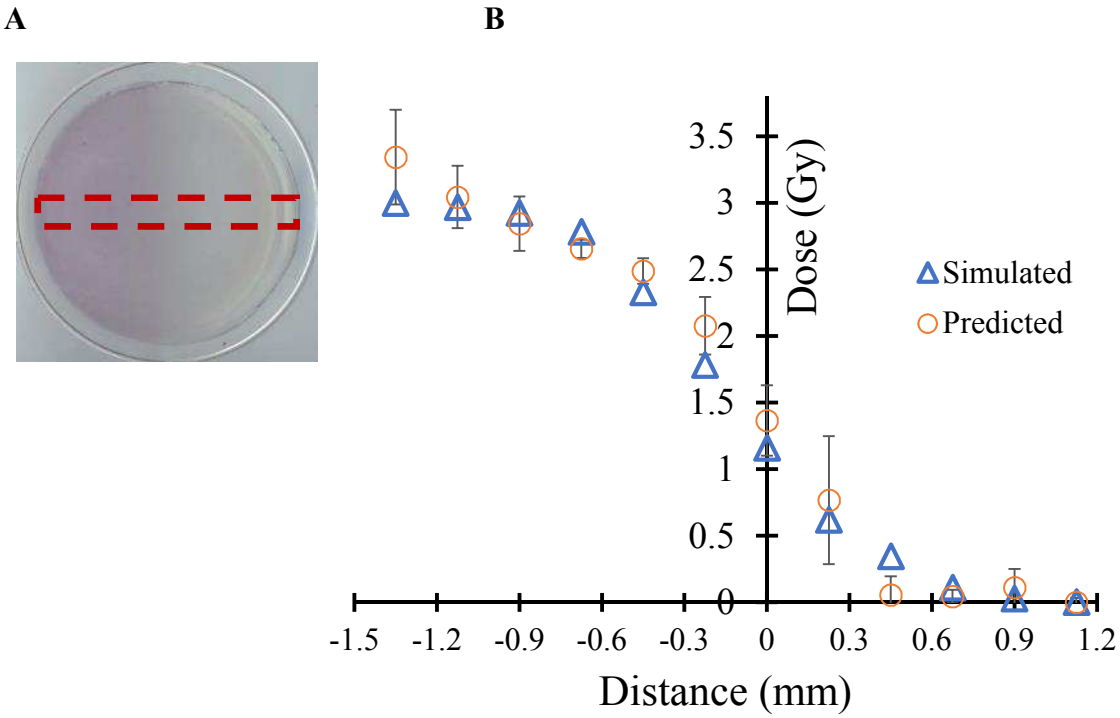

Figure 6.9 (A) Image depicting the colorimetric response of the hydrogel nanosensor irradiated on half with a 3 Gy dose. The appearance of a pink/maroon color illustrates the capability of the hydrogel nanosensor to qualitatively distinguish the irradiated and the non-irradiated regions. **(B)** Dose fall off-profiles comparing the simulated dose (Blue Triangles) with the predicted dose (Orange Circles) indicating the efficacy of the hydrogel nanosensor to quantitatively determine the topographical dose profiles.

Radiotherapy involves the use of a wide range of dose rates for the effective treatment of tumors[241]. To ensure dose rate independence of the hydrogel nanosensor, they were exposed to three different dose rates with a final culminating dose of 3Gy (**Figure 6.10**). No significant differences in the absorbance response was observed emphasizing the dose rate independence of the hydrogel nanosensor. This is not surprising as the number of free radicals generated for the reduction of Au(I) to Au(0) is independent of dose rate and only dependent on the final dose delivered. We further investigate the efficacy of the hydrogel nanosensor in predicting the delivered dose to an anthropomorphic thorax phantom (**Figure**

6.11). The hydrogel discs were kept on top of the skin in the center of the radiation field on the skin of the phantom while being administered a dose of 2.5 Gy. Based on the calibration curve acquired from absorbance spectroscopy, the delivered was calculated to be 2.55 ± 0.02 Gy. The percentage error calculated was 2% which is similar to existing dosimeters which have an uncertainty less than 10%.[230] The distinct visual color change, coupled with a simple quantitative measurement (UV–Visible absorbance) indicates the translational potential of this approach for detecting clinically relevant radiotherapy doses.

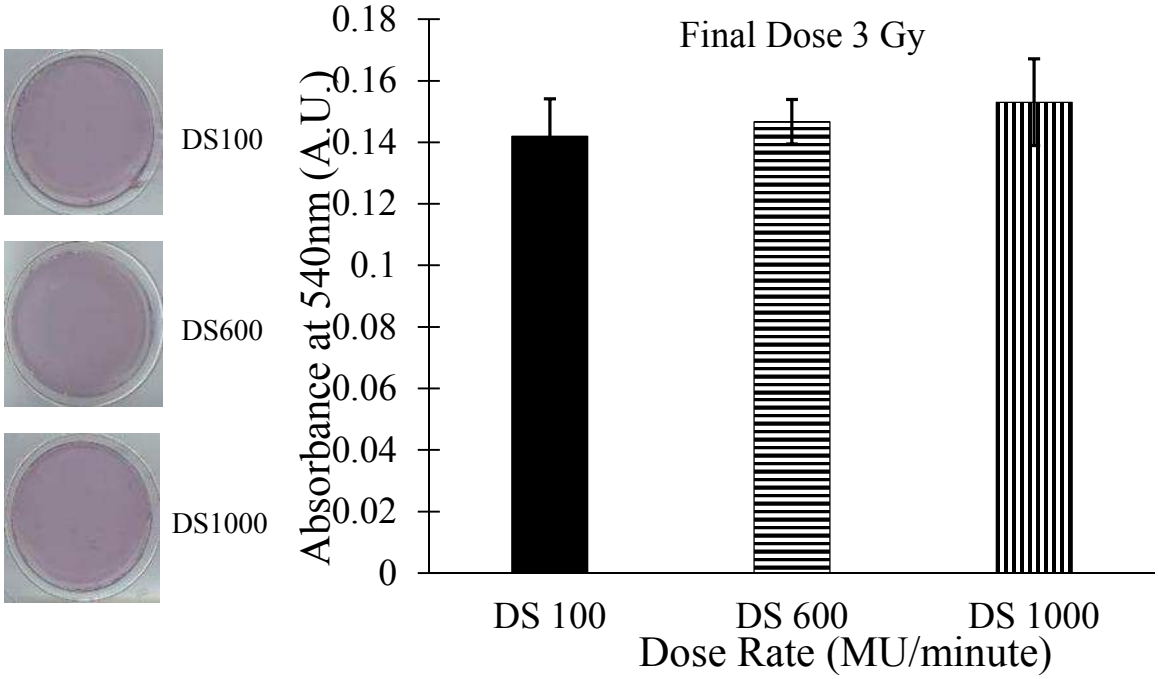

Figure 6.10 Absorbance at 540nm as a function of dose rate. Three different dose rates (100,600 and 1000 MU/minute) were employed in the study. No significant differences were observed indicating dose rate independence. One-way ANOVA with $\alpha = 0.05$ was performed and no significance between all three groups was established.

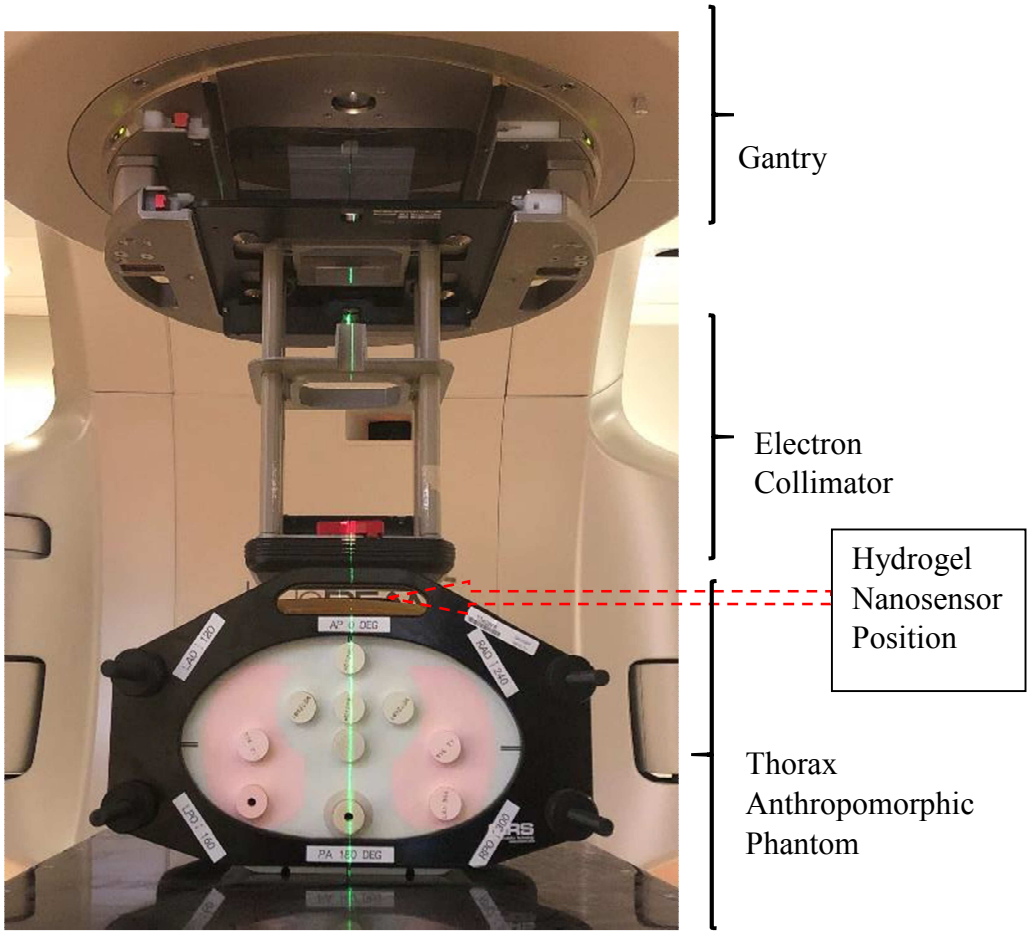

Dose Delivered = 2.5 Gy
Predicted Dose = 2.55 ± 0.02 Gy

Figure 6.11 Setup depicting the anthropomorphic thorax phantom and **(Right)** Image of the hydrogel nanosensor after exposure to 2.5 Gy. The hydrogel nanosensor predicts a radiation dose of 2.55 ± 0.02Gy.

6.4 Conclusions

To our knowledge, this is the first colorimetric plasmonic hydrogel nanosensor for the detection and prediction of radiation dose delivered in electron beam radiotherapy. The hydrogel nanosensor displayed a robust linear calibration between therapeutically relevant radiation dose range (0 – 5) using a simple UV-Visible spectrophotometer. The hydrogel nanosensor was able to predict the radiation dose administered to the anthropomorphic thorax phantom. Finally, we demonstrated the capability of the hydrogel nanosensor to qualitatively and quantitatively distinguish regions exposed to radiation and not exposed to radiation. To further improve the prediction efficacy of the current hydrogel nanosensor, development of novel cationic surfactants and other templating agents is essential. This would allow for the realization of superior control in size and yields of nanoparticles which directly contributes to the hydrogel nanosensor accuracy. In addition, the use of a hydrogel can facilitate adaptations that allows for patient specific dosimetry depending on the patient anatomy. Owing to its facile fabrication and ease in quantification, we anticipate that the hydrogel nanosensor can potentially be translated to clinical electron beam therapy.

Chapter 7 DETERMINATION OF TOPOGRAPHICAL RADIATION DOSE PROFILES USING GEL NANOSENSORS

7.1 Introduction

Rapid development of new technologies has contributed to significant advances in cancer radiotherapy. For example, multileaf collimation and sophisticated planning software permit the delivery of a higher conformal radiation dose to patients, which has led to improved outcomes and quality of life post treatment[242]. These processes involve delivering a high radiation dose to the target tumor while minimizing dose to the surrounding healthy tissue[243]. However, rapid implementation of these new technologies, which were intended to reduce the risks of underdosing or overexposing the patient to radiation, might counterintuitively induce new sources of error[244]. For instance, software errors in linear accelerators could lead to significant radiation overdosing leading to patient morbidity[245]. Independent verification of the radiation dose delivered at and / or near the target tissue can further advance patient safety[246].

Most clinically used sensors including thermoluminescent dosimeters (TLDs), ion chambers and silicon diodes are capable of point dose measurements but are unable to capture topographical radiation dose profiles[247]. Radiographic films were developed to overcome these limitations and have been explored to provide topographical information during radiotherapy. However, their performance is impacted by operating conditions (e.g. humidity) that cause post-irradiation artifacts[248]. The major disadvantage of these

radiographic films is the post-irradiation wait time (>24 hours) required prior to scanning[249], which, in turn, obviates their routine clinical use. There is a critical need for a sensor that can effectively report topographical dose distribution at or near tissues with minimal post-irradiation wait times for applications in treatment planning and verification.

Molecular and nanoscale sensors can overcome limitations with conventional systems and are practical alternatives as facile radiation sensors[161]. Quantum dots and metal organic frameworks (MOFs) demonstrate an intense scintillating response but provide only point dose information limiting their application in the clinic[250, 251]. Polymer gel dosimeters rely on sophisticated readout techniques (e.g. MRI) for post-irradiation analysis, which makes their clinical application cumbersome and expensive[252]. Radiation-triggered conversion of a non-fluorescent monomer to a fluorescence-emitting polymer has been investigated for dose detection[18], but the response was susceptible to decay over time potentially giving rise to challenges in measurement. In light of these limitations, there is a need to develop robust and facile sensors to qualitatively and quantitatively determine topographical (spatial) dose profiles in clinical radiotherapy.

Gold nanoparticles possess unique physical and chemical characteristics that make them an excellent platform for the development of sensors[66, 253-255]. We recently developed a colorimetric sensor in which, ionizing radiation triggers the formation of gold nanoparticles from its corresponding colorless salt precursors[162]. Formulation of a gel-based nanosensor facilitates easier handling and application in clinical radiotherapy[229, 256].

Here, we demonstrate the application of a gel nanosensor formulation for the colorimetric detection of complex distribution profiles leading to topographical mapping of radiation doses along tissues. This approach combines the ease of colorimetric detection and quantification with a fast and robust response. To our knowledge, we demonstrate, for the first time, the use of a molecular and nanoscale technology for determining topographical dose distribution in live canine patients. Taken together, our results demonstrate the potential for clinical translation of this technology for treatment planning and dose verification in cancer radiotherapy.

7.2 Materials and Methods

Materials. Hydrogen tetrachloroaurate trihydrate ($HAuCl_4.3H_2O$), myristyltrimethylammonium bromide ($C_{14}TAB$) (99%), L-ascorbic Acid (AA), Sodium Sulfide nonahydrate ($Na_2S.9H_2O$), sodium chloride, sodium bromide, sodium bromide and molecular biology grade agarose were acquired from Sigma-Aldrich. No further purification of the chemicals was carried out. MilliQ water (18.2 MΩ.cm) was used as solvent for all experiments conducted.

Preparation of the Precursor Gel Nanosensor. Tetrachloroauric acid (30 µL of 10 mM in MilliQ water) was mixed with $C_{14}TAB$ surfactant (600 µL of 75 mM in MilliQ water). From the resulting mixture, 100 µL was discarded prior to further use. Agarose was dissolved in MilliQ water to obtain a final concentration of 2% w/v and heated until a clear

transparent solution was obtained. This heated agarose (500μL) was added to the tetrachloroauric and cationic surfactant mixture. The above liquid (650 μL) was poured into a 24 well tissue culture well plate to form the gel nanosensor with a thickness of ~3 mm and a diameter of ~1.5 cm. Ascorbic acid (650 μL of 10 mM in MilliQ water) was allowed to diffuse from top of the gel for 10 minutes and excess AA was discarded. The gel was washed using MilliQ water to further remove any excess ascorbic acid on the surface. Gel nanosensors were also prepared in 6-well tissue culture plates (~3.6 cm diameter) using similar procedures in order to investigate larger dimensions.

X-Ray Irradiation. All irradiation experiments were carried out at the Banner-MD Anderson Cancer Center in Gilbert, AZ. A Varian TrueBeam Linear Accelerator was used to irradiate the samples with X-rays an energy of 6MV at a dose rate of 600MU/min. For complete exposure of the samples to irradiation, the gel nanosensors were placed within a 10 cm x 10 cm irradiation field. For demonstrating spatial dose distribution, only half the gel nanosensor was placed within the 10 cm x 10 cm irradiation field while the other half was outside the field of irradiation. After irradiation, the samples were analyzed further at Arizona State University in Tempe, AZ. (Travel time of approximately 30 minutes)

Post-processing of irradiated Gel Nanosensors. Various quenching agents, Na_2S and NaX, where X=Cl, Br, or I (650 μL of 5mM), were investigated in order to quench the nanoparticle formation reaction. The quenching agents were added on top of the gel nanosensor at various times post irradiation (5, 9, 15 and 30 minutes) and incubated for 10

minutes. The liquid on the surface was discarded after incubation and the gel nanosensors were used for further quantification.

Absorbance Spectroscopy. A BioTek Synergy 2 plate reader was used to quantify absorbance spectra of all the samples for wavelengths ranging from 300 to 990 nm with a step size of 10 nm. Absorbance measurements for all samples were obtained 2 hours post irradiation although the color formation was seen as early as 5 minutes. The absorbance value of MilliQ water at all wavelengths was used as the blank in all corresponding measurements. These values were then normalized by subtracting the absorbance value at 990 nm wavelength for each gel nanosensor sample. The absorbance value at 540nm was measured for all irradiated and non-irradiated gels and was offset by their corresponding absorbance value at 990nm. These values were further corrected by subtracting the A_{540nm}-A_{990nm} value obtained for MilliQ water. To ensure that the absorbance corresponding to the non-irradiated gel nanosensor (0 Gy) is 0, the absorbance of the non-irradiated gel nanosensor (0 Gy) is subtracted from itself and the absorbance of the irradiated gel nanosensor. These values were plotted as a function of the radiation dose (in Grays or Gy, where 1 Gy = 1 Joule energy absorbed / kg) in order to generate a calibration curve.

Transmission Electron Microscopy (TEM). Irradiated gels were dissolved in 1,2-propane diol (chaotropic agent) in order to facilitate drop casting onto TEM grids and heated to 80°C for 15 minutes. This mixture was centrifuged at 4000 rpm for 10 mins. The supernatant was removed and was further dispersed in MilliQ water. This solution was

further cast onto TEM grids. The samples were dried in air overnight and visualized using a CM200-FEG instrument operating at 200 kV in the LeRoy Eyring Center for Solid State Sciences at ASU. Elemental analysis was carried out in order to determine the composition of the nanoparticles formed.

Topographical Dose Determination in an Anthropomorphic Head and Neck Phantom. An anthropomorphic head and neck phantom was used to determine the efficacy of topographical dose determination of the gel nanosensor in a clinical setting. CT images (1mm) were acquired throughout the head region and transferred to a Philips Pinnacle treatment planning system. In order to simulate an actual clinical treatment, an irregularly shaped GTV (gross target volume) was generated using several CT images. The GTV was defined superficially above the left maxillary sinus and a single 6MV highly conformal photon (X-ray) beam was aimed at a discrete angle at the target in order to avoid nearby critical structures such as the left orbit. A multi leaf collimator (MLC) was used to shape and conform the radiation dose to a target field of 2.5 cm x 1.9 cm. Within this target region, a crescent shaped beam was delivered using the MLC. A 1.5 cm tissue-equivalent bolus material was placed over the target area in order to provide an adequate dose buildup and coverage at the skin surface. A 2 Gy single dose was calculated to d_{max} (1.5cm depth).

Topographical Dose Determination in Canine Cancer Patients Undergoing Radiotherapy. Prior to the canine study, the experimental protocol described below was documented and approved by ASU's Institutional Animal Care and Use Committee

(IACUC). The pet owner signed a consent form approved by ASU's IACUC prior to any study.

Irradiation set up for Canine patients. Prior to irradiation, both canine patients, called A and B here, were anaesthetized to assist immobilization during treatment. Patient A's skin received a radiation dose of 2 Gy within a field size of 4 cm x 4 cm and patient B's skin received a radiation dose of 3 Gy within a field size of 6 cm x 14 cm. To achieve maximum dose deposition and to enable a dose buildup to the skin, a 1.5 cm bolus was wrapped around the leg of patient B. The gel nanosensor (≈3.5 cm diameter) and a Gafchromic EBT3™ film (≈3.5 cm diameter) were wrapped in a plastic bag in order to prevent direct contact with the skin of the patient. One half of the gel nanosensor and the Gafchromic EBT3™ film were placed on the region which was exposed to radiation while the other half of each was placed outside the field of irradiation. For patient A, the gel nanosensor and the Gafchromic EBT3™ film were placed on the skin while for patient B they were placed on top of the bolus. In addition, in the case of patient B, a separate gel nanosensor and Gafchromic EBT3™ film were placed entirely within the radiation field underneath the bolus to validate the delivery of the 3 Gy dose. Following radiation treatment, the gel nanosensor and Gafchromic EBT3™ films were removed and analyzed as described in the following sections.

Topgraphical Mapping of Gafchromic EBT3™ films. Following irradiation with X-rays, an EPSON Expression 10000XL Graphic Arts Scanner was used to scan films prior

to analysis, consistent with clinical practice[257]. After scanning, the RIT dosimetry software (RIT113 Classic V6.0) was used to analyze digitized image of the films. Pixel values at discrete points with a 2 mm spacing between each point were measured along the digitized films. Each pixel value is correlated to the predicted dose using clinical standard calibration curve and a corresponding topographical dose map is acquired. The regions receiving a high radiation dose are depicted in red and those receiving a low irradiation dose are depicted in blue.

Topographical Mapping of Gel Nanosensors. Absorbance values at 540 nm and 990 nm were determined along the surface of the entire gel (diameter of ~1.5 cm) using a 1536 well plate setup in a BioTek Synergy 2 plate reader. Each grid has a finite size of ≈2 mm x 2 mm, which results in approximately 110 grids along the entire gel for which the absorbance values are obtained, leading to a dose map on the gel surface. The final absorbance value at a given grid was calculated based on the method described for generating the calibration curve. The calibration curve was used to predict the radiation dose delivered to each point on the grid and a corresponding topographical dose map over the entire gel surface is obtained. The regions that received high doses of radiation are depicted in red and those receiving low radiation doses are depicted in blue.

Image Acquisition. All images were acquired using an iPhone 7 camera under ambient lighting and automatic settings which were maintained throughout the course of the study. The images were cropped to the desired size for representation. No further editing or post-

processing was carried out. These images were not used for quantification of the dose but only for visualization of the gels.

Statistical Analyses. All irradiation experiments were carried out a minimum of three times independently unless otherwise mentioned. The results are expressed as mean ± one standard deviation. All calculations were carried out using Microsoft Excel 2016.

7.3 Results and Discussion

In conventional fractionated cancer radiotherapy, a patient is administered doses in fractions ranging from 1-5 Gy every day leading to a cumulative dose of 20-90 Gy[258]. However, there are no in-built dosimeters in radiotherapy systems and existing dosimeters lack the ability to report topographical dose distribution along tissues. Facile radiation sensors that are predictive, easy to operate, robust, and cost-effective can lead to the development of wearable detectors and enable clinicians to effectively deliver radiation to target tissues, leading to increased safety and improved patient outcomes.

Here, we demonstrate the efficacious detection of topographical dose distribution of ionizing radiation (e.g. X-rays) using a novel gel-based colorimetric nanosensor. In its original form, gold ion exists in a trivalent (+3) state which is reduced to a metastable +1 valence state via a room temperature reaction with ascorbic acid (vitamin C)[138]. Irradiation of these gels leads to splitting of water molecules (radiolysis) into highly reactive free radicals including hydrated electrons (e^-_{aq}), hydrogen free radicals ($H^\cdot$) and hydroxyl free

radicals($OH^{\cdot}$)[259]. The generated hydrated electrons reduce the monovalent gold to its zerovalent state leading to the formation of gold atoms. These atoms nucleate and mature into gold nanoparticles, which engender a change in color from colorless to red/maroon color in the gel. The increase in color intensity of the gel nanosensor with increasing radiation dose is directly proportional to the formation of gold nanoparticles upon irradiation, and is used for calibrating the response of the gel nanosensor. A quenching agent (Na_2S) is further supplemented in order to preserve dose distribution profiles and generate topographical dose maps.

We first determined the response of the fully irradiated gel in order to establish a calibration of absorbance with dose. The time required for the development of color in the gels (**Figure 7.1)** was dependent on the concentration of the surfactant used and the radiation dose delivered. For a fixed radiation dose (10 Gy), the time required for the development of color increases with an increase in concentration of the surfactant; for concentrations from 50 to 100 mM, the maximum time required for change in color increased from 5 to 15 minutes. However, at the highest surfactant concentration (150 mM) employed in the study, no visible color change was observed even after 30 minutes. We also observed an increase in intensity of color in the gel nanosensor with decreasing surfactant concentration for a fixed radiation dose. We summarize these phenomena using illustrations for low and high concentrations of surfactant as shown in **Figure 7.2**. At all concentrations of C_{14}TAB employed in the study (50-150 mM), the surfactant exists in the form of micelles (CMC ≈ 5mM)[260]. We reason that at any given time there are three distinct species, (1) free gold ions, (2) C_{14}TAB micelles and (3) gold ions bound to C_{14}TAB micelles and that there exists

an equilibrium between them[261]. At low surfactant concentrations, some Au^{1+} are free in solution and others are electrostatically bound to the micelles[142]. With increasing surfactant concentration, there is an increase in the number of C_{14}TAB micelles in the system which drives the formation of more gold ion-bound C_{14}TAB micelles[261]. Consequently, the number of free Au^{1+} decreases with a simultaneous increase in the gold micelle complex. We hypothesize that radiolysis leads to reduction of only free Au^{1+} ions. We reason that this likely leads to a higher yield of nanoparticles with an increased rate of formation at low surfactant concentrations due to the reduction of a higher number of free Au^{1+} ions to Au^0 when compared to the system at high surfactant concentration. These Au^0 atoms mature into gold nanoparticles through surface-assisted reduction of unreacted free Au^{1+} ions[262].

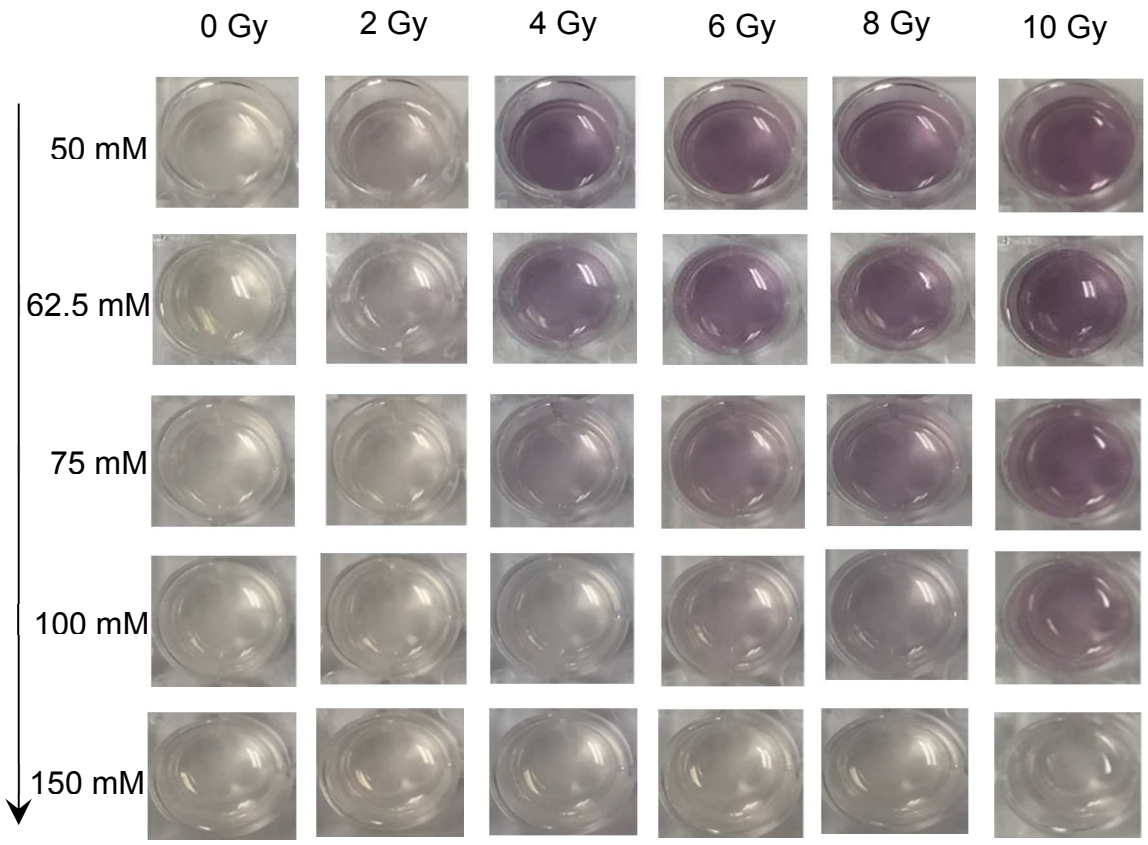

Figure 7.1 Images of gel nanosensors containing various concentrations of C_{14}TAB (50-150mM) following exposure to various doses of ionizing radiation (0-10 Gy). A visible increase in intensity in the maroon color is observed with increasing dose of ionizing radiation for all C_{14}TAB concentrations employed.

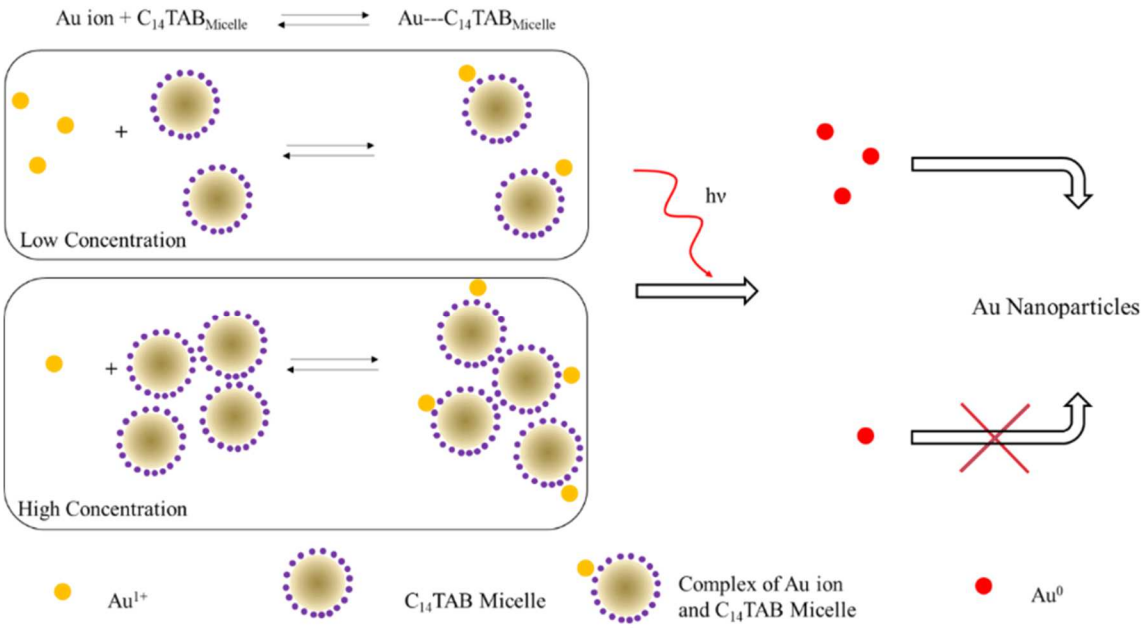

Figure 7.2 Schematic illustration of the proposed mechanism. At low surfactant concentrations, most gold ions are likely free in solution (unbound to micelles). With increasing surfactant concentration, the equilibrium shifts to the right with a decrease in free gold ions. Upon irradiation, the number of Au^0 atoms formed due to reduction at low surfactant concentration is higher due to the presence of a higher number of free gold ions when compared to the system at high surfactant concentration. The higher number of free gold atoms lead to increased yield of gold nanoparticles due to surface assisted reduction with unreacted gold ions.

Following irradiation, a quantitative correlation between the intensity of the color formed in the gels and the delivered dose was determined using absorbance spectroscopy (**Figure 7.3)**. Radiation resulted in the formation quasi-spherical gold nanoparticles that exhibited a characteristic light absorption spectral peak between 500 and 600 nm[253]. A decrease in the width of the spectral profile is observed with increasing radiation dose indicating a

decrease in polydispersity of the nanoparticles formed. A blue-shift in the absorbance peaks with increasing radiation dose suggests a decrease in particle size compared to those obtained at lower radiation doses[162]. The peak absorbance intensity increases with increasing radiation dose corroborating the observed increase in color intensity. A decrease in the peak absorbance at 540 nm with increase in concentration of the cationic surfactant is observed likely due to micellar inhibition of the reduction of Au(I) to Au(0)[142]. We previously observed similar trends in spectral width changes, blue shifts and peak absorbance changes with different levels of ionizing radiation[162, 229, 256]. The maximum peak absorbance at 540 nm was plotted as a function of the delivered radiation dose in order to quantify the gel nanosensor response (**Figure 7.4**). A linear response was observed with increasing radiation dose for all concentrations of the surfactant.

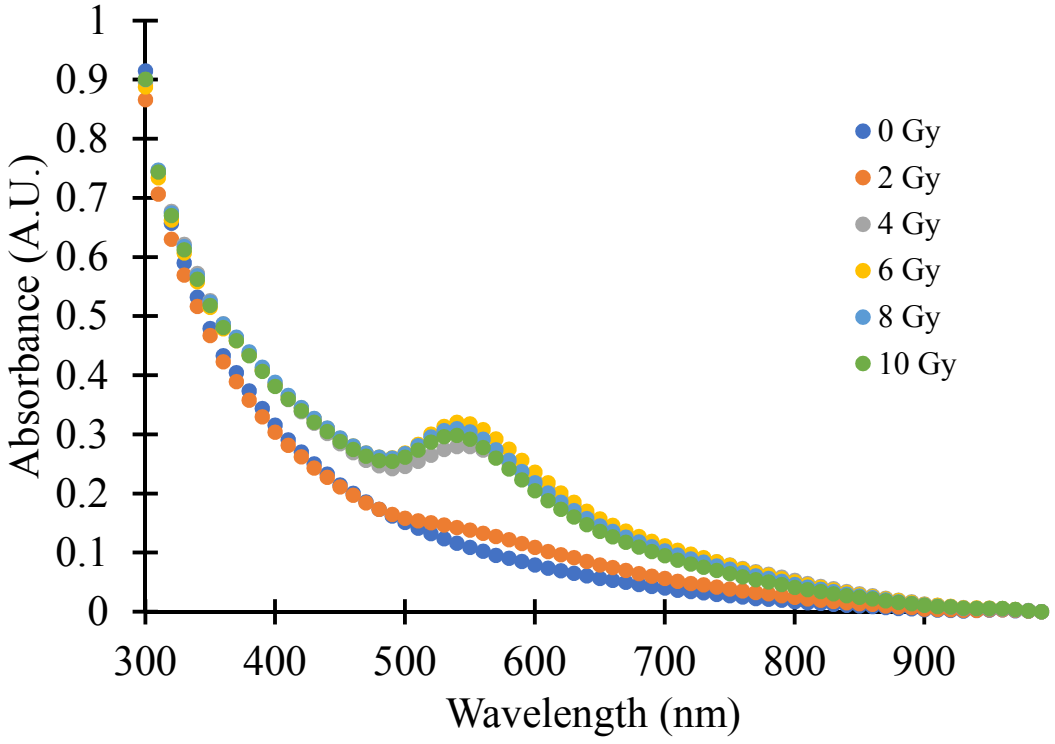

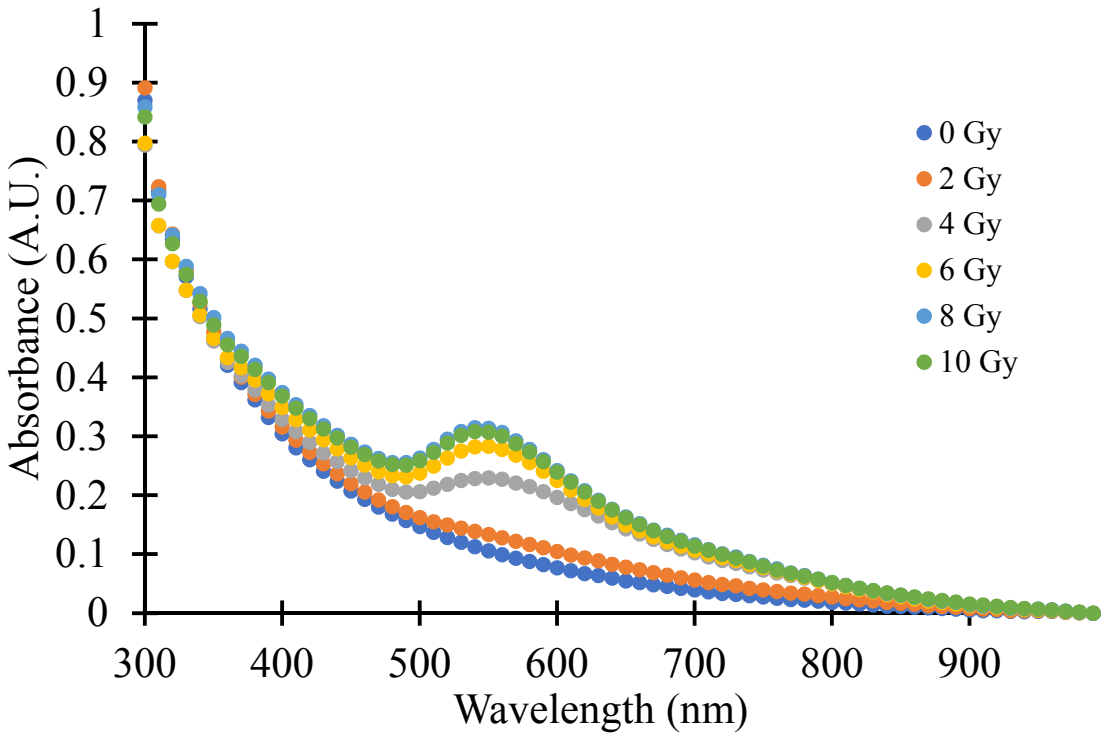
Absorbance (A.U.)
1
0.9
0.8
0.7
0.6
0.5
0.4
0.3
0.2
0.1
0
300
400
500
600
700
800
900
Wavelength (nm)
0 Gy
2 Gy
4 Gy
6 Gy
8 Gy
10 Gy

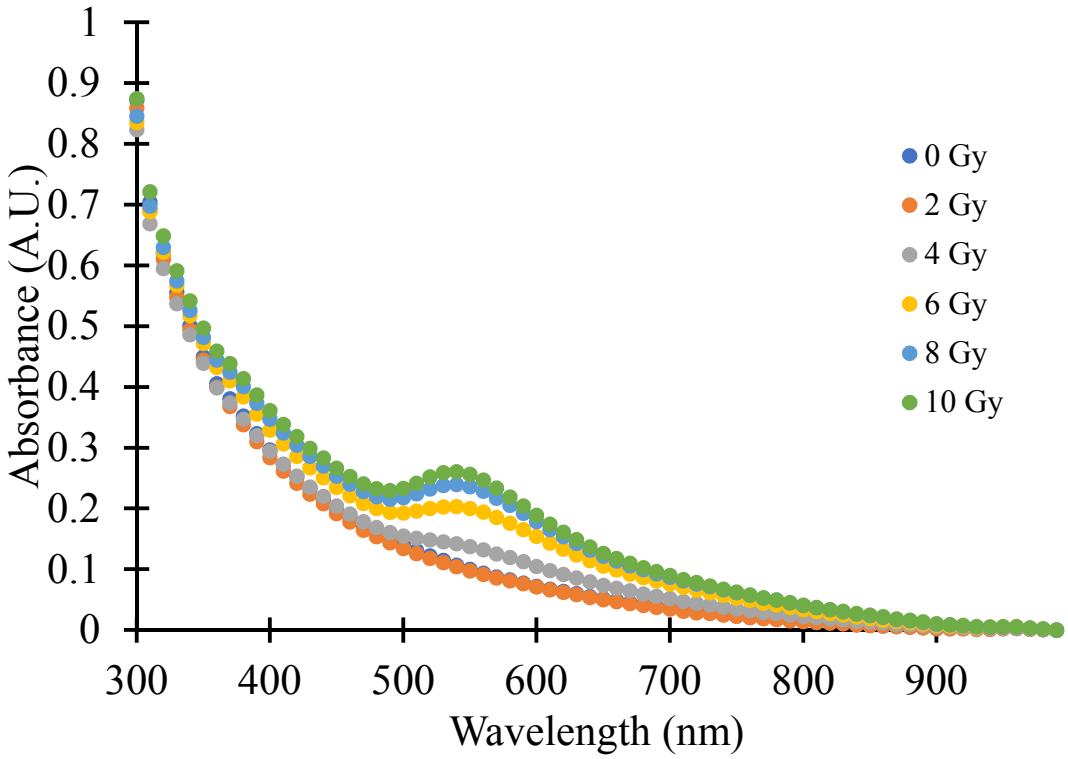
Absorbance (A.U.)
1
0.9
0.8
0.7
0.6
0.5
0.4
0.3
0.2
0.1
0
300
400
500
600
700
800
900
Wavelength (nm)
0 Gy
2 Gy
4 Gy
6 Gy
8 Gy
10 Gy

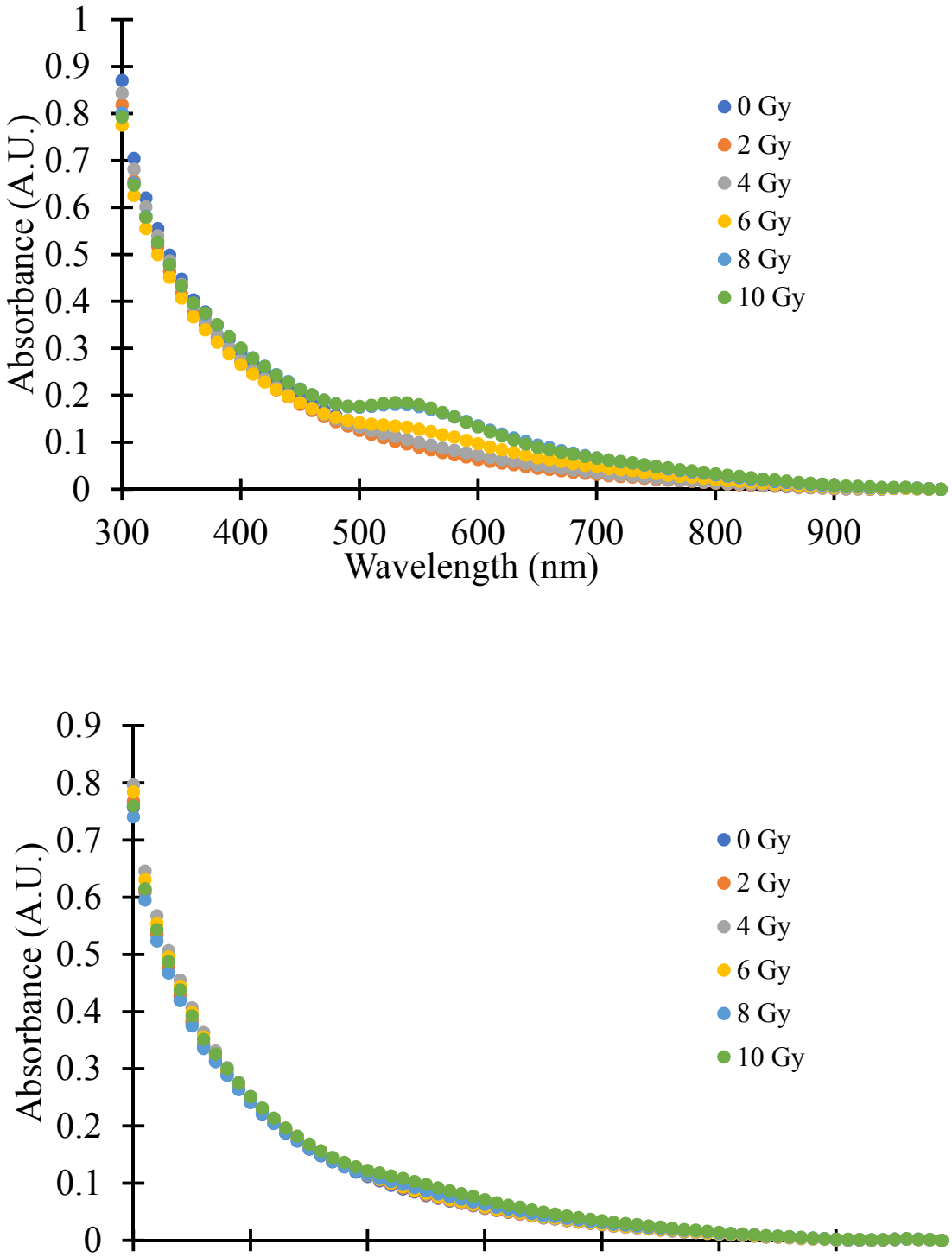

Figure 7.3 From Top to Bottom; Absorbance spectra of gel nanosensor containing (A) 50mM, (B) 62.5mM, (C) 75mM, (D)100mM, (E)150mM. The gels were irradiated with 0, 2, 4, 6, 8 and10 Gy. Characteristic absorbance peaks between 500 and 600nm are indicative of gold nanoparticles. The corresponding radiation dose are mentioned in the legend with increasing radiation dose (top to bottom).

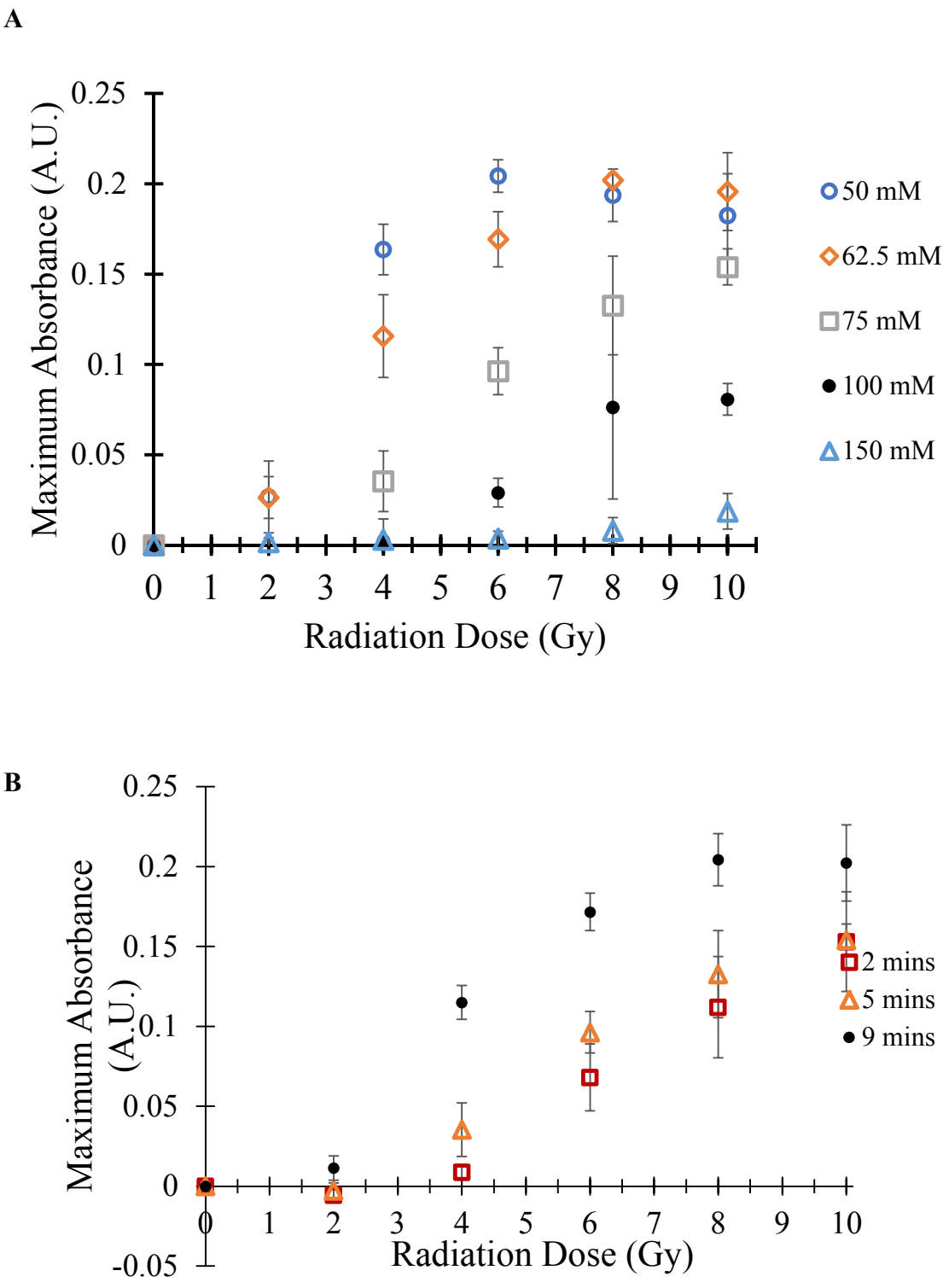

Figure 7.4 Peak absorbance spectra at 540nm plotted versus radiation dose post irradiation. **(A)** The plot indicates the gel nanosensor response as a function of concentration of $C_{14}TAB$ with a fixed Na_2S addition time of 5 minutes. **(B)** The plot indicates the gel nanosensor response as a function of time of addition of Na_2S with a fixed $C_{14}TAB$ of 50mM. These results indicate the adaptability of the sensor to measure various radiation

dose range through simple fine tuning of C_{14}TAB concentration or/and time of addition of sodium sulfide.

We next determined the ability of the gel nanosensor to detect topographical distribution of radiation dose by irradiating one-half of the gel nanosensor with a 4 Gy dose. The near immediate (~2 min) visual appearance of maroon color only in the irradiated region indicates the presence of gold nanoparticles following radiation (**Figure 7.5**). However, the color was observed to "bleed over" to the non-irradiated region 1 h post irradiation (**Figure 7.5A**), which indicated a loss of topographical information in the gel over time. Increasing the weight percent of agarose from 3% to 4%, in order to decrease the pore size[263], did not help preserve topographical integrity of dose distribution (**Figure 7.5B**).

As an approach for maintaining topographical information of the delivered dose, we hypothesized that radiolytically generated gold nanoparticles act as seeds for unreacted gold ions on the non-irradiated region leading to the formation of additional gold nanoparticles[143]. These additional gold nanoparticles, in turn, impart color to non-irradiated regions and drive the bleed over phenomena, which leads to loss of topographical dose information. Incubation for 10 minutes (5 minutes post irradiation) with sodium sulfide (Na_2S) led to complete suppression of the bleed over of color (**Figure 7.5C**); sodium halides (NaX, X = Cl, Br, I), however, were ineffective for this purpose. In the absence of sodium sulfide, growth of gold nanoparticles is a result of two distinct steps[262]. The first step involves the reduction of Au^{1+} to Au^0 atoms, which nucleate and develop into small nanoclusters. The second step determines the overall size and the number of particles

formed. This step involves the growth and maturation of nanoparticles induced due to attachment and reduction of free gold ions on existing nanoclusters. We reason that quenching of the unreacted gold ions in the non-irradiated region is a critical step in preserving topographical dose information. Therefore addition of sodium sulfide, which reduces the unreacted free gold ions to gold sulfide nanoparticles[264] inhibits the bleed over phenomena and retains the topographical dose information required for modern dosimetry(**Figure 7.6**).

A

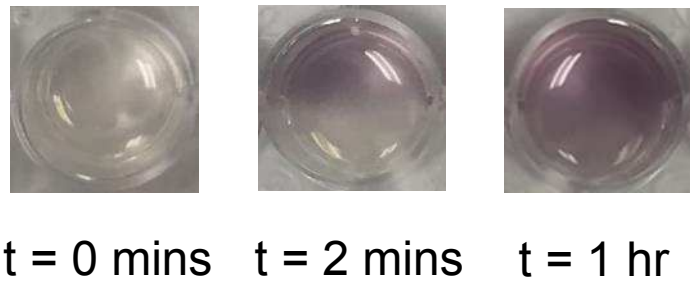

B (i) **B (ii)**

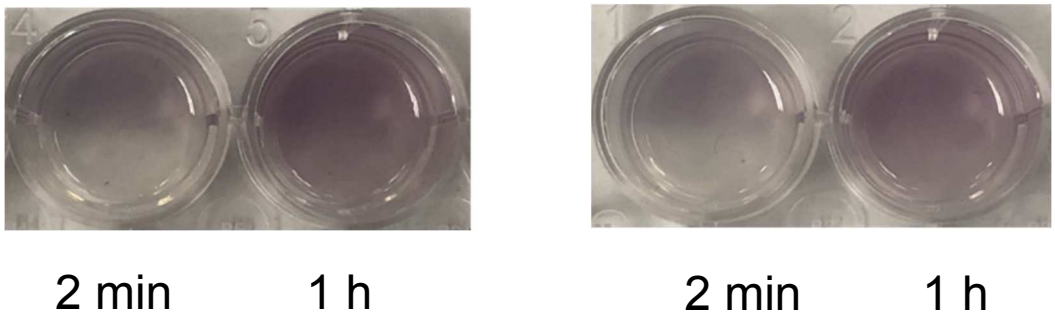

C

Figure 7.5 (A) Image of agarose gel (left) prior to irradiation, (middle) Top half irradiated with 4 Gy and image acquired 2 minutes post irradiation, and (right) Image acquired 1 hour post irradiation. A visible increase in intensity of color in the non-irradiated region leads to loss of topographical information. **(B) i.** Image of 3 w/v % agarose gel (left) 2 minutes post irradiation and (right) 1 hour post irradiation; **ii.** Image of 4 w/v % agarose gel (left) 2 minutes post irradiation and (right) 1 hour post irradiation indicates that increase in agarose weight percentage does not preserve topographical dose information **(C)** Images of gel nanosensor incubated with 5 mM sodium sulfide and various sodium halides for 10 minutes and imaged after 1 hour. No loss of topographical information observed upon incubation with sodium sulfide.

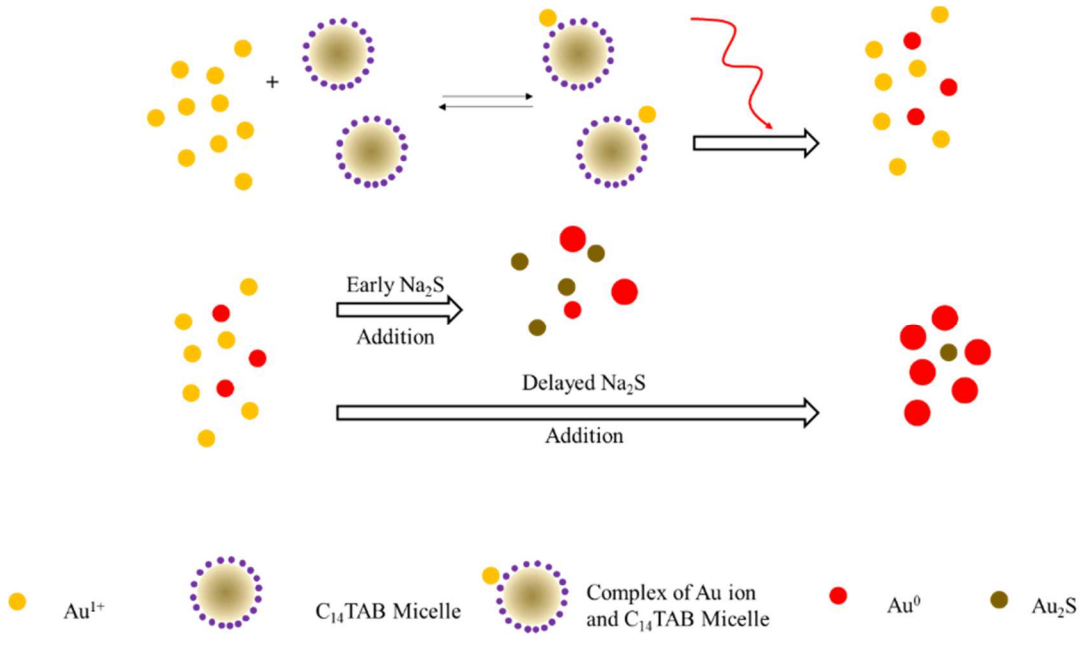

Figure 7.6 Schematic illustration of the proposed mechanism used for detecting spatial dose distribution. Early addition of Na_2S leads to the reduction of unreacted gold ions to

gold sulfide particles, which obviate further reaction and color bleed over. These ions wound have otherwise likely contributed to the growth of radiolytically generated gold nanoparticle resulting in bleed over of the color to non-irradiated regions. Upon delayed addition of Na_2S, most of the radiation-generated gold nanoparticles have matured and further addition of the quenching agent does not affect the final yield of gold nanoparticles in the gel nanosensor. This results in an increase in absorbance in the gel nanosensor as a function of time of addition of Na_2S post-irradiation.

Increasing the wait time post irradiation before incubation with sodium sulfide led to an increase in absorbance for a fixed radiation dose (**Figure 7.4 B**). Specifically, for a fixed radiation dose of 6 Gy, the average absorbance increased from 0.07 to 0.17 with increasing the wait time prior to addition of sodium sulfide post irradiation from 2 to 9 minutes. Addition of Na_2S immediately (i.e. 2 min post irradiation) likely leads to the reduction of unreacted gold ions to gold sulfide particles. This can reduce the growth of radiolytically generated gold nanoparticles, which in turn, can result in lower absorbance values observed for the shorter wait times (**Figure 7.6**). With a delayed addition of Na_2S (i.e. 9 min post irradiation), we hypothesize that most of the radiation-generated gold nanoparticles have matured and further addition of the quenching agent does not affect the final yield of gold nanoparticles. This results in an increase in absorbance as a function of wait time post irradiation before the addition of Na_2S for a given radiation dose (**Figure 7.4 B**). Although it is important that the gel nanosensor detects doses used in conventional fractionated radiotherapy (i.e. 1-2 Gy per fraction), the sensor can be adopted for a wider dose range (2-8 Gy) used in modern radiotherapy by simply fine tuning the concentration of the cationic surfactant and/or modulating the time of addition of sodium sulfide. This level of flexibility is not available in existing dose detection systems, which typically have a fixed linear response.

Upon addition of sodium sulfide, both the irradiated and non-irradiated regions of the same gel were independently visualized using transmission electron microscopy (TEM; please see Experimental Section). Elemental analysis using energy-dispersive X-ray (EDX) spectroscopy indicated two overlapping peaks in the non-irradiated region, (1) M-shell peak at 2.12 keV corresponding to gold and (2) K-shell peak at 2.3 keV likely due to the presence of sulfur (**Figure 7.7 A**)[265]. The irradiated region contains a higher yield of gold nanoparticles and displays a sharp peak corresponding to only the M-shell of gold (**Figure 7.7 B**). Comparison of both spectra indicates the formation of gold sulfide nanoparticles in the presence of Na_2S in the non-irradiated region. The mean diameter of nanoparticles in the non-irradiated region was between 5.6 ± 1.7nm (**Figure 7.8 A**). The irradiated region consists of nanoparticles with a size range of 52.7 ± 23.4nm (**Figure 7.8 B**). The presence of a higher number of nanoparticles with a diameter greater than 2 nm lead to the development of the characteristic color of gold nanoparticles (maroon/pink) observed in the irradiated regions[266].

A

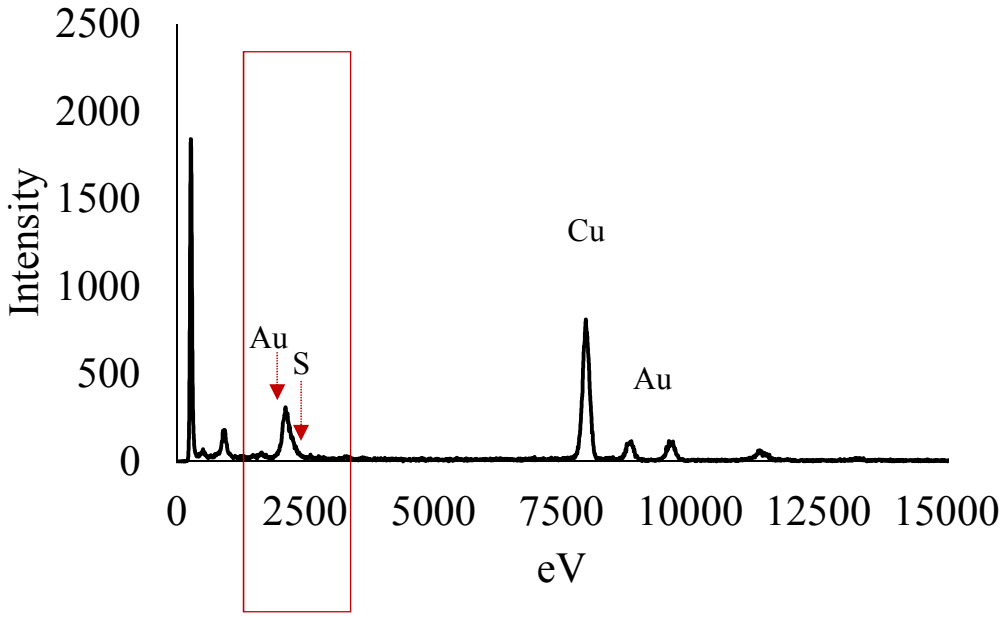

B

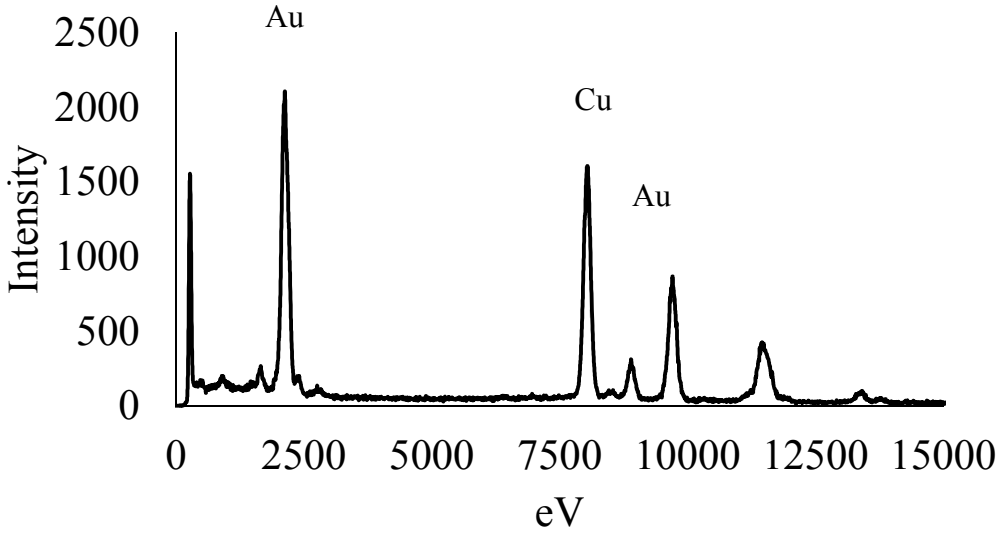

Figure **7.7** Elemental analysis of nanoparticles after incubation with Na_2S in the **(A)** irradiated region and the **(B)** non-irradiated region. The presence of a broadened peak in **A** indicates the presence of gold sulfide nanoparticles. The peak attributions are done based on those in the literature[265].

A

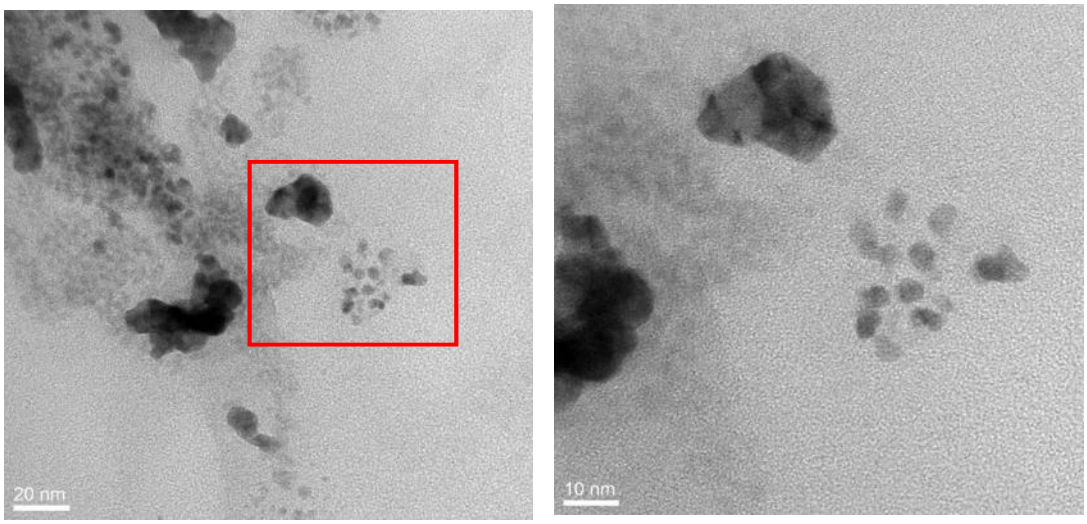

B

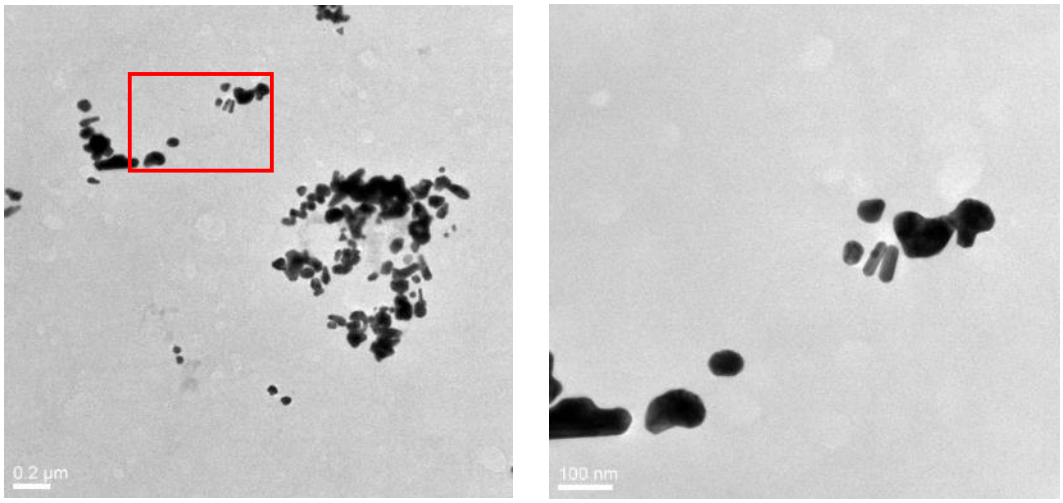

Figure 7.8 TEM image showing presence of nanoparticles **(A)** after incubation with sodium sulfide (nanoparticle dimensions: 5.6 ± 1.7 nm) and **(B)** without incubation with sodium sulfide (nanoparticle dimensions: 52.7 ± 23.4 nm). Corresponding magnified images of the highlighted region are shown on the right. A total of 15 particles were used for quantification of nanoparticle dimensions.

We further investigated the capability of the gel nanosensor for visualizing diverse topographical radiation dose patterns **(Figure 7.9)**. The gel nanosensor was irradiated with

a square field (1 cm x1 cm) with a 1 cm non-irradiated spacing between each field. Each sequential square was irradiated with incremental doses resulting in multiple squares within the gel nanosensor. The increase in intensity of the color is indicative of the increasing dose, while preserving the topographical integrity. Regions that are not irradiated do not demonstrate a change in color (**Figure 7.9A**). We also demonstrated the capability of the gel nanosensor for detecting complex radiation patterns as shown by the model dose that read "ASU" (**Figure 7.9B**). In these studies, the radiation dose was delivered sequentially which results in delayed appearance of the last two letters, viz. "S" and "U" compared to appearance of "A".

A

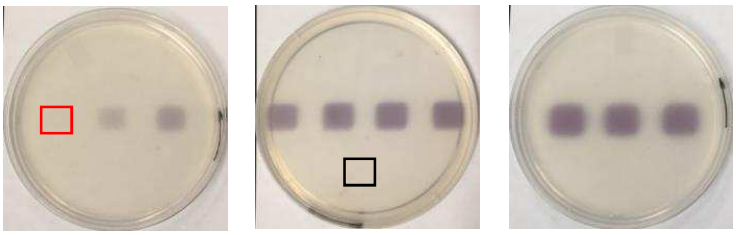

B

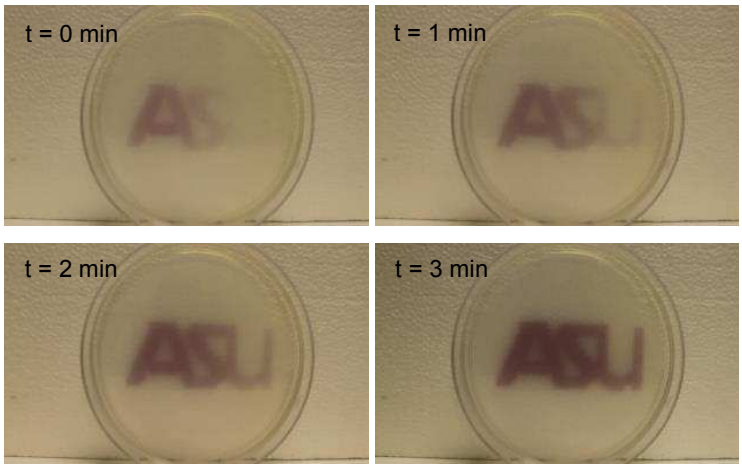

Figure 7.9 (A) Representative image of a petridish containing the gel nanosensor (3mm thick and ≈10cm diameter) irradiated by a 1cm x 1cm square field of X-ray radiation. From left each square indicates increasing radiation dose from 0.5 Gy (Red Box), 1 Gy, 1.5 Gy, 2 Gy, 2.5 Gy, 3 Gy, 3.5 Gy, 4 Gy, 4.5 Gy and 5 Gy; the black box in the middle image shows 0 Gy. **(B)** Representative image of a complex topographical dose pattern (ASU letters) generated using a 2Gy X-ray dose. The petridish has a diameter of 10cm. All gel nanosensors contain 50mM $C_{14}TAB$ and Na_2S was added 30 minutes post irradiation.

Clinical radiotherapy for skin and breast cancer lesions commonly employs radiation field sizes that are larger than 3 cm x 3 cm in area[267-269]. In order to accommodate larger radiation fields, we fabricated a gel nanosensor with the same thickness (~3 mm) but a larger diameter (~3.5 cm). The gel nanosensors were loaded with a surfactant concentration of 75 mM, irradiated over the whole area with doses ranging from 0-4 Gy and treated with 5 mM Na_2S 30 minutes post-irradiation (**Figure 7.10 A**). Following irradiation, peak absorbances at 540 nm of the irradiated and the non-irradiated gel nanosensors were plotted as a function of radiation dose in order to obtain a linear calibration curve between 0-4 Gy (**Figures 7.10 B, C**). The predictive efficacy of the sensor was determined using a dose of 1.5 Gy, which was not used for generating the calibration curve. The change in color was quantified using the previously generated calibration curve and the dose was estimated to be 1.28 ± 0.1 Gy which is comparable to the delivered dose indicating the predictive ability of the gel nanosensor. In order to investigate the ability to detect topographical dose distribution, one-half of the gel was irradiated with 2 Gy by positioning it at the edge of the radiation field and the other half was not irradiated. The absorbance at 540 nm was recorded in finite grids (≈2x2 mm) along the diameter of the gel nanosensor and the radiation dose was predicted using the previously established calibration curve. The topographical radiation dose profile predicted by the gel nanosensor is in excellent agreement with the delivered dose profile

(**Figure 7.11**). These results indicate the potential of the gel nanosenor for qualitatively and quantitatively detecting regions irradiated with ionizing radiation and distinguishing them from those that are not irradiated.

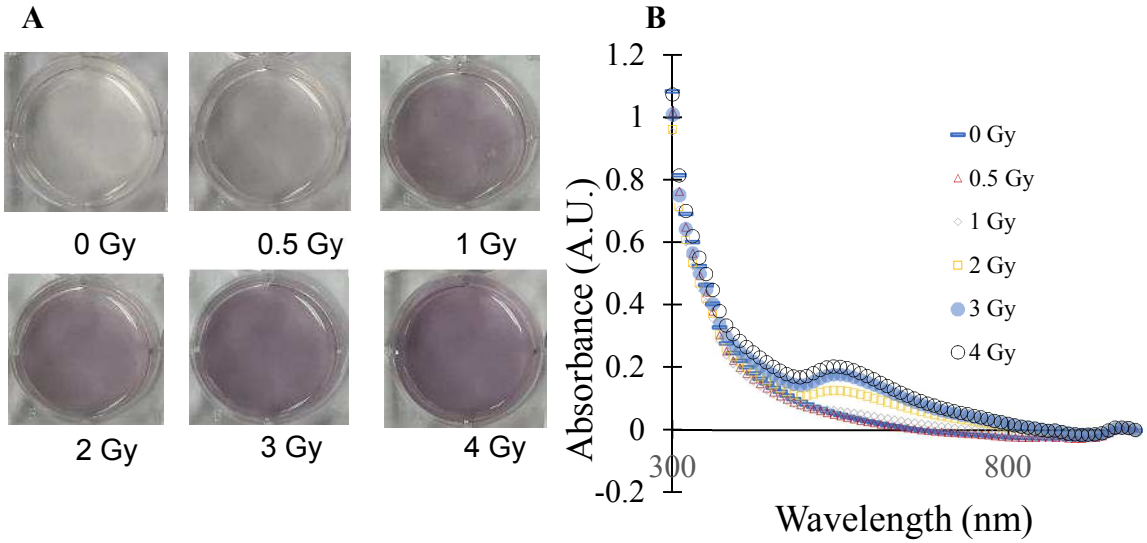

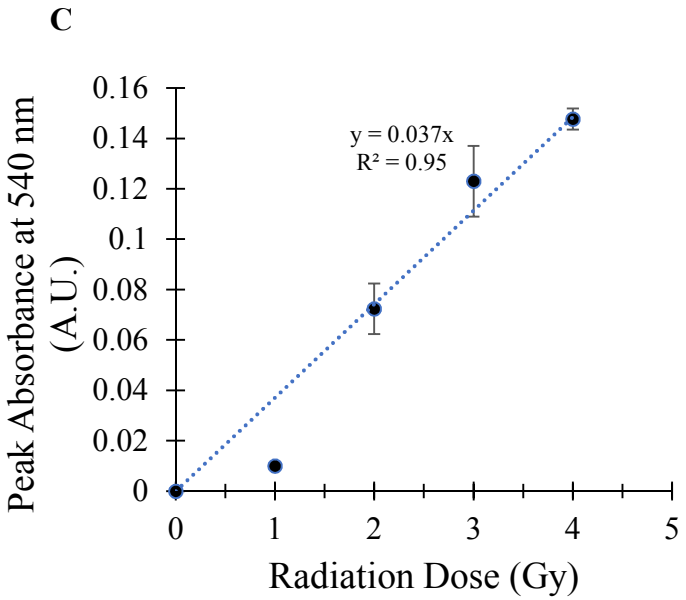

Figure 7.10 (A) Images and **(B)** absorbance spectra of gels containing 75 mM C_{14}TAB following exposure to different doses of ionizing radiation. Characteristic peaks between 500 and 600 nm are indicative of gold nanoparticle formation. **(C)** Absorbance at 540nm as a function of radiation dose is used as a calibration curve to determine unknown doses.

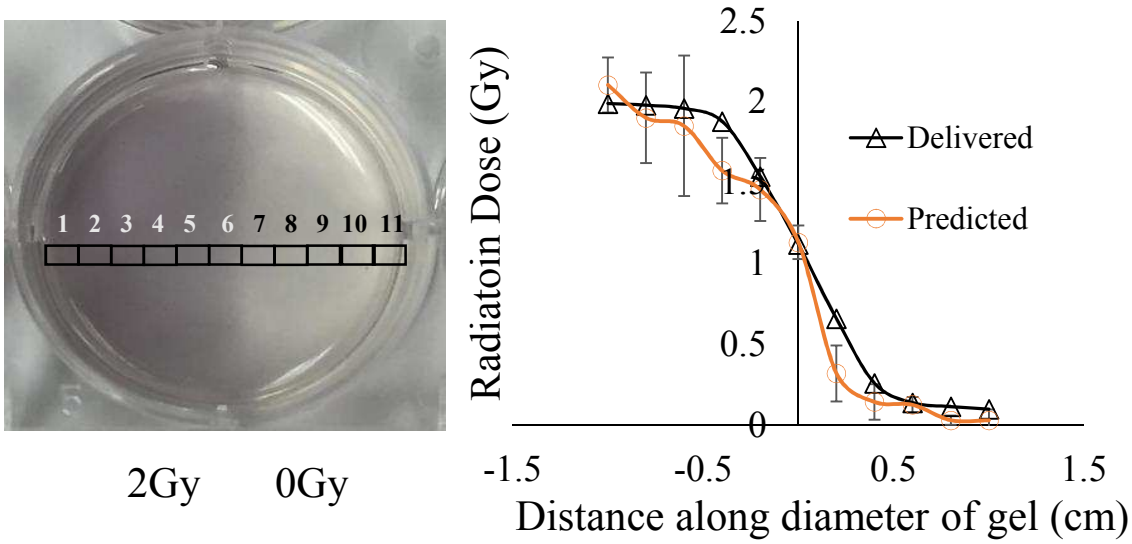

Figure 7.11 (Left) Colorimetric response of the gel nanosenor irradiated on one half with a 2 Gy dose. A visible appearance of maroon color in the irradiated region illustrates the ability of the gel nanosensor to predict topographical dose profiles. **(Right)** Dose fall-off profile for half a gel nanosensor irradiated by 2 Gy. The delivered radiation dose and the predicted are comparable indicating the efficacy of the gel nanosensor in determining topographical information. In all cases, Na_2S was added 30 min post irradiation.

Accidental exposure to radiation can cause significant tissue injury and skin is the first organ exposed to radiation damage; radiation-induced skin injuries range from erythema to necrosis[270]. We investigated the translational capability of the gel nanosensor for predicting radiation doses delivered to a head and neck phantom (**Figures 7.12 A and 7.12**

B). An irregular crescent-shaped radiation dose field was delivered to the phantom in order to mimic clinically administered radiotherapy (**Figures 7.12 C and 7.12 D**). The distinct visual change in color is a qualitative indicator of the radiation delivered to the gel nanosensor (**Figure 7.12 E**). The previously generated calibration curve was employed to predict the dose based on the intensity of the color developed (please see the Experimental section). The predicted absorbance dose is highest in the middle (bright red) of the pattern and decreases in intensity towards the edge (light red) of the field. Specifically, the core of the pattern receives an average dose of 2.3 Gy as determined by the treatment planning system and the gel nanosensor predictions were in excellent agreement with the planned dose profile (**Figures 7.12 F and 7.12 G**). These results suggest the ability of the gel nanosensor for detecting and predicting complex radiation patterns employed during actual clinical human radiotherapy.

A

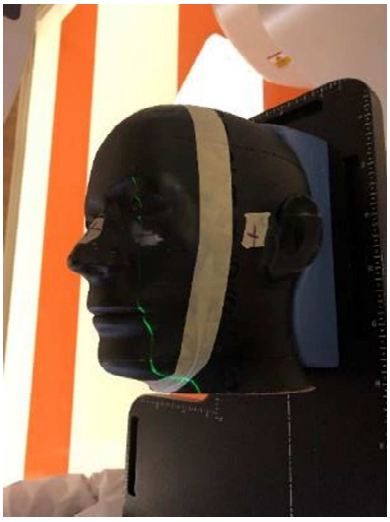

B

C

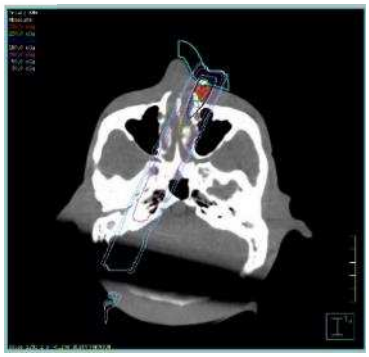

D

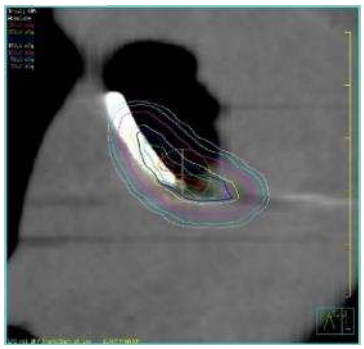

E

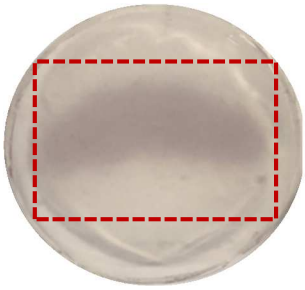

F

	0.0	0.0	0.0	0.0	0.0	0.1	0.0	0.0	0.0	
0.0	0.0	0.1	0.1	0.2	0.2	0.2	0.1	0.1	0.0	0.0
0.1	0.1	0.3	0.7	0.8	0.9	0.7	0.5	0.2	0.1	0.0
0.2	0.6	1.1	1.6	1.9	1.9	1.8	1.4	0.8	0.4	0.1
0.4	1.2	2.0	2.2	2.3	2.3	2.3	2.2	1.7	1.0	0.3
0.7	1.4	1.9	2.0	2.0	2.0	2.1	2.2	2.1	1.6	0.7
0.3	0.8	0.9	1.0	0.9	0.8	1.1	1.4	1.5	1.4	0.6
0.1	0.2	0.2	0.2	0.2	0.2	0.3	0.4	0.5	0.4	0.2
0.0	0.0	0.1	0.1	0.1	0.1	0.1	0.1	0.1	0.1	0.1
	0.0	0.0	0.0	0.0	0.0	0.0	0.0	0.0	0.0	

G

	0.2	0.0	0.0	0.0	0.0	0.0	0.0	0.1	0.4	
0.3	0.0	0.0	0.4	0.0	0.4	0.1	0.1	0.0	0.0	0.1
0.0	0.4	1.6	1.7	2.0	2.1	1.9	1.8	0.7	0.1	0.0
0.2	1.1	1.9	2.2	2.3	2.4	2.4	2.3	2.1	1.6	1.3
2.0	2.3	2.4	2.3	2.3	2.3	2.4	2.5	2.3	2.2	1.8
1.9	2.3	2.1	2.3	1.6	1.3	1.7	1.8	1.9	2.1	1.9
1.2	0.9	0.9	0.3	0.1	0.1	0.2	0.3	0.4	0.5	0.3
0.1	0.0	0.0	0.0	0.0	0.0	0.0	0.0	0.0	0.0	0.0
0.3	0.0	0.0	0.0	0.0	0.0	0.0	0.1	0.0	0.0	0.2
	0.5	0.2	0.1	0.0	0.1	0.1	0.1	0.4	0.4	

Figure 7.12 (A) Image of an anthropomorphic head and neck phantom treated with an irregularly shaped radiation field below the left eye. **(B)** Image of the gel nanosensor positioned on the anthropomorphic phantom in the radiation field mimicking a conventional radiotherapy session. **(C** and **D)** Treatment planning images representing an irregularly shaped radiation field used to deliver a complex radiation pattern under the eye of the phantom. **(E)** Visual image of the irradiated pattern on the gel nanosensor. Only the irradiated region develops a maroon color while the non-irradiated region remains colorless. **(F)** Topographical dose profile of the delivered radiation to the anthropomorphic phantom. The profile is generated from the treatment plan used during the actual irradiation of the head and neck phantom. **(G)** Absorbance along the irradiated gel nanosensor in ≈2mm x 2mm grids was quantified using a calibration curve to quantify a topographical dose profile. The core dose received by the crescent-shaped profile (2.3 Gy) is comparable to the predicted dose profile from the gel nanosensor (2.3 Gy). This suggests the capability of the gel nanosensor to qualitatively and quantitatively predict the complex topographical dose profiles. Colors indicate the intensity of color with red being the highest dose and blue indicating a lower radiation dose. The experiments were performed 3 times independently.

Although mice and rats are widely employed and inexpensive, their small anatomy relative to that of humans can lead to significant differences in dosimetry[271] and can limit the extrapolation of these findings to human patients. Canine patients circumvent these challenges because of their larger size, and similarity in contours and treatment methods to that of human patients. We investigated the gel nanosensors as independent radiation dosimeters for verifying the dose delivered to two canine patients undergoing radiotherapy; the patients are henceforth referred to as “Patient A” and “Patient B”. The efficacy of the gel nanosensor was also compared with conventional radiochromic films used in the clinic. To our knowledge, this is first time a nanoscale based dosimeter has been employed in the detection of radiation dose delivered to live canine patients undergoing clinical treatments.

The surface of patient A was administered a dose of 2 Gy to the skin (**Figures 7.13**). The gel nanosensor was positioned at the edge of the radiation field and the ability to measure

topographical dose information was evaluated (**Figures 7.13**). Upon completion of the treatment, a maroon color on one-half of the gel was clearly seen while the non-irradiated region remained colorless (**Figure 7.13 E**). The previously generated calibration curve was used to predict the delivered dose. Unsurprisingly, the dose delivered is highest in the irradiated region (denoted by red squares). As expected the intensity decreases from left to right (dark red to light red to blue) indicating a decrease in the intensity of the delivered radiation dose. Specifically, the predictions made by the gel nanosensor of ≈2Gy in the irradiated region were in excellent agreement with the treatment planning system and the radiochromic film. The gel nanosensor also predicts minimal radiation dose (≈0.1Gy) outside the irradiation region illustrating its capability it predicting topographical dose profiles. The gel nanosensor predicts the irradiated and the non-irradiated region effectively and the performance is comparable to the predictions of a conventional radiochromic film (**Figures 7.13 E and 7.13 F**).

A

B

C

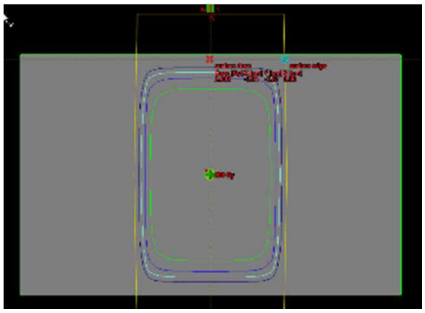

D

2.0	2.0	2.0	2.0	1.6	0.9	0.3	0.1	0.1
2.0	2.0	2.0	2.0	1.6	0.9	0.3	0.1	0.1
2.0	2.0	2.0	2.0	1.6	0.9	0.3	0.1	0.1
2.0	2.0	2.0	2.0	1.6	0.9	0.3	0.1	0.1
2.0	2.0	2.0	2.0	1.6	0.9	0.3	0.1	0.1
2.0	2.0	2.0	2.0	1.6	0.9	0.3	0.1	0.1
2.0	2.0	2.0	2.0	1.6	0.9	0.3	0.1	0.1
2.0	2.0	2.0	2.0	1.6	0.9	0.3	0.1	0.1
2.0	2.0	2.0	2.0	1.6	0.9	0.3	0.1	0.1

E

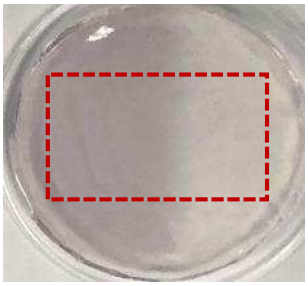

2.4	2.2	2.2	1.9	1.1	0.1	0.0	0.1	0.1
2.2	2.1	2.0	1.7	0.6	0.0	0.0	0.1	0.1
2.1	2.0	2.0	1.8	1.0	0.2	0.0	0.0	0.1
2.1	2.0	2.0	1.7	0.7	0.2	0.1	0.0	0.1
2.2	2.0	2.0	1.9	1.1	0.1	0.0	0.1	0.1
2.0	2.0	2.0	1.9	0.8	0.0	0.0	0.1	0.1
2.1	2.0	2.0	1.9	1.3	0.1	0.1	0.1	0.2
2.3	2.1	2.1	2.0	1.0	0.1	0.1	0.1	0.1
2.4	2.4	2.4	2.1	1.2	0.4	0.2	0.1	0.3

F

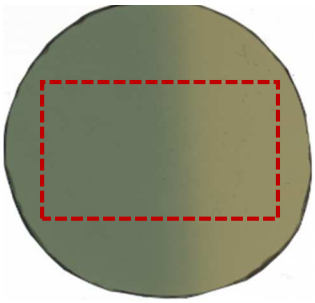

2.2	2.2	2.3	2.1	1.5	0.5	0.2	0.1	0.0
2.2	2.2	2.2	2.1	1.5	0.5	0.1	0.1	0.0
2.2	2.2	2.2	2.1	1.5	0.5	0.1	0.0	0.0
2.2	2.1	2.1	2.1	1.5	0.5	0.1	0.1	0.0
2.2	2.1	2.2	2.1	1.6	0.5	0.1	0.0	0.0
2.2	2.2	2.1	2.0	1.5	0.5	0.1	0.0	0.0
2.1	2.2	2.1	2.0	1.5	0.6	0.2	0.0	0.0
2.0	2.2	2.1	2.1	1.6	0.7	0.1	0.0	0.0
2.0	2.1	2.1	2.0	1.6	0.7	0.1	0.0	0.0

Figure 7.13 Representative image of **(A)** half the gel nanosensor and **(B)** half the radiographic film positioned in the radiation field on patient A. **(C)** Treatment planning software depicting the delivery of a 2 Gy dose delivered to the surface of patient A. **(D)** The expected dose fall-off profile of 2 Gy inside the radiation field and a minimal radiation (0.1 Gy) outside the field. A color change is visible clearly in both the **(E)** gel nansensor whose color changes to maroon and **(F)** radiographic film whose color changes to dark green post-irradiation. The dose map of the predicted dose for both the gel nanosensor and radiographic film is depicted below each corresponding sensor (please see the Experimental section). The dose profiles are similar indicating the efficacy of the gel nanosensor for clinical dosimetry. The time for readout of the gel nanosensor was 1 hour while the radiochromic film required >24 hours prior to readout. The experiments were performed 3 times independently for the gel nanosensor and the radiographic film.

Patient B received a fractionated dose of 3 Gy at the target tumor site on the surface of skin (**Figures 7.14**) and 1.5 Gy on the surface above the bolus. A visible change in color was observed over the entire gel, which was placed underneath the bolus (**Figure 7.14 F**). The gel nanosensor estimates a core uniform dose of ≈2.8 Gy, which closely matches the estimate made by the radiochromic film (≈3.2Gy). It is important to note that the time required for color development and evaluation of the radiochromic film was >24hours, which contrasts to that for the gel nanosensor which was only ~1 hour. In addition, it is possible to generate tissue-conformal formulations with the gel nanosensor, which is difficult with the more rigid radiographic films. To capture the topographical profile of the administered dose, half the gel nanosensor was placed on top of the bolus and exposed to radiation. As expected, the irradiated region turned maroon while the non-irradiated area remained colorless (**Figure 7.14 H**). The core of the irradiated region was estimated to receive a dose of ≈1.7 Gy as is closely predicted by the radiochromic film (≈1.4Gy). The regions outside the irradiated region received minimal dose (≈0 Gy) as predicted by the gel nanosensor, which closely matches the predictions of the radiochromic film. Using the gel

nanosensor, we were able to independently corroborate the efficacy of the treatment plan used to treat Patient B. All these results taken together, along with the simplicity in fabrication with minimal equipment requirement, operation, readout and cost effectiveness (≈5 cents per gel; only material cost considered) demonstrates the translational potential of the colorimetric gel nanosensor for detecting and predicting topographical radiation doses in clinical radiotherapy.

A

B

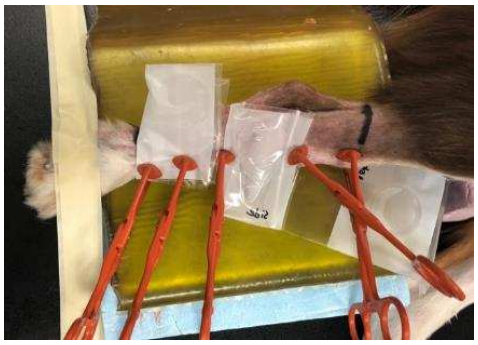

C

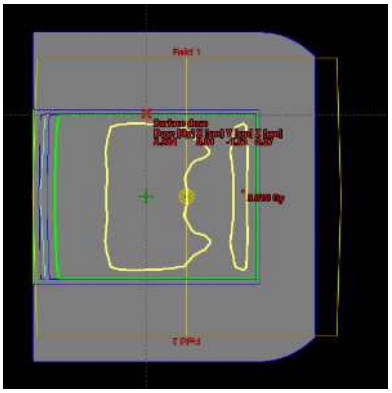

D

3.0	3.0	3.0	3.0	3.0	3.0	3.0	3.0	3.0	3.0
3.0	3.0	3.0	3.0	3.0	3.0	3.0	3.0	3.0	3.0
3.0	3.0	3.0	3.0	3.0	3.0	3.0	3.0	3.0	3.0
3.0	3.0	3.0	3.0	3.0	3.0	3.0	3.0	3.0	3.0
3.0	3.0	3.0	3.0	3.0	3.0	3.0	3.0	3.0	3.0
3.0	3.0	3.0	3.0	3.0	3.0	3.0	3.0	3.0	3.0
3.0	3.0	3.0	3.0	3.0	3.0	3.0	3.0	3.0	3.0
3.0	3.0	3.0	3.0	3.0	3.0	3.0	3.0	3.0	3.0
3.0	3.0	3.0	3.0	3.0	3.0	3.0	3.0	3.0	3.0
3.0	3.0	3.0	3.0	3.0	3.0	3.0	3.0	3.0	3.0

E

	0.1	0.1	0.4	0.9	1.3	1.5	1.5	1.5	
0.1	0.1	0.1	0.4	0.9	1.3	1.5	1.5	1.5	1.5
0.1	0.1	0.1	0.4	0.9	1.3	1.5	1.5	1.5	1.5
0.1	0.1	0.1	0.4	0.9	1.3	1.5	1.5	1.5	1.5
0.1	0.1	0.1	0.4	0.9	1.3	1.5	1.5	1.5	1.5
0.1	0.1	0.1	0.4	0.9	1.3	1.5	1.5	1.5	1.5
0.1	0.1	0.1	0.4	0.9	1.3	1.5	1.5	1.5	1.5
0.1	0.1	0.1	0.4	0.9	1.3	1.5	1.5	1.5	1.5
0.1	0.1	0.1	0.4	0.9	1.3	1.5	1.5	1.5	1.5
	0.1	0.1	0.4	0.9	1.3	1.5	1.5	1.5	

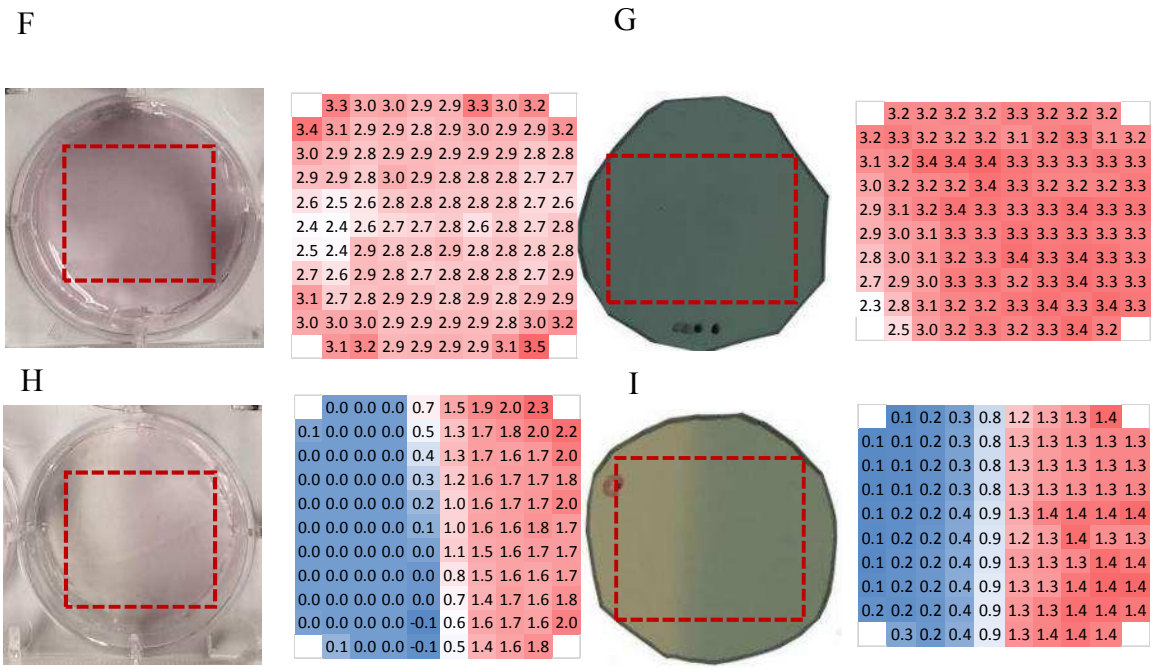

Figure 7.14 (A) Representative image of the final setup of Patient B. Half the gel nanosensor and the Gafchromic EBT3™ film is placed on the radiation field on top of the bolus which was delivered a radiation dose of 1.5Gy (Image does not contain the gel nanosensor and the Gafchromic EBT3™). **(B)** Representative image of the gel nanosensor placed on the treated region which was delivered a radiation dose of 3Gy. **(C)** Treatment planning software depicting the delivery of a 3Gy dose delivered to the skin of patient B. **(D)** The expected dose delivered to the skin of the patient and **(E)** surface dose (1.5cm above the bolus). A color change is visible clearly in both the **(F)** gel nansensor to pink/maroon **(G)** radiographic film to dark green post-irradiation. The heat map of the predicted dose for both the gel nanosensor and radiographic film is depicted below each corresponding sensor(See experimental section). The dose profiles are similar in all cases indicating the efficacy of the gel nansensor to clinical dosimetry. The time for readout of the gel nanosensor was 1 hour while the radiochromic film required >24 hours prior to readout. The experiments were performed 3 times independently for the gel nanosensor and the radiographic film.

7.4 Conclusions

To our knowledge, this is the first demonstration of a colorimetric gel nanosensor for detecting and distinguishing regions exposed to irradiation. The addition of a chemical quenching agent, sodium sulfide, reveals topographical dose distribution obtained during clinical radiotherapy. We also demonstrated the ability of the gel nanosensor to respond to varying levels of ionizing radiation by tuning the concentration of the surfactant used and time of addition of the quenching agent. Various simple and complex motifs were patterned on the gel nanosensor illustrating the ability of the sensor to capture dose profiles obtained in fractionated clinical radiotherapy. The effectiveness of the sensor was evaluated for predicting complex topographical dose profiles delivered to an anthropomorphic head and neck phantom. The efficacy of the colorimetric gel nanosensor was demonstrated for visualizing and quantifying topographical dose distribution in live canine patients. The effectiveness of the gel nanosensor was comparable to Gafchromic EBT3™ films, which required more than 24 hours before readout, indicating significant advantages of the former. The ease of fabrication, simple operation procedures that require only a spectrophotometer without any sophisticated training, rapid and stable readout, possibility of formulating tissue-conformal geometries and relatively low cost (≈$0.50 per gel nanosensor only material cost considered) indicate the high disruptive and translational potential of the gel nanosensor technology for determining complex topographical dose distribution profiles in clinical radiotherapy. It is anticipated that clinical adoption of the gel nanosensor technology for determining topographical dose distributions in tissues will lead to improved patient safety and outcomes.

Chapter 8 MOLECULAR ENGINEERING OF AN AMINO ACID DOSIMETER FOR CLINICAL RADIOTHERAPY

8.1 Introduction

Approximately three new cases and one mortality are reported due to cancer every minute in the US[272]. Despite promising advances in therapeutic interventions, radiotherapy remains a mainstay of clinical intervention for several cancers. Nearly two-thirds of patients receive some form of radiation as treatment[273]. The primary intention of curative radiotherapy is twofold: to deliver a high and uniform dose to the target lesion to achieve local tumor control while simultaneously minimizing the dose to normal tissue to avoid long term complications to the patient[243]. To manage safe and accurate dose delivery to the patient, radiotherapy relies on dosimetry for optimization of prescribed dose during treatment. Human error, equipment failures and faulty operating procedures could potentially lead to inaccurate dosing leading to morbidity in patients. Dynamically changing radiation fields and smaller beam sizes, have introduced new challenges for routine dosimetry and quality assurance[274]. A change in paradigm in accurate dosimetry is necessary not only for treatment optimization but also for radiation protection of the patient.

The available dosimeters are not sufficient for many clinical applications especially to provide accurate radiation dose information with minimal post processing. Thermoluminescent dosimeters have attracted attention but their routine use is challenging due to its labor intensive operation and extensive training required prior to their operation[220]. Silicon diode detectors response are subject to design and the operating

environment making them unreliable for periodic operation[275]. In addition, current dosimeters are not compliant to conform to the human anatomy routinely encountered during radiotherapy. Polymer gel dosimeters have a much better tissue conformity, but toxic components involved in fabricating the sensor and the requirement of sophisticated readout techniques like MRI have prevented their clinical translation[252]. Due to the limitations of existing sensors, there is an unmet need to develop a new and effective dosimeter that ensures accurate predictions of prescribed dose along with ease of operation.

Molecular and nanoscale systems offer unrealized potential for the development of dosimeters that could lead to simple yet effective approaches for detecting therapeutic levels of ionizing radiation[161]. Quantum dots have demonstrated a strong scintillation response upon exposure to ionizing radiation but current synthesis techniques result in batch-to-batch variations making them unreliable as a dosimetry standard[276]. Investigation of carbon nanotubes as active transducers for the detection of gamma-ray radiation lack the sensitivity towards therapeutic levels of ionizing radiation restricting their applicability in the clinic[277]. Metal organic framework as scintillators have limited applicability due to the toxicity of metal ions used during development and fabrication[278]. In light of these disadvantages, there is still a need to develop a robust yet simple dosimeter that is easy to fabricate which could potentially provide additional safeguards during clinical radiotherapy.

The unique properties associated with the size and shape of gold nanoparticles has facilitated its widespread use in chemical and biological sensing[253]. We have recently pioneered the development of a sensor based on the formation of gold nanoparticles from its colorless precursor salt solution upon exposure to therapeutic levels of radiation[162, 229, 256]. Although this is a powerful approach, it is limited in its translational due to the use of toxic functional components like cationic surfactants[279]. In order to relieve concerns regarding potential toxicity during handling and application over a patient, we have developed the first biocompatible sensor to detect radiation by employing amino acids to perform a similar function as that of the cationic surfactant. We have also employed the developed sensor to detect prescribed dose delivered to a canine patient which is a first based on our understanding of the literature.

8.2 Materials and Methods

Materials. Gold (III) chloride trihydrate ($HAuCl_4$, $3H_2O$), 20 natural amino acids, glutathione, β-alanine, m-Fluoro-DL-phenylalanine, 5-aminovaleric acid, L-ornithine monohydrochloride were purchased from Sigma-Aldrich. N-Acetyl-L-cysteine was purchased from Fisher chemicals. 4-aminobutyric acid was purchased from Acros organics. D-Valine, D-Aspartic acid, D-Leucine, D-Threonine, D-Aspartame and D-Phenylalanine were purchased from Alfa-Aesar. All chemicals were used as received from the manufacturer without additional purification. MilliQ water (18.2 MΩ-cm) was used as a solvent unless otherwise specified.

Sample Preparation for Primary Screening. For the primary screening, 30µL of 10 mM amino acids were mixed with 30µL of 1 mM $HAuCl_4 \cdot 3H_2O$. To this mixture 940µL MilliQ water (18.2 MΩ-cm) was added and the final pH of the precursor solution was around ~6. Samples were prepared at Banner-MD Anderson Cancer Center, Gilbert, AZ prior to radiation.

Irradiation of Samples. A Varian TrueBeam linear accelerator was used to irradiate samples at a dose rate of 600 MU/min with a 6MeV photon energy at Banner-MD Anderson Cancer Center, Gilbert, AZ. The final delivered dose to samples are mentioned in the manuscript and in their respective figure captions. After irradiation the samples were transported back to Arizona State University in Tempe, AZ for analysis.

Absorbance Spectroscopy to Evaluate the Primary Screen. UV-Visible absorbance profiles of the samples were measured using a BioTek Synergy 2 plate reader. Absorbance values from 150 µL of each sample were measured from 300 to 900 nm with a step size of 10 nm in a 96 well plate. Nanopure water (18.2 MΩcm) was used as a blank in all cases. The absorbance value was further offset by subtracting A_{900}. The maximum absorbance between 500 and 600nm was used to determine the as a pseudo indicator to characterize the yield of nanoparticles.

Hydrogel synthesis for radiation experiments. L-(-)-Phenylalanine (25 μL of 25 mM) was incubated with gold (III) chloride trihydrate (30 μL of 10 mM) for 15 mins in Eppendorf tubes. In the meantime, a clear solution of 1 % w/v agarose is prepared through heating. This heated liquid agarose (750 μL) was mixed with the gold-phenylalanine mixture. From this resulting mixture, 700 μL was allowed to set in prefabricated circular molds (~1.5 cm diameter & ~3 mm thickness). Prior to irradiation, 400 μL of 10 mM L-(-)-Tryptophan is incubated on the preformed hydrogel to diffuse into the gel for five mins. These transparent hydrogel discs were used for subsequent irradiation studies. Glutathione (700 μL of 5 mM) was incubated on the irradiated gels after 10mins upon completion of radiation. Absorbance was recorded 1 hour after radiation exposure.

Irradiation of Hydrogels. A Varian Truebeam linear accelerator radiation therapy system at the Banner M.D. Anderson Cancer Center in Gilbert, AZ delivering a 6 MeV photon beam was used for irradiation at a dose rate of 600 MU/min. The samples were irradiated with doses of 1, 2, 3, 4, 5, 6 and 7.5 Gy.

Absorbance Spectroscopy to Evaluate the Hydrogel Nanosensor. A BioTek Synergy 2 plate reader was used to measure the absorbance profiles for all irradiated and control gel samples. Absorbance was recorded between 300 nm and 990 nm with a step size of 10 nm. The characteristic plasmonic absorption peak observed at 530 nm is used to identify the presence of gold nanoparticles.

Generation of Calibration Curve using UV-Visible Absorbance. To generate the calibration curve, the absorbance at 530nm is subtracted from the absorbance at 990nm from the previously generated UV-Visible spectrum. The final absorbance of the non-irradiated hydrogel (0Gy) is further offset from itself and the absorbance of the irradiated hydrogels. These final absorbance values are plotted as a function of radiation dose and is used to generate the calibration curve.

NMR Spectroscopy. NMR samples were prepared by dissolving the corresponding amino acid (L-alanine, L-phenylalanine, D-phenylalanine) and Gold (III) chloride trihydrate salt in 1:1 DMSO-D_6 and D_2O mixture. Final concentration of the pure amino acid solution used for ^1H NMR spectra was 0.78 mM. The final concentration used for ^1H NMR for the mixture of amino acid and chloroauric acid was 0.78 mM and 0.37 mM respectively. A Varian 500 MHz NMR instrument was employed in these studies to collect ^1H NMR data.

Sample preparation for Transmission Electron Microscopy. 1,2-propane diol (chaotropic agent) was added to the hydrogels and dissolved by heating to 80 °C for 15 minutes. This mixture was centrifuged at 4000 rpm for 10 mins. The supernatant was removed and was further dispersed in MilliQ water. The transmission electron microscopy samples were prepared by drop casting this solution onto the TEM grids. The samples were air dried overnight and visualized using a CM200-FEG instrument operating at 200 kV in the LeRoy Eyring Center for Solid State Sciences at ASU.

Cell culture using BJ5ta Human fibroblast cell line. BJ5ta human fibroblast cells were used to assess the toxicity levels of the irradiated and non-irradiated gel sensors. Cells were sub-cultured in DMEM containing 10% fetal calf serum from a cryo-stock, until they were at least 70%–80% confluent. 3 mL trypsin was added to detach the cells from the surface of the culture flask. Culture flasks were further incubated at 37 °C for five minutes and cell detachment was verified under the microscope. Once the cells were detached, 7 mL DMEM was added to dilute trypsin and were transferred to a sterile centrifuge tube. The tube was centrifuged at 800 rpm for 5 minutes followed by dilution with culture medium to attain a desired cell density. Quantification was achieved using a hemocytometer. 24-well plates containing non-irradiated and irradiated (at 5 Gy) gels were seeded with above cell suspension, resulting in 100,000 cells in each well. Pure agarose gels were used as a control for determining the toxicity of our nanosensor. The plates with cells were incubated at 37 °C in a humidified atmosphere (5% CO_2/95% O_2) for 24 hours. After 24 hours standard procedures for live-dead assay and XTT assay were followed to quantify the cytotoxicity.

Evaluation of Hydrogel Toxicity Using Live-Dead Assay. 5µL calcein and 20µL ethidium homodimer-1 to 10ml of cell culture media. After 24 hours of cell seeding, the cell culture media from the well plate is removed and replaced with 1ml of the Live/Dead assay mixture. The cells were incubated for 1 hour. After staining, samples were washed and observed using Evos FL Auto Live Cell Imaging System.

.

Evaluation of Hydrogel Toxicity Using XTT Assay. After 24 hours, the cells were transferred to a sterile tube. The tube was centrifuged at 800 rpm for 5 minutes and the culture medium was removed and replaced with serum free media. XTT labeling mixture was added to the serum free media and incubated for 4 hours prior to analysis. The absorbance at 475 and 660nm was determined using a plate reader (Bio-Tek Synergy 2). The value of $A_{475} - A_{660}$ was evaluated. The relative cell viability was calculated from test/control x 100% where test and control are the offset absorbance values of the agarose hydrogel containing the gold-amino acid mixture and pure agarose hydrogel.

Gel Dosimetry in an Anthropomorphic Thorax Phantom. All phantom experiments were carried out at the Banner M.D. Anderson Cancer Center in Gilbert, AZ. A CIRS tissue equivalent thorax phantom was aligned on a Philips RT CT table with aligning lasers. The hydrogel nanosensor is positioned in the middle of the radiation field and a known dose of 3 Gy dose was delivered to the skin of the phantom. The change in color post-irradiation is evaluated using UV-Visible spectroscopy. The final absorbance values are calculated as previously mentioned and the radiation delivered is predicted using the calibration curve.

Institutional Animal Care and Use Committee (IACUC). Prior to canine experiments, the experimental protocol that would be performed on the canine patient was documented and approved by ASU's IACUC. A consent form approved by ASU's IACUC was signed by the pet owner prior to any experiment conducted.

Canine experiments. A canine patient being treated using radiotherapy was selected in the pilot study. A fractional dose of 3 Gy was delivered each day to the region being treated. A 1.5cm bolus is placed on top of the patient. Our gel nanosensor was placed on top of the bolus and exposed to the prescribed ionizing radiation dose from a Varian Trilogy linear accelerator radiation therapy system. All canine experiments were performed at the Arizona Veterinary Oncology Center in Gilbert, AZ (approx. 14 miles distance from ASU) with owner's approval. Similar to the placement of the hydrogel nanosensor, a NanoDOT™ was also placed on top of the bolus. The NanoDOT™ was used to evaluate the performance of our hydrogel sensor. The change in color post-irradiation is evaluated using UV-Visible spectroscopy. The final absorbance values are calculated as previously mentioned and the radiation delivered is predicted using the calibration curve.

Image Processing. All images were acquired using an Iphone 7S plus camera under suitable lighting and automatic settings. The images were cropped to the desired size for representation. No further editing was carried out on the pictures reported here.

Statistical Analyses. All irradiation experiments were carried out a minimum of three times independently unless otherwise mentioned. The results are expressed as mean ± standard deviation. All the calculations were carried out using Microsoft Excel 2016.

8.3 Results and Discussion

Facile radiation sensors are required to ensure the accurate delivery of high radiation dose to the target region whilst minimizing radiation to the healthy surrounding tissue. Here, we show the development of a biocompatible plasmonic hydrogel based nanosensor as a simple colorimetric reporter for therapeutic levels of ionizing radiation. Prior to the development of the hydrogel nanosensor, a library of 32 amino acids and their derivatives were screened for their gold nanoparticle formation efficacy in order to identify the lead amino acid which would then be later used to develop the nanosensor. The preliminary screen was carried out with $HAuCl_4$: amino acid (Molar ratio of 1:10) at a radiation dose 325 Gy (**Figure 8.1**). In the current system reduction of Au^{3+} ions to Au^0 occurs through a free radical mechanism. Ionizing radiation (X-Rays) splits water into three major free radical components namely $H^{\cdot}$, $OH^{\cdot}$ and e^-_{aq}. These short-lived solvated electrons and hydrogen free radicals facilitate the reduction processes to Au^0. Successful reduction to Au^0 followed by nucleation and growth leads to mature nanoparticles stabilized by amino acids. Upon exposure to irradiation, the nanoparticle yields were measured 2 hours and 6 hours post irradiation and were compared with control experiments (0Gy) to establish increased nanoparticle formation.

A

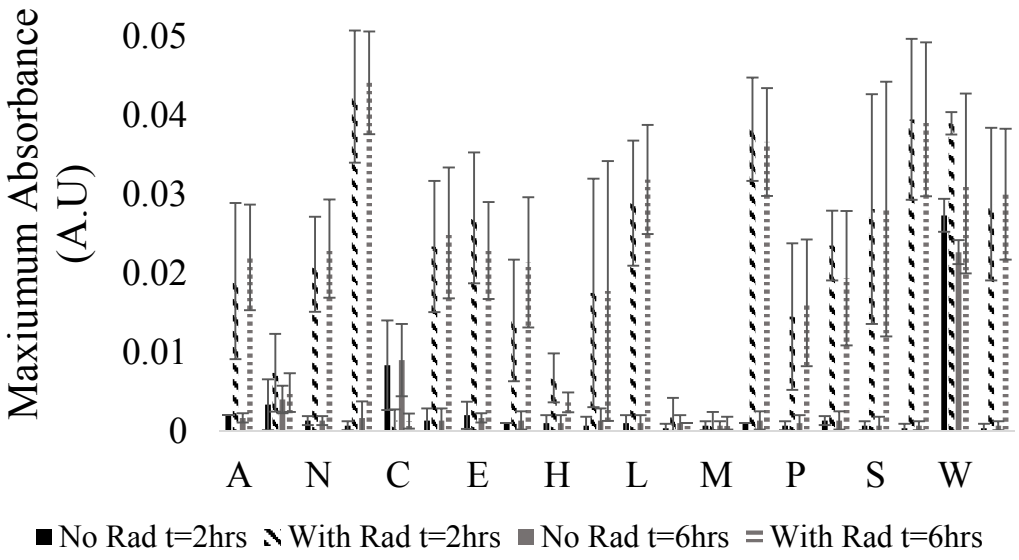
Maxiumum Absorbance (A.U)
0.05
0.04
0.03
0.02
0.01
0
A
N
C
E
H
L
M
P
S
W
No Rad t=2hrs
With Rad t=2hrs
No Rad t=6hrs
With Rad t=6hrs

B

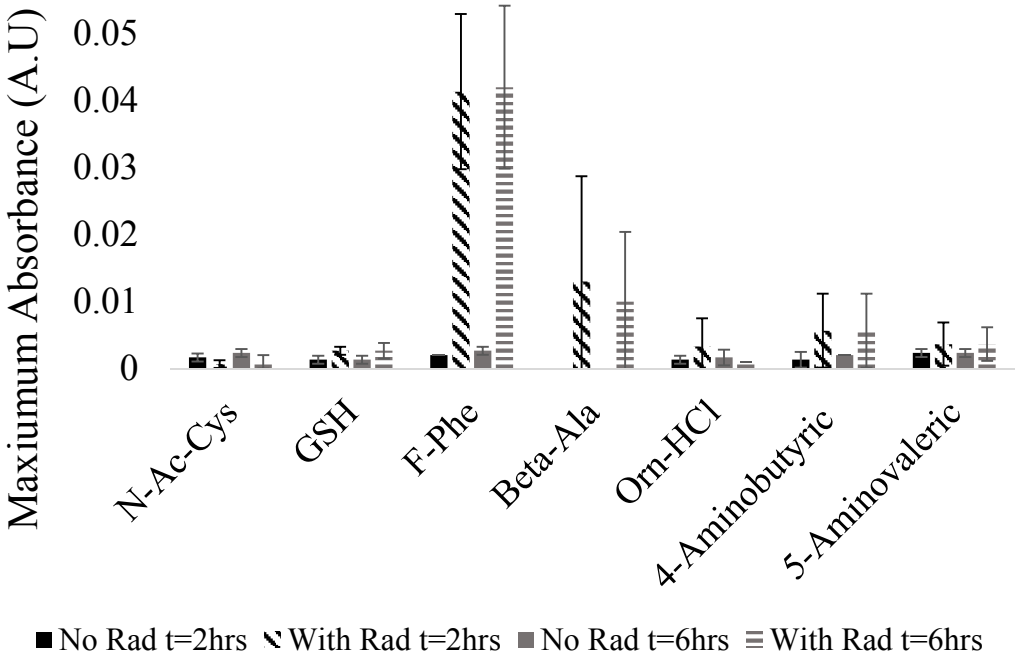
Maxiumum Absorbance (A.U)
0.05
0.04
0.03
0.02
0.01
0
N-Ac-Cys
GSH
F-Phe
Beta-Ala
Orn-HCl
4-Aminobutyric
5-Aminovaleric
No Rad t=2hrs
With Rad t=2hrs
No Rad t=6hrs
With Rad t=6hrs

C

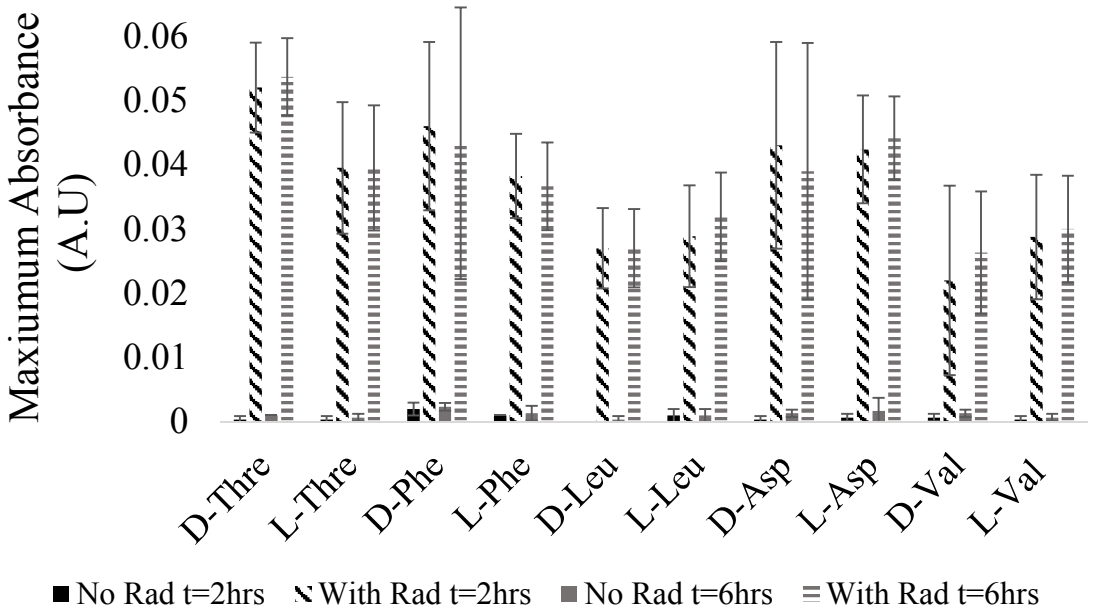

Figure 8.1 Maximum absorbance proportional to concentration of gold nanoparticles following irradiation of 325 Gy measured at discrete time intervals. Black: 0 Gy and 2 hours post irradiation, Black diagonal stripes: 325 Gy and 2 hours post irradiation, Dark Yellow: 0 Gy and 6 hours post irradiation, Dark Yellow Horizontal stripes 325 Gy and 6 hours post irradiation.

Among the screened amino acids, tryptophan readily reduces chloroaurate ions to gold nanoparticles in the absence of irradiation. The reduction propensity of tryptophan involves oxidation of the indole moiety leading to spontaneous reduction of metal ions[280]. A significant increase in absorbance is not observed upon incidence of ionizing radiation suggesting that the bulk of the reduction is carried out by tryptophan. Cysteine, methionine, N-acetyl cysteine and glutathione form an important class of amino acids containing a thiol or thioether functional group in the side chain[281]. Choloroaurate ions being soft lewis acids show high affinity towards ligands containing a sulfur donor atom. This allows for the

formation of a stable metal complex. Histidine similarly forms a stable metal complex through their α-amino nitrogen[282]. We expect the complexation of these amino acids with choloraurate ions to decrease the redox potential making the metallo-complex inactive towards the radiolysis generated reducing species[112]. Positively charged amino acids (arginine and lysine) do not exhibit nanoparticle formation tendency in the presence of ionizing radiation. We hypothesize that these positively charged ligands do not effectively chelate the metal center due to charge repulsion and a certain degree of complexation is required to initiate the reduction process in the presence of ionizing radiation[112].

Radiotherapy involves complex treatment plans to deliver curative levels of radiation to the target (2-5Gy) and simultaneously reduce radiation induced toxicity to healthy tissues. The potential benefit of these are improvement in survival rates and quality of life post treatment. Poor treatment planning and delivery could lead to an opposite adverse outcome. There is a need for a robust dose verification system, which can be fabricated in house requiring minimal training to operate. Towards this effort, we propose a sensor that changes color upon exposure to ionizing radiation and the intensity of color developed will qualitatively and quantitatively report for the intensity of radiation dose. Five amino acids including phenylalanine, aspartic acid, valine, leucine and threonine were identified as lead candidates from the screen and were evaluated for their ability to template gold nanoparticles at lower radiation levels (0, 5, 25, 50, 100 and 200Gy) **(Figure 8.2 A)**. Among these five lead amino acid candidates, phenylalanine exhibited the highest nanoparticle templating efficacy and synergistic effects were not observed when phenylalanine was employed in concert with other leads amino acids or as a dipeptide

(aspartame) **(Figure 8.2 B)**. Phenylalanine was chosen as the lead candidate to facilitate the development of the hydrogel nanosensor. To facilitate handling and application concerns associated with liquid sensor systems, phenylalanine was integrated in an agarose hydrogel matrix prior to irradiation. Irradiation of the gold alone hydrogel or the gold-phenylalanine hydrogel with 7.5Gy displayed minimal tendency to form gold nanoparticles based on the absence of the characteristic maroon/pink color associated with gold nanoparticles (**Figure 8.3**). To facilitate reduction in the presence of ionizing radiation, tryptophan that could reduce and template gold nanoparticles spontaneously was supplemented externally to the gold-phenylalanine hydrogel. Interestingly, in the presence of phenylalanine, gold nanoparticle formation tendency is hindered when compared to the only gold hydrogel control. We deliberate that in such quasi-equilibrium conditions, therapeutic levels of ionizing radiation would be sufficient to reduce chloroauric acid to gold nanoparticles. Indeed, the appearance of the maroon/pink color associated with gold nanoparticles upon exposure to 7.5Gy suggests the use of the hydrogel as a colorimetric sensor for detection of therapeutic levels of ionizing radiation. All these results taken together, we rationalize the need for Au (III), phenylalanine and tryptophan.

A

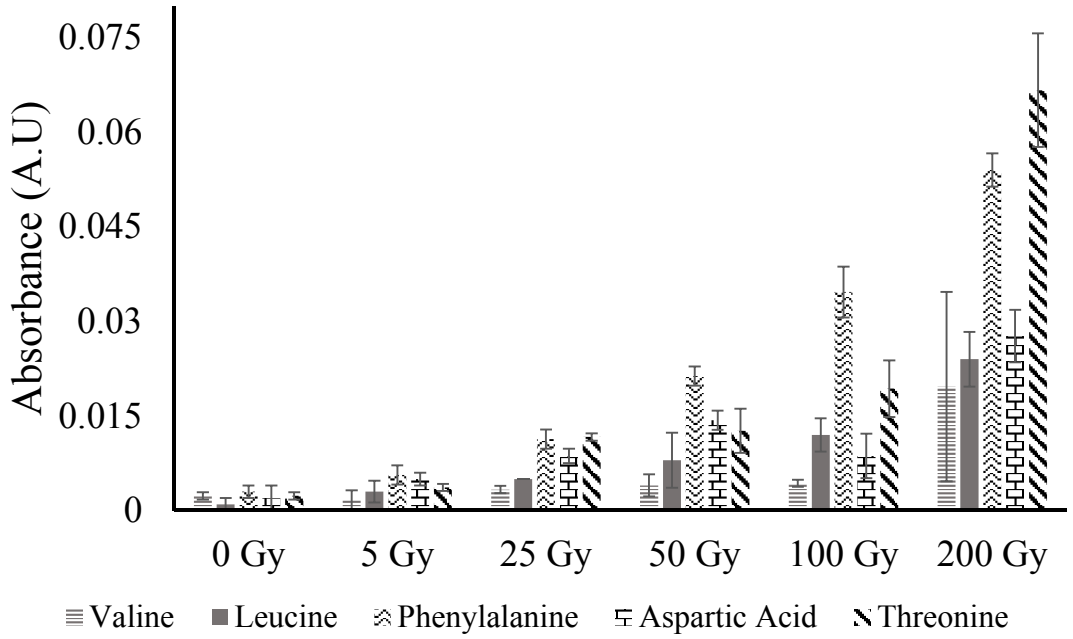

B

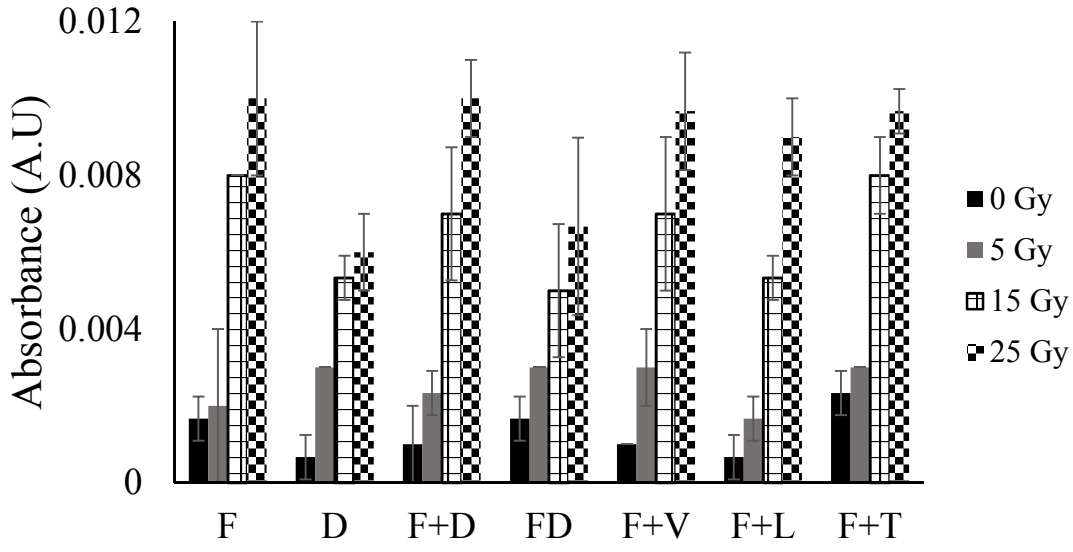

Figure 8.2 (A). Maximum absorbance as a function of radiation dose for the lead amino acids. Gold stripes: valine (V), Gold solid: leucine (L), black wavy: phenylalanine (F), black brick: aspartic acid (D), black diagonal: threonine. **(B).** Maximum absorbance as a function of radiation dose. Amino acids employed for the study Phenylalanine (F), aspartic acid (D), valine (V), leucine (L), threonine and Aspartame (FD). All absorbance measurements were carried out 2 hours post irradiation.

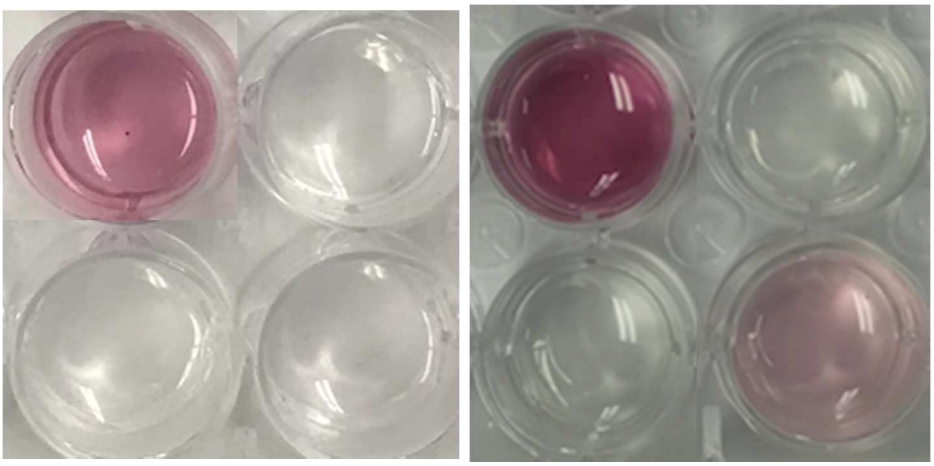

0 Gy 7.5 Gy

Figure 8.3 Representative images of the agarose hydrogel containing various combinations of Au^{3+}, L-Phenylalanine and Tryptophan following irradiation with 0 Gy and 7.5 Gy. Each hydrogel has the following combination, Au^{3+} + Tryptophan (Top Left), Au^{3+} + Phenylalanine (Top Right), Only Au (Bottom Left) and Au^{3+} + Phenylalanine + Tryptophan (Bottom Right). There is a clear visual change in the system containing all three components in case of 7.5 Gy and no change in color in the absence of radiation. These indicate the requirement of tryptophan for irradiation induced gold nanoparticles formation. The Au^{3+} tryptophan system forms gold nanoparticles spontaneously in the absence of radiation (0Gy).

We carried out experiments to investigate delayed nanoparticle kinetics in the presence of phenylalanine. We hypothesized that the electron rich phenyl side chain of phenylalanine is involved in electrostatic interaction with the indole moiety of tryptophan, responsible for the spontaneous reduction of chloroaurate ions. To evaluate the role of the phenyl ring in protecting gold ions against spontaneous reduction in the presence of tryptophan glycine, (L)-phenylalanine, (D)-phenylalanine and (L)-alanine were incorporated in an agarose matrix along with chloroauric acid. In the presence of chloroauric acid alone and hydrogels

containing glycine-chloroauric acid and (L)-alanine-chloroauric acid, tryptophan was adequate to reduce Au(III) to nanoparticles within 10 minutes **(Figure 8.4)**. This is can be visually observed through the development of a pink color from the previously colorless hydrogel. However in the presence of a phenyl ring containing amino acids there is a noticeable delay in color development (20 mins). To investigate further the presence of a free phenyl ring in the presence of chloroaurate ions, we probed L-phenylalanine and a mixture of L-phenylalanine and chloroaurate ions through ^{1}H NMR. **(Figure 8.5 A and 8.5 B)**. The absence of peak shifts in the side chain phenyl protons coupled with downfield shifts in the chiral proton(H-α) and CH_2 protons(H-β) indicate minimal interaction between the phenyl ring and chloroaurate ions. Similar peak shifts were observed in structurally similar molecules to phenylalanine including alanine and D-phenylalanine (**Figure 8.5 C-8.5 F**). These results taken together suggest the presence of a free phenyl ring, which could potentially inhibit spontaneous nanoparticle formation in the presence of tryptophan. Additionally, the gold-phenylalanine-tryptophan hydrogel was incubated with glutathione post-irradiation to sequester the unreacted gold ions through the formation of stable-metal complex inhibiting spontaneous nanoparticle formation in the absence of radiation (**Figure 8.6, 8.7**). This formulation would constitute the plasmonic nanosensor for further experiments.

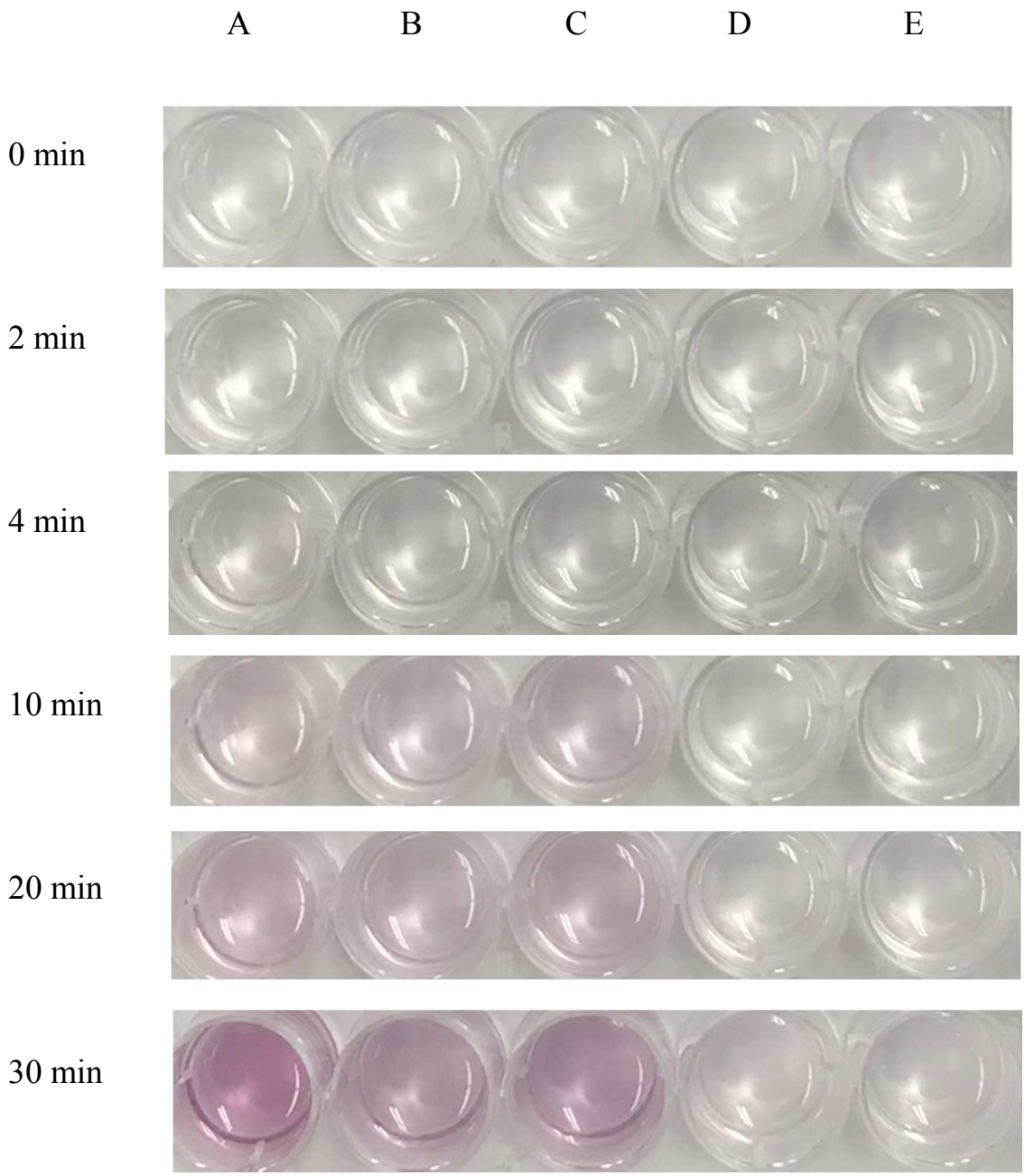

Figure 8.4 Optical images of agarose hydrogel containing mixtures of chloroauric acid with (A) no additive, (B) glycine, (C) alanine, (D) D-phenylalanine, and (E) L-phenylalanine. After addition of tryptophan, a visual change in color is observed within 4 minutes in case of hydrogels containing no amino acid and amino acids without a phenyl ring i.e. in A, B, C. In the presence of amino acids containing the phenyl ring, a faint visual change in color is observed after 20 minutes (D and E).

(A) L-Phenylalanine

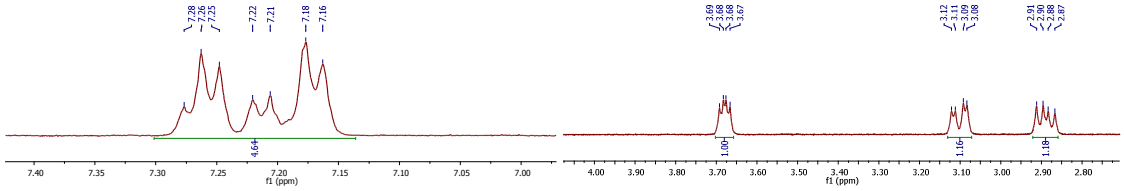

(B) Chloroauric acid + L-Phenylalanine

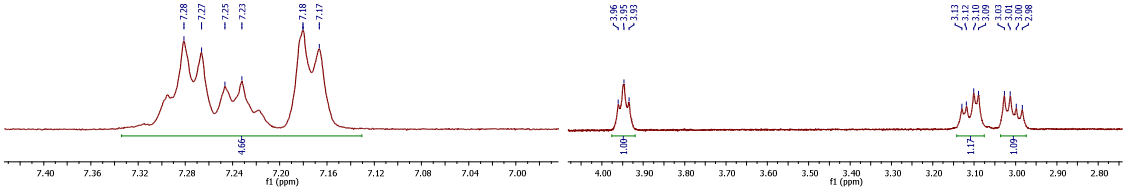

(C) D-Phenylalanine

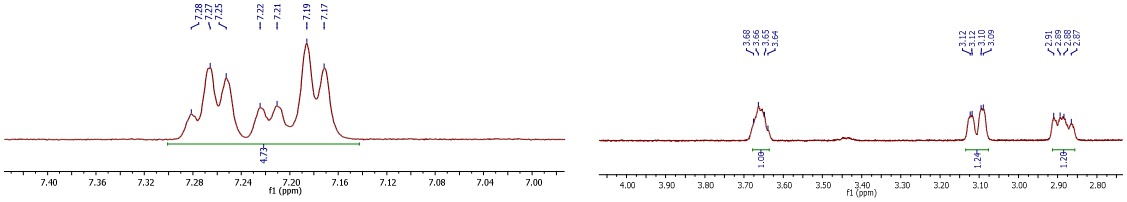

(D) Chloroauric acid + D-Phenylalanine

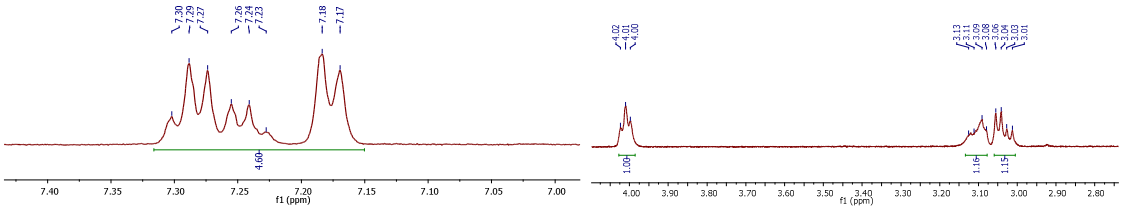

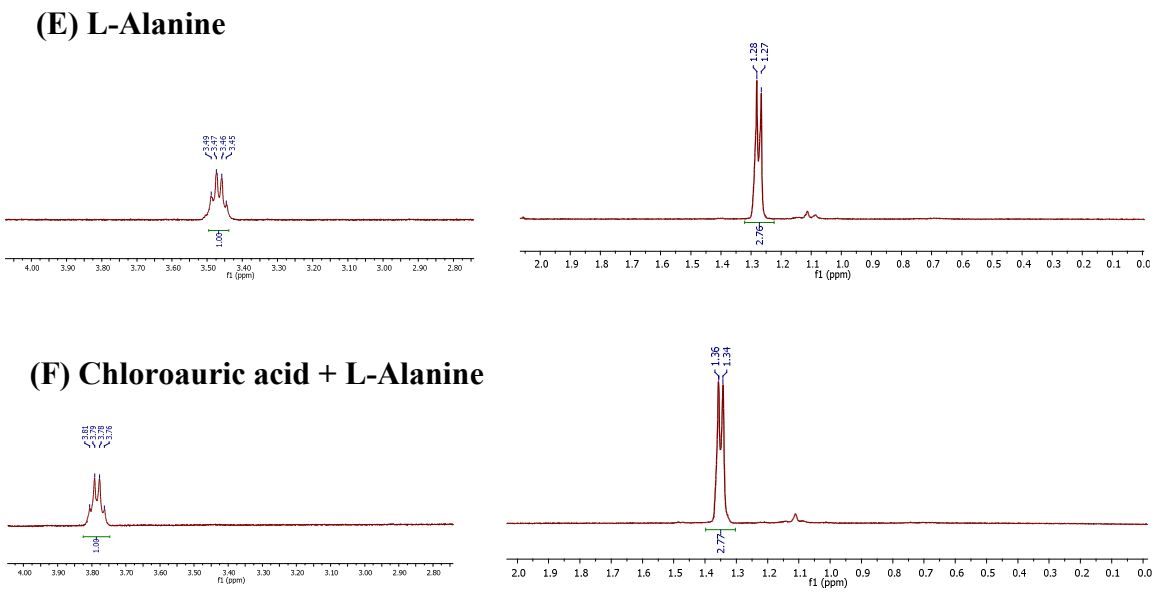

Figure 8.5 ^{1}HNMR spectra between pure amino acids and a mixture of amino acid and chloroauric acid. ^{1}H NMR spectra of **(A)** pure (L)-phenylalanine, which indicates a multiplet peak at ∂7.22 ppm for phenyl ring protons; a doublet of doublet peak at ∂3.68 ppm for the chiral proton (H-α) and two doublet of doublet peaks at ∂3.10 ppm & ∂2.89 ppm for the diastereotopic CH_2 protons (H-β), **(B)** a mixture of L-phenylalanine with chloroauric acid, which shows a downfield shift in the chiral proton (H-α) to ∂3.95 ppm as a triplet and CH_2 proton (H-β) peaks appear at ∂3.11 & ∂3.01 ppm merged with each other. Minimal peak shifts is observed for the side chain phenyl ring protons (at ∂7.22 ppm), **(C)** pure D-phenylalanine, which indicates a multiplet peak at ∂7.22 ppm for phenyl ring protons; a doublet of doublet peak at ∂3.66 ppm for the chiral proton (H-α) and two doublet of doublet peaks at ∂3.11 ppm & ∂2.89 ppm for the diastereotopic CH_2 protons (H-β), **(D)** a mixture of D-phenylalanine with chloroauric acid, which indicates a downfield shift in the chiral proton (H-α) to ∂4.01 ppm as a triplet and CH_2 proton (H-β) peaks appear at ∂3.11 & ∂3.04 ppm merged with each other. Minimal peak shifts are observed for the side chain phenyl ring protons (at ∂7.23 ppm), **(E)** pure L-alanine, which indicates a quartet peak at ∂3.47 ppm for the chiral proton (H-α) and a doublet peak at ∂1.28 ppm for the methyl protons, **(F)** a mixture of L-alanine with chloroauric acid, which indicates a downfield shift in the chiral proton (H-α) and the methyl proton peak to ∂3.78 ppm and ∂1.35 ppm are observed respectively. These results indicate preferential interaction to the amine and carboxylate moieties and minimal interaction of chloroaurate ions with the phenyl ring.

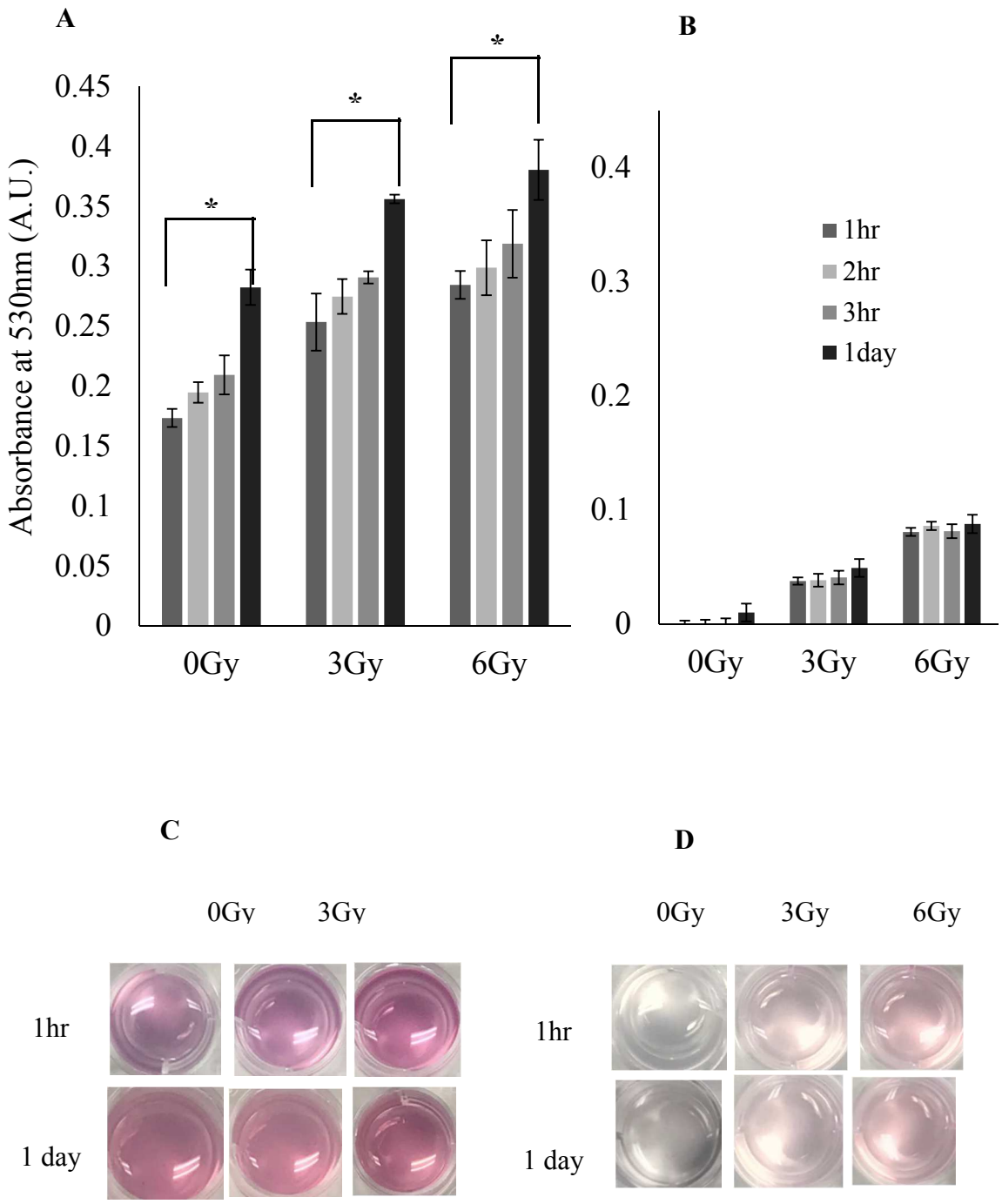

Figure 8.6 Absorbance profiles of the hydrogel nanosensor as a function of time **(A)** without and **(B)** with glutathione incubation. Significant differences were observed after one day in all cases indicating the need of glutathione supplementation for inhibiting gold nanoparticle growth. **(C)** Optical images are shown illustrating the increase in intensity of the developed maroon color over time in the absence of glutathione incubation **(D)** No such increase in intensity of the radiation-induced maroon color was observed after incubation

with glutathione. A two-way paired Student's t-test was performed and p-values < 0.05, considered statistically significant, are denoted with an asterisk (*) on the respective column.

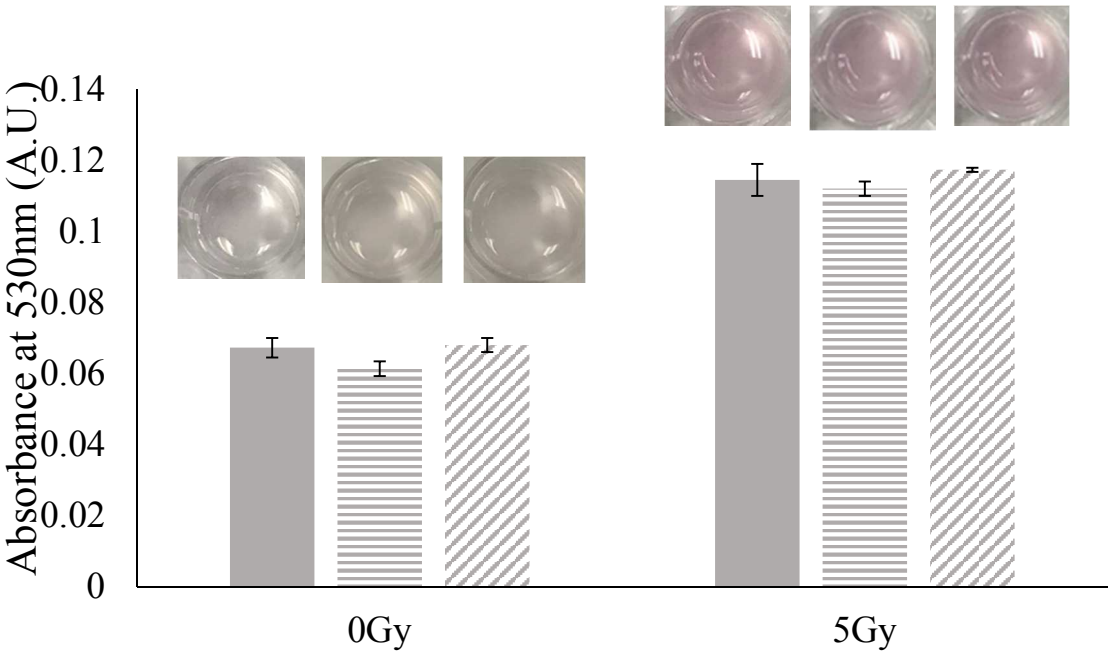

Figure 8.7 Effect of radiation post glutathione addition. Hydrogel nanosensors exposed to 0Gy and 5Gy were incubated with glutathione prior to an additional exposure of 10Gy. The absorbance exposed to a single treatment of radiation (**solid gold bars**), absorbance value after 1hour post irradiation with 10 Gy (bars with **horizontal gold stripes**) and absorbance value after 24 hours post irradiation with 10Gy (bars with d**iagonal gold stripes**). Visually, no changes in the hydrogel nanosensor were observed and no significant differences were detected when comparing the mean absorbance values indicating the sequestering of unreacted gold ions by glutathione inhibiting further gold nanoparticle growth. A two-way paired Student's t-test was performed and p-values < 0.05, considered statistically significant, are denoted with an asterisk (*) on the respective column.

The precursor nanosensor hydrogel were irradiated with various levels of therapeutically relevant radiation doses. This resulted in the formation of gold nanoparticles rendering a pink color to the hydrogel (**Figure 8.8**). Exposure to ionizing radiation results in the formation of free radicals including e^-_{aq} and $H^{\cdot}$ which aids in the reduction of Au(III) to Au(0). Further nucleation and growth leads to formation of clusters which over time mature and lead to the formation of gold nanoparticles. Gold nanoparticles generated upon radiolysis are likely to be stabilized by amino acids in the system. The intensity of color developed in the hydrogel is dependent on the concentration of the gold nanoparticles which is directly associated with the intensity of the prescribed radiation dose. The increase in color is directly proportional to the increased generation of free radicals at higher doses. Morphology and size of the nanoparticles generated in the hydrogel sensor irradiated with 2 and 7.5 Gy were evaluated through transmission electron microscopy (**Figure 8.9**). Quasi-spherical nanoparticles were observed in both the 2 and 7.5 Gy condition with an average size of 34.2 ± 9.7 nm and 21.6 ± 3.6 nm correspondingly. Interestingly we also noticed the presence of smaller nanoparticles in the non-irradiated control (1.8 ± 1.5 nm). The small size of nanoparticles is in agreement with the absence of a plasmon peak in the absorbance spectrum[266].

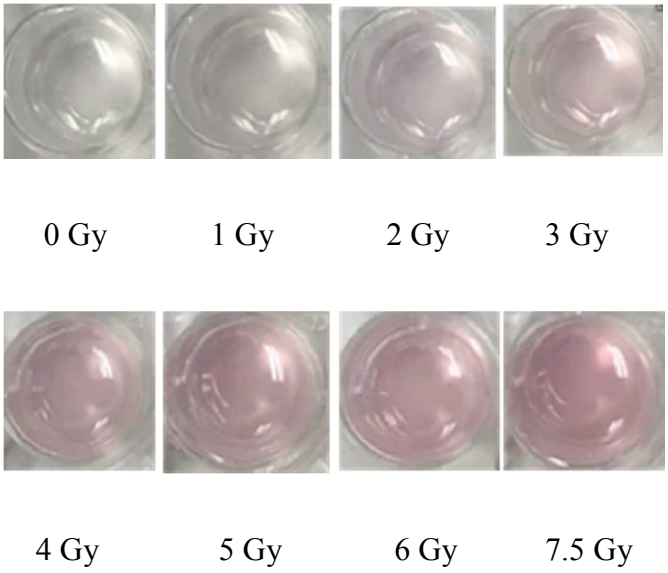

Figure 8.8 Optical images of hydrogels irradiated radiation doses used routinely in clinical fractionated radiotherapy. The radiation dose corresponding to the visual color change is indicated below each image in gray (Gy).

A

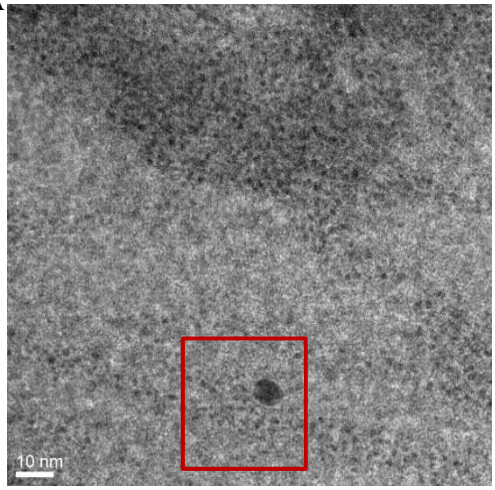

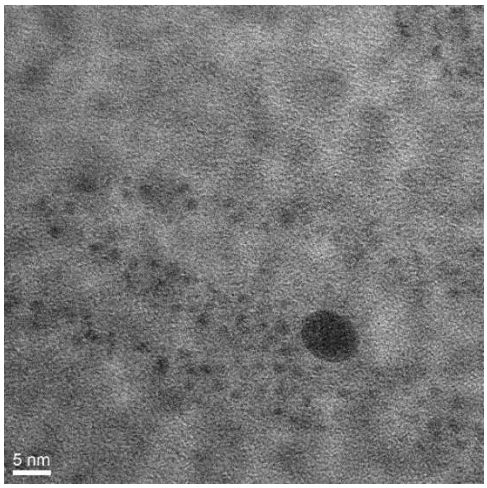

B

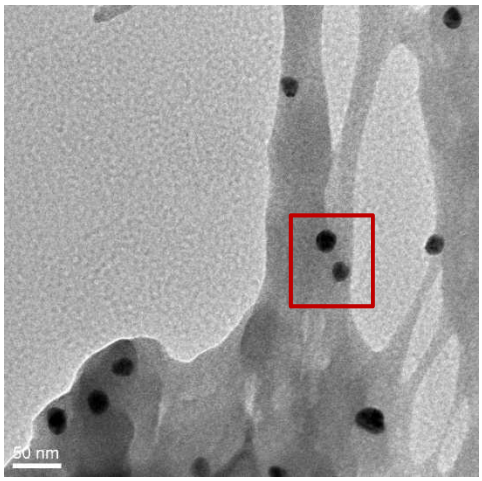

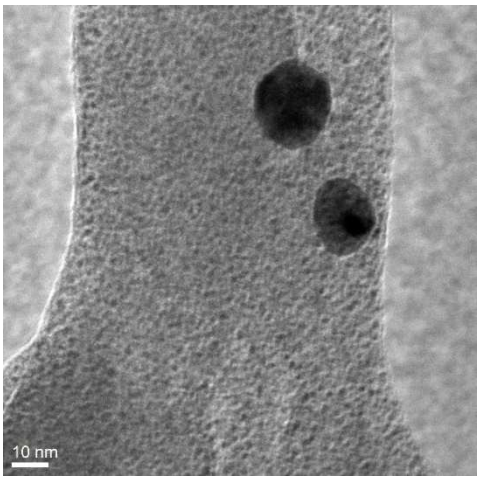

C

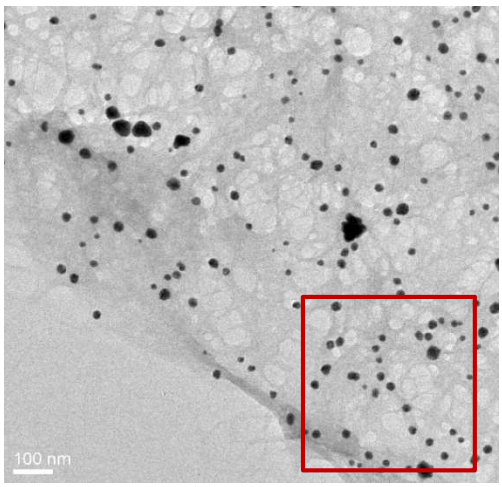

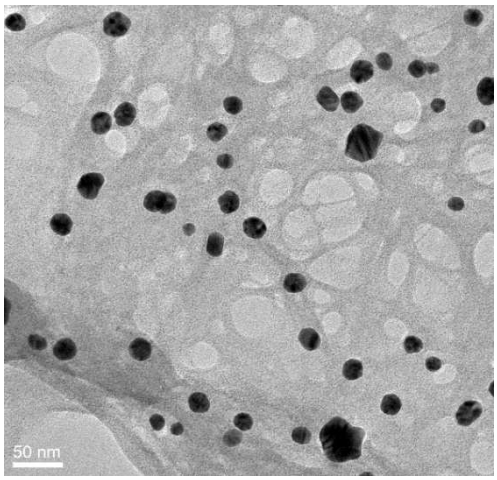

Figure 8.9 Representative transmission electron microscopy (TEM) images of gold nanoparticles formed at **(A)** 0 Gy (left, scale bar of 5 nm), **(B)** 2 Gy (middle, scale bar of 50 nm) and **(C)** 7.5 Gy (right, scale bar of 100 nm). The average nanoparticle size varies from 1.8 ± 1.5 for 0 Gy, 34.2 ± 9.7 for 2 Gy and 21.6 ± 3.6 for 7.5 Gy.

The change in color of the irradiated hydrogels was visible to the naked eye as early as 10 minutes while higher levels of radiation (4-7.5 Gy) required only <5 mins. This increase in color in the irradiated hydrogels were quantified based on a simple, bench top UV-vis spectrophotometer (**Figure 8.10 A**). The earliest time point where we quantified the change in color was 1 hr. A typical spectral peak between 500 nm and 600 nm is used as an index to demonstrate the existence of gold nanoparticles. To further quantify the nanoparticle concentration with different radiation dose levels, the peak absorbance at 530 nm was plotted as a function of radiation dose (**Figure 8.10 B**). A linear calibration curve was obtained between 1-6 Gy. These radiation levels are employed during conventional and hypofractionated radiation therapy. Post-irradiation stability over a period of 7 days was monitored under natural lighting and at room temperature (**Figure 8.11**). No significant differences in absorbance were observed after a week demonstrating post-irradiation stability unlike conventional dosimeters where fading of the output over time and during readout is observed.

A

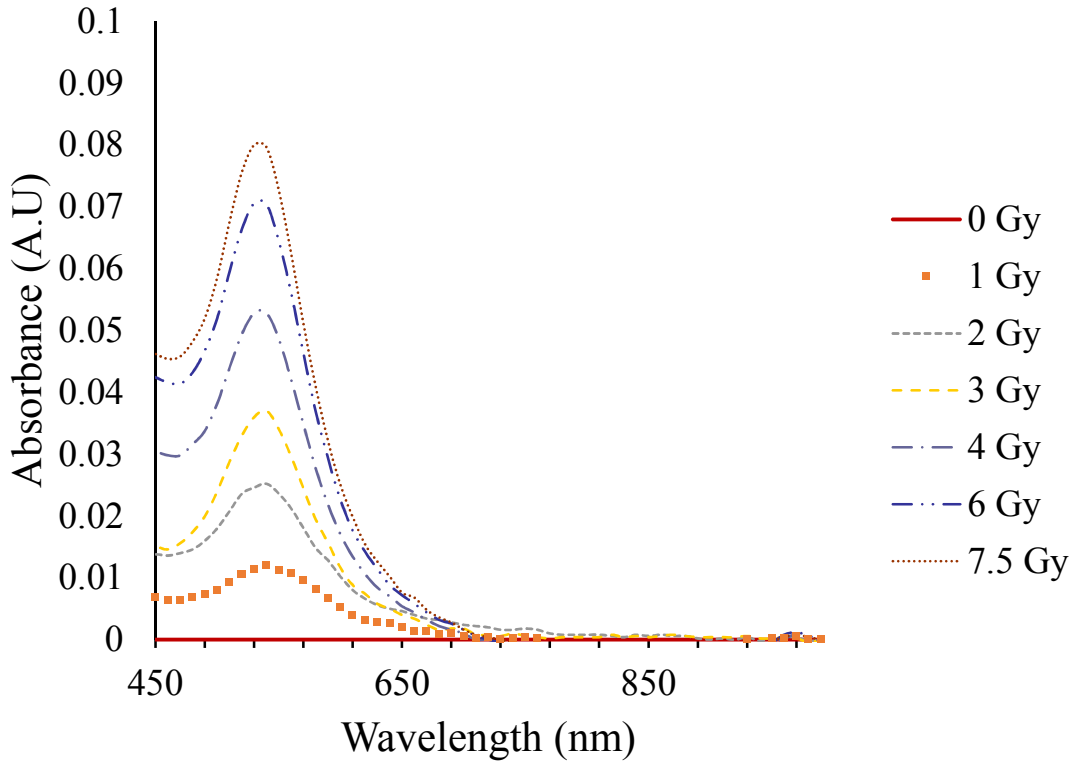
0.1
0.09
0.08
0.07
0.06
0.05
0.04
0.03
0.02
0.01
0
Absorbance (A.U)
450
650
850
Wavelength (nm)
0 Gy
1 Gy
2 Gy
3 Gy
4 Gy
6 Gy
7.5 Gy

B

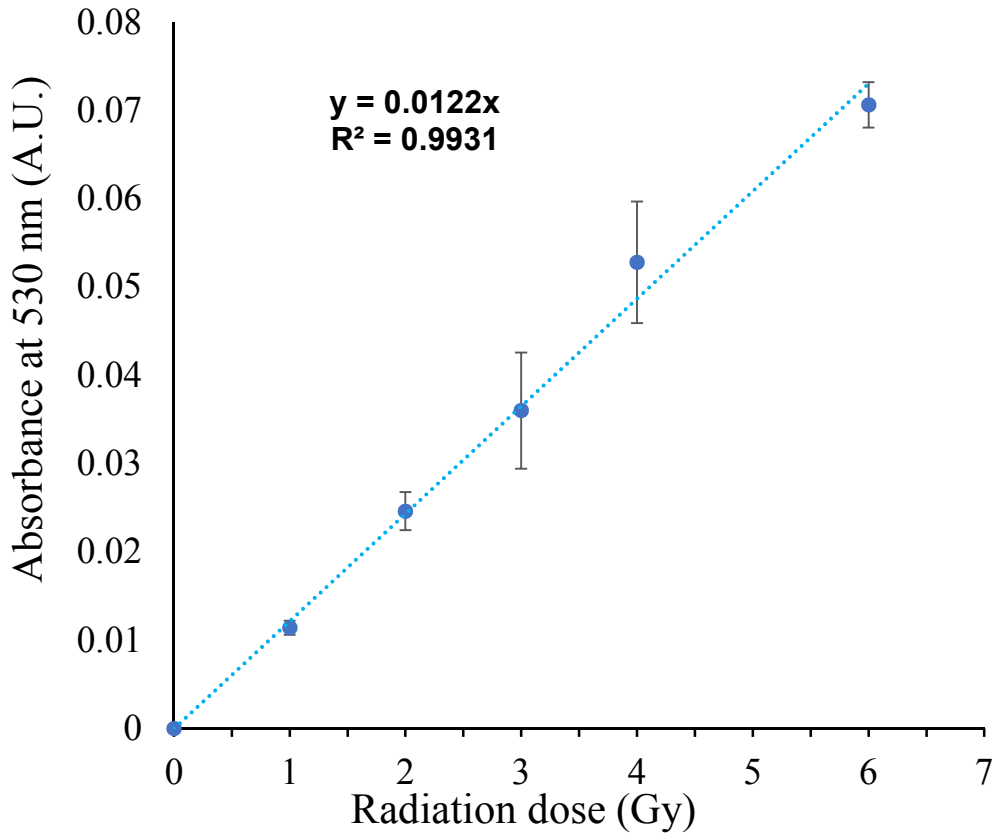
y = 0.0122x
R² = 0.9931
0.08
0.07
0.06
0.05
0.04
0.03
0.02
0.01
0
Absorbance at 530 nm (A.U.)
0
1
2
3
4
5
6
7
Radiation dose (Gy)

Figure 8.10 (A) UV-Vis absorption spectra of the control (0 Gy) gels and gels irradiated with different doses of X-ray radiation. **(B)** Maximum absorbance vs. radiation dose which serves as the calibration curve for the sensor at various therapeutic doses of radiation between 0 Gy and 6 Gy.

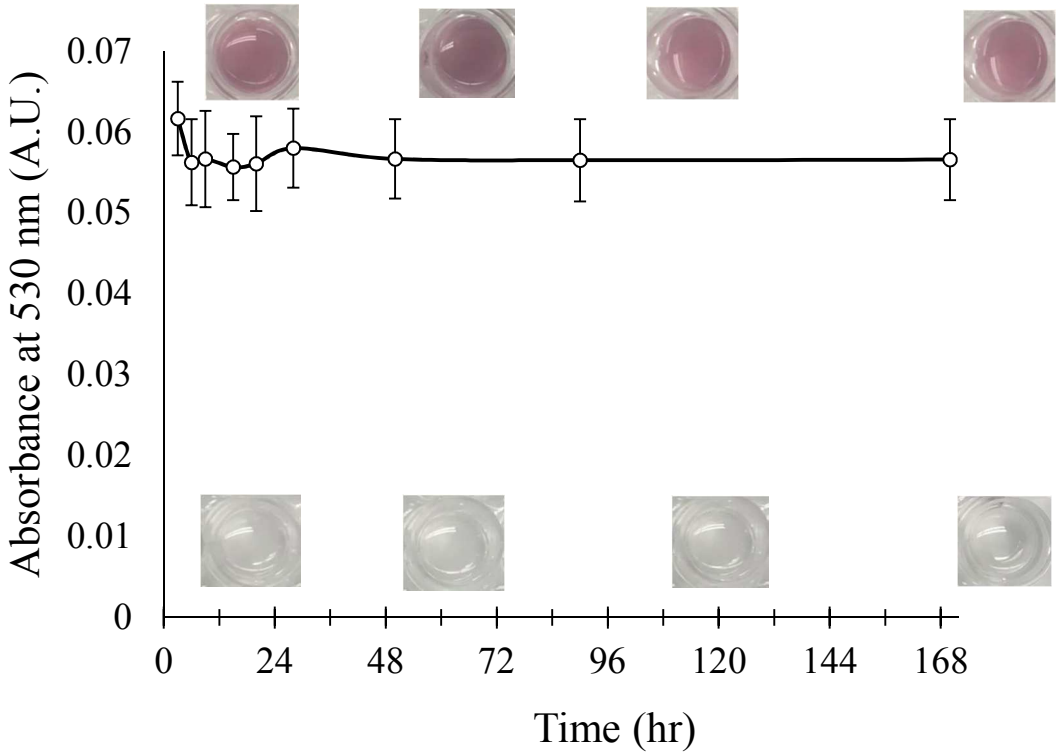

Figure 8.11 Post irradiation stability of the hydrogel sensor irradiated with 5 Gy. No significant changes in the absorbance profile observed for at least a week. Insets display demonstrate no significant visual change over time corroborating the stability of the absorbance profile.

The efficacy of our sensor was determined by delivering a dose of 5 Gy (not used to generate the calibration curve). The color change was quantified and based on the calibration curve, the predicted dose was 5.32 ± 0.24 Gy with an error percentage of 6.4%. With the increase in complexity of radiation delivery techniques, localized radiation

injuries are common and the skin is the first organ affected due to ionizing radiation. There is a need to monitor the dose prescribed to the skin. To demonstrate the efficacy of our biocompatible hydrogel nanosensor, we placed the hydrogel nanosensor disc on the surface of an anthropomorphic phantom mimicking the thorax of an adult human (**Figure 8.12**). A prescribed dose of 3 Gy was delivered the skin surface and the change in color was recorded. Based on the calibration curve, our nanosensor hydrogel discs predicted a dose of 3.03 ± 0.47 Gy with an error percentage of 1%.

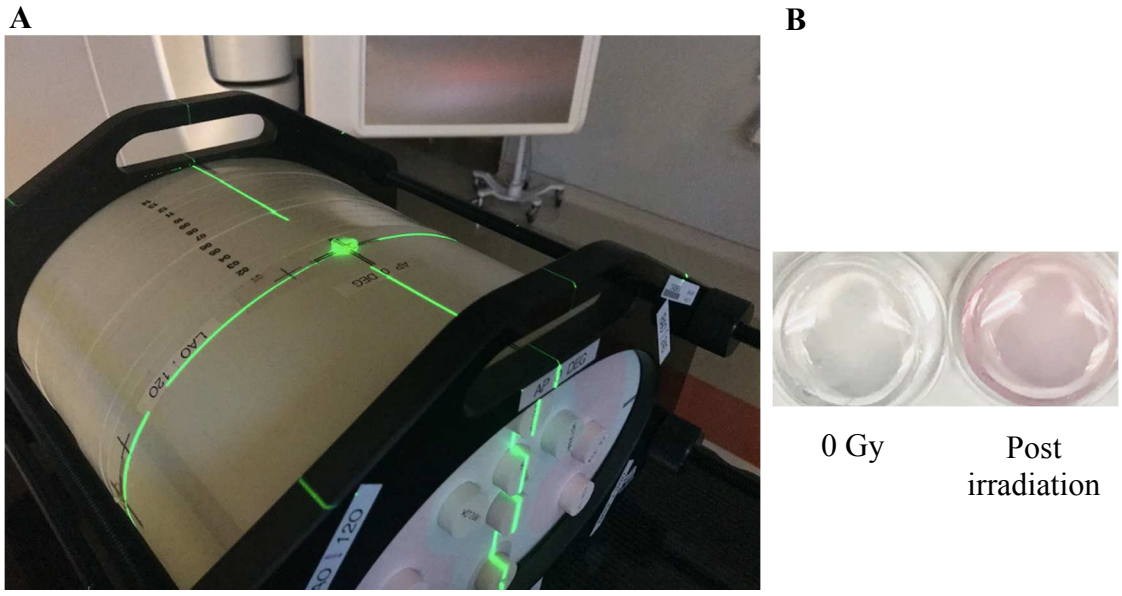

Figure 8.12 (A) Digital image of the hydrogel sensor (positioned in the intersection of the green lasers) on top of an anthropomorphic thorax phantom. The phantom was treated with a dose of 3 Gy, Optical image of the hydrogel sensor on the surface of the phantom prior to irradiation (0 Gy) and post irradiation.

To demonstrate feasibility and applicability for potential clinical use, we used a live canine patient as a model to verify the efficacy of the sensor. Ahead of the use on live canine patients, we ensured the biocompatibility of the sensor by carrying out XTT and live dead assay (**Figure 8.13**). We found no change in cell viability when compared to the pure

agarose hydrogel. The use of low concentration gold salt and biocompatible templating agents provide strong support to the biocompatible nature of the functional components of the hydrogel nanosensor. We further investigated the translational capability of our biocompatible hydrogel nanosensor to verify the dose delivered to a canine patient. The prescribed surface dose to the canine was 1.34 Gy (**Figure 18**). Hydrogel nanosensor discs were placed on the surface of the bolus to record the surface dose. Upon execution of the treatment plan the hydrogel discs were removed and the absorbance relating to the distinct color change was recorded. Based on the previously generated calibration curve, the dose was estimated to be 1.25 ± 0.34 Gy. Clinically prevalent nanoDot™ reported a prescribed dose of 1.29 ± 0.02 Gy with an error percentage of 3.7%. Other clinical dosimeters like TLDs have a 5% error which is comparable to the 6.7% error of the hydrogel nanosensor. NanoDOT™ and the TLDs are prone to loss of readout signal and more cumbersome to operate making the hydrogel nanosensor an easier adaption into the clinic. As far we know, this is the first reported molecular and nanoscale sensor that has been used to verify the dose delivered to an actual patient. The ease of production, operation and measurement of its distinct color change along with its radiation dose resolution, indicates tremendous potential of the nanosensor to be widely used in the clinic.

A B C

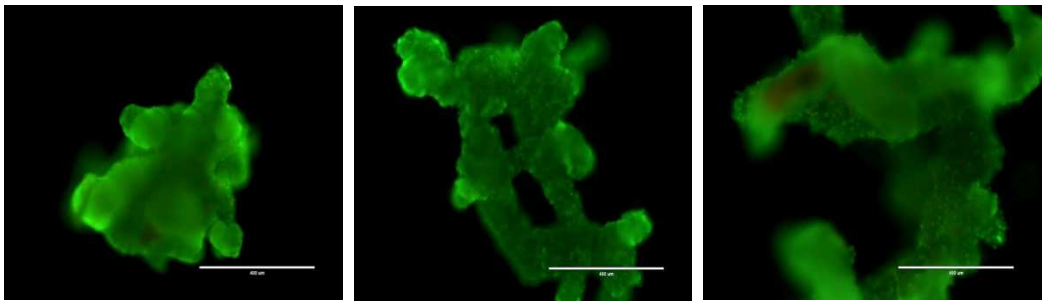

D

Pure agarose	Sensor with 0 Gy	Sensor with 5 Gy
100%	135 ± 15 %	133 ± 8 %

Figure 8.13 Live/Dead® cell viability assay showing live BJ5ta human fibroblast cell line stained with calcein-AM (green) and dead cells with EthD-1(red). Cells were seeded on the 0 Gy and 5 Gy hydrogel post irradiation (≈2hours). Absence of significant dead cells when compared to the **(A)** agarose control indicate the biocompatibility of the functional components of the sensor. All images have scale bar of 400 µm. Cell viability was quantified using XTT and no significant changes were observed.

A B

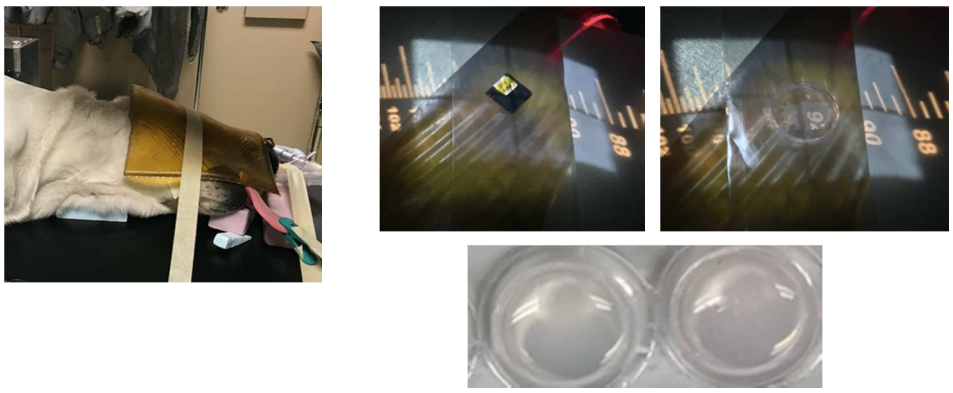

0 Gy Post irradiation

Figure 8.14 (A). Representative image of the experimental setup for the radiotherapy treatment of canine patient, **(B).** Images of Nanodot^{TM} OSLD and the hydrogel sensor placed on the canine patient (top right) show the gel prior to irradiation (0 Gy) and post irradiation with 1.34 Gy (bottom right). The change in color was quantified using UV-Vis spectrophotometer and the gel nanosensor calibration predicted a dose of 1.25 ± 0.34 Gy, which was an error of 6.7% compared to the planned dose.

8.4 Conclusions

To our knowledge, this is the first demonstration of a colorimetric biocompatible molecular and nanoscale radiation sensor. The formation of gold nanoparticles in response to ionizing radiation is qualitatively visualized through a distinct color change and quantitatively measured using a simple UV-vis spectrophotometer. The developed sensor demonstrated the ability to detect therapeutic levels of ionizing radiation and present a linear response between 1-6 Gy commonly used during conventional and hypofractionated radiotherapy. The nanosensor was accurately able to predict the prescribed radiation dose to an anthropomorphic phantom and a live canine patient. The efficacy of the hydrogel nanosensor was comparable to clinical dosimeters. The fabrication of a hydrogel-based sensor would facilitate adaptation into various shapes, which could potentially result in personalized dosimetry based on anatomical variation on the patient. We anticipate that this new sensor could accelerate and lead to development of next generation radiation sensors assisting physicists and clinicians in providing valuable information regarding the prescribed dose to the patient.

Chapter 9 CONCLUSION AND FUTURE PERSPECTIVES

9.1 Conclusion

The purpose of the research conducted upto this point has revolved around the development of a novel plasmonic nanosensor that can be effectively be employed in the clinic to qualitatively and quantitatively predict the radiation dose delivered to patients undergoing radiotherapy. To this end we have: 1) developed the first gold nanoparticle based sensor to detect therapeutic levels of ionizing radiation, 2) to enable safe handling, the second generation gold nanoparticle based sensor was developed in a biocompatible hydrogel, 3) the applicability to detect high energy photons, protons and electrons was demonstrated, 4) improved the capability of the hydrogel sensor to qualitatively and quantitively predict dose in a two-dimensional space, 5) Finally, to reduce the toxicity of the hydrogel nanosensor, a completely novel amino acid based nanosensor was developed. The following framework represents the work that I believe is required for the evolution in the technology.

Future Direction 1. A Proof of Concept Nanotechnology Based Gel Dosimeter for In Vivo Use in Brachytherapy

Introduction

Brachytherapy is a procedure that involves the use of radioactive isotopes to treat cancer.[283] The radioactive source is generally placed temporarily or permanently inside the patient to induce radiation damage to cancerous cells while maintaining the viability of healthy cells.[284] The current technology employed is to use 3D imaging-based dose calculations to predict the dose delivered to organs at risk(OAR)[285] However, organ movement between imaging and treatment and dose calculation uncertainties result in unpredictability requiring the need for *in vivo* dosimetry.[285] The motivation will be to assess the radiation dose delivered to organs at risk (OAR) by direct measurements using the hydrogel nanosensor as described previously. As a proof of concept, the capability of the hydrogel nanosensor in detecting and predicting radiation dose delivered through a radioactive isotope, an ^{192}Ir source is shown.

Experimental

Materials. Molecular biology grade agarose, L-ascorbic acid (AA), gold(III) chloride trihydrate ($HAuCl_4.3H_2O$) and myristyltrimethylammonium bromide($C_{14}TAB$)(≥99%) were acquired from Sigma-Aldrich. The chemicals were employed in the study with no further processing or purification. The solvent employed in the study was MilliQ water (18.2 MΩ.cm).

Hydrogel Nanosensor Preparation for Valencia Applicator. To fabricate a hydrogel nanosensor a petri dish with a glass bottom mold with a diameter of ≈1 cm and thickness of 0.5 mm is used. Briefly, 600 μL of a 50 mM stock solution of C_{14}TAB was prepared and mixed with 30 μL of 10 mM $HAuCl_4$ in a 1.7 mL microcentrifuge tubes. From this mixture, 100 μL was removed prior to the addition of heated 2% (w/v) liquid molecular grade agarose (500 μL). From this mixture, 500 μL was removed and poured into the molds. The excess liquid was removed from the sides before the setting of the gel (10-15secs). The gels were then incubated in 10 mM Ascorbic Acid (500μL) for 1 minute on the hydrogel nanosensor resulting in translucent hydrogels.

X-ray irradiation. Experiments for irradiations related to the Valencia applicator were conducted at the Banner-MD Anderson Cancer Center in Gilbert. The radiation source employed was an ^{192}Ir source.

Absorbance Spectroscopy. The absorbance spectra for the non-irradiated and the irradiated hydrogel nanosensor were obtained using a BioTek Synergy™ 2 plate reader. Absorbance values were measured from 300 nm to 990 nm with a step size of 10 nm. MilliQ water was used as blank for all experiments. To normalize the absorbance spectra for further analysis, the absorbance at 990nm was subtracted from the absorbance of all wavelengths. The maximum absorbance between 500 and 600nm wavelength is used as a measure of intensity in the change in color. To ensure that the 0 Gy absorbance is 0, the absorbance value corresponding to 0 Gy is subtracted from all the irradiated absorbance

values. This is plotted as a function of radiation dose to generate the calibration curve which is used to determine unknown radiation doses.

Image Acquisition. All images were acquired using an iPhone 8. Furthermore, images were cropped to the required size and no further editing or post processing of the images was carried out.

Statistical Analysis. All experiments were performed in quintuples unless otherwise specified. Data analysis for all independent experiments was performed using Microsoft Excel. Data reported in the manuscript are represented as mean ± one standard deviation.

RESULTS AND DISCUSSION

High dose rate brachytherapy is operated widely in the treatment of skin lesions. Several applicator designs including the Valencia applicator have been introduced in order to deliver a homogenous absorbed radiation dose to the cancerous lesion and avoid radiation leakage to the healthy tissue.[286] As a proof of concept, we have developed an accessory to the Valencia applicator that could be mounted instead of the cap and could potentially be used to monitor the delivered radiation dose (**Figure 1**). Irradiation of the hydrogel nanosensor with different doses of ionizing radiation with a ^{192}Ir source resulted in the formation of gold nanoparticles rendering a change in color from translucent to pink/maroon. The intensity of color developed is dependent on the yield of gold nanoparticles, which in turn is directly proportional to the intensity of ionizing radiation.

Increasing the intensity of ionizing radiation results in an increased generation of reducing free radical species which can further facilitate additional reduction of Au(I) to Au(0). The change in color in the hydrogel nanosensor after exposure to ionizing radiation was visible as early as 10 minutes. The change in color was further quantified using UV-Visible spectroscopy 1-hour post-irradiation. A characteristic spectral peak between 500 and 600nm is observed for all the irradiated hydrogel nanosensors. The maximum absorbance was plotted as a function of the radiation dose from 0-4 Gy to obtain a linear calibration curve with an equation ($y= 0.012 \times X$; y = maximum absorbance between 500-600nm and X = radiation dose in Gy). An known radiation dose of 2.25Gy (not employed in generating the calibration curve) is employed to determine the efficacy of the hydrogel nanosensor in predicting the radiation dose. The use of the calibration curve resulted in a prediction of 1.96 ± 0.23Gy for a dose of 2.25 Gy.

In the future, the effect of various dose rates due to radioactive decay of the isotope on the signal (absorbance) of the hydrogel nanosensor has to be verified. The technology can be extended to other applicators (Leipzig) and other applicators designed to treat other organs of interest (prostate).

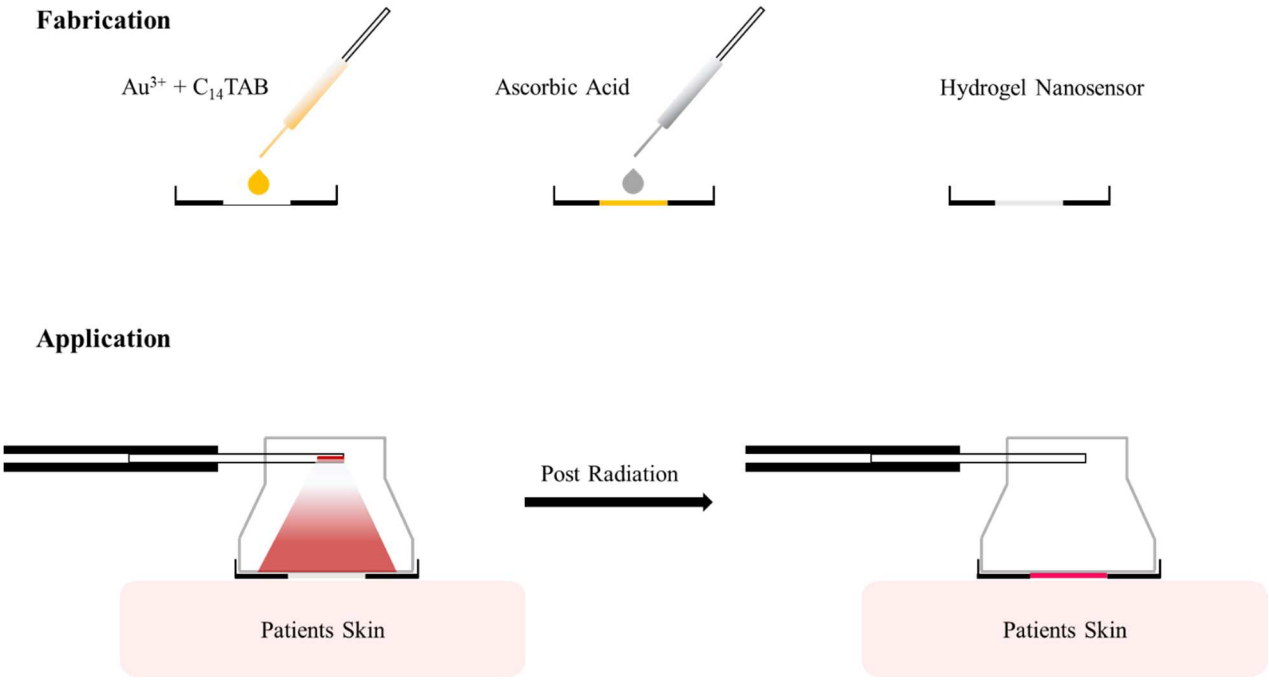

Figure 9.1 Schematic illustrating the fabrication technique and potential applicability of the Valencia applicator.

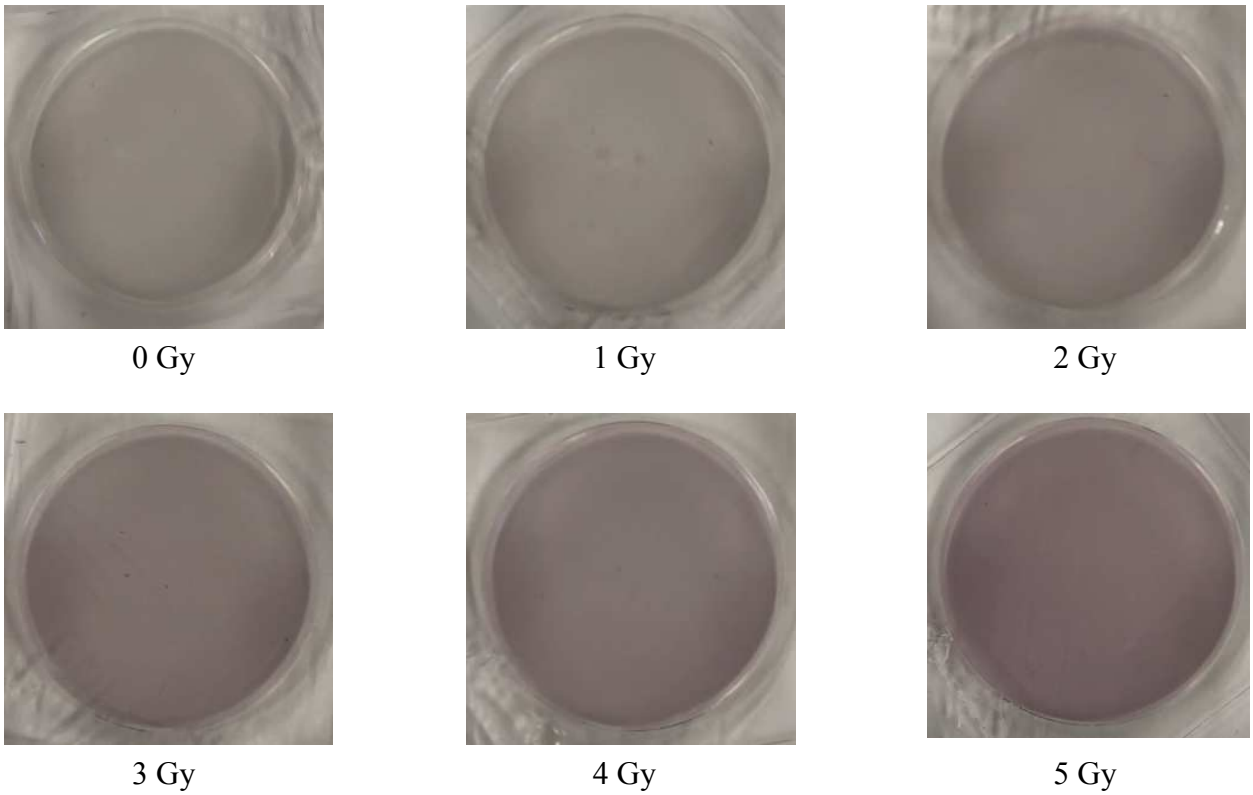

Figure 9.2 Images of the hydrogel nanosensor following exposure to various levels of ionizing radiation from an ^{192}Ir source. Images were acquired 1-hour post-irradiation.

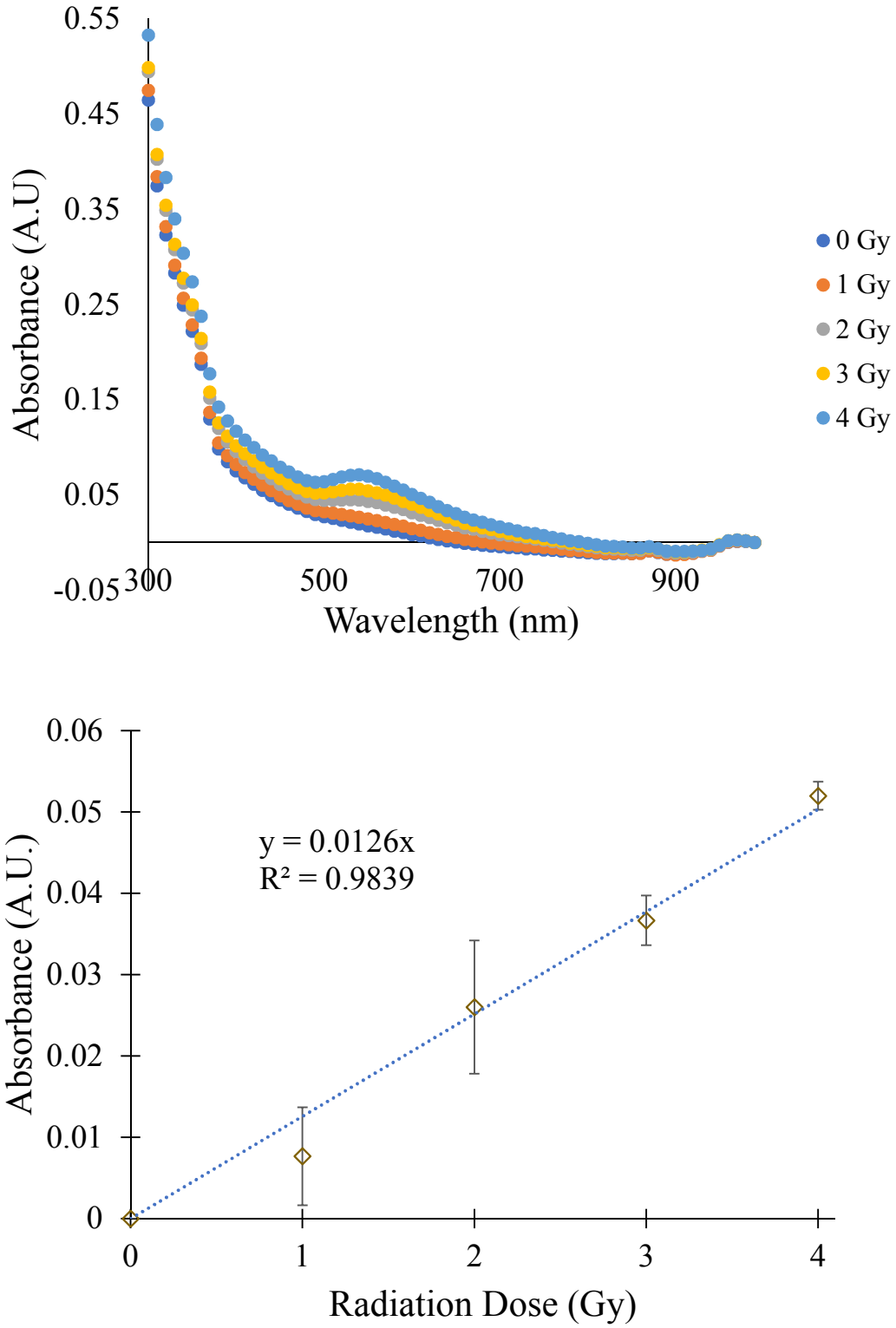

Figure 9.3 (A) Plot of absorbance as a function of radiation dose and **(B)** Maximum absorbance response between 500 and 600nm versus radiation dose 1-hour post-irradiation.

Future Direction 2. Three-dimensional radiation dosimetry using plasmonic hydrogel nanosensors

Introduction

Modern radiotherapy involves delivery of high levels of ionizing radiation to the target volume while simultaneously minimizing the dose delivered to the surrounding healthy tissue[287]. With the introduction of sophisticated treatment delivery modalities like intensity modulated radiation therapy(IMRT), volumetrically modulated arc therapy(VMAT) and stereotactic radiosurgery (SRS), control over the total dose distributed in an ideal three-dimensional (3D) shape is conceivable[288]. These treatment techniques involve delivery of high levels of ionizing radiation with steep dose gradients near the target volume making them highly susceptible to errors[289]. In addition, any deviation during the complex movement of the multileaf collimator and gantry will affect the accuracy of the delivered treatment plan[289]. To accommodate these new treatment modalities, quality assurance of the patient's treatment plan is recommended, and verification of the treatment plan is essential prior to treating patients. There is still a pressing need for a practical 3D dosimetry system, convenient for clinical use, and with the accuracy and resolution to enable comprehensive verification of the complex dose distributions typical of modern radiation therapy.

To aid in the measurement of 3D dose distributions, various 3D gels have been fabricated as a potential solution to this challenge. Fricke ferrous sulfate dosimeters are easy to fabricate and use but suffer from poor post-irradiation stability post due to ion diffusion

which eventually erases topographical dose profiles[290]. Polymer gel dosimetry were developed to overcome post-irradiation instability but requires upwards of 40 hours from fabrication to imaging making routine employment labor intensive and time-consuming[291]. The fabrication and the diffusion concerns were overcome with the development of solid radiochromic dosimeters[292]. These dosimeters are easy to handle and mold into various shapes depending on the application. But current dyes incorporated within the solid radiochromic dosimeters are prone to post-irradiation photo bleaching[293]. These limitations within existing systems warrant further development of a simple yet robust 3D dosimeters that can potentially assist physicists and clinicians in generating safe and effective treatment plans to improve patient safety and post quality of life.

Nanotechnology-enabled sensors provide new solutions towards detection of ionizing radiation with increased selectivity and sensitivity[224]. We have previously developed a colorimetric sensor wherein ionizing radiation facilitates the generation of gold nanoparticles from its ionic precursor solutions. To achieve easy handling and to overcome any application concerns, we incorporated the precursor solution in agarose hydrogels. Furthermore, we illustrate the robust performance of the hydrogel nanosensor to qualitatively and quantitatively determine topographical radiation dose profiles and its clinical translation by demonstrating its efficacy in determining radiation dose delivered to live canine patients. Here, we illustrate the capability of the hydrogel nanosensor to detect radiation dose profiles in 3D which represents a significant step forward in the field of 3D dosimetry. To our knowledge, no such nanoscale technologies exist which can detect radiation dose profiles in all three dimensions.

Experimental

Materials. Hydrogen tetrachloroaurate trihydrate ($HAuCl_4.3H_2O$), myristyltrimethylammonium bromide ($C_{14}TAB$) (99%), L-ascorbic Acid and molecular biology grade agarose were acquired from Sigma-Aldrich. No further purification of the chemicals was carried out. MilliQ water (18.2 MΩ.cm) was used as solvent for all experiments conducted.

Preparation of three-dimensional (3D) Hydrogel Nanosensor. Stock solutions of $C_{14}TAB$ (75mM), Ascorbic acid (10mM) and hydrogen tetrachloroaurate (10mM) was prepared. This constitutes Part A of the hydrogel nanosensor mixture. Simultaneously 1% w/v agarose was heated in a microwave until a clear solution was observed. This constitutes Part B of the hydrogel nanosensor mixture. Equal parts by volume of both Part A and Part B are mixed to fabricate the final 3D hydrogel nanosensor. For example, to prepare a 3D hydrogel nanosensor with a final volume of 30ml, the volumes of each the individual components in part A are determined by the following equation.

30uL of 10mM $HAuCl_4$ x **C** + 600uL of 75mM $C_{14}TAB$ x **C** + 60uL of AA x **C** = 15 mL

$$\mathbf{C} = 21.7$$

The surfactant is added to hydrogen tetrachloroaurate initially and left undisturbed for 5 minutes prior to the addition of ascorbic acid. To this mixture the liquid agarose (Part B) at 40°C is added and allowed to gel at room temperature prior to irradiation experiments.

Irradiation Experiments. Experiments for irradiations were carried out at Banner-MD Anderson Cancer Center in Gilbert. The radiation source employed was a 6MV photon beam at a dose rate of 100MU per minute.

Results and Discussion

Here, we demonstrate the ability of the hydrogel nanosensor to qualitatively and quantitatively determine radiation dose delivery in 3D. As a proof of concept, we verified the ability of the 3D hydrogel nanosensor to qualitatively retain spatial dose information post-irradiation. 30mL of the hydrogel nanosensor was allowed in set in 50 ml centrifuge tubes prior to irradiation (**Figure 1**). A clear translucent hydrogel is observed when the tubes are not exposed to radiation and remains stable over the course of 3 days. Exposing the tubes to 2 and 5Gy results in the hydrogel nanosensor displaying colors with varying intensity of maroon/pink. This increment in color is likely due to the increase in the number of free radicals with increasing radiation dose resulting in a higher yield of nanoparticles. To visualize post irradiation diffusion and/or photo bleaching, one of the tubes was irradiated with both 2 and 5Gy transversely with minimal diffusion or post-irradiation photobleaching observed over time. To ensure no diffusion arises over time along the sagittal plane, one of the tubes was exposed to a 5 Gy dose. Similar stability profile is observed indicating post-irradiation stability of the hydrogel nanosensor.

In the future, the change in color in these three-dimensional hydrogel nanosensors will be required to be quantifiable. We propose the use of an Optical Computed Tomography

(OCT) scanner. This technique will involve the use of data obtained from the transmitted and attenuated light beams to reconstruct a volumetric model of the irradiated regions. The development of 3D dosimeters which are easy to fabricate and use simple optical scanning measurements would better assist clinicians during patient treatment to determine the effectiveness of the treatment plan and ensure patient safety.

t = 2 hours

t = 1 day

t = 3 days

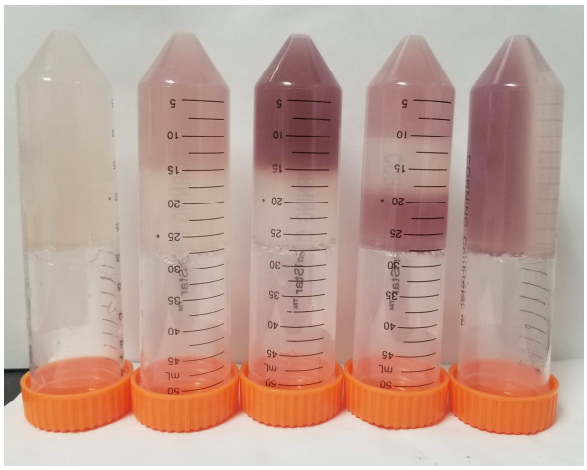

Figure 9.4 Digital images of hydrogel nanosensor exposed to four different radiation conditions. From Left. 0 Gy (No Radiation Control), Half the hydrogel nanosensor exposed to 2 Gy horizontally, Half the hydrogel nanosensor exposed to 5 Gy horizontally, Top one third exposed to 2 Gy and the bottom one third exposed to 5 Gy while the middle section remains not exposed to radiation and 5 Gy radiation delivered vertically. These images illustrate minimal post-irradiation fadeout diffusion over the course of 72 hours.

REFERENCES

1. Chaikh, A.; Beuve, M.; Balosso, J., Nanotechnology in radiation oncology: The need for implantable nano dosimeters for in-vivo real time measurements. *International Journal of Cancer Therapy and Oncology* **2015,** *3* (2).

2. Jeremic, B.; Shibamoto, Y.; Acimovic, L.; Milisavljevic, S., Initial versus delayed accelerated hyperfractionated radiation therapy and concurrent chemotherapy in limited small-cell lung cancer: a randomized study. *Journal of Clinical Oncology* **1997,** *15* (3), 893-900.

3. Jeremic, B.; Shibamoto, Y.; Milicic, B.; Nikolic, N.; Dagovic, A.; Aleksandrovic, J.; Vaskovic, Z.; Tadic, L., Hyperfractionated Radiation Therapy With or Without Concurrent Low-Dose Daily Cisplatin in Locally Advanced Squamous Cell Carcinoma of the Head and Neck: A Prospective Randomized Trial. *Journal of Clinical Oncology* **2000,** *18* (7), 1458-1464.

4. Kacprowska, A.; Jassem, J., Hypofractionated radiotherapy for early breast cancer: Review of phase III studies. *Reports of Practical Oncology & Radiotherapy* **2012,** *17* (2), 66-70.

5. Song, D. Y.; Benedict, S. H.; Cardinale, R. M.; Chung, T. D.; Chang, M. G.; Schmidt-Ullrich, R. K., Stereotactic Body Radiation Therapy of Lung Tumors: Preliminary Experience Using Normal Tissue Complication Probability-Based Dose Limits. **2005,** *28* (6), 591-596.

6. Ajlouni, M., Radiation-induced proctitis. *Current Treatment Options in Gastroenterology* **1999,** *2* (1), 20-26.

7. Vanagunas, A.; Jacob, P.; Olinger, E., Radiation-Induced Esophageal Injury - A Spectrum From Esophagitis To Cancer *American Journal of Gastroenterology* **1990,** *85* (7), 808-812.

8. Morrish Jr., R. B.; Chan, E.; Silverman Jr., S.; Meyer, J.; Fu, K. K.; Greenspan, D., Osteonecrosis in patients irradiated for head and neck carcinoma. **1981,** *47* (8), 1980-1983.

9. Thimbleby, H.; Lewis, A.; Williams, J., Making healthcare safer by understanding, designing and buying better IT. *Clinical Medicine* **2015,** *15* (3), 258-262.

10. Furlow, B., Radiotherapy errors spark investigations and reform. *The Lancet Oncology* **2009,** *10* (1), 11-12.

11. Derreumaux, S.; Etard, C.; Huet, C.; Trompier, F.; Clairand, I.; Bottollier-Depois, J.-F.; Aubert, B.; Gourmelon, P., Lessons from recent accidents in radiation therapy in France. *Radiation Protection Dosimetry* **2008,** *131* (1), 130-135.

12. Den, R. B.; Nowak, K.; Buzurovic, I.; Cao, J.; Harrison, A. S.; Lawrence, Y. R.; Dicker, A. P.; Showalter, T. N., Implanted Dosimeters Identify Radiation Overdoses During IMRT for Prostate Cancer. *International Journal of Radiation Oncology*Biology*Physics* **2012,** *83* (3), e371-e376.

13. Lee, B.; Jang, K. W.; Cho, D. H.; Yoo, W. J.; Tack, G.-R.; Chung, S.-C.; Kim, S.; Cho, H., Measurements and elimination of Cherenkov light in fiber-optic scintillating detector for electron beam therapy dosimetry. *Nuclear Instruments and Methods in Physics Research Section A: Accelerators, Spectrometers, Detectors and Associated Equipment* **2007,** *579* (1), 344-348.

14. Demchenko, A. P., *Introduction to Fluorescence Sensing*. Springer Netherlands: 2008.

15. Warman, J. M.; Haas, M. P. d.; Luthjens, L. H., High-energy radiation monitoring based on radio-fluorogenic co-polymerization. I: small volume in situ probe. *Physics in Medicine and Biology* **2009,** *54* (10), 3185.

16. Warman, J. M.; Abellon, R. D.; Verhey, H. J.; Verhoeven, J. W.; Hofstraat, J. W., Maleimido-fluoroprobe: A Dual-Purpose Fluorogenic Probe of Polymerization Dynamics. *The Journal of Physical Chemistry B* **1997,** *101* (25), 4913-4916.

17. Warman, J. M.; de Haas, M. P.; Luthjens, L. H.; Denkova, A. G.; Kavatsyuk, O.; van Goethem, M. J.; Kiewiet, H. H.; Brandenburg, S., Fixed fluorescent images of an 80 MeV proton pencil beam. *Radiation Physics and Chemistry* **2013,** *85*, 179-181.

18. Warman, J. M.; de Haas, M. P.; Luthjens, L. H.; Murrer, L. H. P., A Radio-Fluorogenic Organic Gel for Real-Time, 3D Radiation Dosimetry. *Advanced Materials* **2011,** *23* (42), 4953-4955.

19. Warman, J. M.; Luthjens, L. H.; Haas, M. P. d., High-energy radiation monitoring based on radio-fluorogenic co-polymerization II: fixed fluorescent images of collimated x-ray beams using an RFCP gel. *Physics in Medicine and Biology* **2011,** *56* (5), 1487.

20. Warman, J. M.; de Haas, M. P.; Luthjens, L. H.; Hom, M. L., High-energy radiation monitoring based on radio-fluorogenic co-polymerization III: Fluorescent images of the cross-section and depth-dose profile of a 3 MV electronbeam. *Radiation Physics and Chemistry* **2013,** *84*, 129-135.

21. Benevides, C. A.; Duarte de Menezes, F.; de Araujo, R. E., Evaluation of fluorescent dye degradation indirectly induced by x-ray ionizing radiation. *Applied Optics* **2015,** *54* (22), 6935-6939.

22. Jonah, C. D., A Short History of the Radiation Chemistry of Water. *Radiation Research* **1995,** *144* (2), 141-147.

23. Han, J.-M.; Xu, M.; Wang, B.; Wu, N.; Yang, X.; Yang, H.; Salter, B. J.; Zang, L., Low Dose Detection of γ Radiation via Solvent Assisted Fluorescence Quenching. *Journal of the American Chemical Society* **2014,** *136* (13), 5090-5096.

24. Liu, Z.; Xue, W.; Cai, Z.; Zhang, G.; Zhang, D., A facile and convenient fluorescence detection of gamma-ray radiation based on the aggregation-induced emission. *Journal of Materials Chemistry* **2011,** *21* (38), 14487-14491.

25. Dong, X.; Hu, F.; Liu, Z.; Zhang, G.; Zhang, D., A fluorescent turn-on low dose detection of gamma-radiation based on aggregation-induced emission. *Chemical Communications* **2015,** *51* (18), 3892-3895.

26. Han, J.-M.; Wu, N.; Wang, B.; Wang, C.; Xu, M.; Yang, X.; Yang, H.; Zang, L., Gamma radiation induced self-assembly of fluorescent molecules into nanofibers: a stimuli-responsive sensing. *Journal of Materials Chemistry C* **2015,** *3* (17), 4345-4351.

27. Elsa, R.; Curtis, W. F.; James, H. O. D.; David, J. T. H., Radiation Effects on Polymeric Materials. In *Irradiation of Polymeric Materials*, American Chemical Society: 1993; Vol. 527, pp 1-8.

28. Graham, S. C.; Friend, R. H.; Fung, S.; Moratti, S. C., The effect of X-ray irradiation on poly(p-phenylene vinylene) and derivatives. *Synthetic Metals* **1997,** *84* (1–3), 903-904.

29. Silva, E. A. B.; Borin, J. F.; Nicolucci, P.; Graeff, C. F. O.; Netto, T. G.; Bianchi, R. F., Low dose ionizing radiation detection using conjugated polymers. *Applied Physics Letters* **2005,** *86* (13), 1319021-1319023.

30. Bronze-Uhle, E. S.; Batagin-Neto, A.; Lavarda, F. C.; Graeff, C. F. O., Ionizing radiation induced degradation of poly (2-methoxy-5-(2'-ethyl-hexyloxy) -1,4-phenylene vinylene) in solution. *Journal of Applied Physics* **2011,** *110* (7), 0735101-0735109.

31. Bronze-Uhle, E. S.; Borin, J. F.; Batagin-Neto, A.; Alves, M. C. O.; Graeff, C. F. O., MEH-PPV hypsochromic shifts in halogenated solvents induced by γ-rays. *Materials Chemistry and Physics* **2012,** *132* (2–3), 846-851.

32. Lee, K. W.; Mo, K. H.; Jang, J. W.; Lee, C. E., Proton-irradiation effect on the luminescence of the MEH–PPV conjugated polymer. *Solid State Communications* **2007,** *141* (2), 57-60.

33. van Eijk, C. W. E., Inorganic-scintillator development. *Nuclear Instruments and Methods in Physics Research Section A: Accelerators, Spectrometers, Detectors and Associated Equipment* **2001,** *460* (1), 1-14.

34. Haizheng Zhong and YongSheng Zhao and Yongfang Li and Qibing, P., Photoluminescence quenching of conjugated polymer nanocomposites for gamma ray detection. *Nanotechnology* **2008,** *19* (50), 505503.

35. Zhao, Y. S.; Yu, Z.; Douraghy, A.; Chatziioannou, A. F.; Mo, Y.; Pei, Q., A facile route to bulk high-Zpolymer composites for gamma ray scintillation. *Chemical Communications* **2008,** (45), 6008-6010.

36. Ivan, V. K.; Pieter, D., Nonproportional response of LaBr 3 :Ce and LaCl 3 :Ce scintillators to synchrotron x-ray irradiation. *Journal of Physics: Condensed Matter* **2010,** *22* (48), 485402.

37. Zhao, Y. S.; Zhong, H.; Pei, Q., Fluorescence resonance energy transfer in conjugated polymer composites for radiation detection. *Physical Chemistry Chemical Physics* **2008,** *10* (14), 1848-1851.

38. Cigna, A. A.; Nassisi, D.; Masenga, D.; Raffo, R.; Rotta, P., Dose due to scattered radiation in external radiotherapy: a prostate cancer case history. *Radiation Protection Dosimetry* **2004,** *108* (1), 27-32.

39. Cumberlin, R. L.; Dritschilo, A.; Mossman, K. L., Carcinogenic effects of scattered dose associated with radiation therapy. *International Journal of Radiation Oncology • Biology • Physics 17* (3), 623-629.

40. Bronze-Uhle, E. S.; Batagin-Neto, A.; Fernandes, D. M.; Fratoddi, I.; Russo, M. V.; Graeff, C. F. O., Poly [1,1'-bis(ethynyl)-4,4'-biphenyl(bis-tributylphosphine)Pt(II)] solutions used as low dose ionizing radiation dosimeter. *Applied Physics Letters* **2013,** *102* (24), 2419171-2419174.

41. Batagin-Neto, A.; Bronze-Uhle, E. S.; Fernandes, D. M.; Fratoddi, I.; Venditti, I.; Decker, F.; Bodo, E.; Russo, M. V.; Graeff, C. F. O., Optical Behavior of Conjugated Pt-Containing Polymetallaynes Exposed to Gamma-Ray Radiation Doses. *The Journal of Physical Chemistry B* **2011,** *115* (25), 8047-8053.

42. Fratoddi, I.; Bronze-Uhle, E. S.; Batagin-Neto, A.; Fernandes, D. M.; Bodo, E.; Battocchio, C.; Venditti, I.; Decker, F.; Russo, M. V.; Polzonetti, G.; Graeff, C. F. O., Structural Changes of Conjugated Pt-Containing Polymetallaynes Exposed to Gamma Ray Radiation Doses. *The Journal of Physical Chemistry A* **2012,** *116* (34), 8768-8774.

43. Nikl, M.; Yoshikawa, A., Recent R&D Trends in Inorganic Single-Crystal Scintillator Materials for Radiation Detection. *Advanced Optical Materials* **2015,** *3* (4), 463-481.

44. Weber, M. J., Inorganic scintillators: today and tomorrow. *Journal of Luminescence* **2002,** *100* (1–4), 35-45.

45. Fraboni, B.; Ciavatti, A.; Basirico, L.; Fraleoni-Morgera, A., Organic semiconducting single crystals as solid-state sensors for ionizing radiation. *Faraday Discussions* **2014,** *174* (0), 219-234.

46. Fraboni, B.; Ciavatti, A.; Merlo, F.; Pasquini, L.; Cavallini, A.; Quaranta, A.; Bonfiglio, A.; Fraleoni-Morgera, A., Organic Semiconducting Single Crystals as Next

Generation of Low-Cost, Room-Temperature Electrical X-ray Detectors. *Advanced Materials* **2012,** *24* (17), 2289-2293.

47. Basirico, L.; Ciavatti, A.; Sibilia, M.; Fraleoni-Morgera, A.; Trabattoni, S.; Sassella, A.; Fraboni, B., Solid State Organic X-Ray Detectors Based on Rubrene Single Crystals. *Nuclear Science, IEEE Transactions on* **2015,** *62* (4), 1791-1797.

48. Ciavatti, A.; Capria, E.; Fraleoni-Morgera, A.; Tromba, G.; Dreossi, D.; Sellin, P. J.; Cosseddu, P.; Bonfiglio, A.; Fraboni, B., Toward Low-Voltage and Bendable X-Ray Direct Detectors Based on Organic Semiconducting Single Crystals. *Advanced Materials* **2015,** *27* (44), 7213-7220.

49. Mattoussi, H.; Palui, G.; Na, H. B., Luminescent quantum dots as platforms for probing in vitro and in vivo biological processes. *Advanced Drug Delivery Reviews* **2012,** *64* (2), 138-166.

50. Dai, S.; Saengkerdsub, S.; Im, H. J.; Stephan, A. C.; Mahurin, S. M., Nanocrystal□based Scintillators for Radiation Detection. *AIP Conference Proceedings* **2002,** *632*, 220-224.

51. Withers, N. J.; Sankar, K.; Akins, B. A.; Memon, T. A.; Gu, T.; Gu, J.; Smolyakov, G. A.; Greenberg, M. R.; Boyle, T. J.; Osiński, M., Rapid degradation of CdSe/ZnS colloidal quantum dots exposed to gamma irradiation. *Applied Physics Letters* **2008,** *93* (17), 1731011-173103.

52. Stodilka, R. Z.; Carson, J. J. L.; Yu, K.; Zaman, M. B.; Li, C.; Wilkinson, D., Optical Degradation of CdSe/ZnS Quantum Dots upon Gamma-Ray Irradiation. *The Journal of Physical Chemistry C* **2009,** *113* (6), 2580-2585.

53. Lecavalier, M.-E.; Goulet, M.; Allen, C. N.; Beaulieu, L.; Lariviere, D., Water-dispersable colloidal quantum dots for the detection of ionizing radiation. *Chemical Communications* **2013,** *49* (99), 11629-11631.

54. Noh, M.; Kim, T.; Lee, H.; Kim, C.-K.; Joo, S.-W.; Lee, K., Fluorescence quenching caused by aggregation of water-soluble CdSe quantum dots. *Colloids and Surfaces A: Physicochemical and Engineering Aspects* **2010,** *359* (1–3), 39-44.

55. Guss, P.; Guise, R.; Yuan, D.; Mukhopadhyay, S. In *Preliminary results from an investigation into nanostructured nuclear radiation detectors for non-proliferation applications*, Penetrating Radiation Systems and Applications XIII, SPIE: 2012; pp 85090D-85090D-13.

56. Létant, S. E.; Wang, T. F., Semiconductor Quantum Dot Scintillation under γ-Ray Irradiation. *Nano Letters* **2006,** *6* (12), 2877-2880.

57. Létant, S. E.; Wang, T.-F., Study of porous glass doped with quantum dots or laser dyes under alpha irradiation. *Applied Physics Letters* **2006,** *88* (10), 1031101-1031103.

58. Shani, G., *Radiation Dosimetry Instrumentation and Methods*. Taylor & Francis: 2000.

59. Baharin, R.; Hobson, P. R.; Leslie, D. E.; Smith, D. R. In *Development of an ionising radiation detector based on quantum dots absorbed in porous glass*, Nanotechnology (IEEE-NANO), 2012 12th IEEE Conference on, 20-23 Aug. 2012; 2012; pp 1-5.

60. Baharin, R.; Hobson, P. R.; Leslie, D. E.; Smith, D. R. In *Effect of gamma radiation on potential ionising radiation detectors and dosimeters based on quantum dots*, Nuclear Science Symposium and Medical Imaging Conference (NSS/MIC), 2012 IEEE, Oct. 27 2012-Nov. 3 2012; 2012; pp 3228-3231.

61. Campbell, I. H.; Crone, B. K., Quantum-Dot/Organic Semiconductor Composites for Radiation Detection. *Advanced Materials* **2006,** *18* (1), 77-79.

62. Kang, Z.; Zhang, Y.; Menkara, H.; Wagner, B. K.; Summers, C. J.; Lawrence, W.; Nagarkar, V., CdTe quantum dots and polymer nanocomposites for x-ray scintillation and imaging. *Applied Physics Letters* **2011,** *98* (18), 1819141-1819143.

63. Gaur, G.; Koktysh, D. S.; Fleetwood, D. M.; Weller, R. A.; Reed, R. A.; Rogers, B. R.; Weiss, S. M., Influence of interfacial oxide on the optical properties of single layer CdTe/CdS quantum dots in porous silicon scaffolds. *Applied Physics Letters* **2015,** *107*, 0631061-0631065.

64. Godt, J.; Scheidig, F.; Grosse-Siestrup, C.; Esche, V.; Brandenburg, P.; Reich, A.; Groneberg, D. A., The toxicity of cadmium and resulting hazards for human health. *Journal of Occupational Medicine and Toxicology (London, England)* **2006,** *1*, 22-22.

65. Huang, X.; El-Sayed, M. A., Gold nanoparticles: Optical properties and implementations in cancer diagnosis and photothermal therapy. *Journal of Advanced Research* **2010,** *1* (1), 13-28.

66. Huang, H.-C.; Ramos, J.; Grandhi, T. S. P.; Potta, T.; Rege, K., Gold Nanoparticles in Cancer Imaging and Therapeutics. *Nano LIFE* **2010,** *01* (03n04), 289-307.

67. Huang, H. C.; Barua, S.; Sharma, G.; Dey, S. K.; Rege, K., Inorganic nanoparticles for cancer imaging and therapy. *Journal of controlled release : official journal of the Controlled Release Society* **2011,** *155* (3), 344-57.

68. Dou, Y.; Guo, Y.; Li, X.; Li, X.; Wang, S.; Wang, L.; Lv, G.; Zhang, X.; Wang, H.; Gong, X.; Chang, J., Size-Tuning Ionization To Optimize Gold Nanoparticles for Simultaneous Enhanced CT Imaging and Radiotherapy. *ACS Nano* **2016,** *10* (2), 2536-2548.

69. Tian, F.; Bonnier, F.; Casey, A.; Shanahan, A. E.; Byrne, H. J., Surface enhanced Raman scattering with gold nanoparticles: effect of particle shape. *Analytical Methods* **2014,** *6* (22), 9116-9123.

70. Baffa, O.; Kinoshita, A., Clinical applications of alanine/electron spin resonance dosimetry. *Radiation and Environmental Biophysics* **2014,** *53* (2), 233-240.

71. Razzak, M. T.; Sudiro, S.; Sudradjat, A.; Waskito, A.; Djamili, M. F., Preparation of alanine/esr dosimeter using different binder of polymer blend. *Radiation Physics and Chemistry* **1995,** *46* (4–6, Part 2), 1263-1267.

72. Weil, J. A.; Bolton, J. R., *Electron Paramagnetic Resonance: Elementary Theory and Practical Applications*. Wiley: 2007.

73. Regulla, D. F.; Deffner, U., Dosimetry by ESR spectroscopy of alanine. *The International Journal of Applied Radiation and Isotopes* **1982,** *33* (11), 1101-1114.

74. Marrale, M.; Longo, A.; Spanò, M.; Bartolotta, A.; D'Oca, M. C.; Brai, M., Sensitivity of Alanine Dosimeters with Gadolinium Exposed to 6 MV Photons at Clinical Doses. *Radiation Research* **2011,** *176* (6), 821-826.

75. Guidelli, E. J.; Ramos, A. P.; Zaniquelli, M. E. D.; Nicolucci, P.; Baffa, O., Synthesis and characterization of silver/alanine nanocomposites for radiation detection in medical applications: the influence of particle size on the detection properties. *Nanoscale* **2012,** *4* (9), 2884-2893.

76. Guidelli, E. J.; Ramos, A. P.; Zaniquelli, M. E. D.; Nicolucci, P.; Baffa, O., Synthesis and Characterization of Gold/Alanine Nanocomposites with Potential Properties for Medical Application as Radiation Sensors. *ACS Applied Materials & Interfaces* **2012,** *4* (11), 5844-5851.

77. Xiao-Wu Tang and Yong Yang and Woong Kim and Qian Wang and Pengfei Qi and Hongjie Dai and Lei, X., Measurement of ionizing radiation using carbon nanotube field effect transistor. *Physics in Medicine and Biology* **2005,** *50* (3), N23.

78. Jiazhi, M.; Yeow, J. T. W.; Chow, J. C. L.; Barnett, R. B., A Customized Radiation Sensor for Ionization Collection. *Sensors Journal, IEEE* **2006,** *6* (6), 1523-1530.

79. Ma, J.; Yeow, J. T. W.; Chow, J. C. L.; Barnett, R. B., A carbon fiber-based radiation sensor for dosimetric measurement in radiotherapy. *Carbon* **2008,** *46* (14), 1869-1873.

80. Boul, P. J.; Turner, K.; Li, J.; Pulikkathara, M. X.; Dwivedi, R. C.; Sosa, E. D.; Lu, Y.; Kuznetsov, O. V.; Moloney, P.; Wilkins, R.; O'Rourke, M. J.; Khabashesku, V. N.; Arepalli, S.; Yowell, L., Single Wall Carbon Nanotube Response to Proton Radiation. *The Journal of Physical Chemistry C* **2009,** *113* (32), 14467-14473.

81. Lobez, J. M.; Swager, T. M., Radiation Detection: Resistivity Responses in Functional Poly(Olefin Sulfone)/Carbon Nanotube Composites. *Angewandte Chemie International Edition* **2010,** *49* (1), 95-98.

82. Doty, F. P.; Bauer, C. A.; Skulan, A. J.; Grant, P. G.; Allendorf, M. D., Scintillating Metal-Organic Frameworks: A New Class of Radiation Detection Materials. *Advanced Materials* **2009,** *21* (1), 95-101.

83. Feng, P. L.; Branson, J. V.; Hattar, K.; Vizkelethy, G.; Allendorf, M. D.; Patrick Doty, F., Designing metal-organic frameworks for radiation detection. *Nuclear Instruments and Methods in Physics Research Section A: Accelerators, Spectrometers, Detectors and Associated Equipment* **2011,** *652* (1), 295-298.

84. Wang, C.; Volotskova, O.; Lu, K.; Ahmad, M.; Sun, C.; Xing, L.; Lin, W., Synergistic Assembly of Heavy Metal Clusters and Luminescent Organic Bridging Ligands in Metal–Organic Frameworks for Highly Efficient X-ray Scintillation. *Journal of the American Chemical Society* **2014,** *136* (17), 6171-6174.

85. Jacobs, G. P., A review: Radiation sterilization of pharmaceuticals. *Radiation Physics and Chemistry (1977)* **1985,** *26* (2), 133-142.

86. Kabanov, V. Y., Radiation chemistry of smart polymers (A Review). *High Energy Chemistry* **2000,** *34* (4), 203-211.

87. Saif, S. A.; Simon, D.; Rajesh, J.; Michael, V. W.; Neil, G. B., Advances in radiotherapy. *BMJ* **2012,** *345*.

88. Baldock, C.; Deene, Y. D.; Doran, S.; Ibbott, G.; Jirasek, A.; Lepage, M.; McAuley, K. B.; Oldham, M.; Schreiner, L. J., Polymer gel dosimetry. *Physics in Medicine and Biology* **2010,** *55* (5), R1.

89. Roos, J. M. a. P. A. a. E. G. a. O. M. a. A. M. a. M., Ionization chamber dosimetry of proton beams using cylindrical and plane parallel chambers. N w versus N K ion chamber calibrations. *Physics in Medicine and Biology* **1995,** *40* (7), 1161.

90. Sidney, L. N.; Lynch, D. C.; Willet, P. S., A new radiochromic dosimeter film. *International Journal of Radiation Applications and Instrumentation. Part C. Radiation Physics and Chemistry* **1990,** *35* (4–6), 779-782.

91. Nasr, K. B. M. a. A. T., Fundamentals of gel dosimeters. *Journal of Physics: Conference Series* **2013,** *444* (1), 012001.

92. Huang, T.; Xu, X. H. N., Synthesis and characterization of tunable rainbow colored colloidal silver nanoparticles using single-nanoparticle plasmonic microscopy and spectroscopy. *Journal of Materials Chemistry* **2010,** *20* (44), 9867-9876.

93. Walker, C. R.; Pushpavanam, K.; Nair, D. G.; Potta, T.; Sutiyoso, C.; Kodibagkar, V. D.; Sapareto, S.; Chang, J.; Rege, K., Generation of Polypeptide-

Templated Gold Nanoparticles using Ionizing Radiation. *Langmuir* **2013,** *29* (32), 10166-10173.

94. Hamill, W. H., Model for the radiolysis of water. *The Journal of Physical Chemistry* **1969,** *73* (5), 1341-1347.

95. Daniel, M.-C.; Astruc, D., Gold Nanoparticles: Assembly, Supramolecular Chemistry, Quantum-Size-Related Properties, and Applications toward Biology, Catalysis, and Nanotechnology. *Chemical Reviews* **2003,** *104* (1), 293-346.

96. Huang, H. C.; Koria, P.; Parker, S. M.; Selby, L.; Megeed, Z.; Rege, K., Optically responsive gold nanorod-polypeptide assemblies. *Langmuir : the ACS journal of surfaces and colloids* **2008,** *24* (24), 14139-44.

97. Meyer, D. E.; Chilkoti, A., Genetically Encoded Synthesis of Protein-Based Polymers with Precisely Specified Molecular Weight and Sequence by Recursive Directional Ligation: Examples from the Elastin-like Polypeptide System. *Biomacromolecules* **2002,** *3* (2), 357-367.

98. Huang, H.-C.; Koria, P.; Parker, S. M.; Selby, L.; Megeed, Z.; Rege, K., Optically Responsive Gold Nanorod-Polypeptide Assemblies. *Langmuir* **2008,** *24* (24), 14139-14144.

99. Abedini, A.; Daud, A.; Abdul Hamid, M.; Kamil Othman, N.; Saion, E., A review on radiation-induced nucleation and growth of colloidal metallic nanoparticles. *Nanoscale Research Letters* **2013,** *8* (1), 1-10.

100. Misra, N.; Biswal, J.; Dhamgaye, V. P.; Lodha, G. S.; Sabharwal, S., A Comparative Study Of Gamma, Electron Beam, And Synchrotron X-ray Irradiation Method For Synthesis Of Silver Nanoparticles In PVP. *Advanced Materials Letters* **2013,** *4* (6), 458-463.

101. Huang, H. C.; Yang, Y.; Nanda, A.; Koria, P.; Rege, K., Synergistic administration of photothermal therapy and chemotherapy to cancer cells using polypeptide-based degradable plasmonic matrices. *Nanomedicine (Lond)* **2011,** *6* (3), 459-73.

102. Huang, H.-C.; Walker, C. R.; Nanda, A.; Rege, K., Laser Welding of Ruptured Intestinal Tissue Using Plasmonic Polypeptide Nanocomposite Solders. *ACS Nano* **2013,** *7* (4), 2988-2998.

103. Aqil, A.; Qiu, H.; Greisch, J.-F.; Jérôme, R.; De Pauw, E.; Jérôme, C., Coating of gold nanoparticles by thermosensitive poly(N-isopropylacrylamide) end-capped by biotin. *Polymer* **2008,** *49* (5), 1145-1153.

104. Li, C.; Li, D.; Wan, G.; Xu, J.; Hou, W., Facile synthesis of concentrated gold nanoparticles with low size-distribution in water: temperature and pH controls. *Nanoscale Research Letters* **2011,** *6* (1), 1-10.

105. Gurunathan, S.; Kalishwaralal, K.; Vaidyanathan, R.; Venkataraman, D.; Pandian, S. R. K.; Muniyandi, J.; Hariharan, N.; Eom, S. H., Biosynthesis, purification and characterization of silver nanoparticles using Escherichia coli. *Colloids and Surfaces B: Biointerfaces* **2009,** *74* (1), 328-335.

106. Deepak, V.; Umamaheshwaran, P. S.; Guhan, K.; Nanthini, R. A.; Krithiga, B.; Jaithoon, N. M. H.; Gurunathan, S., Synthesis of gold and silver nanoparticles using purified URAK. *Colloids and Surfaces B: Biointerfaces* **2011,** *86* (2), 353-358.

107. Dykman, L.; Khlebtsov, N., Gold nanoparticles in biomedical applications: recent advances and perspectives. *Chemical Society Reviews* **2012,** *41* (6), 2256-2282.

108. Yu, A. K.; Kudrinskiy, A. A.; Olenin, A. Y.; Lisichkin, G. V., Synthesis and properties of silver nanoparticles: advances and prospects. *Russian Chemical Reviews* **2008,** *77* (3), 233.

109. Boote, B.; Byun, H.; Kim, J.-H., One-pot synthesis of various Ag–Au bimetallic nanoparticles with tunable absorption properties at room temperature. *Gold Bulletin* **2013,** *46* (3), 185-193.

110. Stevenson, A.; Blanco Bea, D.; Civit, S.; Antoranz Contera, S.; Iglesias Cerveto, A.; Trigueros, S., Three strategies to stabilise nearly monodispersed silver nanoparticles in aqueous solution. *Nanoscale Research Letters* **2012,** *7* (1), 151.

111. Belloni, J., Nucleation, growth and properties of nanoclusters studied by radiation chemistry: Application to catalysis. *Catalysis Today* **2006,** *113* (3–4), 141-156.

112. Tan, Y. N.; Lee, J. Y.; Wang, D. I. C., Uncovering the Design Rules for Peptide Synthesis of Metal Nanoparticles. *J. Am. Chem. Soc.* **2010,** *132* (16), 5677-5686.

113. Selvakannan, P. R.; Mandal, S.; Phadtare, S.; Gole, A.; Pasricha, R.; Adyanthaya, S. D.; Sastry, M., Water-dispersible tryptophan-protected gold nanoparticles prepared by the spontaneous reduction of aqueous chloroaurate ions by the amino acid. *Journal of Colloid and Interface Science* **2004,** *269* (1), 97-102.

114. Treguer, M.; de Cointet, C.; Remita, H.; Khatouri, J.; Mostafavi, M.; Amblard, J.; Belloni, J.; de Keyzer, R., Dose Rate Effects on Radiolytic Synthesis of Gold−Silver Bimetallic Clusters in Solution. *The Journal of Physical Chemistry B* **1998,** *102* (22), 4310-4321.

115. Prasanna, A.; Ahmed, M. M.; Mohiuddin, M.; Coleman, C. N., Exploiting sensitization windows of opportunity in hyper and hypo-fractionated radiation therapy. *Journal of Thoracic Disease* **2014,** *6* (4), 287-302.

116. Hall, E. J.; Giaccia, A. J., *Radiobiology for the Radiologist*. Lippincott Williams & Wilkins: 2006.

117. Akimoto, T.; Muramatsu, H.; Takahashi, M.; Saito, J.-i.; Kitamoto, Y.; Harashima, K.; Miyazawa, Y.; Yamada, M.; Ito, K.; Kurokawa, K.; Yamanaka, H.; Nakano, T.; Mitsuhashi, N.; Niibe, H., Rectal bleeding after hypofractionated radiotherapy for prostate cancer: Correlation between clinical and dosimetric parameters and the incidence of grade 2 or worse rectal bleeding. *International Journal of Radiation Oncology*Biology*Physics* **2004,** *60* (4), 1033-1039.

118. Delwiche, F. A., Mapping the literature of radiation therapy. *Journal of the Medical Library Association : JMLA* **2013,** *101* (2), 120-127.

119. Schreiner, L. J., Dosimetry in modern radiation therapy: limitations and needs. *Journal of Physics: Conference Series* **2006,** *56* (1), 1.

120. Engström, P. E.; Haraldsson, P.; Landberg, T.; Sand Hansen, H.; Aage Engelholm, S.; Nyström, H., In vivo dose verification of IMRT treated head and neck cancer patients. *Acta Oncologica* **2005,** *44* (6), 572-578.

121. Kevin, J., Review of recent advances in radiochromic materials for 3D dosimetry. *Journal of Physics: Conference Series* **2010,** *250* (1), 012043.

122. Hsi, W. C.; Fagundes, M.; Zeidan, O.; Hug, E.; Schreuder, N., Image-guided method for TLD-based in vivo rectal dose verification with endorectal balloon in proton therapy for prostate cancer. *Medical Physics* **2013,** *40* (5).

123. Essers, M.; Mijnheer, B., In vivo dosimetry during external photon beam radiotherapy. *International Journal of Radiation Oncology*Biology*Physics* **1999,** *43* (2), 245-259.

124. Beyer, G. P.; Scarantino, C. W.; Prestidge, B. R.; Sadeghi, A. G.; Anscher, M. S.; Miften, M.; Carrea, T. B.; Sims, M.; Black, R. D., Technical Evaluation of Radiation Dose Delivered in Prostate Cancer Patients as Measured by an Implantable MOSFET Dosimeter. *International Journal of Radiation Oncology • Biology • Physics 69* (3), 925-935.

125. Kumar, A. S.; Sharma, S. D.; Ravindran, B. P., Characteristics of mobile MOSFET dosimetry system for megavoltage photon beams. *Journal of Medical Physics* **2014,** *39* (3), 142-149.

126. Ahmed, S. N., *Physics and Engineering of Radiation Detection*. Elsevier Science: 2014.

127. Holmberg, O., Accident prevention in radiotherapy. *Biomedical Imaging and Intervention Journal* **2007,** *3* (2), e27.

128. Williams, M. V., Radiotherapy Near Misses, Incidents and Errors: Radiotherapy Incident at Glasgow. *Clinical Oncology 19* (1), 1-3.

129. Eustis, S.; El-Sayed, M. A., Why gold nanoparticles are more precious than pretty gold: Noble metal surface plasmon resonance and its enhancement of the radiative and nonradiative properties of nanocrystals of different shapes. *Chemical Society Reviews* **2006,** *35* (3), 209-217.

130. Grzelczak, M.; Perez-Juste, J.; Mulvaney, P.; Liz-Marzan, L. M., Shape control in gold nanoparticle synthesis. *Chemical Society Reviews* **2008,** *37* (9), 1783-1791.

131. Urie, R.; Rege, K., Nanoscale inorganic scaffolds as therapeutics and delivery vehicles. *Current Opinion in Chemical Engineering* **2015,** *7*, 120-128.

132. Sau, T. K.; Rogach, A. L., Nonspherical Noble Metal Nanoparticles: Colloid-Chemical Synthesis and Morphology Control. *Advanced Materials* **2010,** *22* (16), 1781-1804.

133. Abedini, A.; Daud, A.; Abdul Hamid, M.; Kamil Othman, N.; Saion, E., A review on radiation-induced nucleation and growth of colloidal metallic nanoparticles. *Nanoscale Research Letters* **2013,** *8* (1), 474.

134. Misra, N.; Biswal, J.; Gupta, A.; Sainis, J. K.; Sabharwal, S., Gamma radiation induced synthesis of gold nanoparticles in aqueous polyvinyl pyrrolidone solution and its application for hydrogen peroxide estimation. *Radiation Physics and Chemistry* **2012,** *81* (2), 195-200.

135. Liu, Y.; Chen, S.; Zhong, L.; Wu, G., Preparation of high-stable silver nanoparticle dispersion by using sodium alginate as a stabilizer under gamma radiation. *Radiation Physics and Chemistry* **2009,** *78* (4), 251-255.

136. Piñeiro, L.; Novo, M.; Al-Soufi, W., Fluorescence emission of pyrene in surfactant solutions. *Advances in Colloid and Interface Science* **2015,** *215* (0), 1-12.

137. Zeng, J.; Ma, Y.; Jeong, U.; Xia, Y., AuI: an alternative and potentially better precursor than AuIII for the synthesis of Au nanostructures. *Journal of Materials Chemistry* **2010,** *20* (12), 2290-2301.

138. Anandhakumar, S.; Rajaram, R.; Mathiyarasu, J., Unusual seedless approach to gold nanoparticle synthesis: application to selective rapid naked eye detection of mercury(ii). *Analyst* **2014,** *139* (13), 3356-3359.

139. Jain, T.; Tehrani-Bagha, A. R.; Shekhar, H.; Crawford, R.; Johnson, E.; Norgaard, K.; Holmberg, K.; Erhart, P.; Moth-Poulsen, K., Anisotropic growth of gold nanoparticles using cationic gemini surfactants: effects of structure variations in head and tail groups. *Journal of Materials Chemistry C* **2014,** *2* (6), 994-1003.

140. Nikoobakht, B.; El-Sayed, M. A., Preparation and Growth Mechanism of Gold Nanorods (NRs) Using Seed-Mediated Growth Method. *Chemistry of Materials* **2003,** *15* (10), 1957-1962.

141. Jana, N. R.; Gearheart, L.; Murphy, C. J., Wet Chemical Synthesis of High Aspect Ratio Cylindrical Gold Nanorods. *The Journal of Physical Chemistry B* **2001,** *105* (19), 4065-4067.

142. Pérez-Juste, J.; Liz-Marzán, L. M.; Carnie, S.; Chan, D. Y. C.; Mulvaney, P., Electric-Field-Directed Growth of Gold Nanorods in Aqueous Surfactant Solutions. *Advanced Functional Materials* **2004,** *14* (6), 571-579.

143. Edgar, J. A.; McDonagh, A. M.; Cortie, M. B., Formation of Gold Nanorods by a Stochastic "Popcorn" Mechanism. *ACS Nano* **2012,** *6* (2), 1116-1125.

144. Fowler, J. F., The radiobiology of prostate cancer including new aspects of fractionated radiotherapy. *Acta Oncologica* **2005,** *44* (3), 265-276.

145. Mata, J.; Varade, D.; Bahadur, P., Aggregation behavior of quaternary salt based cationic surfactants. *Thermochimica Acta* **2005,** *428* (1), 147-155.

146. Cui, X.; Mao, S.; Liu, M.; Yuan, H.; Du, Y., Mechanism of Surfactant Micelle Formation. *Langmuir* **2008,** *24* (19), 10771-10775.

147. Alexiev, A.; Rubio, S.; Deyanova, M.; Stoyanova, A.; Sicilia, D.; Pérez Bendito, D., Improved catalytic photometric determination of iron(III) in cetylpyridinium premicellar aggregates. *Analytica Chimica Acta* **1994,** *295* (1–2), 211-219.

148. Sanguanmith, S.; Meesungnoen, J.; Muroya, Y.; Lin, M.; Katsumura, Y.; Jay-Gerin, J.-P., On the spur lifetime and its temperature dependence in the low linear energy transfer radiolysis of water. *Physical Chemistry Chemical Physics* **2012,** *14* (48), 16731-16736.

149. Vriezema, D. M.; Comellas Aragonès, M.; Elemans, J. A. A. W.; Cornelissen, J. J. L. M.; Rowan, A. E.; Nolte, R. J. M., Self-Assembled Nanoreactors. *Chemical Reviews* **2005,** *105* (4), 1445-1490.

150. Khan, Z.; Singh, T.; Hussain, J. I.; Hashmi, A. A., Au(III)–CTAB reduction by ascorbic acid: Preparation and characterization of gold nanoparticles. *Colloids and Surfaces B: Biointerfaces* **2013,** *104* (0), 11-17.

151. Xu, F.; Zhang, Q.; Gao, Z., Simple one-step synthesis of gold nanoparticles with controlled size using cationic Gemini surfactants as ligands: Effect of the variations in concentrations and tail lengths. *Colloids and Surfaces A: Physicochemical and Engineering Aspects* **2013,** *417* (0), 201-210.

152. del Rio, J. M.; Prieto, G.; Sarmiento, F.; Mosquera, V., Thermodynamics of Micellization of N-Octyltrimethylammonium Bromide in Different Media. *Langmuir* **1995,** *11* (5), 1511-1514.

153. Liz-Marzán, L. M.; Kamat, P. V., *Nanoscale Materials*. Springer US: 2007.

154. Huang, D.; Qi, Y.; Bai, X.; Shi, L.; Jia, H.; Zhang, D.; Zheng, L., One-Pot Synthesis of Dendritic Gold Nanostructures in Aqueous Solutions of Quaternary Ammonium Cationic Surfactants: Effects of the Head Group and Hydrocarbon Chain Length. *ACS Applied Materials & Interfaces* **2012,** *4* (9), 4665-4671.

155. Zhu, C.; Peng, H.-C.; Zeng, J.; Liu, J.; Gu, Z.; Xia, Y., Facile Synthesis of Gold Wavy Nanowires and Investigation of Their Growth Mechanism. *Journal of the American Chemical Society* **2012,** *134* (50), 20234-20237.

156. Smeenk, R. J.; Teh, B. S.; Butler, E. B.; van Lin, E. N. J. T.; Kaanders, J. H. A. M., Is there a role for endorectal balloons in prostate radiotherapy? A systematic review. *Radiotherapy and Oncology* **2010,** *95* (3), 277-282.

157. Ray, P. C.; Yu, H.; Fu, P. P., Toxicity and Environmental Risks of Nanomaterials: Challenges and Future Needs. *Journal of environmental science and health. Part C, Environmental carcinogenesis & ecotoxicology reviews* **2009,** *27* (1), 1-35.

158. Erhola, M.; Toyokuni, S.; Okada, K.; Tanaka, T.; Hiai, H.; Ochi, H.; Uchida, K.; Osawa, T.; Nieminen, M. M.; Alho, H.; Kellokumpu-Lehtinen, P., Biomarker evidence of DNA oxidation in lung cancer patients: association of urinary 8-hydroxy-2′-deoxyguanosine excretion with radiotherapy, chemotherapy, and response to treatment. *FEBS Letters* **1997,** *409* (2), 287-291.

159. Fang-Fang Yin and Mark Oldham and Jing Cai and Qiuwen, W., Dosimetry challenges for implementing emerging technologies. *Journal of Physics: Conference Series* **2010,** *250* (1), 012002.

160. Baldock, C.; De Deene, Y.; Doran, S.; Ibbott, G.; Jirasek, A.; Lepage, M.; McAuley, K. B.; Oldham, M.; Schreiner, L. J., Topical Review: Polymer gel dosimetry. *Physics in medicine and biology* **2010,** *55* (5), R1-R63.

161. Pushpavanam, K.; Narayanan, E.; Rege, K., Molecular and Nanoscale Sensors for Detecting Ionizing Radiation in Radiotherapy. *ChemNanoMat* **2016,** *2* (5), 385-395.

162. Pushpavanam, K.; Narayanan, E.; Chang, J.; Sapareto, S.; Rege, K., A Colorimetric Plasmonic Nanosensor for Dosimetry of Therapeutic Levels of Ionizing Radiation. *ACS Nano* **2015,** *9* (12), 11540-11550.

163. Polte, J.; Erler, R.; Thünemann, A. F.; Sokolov, S.; Ahner, T. T.; Rademann, K.; Emmerling, F.; Kraehnert, R., Nucleation and Growth of Gold Nanoparticles Studied via in situ Small Angle X-ray Scattering at Millisecond Time Resolution. *ACS Nano* **2010,** *4* (2), 1076-1082.

164. Wang, X.; Egan, C. E.; Zhou, M.; Prince, K.; Mitchell, D. R. G.; Caruso, R. A., Effective gel for gold nanoparticle formation, support and metal oxide templating. *Chemical Communications* **2007,** (29), 3060-3062.

165. Marras-Marquez, T.; Peña, J.; Veiga-Ochoa, M. D., Agarose drug delivery systems upgraded by surfactants inclusion: Critical role of the pore architecture. *Carbohydrate Polymers* **2014,** *103*, 359-368.

166. Sakai, S.; Hashimoto, I.; Kawakami, K., Synthesis of an agarose-gelatin conjugate for use as a tissue engineering scaffold. *Journal of Bioscience and Bioengineering* **2007,** *103* (1), 22-26.

167. Torigoe, K.; Esumi, K., Preparation of colloidal gold by photoreduction of tetracyanoaurate(1-)-cationic surfactant complexes. *Langmuir* **1992,** *8* (1), 59-63.

168. Khan, Z.; Singh, T.; Hussain, J. I.; Hashmi, A. A., Au(III)–CTAB reduction by ascorbic acid: Preparation and characterization of gold nanoparticles. *Colloids and Surfaces B: Biointerfaces* **2013,** *104*, 11-17.

169. Tyagi, H.; Kushwaha, A.; Kumar, A.; Aslam, M., PVA Stabilized Gold Nanoparticles Using Ascorbic Acid as A Reducing Agent. *AIP Conference Proceedings* **2011,** *1349* (1), 419-420.

170. Abedini, A.; Daud, A. R.; Abdul Hamid, M. A.; Kamil Othman, N.; Saion, E., A review on radiation-induced nucleation and growth of colloidal metallic nanoparticles. *Nanoscale Research Letters* **2013,** *8* (1), 1-10.

171. Wu, M.-L.; Chen, D.-H.; Huang, T.-C., Synthesis of Au/Pd Bimetallic Nanoparticles in Reverse Micelles. *Langmuir* **2001,** *17* (13), 3877-3883.

172. Cheng, W.; Dong, S.; Wang, E., Synthesis and Self-Assembly of Cetyltrimethylammonium Bromide-Capped Gold Nanoparticles. *Langmuir* **2003,** *19* (22), 9434-9439.

173. Dzaugis, M. E.; Spivack, A. J.; D'Hondt, S., A quantitative model of water radiolysis and chemical production rates near radionuclide-containing solids. *Radiation Physics and Chemistry* **2015,** *115*, 127-134.

174. Ramani, R.; Russell, S.; O'Brien, P., Clinical dosimetry using mosfets. *International Journal of Radiation Oncology*Biology*Physics* **1997,** *37* (4), 959-964.

175. Brans, B.; Bodei, L.; Giammarile, F.; Linden, O.; Luster, M.; Oyen, W. J. G.; Tennvall, J., Clinical radionuclide therapy dosimetry: the quest for the "Holy Gray". *European Journal of Nuclear Medicine and Molecular Imaging* **2007,** *34* (5), 772-786.

176. Bushberg, J. T.; Seibert, J. A.; Leidholdt, E. M.; Boone, J. M., *The Essential Physics of Medical Imaging*. Wolters Kluwer Health: 2011.

177. Alkilany, A. M.; Murphy, C. J., Toxicity and cellular uptake of gold nanoparticles: what we have learned so far? *Journal of Nanoparticle Research* **2010,** *12* (7), 2313-2333.

178. Baumann, M.; Krause, M.; Overgaard, J.; Debus, J.; Bentzen, S. M.; Daartz, J.; Richter, C.; Zips, D.; Bortfeld, T., Radiation oncology in the era of precision medicine. *Nat Rev Cancer* **2016,** *16* (4), 234-49.

179. Wayne, D. N. a. R. Z., The physics of proton therapy. *Physics in Medicine & Biology* **2015,** *60* (8), R155.

180. Wilson, R. R., Radiological use of fast protons. *Radiology* **1946,** *47* (5), 487-91.

181. Bethe, H., Zur Theorie des Durchgangs schneller Korpuskularstrahlen durch Materie. *Annalen der Physik* **1930,** *397* (3), 325-400.

182. Vargas, C. E.; Hartsell, W. F.; Dunn, M.; Keole, S. R.; Doh, L.; Chang, J.; Larson, G. L., Image-guided hypofractionated proton beam therapy for low-risk prostate cancer: Analysis of quality of life and toxicity, PCG GU 002. *Reports of practical oncology and radiotherapy : journal of Greatpoland Cancer Center in Poznan and Polish Society of Radiation Oncology* **2016,** *21* (3), 207-12.

183. Ono, T.; Yabuuchi, T.; Nakamura, T.; Kimura, K.; Azami, Y.; Hirose, K.; Suzuki, M.; Wada, H.; Kikuchi, Y.; Nemoto, K., High Dose Hypofractionated Proton Beam Therapy is a Safe and Feasible Treatment for Central Lung Cancer. *Radiol Oncol* **2017,** *51* (3), 324-330.

184. Hong, T. S.; Wo, J. Y.; Yeap, B. Y.; Ben-Josef, E.; McDonnell, E. I.; Blaszkowsky, L. S.; Kwak, E. L.; Allen, J. N.; Clark, J. W.; Goyal, L.; Murphy, J. E.; Javle, M. M.; Wolfgang, J. A.; Drapek, L. C.; Arellano, R. S.; Mamon, H. J.; Mullen, J. T.; Yoon, S. S.; Tanabe, K. K.; Ferrone, C. R.; Ryan, D. P.; DeLaney, T. F.; Crane, C. H.; Zhu, A. X., Multi-Institutional Phase II Study of High-Dose Hypofractionated Proton Beam Therapy in Patients With Localized, Unresectable Hepatocellular Carcinoma and Intrahepatic Cholangiocarcinoma. *Journal of clinical oncology : official journal of the American Society of Clinical Oncology* **2016,** *34* (5), 460-8.

185. Klein, E. E.; Drzymala, R. E.; Purdy, J. A.; Michalski, J., Errors in radiation oncology: a study in pathways and dosimetric impact. *Journal of applied clinical medical physics* **2005,** *6* (3), 81-94.

186. Low, D. A.; Moran, J. M.; Dempsey, J. F.; Dong, L.; Oldham, M., Dosimetry tools and techniques for IMRT. *Medical physics* **2011,** *38* (3), 1313-38.

187. Niroomand-Rad, A.; Blackwell, C. R.; Coursey, B. M.; Gall, K. P.; Galvin, J. M.; McLaughlin, W. L.; Meigooni, A. S.; Nath, R.; Rodgers, J. E.; Soares, C. G., Radiochromic film dosimetry: recommendations of AAPM Radiation Therapy Committee Task Group 55. American Association of Physicists in Medicine. *Medical physics* **1998,** *25* (11), 2093-115.

188. Daniel, M. C.; Astruc, D., Gold nanoparticles: assembly, supramolecular chemistry, quantum-size-related properties, and applications toward biology, catalysis, and nanotechnology. *Chemical reviews* **2004,** *104* (1), 293-346.

189. Sener, G.; Uzun, L.; Denizli, A., Colorimetric sensor array based on gold nanoparticles and amino acids for identification of toxic metal ions in water. *ACS applied materials & interfaces* **2014,** *6* (21), 18395-400.

190. Nilam, M.; Hennig, A.; Nau, W. M.; Assaf, K. I., Gold nanoparticle aggregation enables colorimetric sensing assays for enzymatic decarboxylation. *Analytical Methods* **2017,** *9* (19), 2784-2787.

191. Krpetic, Z.; Guerrini, L.; Larmour, I. A.; Reglinski, J.; Faulds, K.; Graham, D., Importance of nanoparticle size in colorimetric and SERS-based multimodal trace detection of Ni(II) ions with functional gold nanoparticles. *Small (Weinheim an der Bergstrasse, Germany)* **2012,** *8* (5), 707-14.

192. Karthik Pushpavanam, E. N., and Kaushal Rege, Molecular and Nanoscale Sensors for Detecting Ionizing Radiation in Radiotherapy. *ChemNanoMat* **2016,** *2* (5), 385-395.

193. Pushpavanam, K.; Inamdar, S.; Chang, J.; Bista, T.; Sapareto, S.; Rege, K., Detection of Therapeutic Levels of Ionizing Radiation Using Plasmonic Nanosensor Gels. *Advanced Functional Materials* **2017,** *27* (21), 1606724-n/a.

194. Jana, N. R.; Gearheart, L.; Murphy, C. J., Wet chemical synthesis of high aspect ratio cylindrical gold nanorods. *J Phys Chem B* **2001,** *105* (19), 4065-4067.

195. Pushpavanam, K.; Chang, J.; Sapareto, S.; Rege, K., Polypeptide-Facilitated Formation of Bimetallic Plasmonic Nanoparticles in Presence of Ionizing Radiation. *Nano LIFE* **2017,** *07* (01), 1650006.

196. Paganetti, H., Relative biological effectiveness (RBE) values for proton beam therapy. Variations as a function of biological endpoint, dose, and linear energy transfer - IOPscience. *Physics in Medicine & Biology* **2014,** *59* (22), 419-472.

197. Pimblott, S. M.; LaVerne, J. A., Stochastic simulation of the electron radiolysis of water and aqueous solutions. *J Phys Chem A* **1997,** *101* (33), 5828-5838.

198. Chitose, N.; Katsumura, Y.; Domae, M.; Cai, Z. L.; Muroya, Y.; Murakami, T.; LaVerne, J. A., Radiolysis of aqueous solutions with pulsed ion beams. 4. Product yields for proton beams in solutions of thiocyanate and methyl viologen/formate. *J Phys Chem A* **2001,** *105* (20), 4902-4907.

199. Yen, G. C.; Duh, P. D.; Tsai, H. L., Antioxidant and pro-oxidant properties of ascorbic acid and gallic acid. *Food Chem* **2002,** *79* (3), 307-313.

200. Khan, Z.; Singh, T.; Hussain, J. I.; Hashmi, A. A., Au(III)-CTAB reduction by ascorbic acid: preparation and characterization of gold nanoparticles. *Colloids Surf B Biointerfaces* **2013,** *104* (0), 11-7.

201. Wen, X. L.; Han, Z. X.; Rieker, A.; Liu, Z. L., Significant micellar effect on the oxidative electrochemistry of ascorbic acid. *J Chem Res-S* **1997,** (3), 108-109.

202. Akisada, H.; Kuwahara, J.; Koga, A.; Motoyama, H.; Kaneda, H., Unusual behavior of CMC for binary mixtures of alkyltrimethylammonium bromides: dependence on chain length difference. *J Colloid Interface Sci* **2007,** *315* (2), 678-84.

203. Patterson, L. K.; Gratzel, M., Behavior of Hydrated Electrons in Micellar Solution - Studies with Cetyltrimethylammonium Bromide Cetylpyridinium Chloride Mixed Micelles. *J Phys Chem-Us* **1975,** *79* (10), 956-960.

204. Thanacharoenchumrut, S.; Angboonpong, N.; Pakawatpanurut, P., Cationic cetylpyridinium micelle as a novel electrolyte system for dye-sensitized solar cells. *J Power Sources* **2016,** *307*, 443-448.

205. Szajdzinska-Pietek, E.; Gebicki, J. L.; Kroh, J., Pulse Radiolytic Investigation on Intermicellar Transport of Hydrated Electron in Cationic Micellar Solutions of Alkyltrimethylammonium Halides. *Journal of Colloid and Interface Science* **1995,** *176* (1), 264-266.

206. Buxton, G. V.; Greenstock, C. L.; Helman, W. P.; Ross, A. B., Critical Review of rate constants for reactions of hydrated electrons, hydrogen atoms and hydroxyl radicals (·OH/·O− in Aqueous Solution. *http://dx.doi.org/10.1063/1.555805* **1988,** *17* (2), 513-886.

207. Kuznetsov, V. S.; Usol'tseva, N. V.; Bykova, V. V., Electrostatic interactions in micellar solutions of sodium n-alkyl sulfates and applicability of the poisson-boltzmann equation for their calculation. *J Struct Chem+* **2012,** *53* (1), 82-92.

208. Ray, G. B.; Chakraborty, I.; Ghosh, S.; Moulik, S. P.; Palepu, R., Self-Aggregation of Alkyltrimethylammonium Bromides (C10-, C12-, C14-, and C16TAB) and Their Binary Mixtures in Aqueous Medium: A Critical and Comprehensive Assessment of Interfacial Behavior and Bulk Properties with Reference to Two Types of Micelle Formation. *Langmuir* **2005,** *21* (24), 10958-10967.

209. Ibbott, G. S.; Molineu, A.; Followill, D. S., Independent evaluations of IMRT through the use of an anthropomorphic phantom. *Technology in cancer research & treatment* **2006,** *5* (5), 481-7.

210. Kohno, R.; Hotta, K.; Matsubara, K.; Nishioka, S.; Matsuura, T.; Kawashima, M., In vivo proton dosimetry using a MOSFET detector in an anthropomorphic phantom with tissue inhomogeneity. *Journal of applied clinical medical physics* **2012,** *13* (2), 3699.

211. Nguyen, H. H.; Payré, B.; Fitremann, J.; Viguerie, N. L.-d.; Marty, J.-D., Thermoresponsive Properties of PNIPAM-Based Hydrogels: Effect of Molecular Architecture and Embedded Gold Nanoparticles. *Langmuir* **2015,** *31* (16), 4761-4768.

212. Nakata, K.; Tsuchido, T.; Matsumura, Y., Antimicrobial cationic surfactant, cetyltrimethylammonium bromide, induces superoxide stress in Escherichia coli cells. *J Appl Microbiol* **2011,** *110* (2), 568-79.

213. Barcellos-Hoff, M. H.; Park, C.; Wright, E. G., Radiation and the microenvironment – tumorigenesis and therapy. *Nature Reviews Cancer* **2005,** *5*, 867.

214. Baskar, R.; Lee, K. A.; Yeo, R.; Yeoh, K. W., Cancer and Radiation Therapy: Current Advances and Future Directions. In *Int J Med Sci*, 2012; Vol. 9, pp 193-199.

215. Shirato, H.; Le, Q.-T.; Kobashi, K.; Prayongrat, A.; Takao, S.; Shimizu, S.; Giaccia, A.; Xing, L.; Umegaki, K. J. J. o. r. r., Selection of external beam radiotherapy approaches for precise and accurate cancer treatment. **2018,** *59* (suppl_1), i2-i10.

216. Kry, S. F.; Smith, S. A.; Weathers, R.; Stovall, M., Skin dose during radiotherapy: a summary and general estimation technique. *Journal of Applied Clinical Medical Physics* **2012,** *13* (3), 20-34.

217. Hall, S.; Rudrawar, S.; Zunk, M.; Bernaitis, N.; Arora, D.; McDermott, C. M.; Anoopkumar-Dukie, S., Protection against Radiotherapy-Induced Toxicity. *Antioxidants* **2016,** *5* (3), 22.

218. Allen, C.; Borak, T. B.; Tsujii, H.; Nickoloff, J. A., Heavy Charged Particle Radiobiology: Using Enhanced Biological Effectiveness and Improved Beam Focusing to Advance Cancer Therapy. *Mutation research* **2011,** *711* (1-2), 150-157.

219. Kainz, K. K.; Hogstrom, K. R.; Antolak, J. A.; Almond, P. R.; Bloch, C. D.; Chiu, C.; Fomytskyi, M.; Raischel, F.; Downer, M.; Tajima, T., Dose properties of a laser accelerated electron beam and prospects for clinical application. **2004,** *31* (7), 2053-2067.

220. Jafari, S. M.; Jordan, T. J.; Distefano, G.; Bradley, D. A.; Spyrou, N. M.; Nisbet, A.; Clark, C. H., Feasibility of using glass-bead thermoluminescent dosimeters for radiotherapy treatment plan verification. *The British journal of radiology* **2015,** *88* (1055), 20140804-20140804.

221. Saini, A. S.; Zhu, T. C., Dose rate and SDD dependence of commercially available diode detectors. **2004,** *31* (4), 914-924.

222. Sipilä, P.; Ojala, J.; Kaijaluoto, S.; Jokelainen, I.; Kosunen, A., Gafchromic EBT3 film dosimetry in electron beams — energy dependence and improved film read-out. **2016,** *17* (1), 360-373.

223. Tanooka, M.; Doi, H.; Miura, H.; Inoue, H.; Niwa, Y.; Takada, Y.; Fujiwara, M.; Sakai, T.; Sakamoto, K.; Kamikonya, N.; Hirota, S., Three-dimensional radiochromic film dosimetry for volumetric modulated arc therapy using a spiral water phantom. *Journal of Radiation Research* **2013,** *54* (6), 1153-1159.

224. Pushpavanam, K.; Narayanan, E.; Rege, K., Molecular and Nanoscale Sensors for Detecting Ionizing Radiation in Radiotherapy. **2016,** *2* (5), 385-395.

225. Mahan, M. M.; Doiron, A. L., Gold Nanoparticles as X-Ray, CT, and Multimodal Imaging Contrast Agents: Formulation, Targeting, and Methodology %J Journal of Nanomaterials. **2018,** *2018*, 15.

226. Chandran, P. R.; Thomas, R. T., Chapter 14 - Gold Nanoparticles in Cancer Drug Delivery. In *Nanotechnology Applications for Tissue Engineering*, Thomas, S.; Grohens, Y.; Ninan, N., Eds. William Andrew Publishing: Oxford, 2015; pp 221-237.

227. Huang, H.-C.; Barua, S.; Sharma, G.; Dey, S.; Rege, K., *Inorganic Nanoparticles for Cancer Imaging and Therapy*. 2011; Vol. 155, p 344-57.

228. Daniela, C.; Andreea, C.; Rebecca, P.; Alexandru Mihai, G., Biomedical Applications of Gold Nanoparticles. *Current Topics in Medicinal Chemistry* **2015,** *15* (16), 1605-1613.

229. Inamdar, S.; Pushpavanam, K.; Lentz, J. M.; Bues, M.; Anand, A.; Rege, K., Hydrogel Nanosensors for Colorimetric Detection and Dosimetry in Proton Beam Radiotherapy. *ACS Applied Materials & Interfaces* **2018,** *10* (4), 3274-3281.

230. Pushpavanam, K.; Inamdar, S.; Chang, J.; Bista, T.; Sapareto, S.; Rege, K., Detection of Therapeutic Levels of Ionizing Radiation Using Plasmonic Nanosensor Gels. **2017,** *27* (21), 1606724.

231. Piotrowski, T.; Milecki, P.; Skórska, M.; Fundowicz, D., Total skin electron irradiation techniques: a review. *Advances in Dermatology and Allergology/Postępy Dermatologii I Alergologii* **2013,** *30* (1), 50-55.

232. Licona, I.; Figueroa-Medina, E.; Gamboa-deBuen, I., Dose distributions and percentage depth dose measurements for a total skin electron therapy. *Radiation Measurements* **2017,** *106*, 365-372.

233. Pimblott, S. M.; LaVerne, J. A., Effect of Electron Energy on the Radiation Chemistry of Liquid Water. *Radiation Research* **1998,** *150* (2), 159-169.

234. Nowicka, A. M.; Hasse, U.; Hermes, M.; Scholz, F., Hydroxyl Radicals Attack Metallic Gold. **2010,** *49* (6), 1061-1063.

235. Zarrintaj, P.; Manouchehri, S.; Ahmadi, Z.; Saeb, M. R.; Urbanska, A. M.; Kaplan, D. L.; Mozafari, M., Agarose-based biomaterials for tissue engineering. *Carbohydrate Polymers* **2018,** *187*, 66-84.

236. Pérez-Juste, J.; Liz-Marzán, L. M.; Carnie, S.; Chan, D. Y. C.; Mulvaney, P., Electric-Field-Directed Growth of Gold Nanorods in Aqueous Surfactant Solutions. **2004,** *14* (6), 571-579.

237. Sharma, V. K.; Mitra, S.; Sakai, V. G.; Mukhopadhyay, R., Dynamical Features in Cationic Micelles of Varied Chain Length. *The Journal of Physical Chemistry B* **2012,** *116* (30), 9007-9015.

238. Yeh, Y.-C.; Creran, B.; Rotello, V. M., Gold nanoparticles: preparation, properties, and applications in bionanotechnology. *Nanoscale* **2012,** *4* (6), 1871-1880.

239. Safigholi, H.; Song, W. Y.; Meigooni, A. S., Optimum radiation source for radiation therapy of skin cancer. **2015,** *16* (5), 219-227.

240. Engel, S.; Fritz, E.-C.; Ravoo, B. J., New trends in the functionalization of metallic gold: from organosulfur ligands to N-heterocyclic carbenes. *Chemical Society Reviews* **2017,** *46* (8), 2057-2075.

241. Hall, E. J.; Brenner, D. J., The dose-rate effect revisited: Radiobiological considerations of importance in radiotherapy. *International Journal of Radiation Oncology*Biology*Physics* **1991,** *21* (6), 1403-1414.

242. Zelefsky, M. J.; Deasy, J. O., Improved Long-Term Outcomes With IMRT: Is It Better Technology or Better Physics? *International journal of radiation oncology, biology, physics* **2013,** *87* (5), 867-868.

243. Prasanna, P. G. S.; Stone, H. B.; Wong, R. S.; Capala, J.; Bernhard, E. J.; Vikram, B.; Coleman, C. N., Normal tissue protection for improving radiotherapy: Where are the Gaps? *Translational cancer research* **2012,** *1* (1), 35-48.

244. Huang, G.; Medlam, G.; Lee, J.; Billingsley, S.; Bissonnette, J.-P.; Ringash, J.; Kane, G.; Hodgson, D. C., Error in the delivery of radiation therapy: Results of a quality assurance review. *International Journal of Radiation Oncology*Biology*Physics* **2005,** *61* (5), 1590-1595.

245. Patton, G. A.; Gaffney, D. K.; Moeller, J. H., Facilitation of radiotherapeutic error by computerized record and verify systems. *International Journal of Radiation Oncology • Biology • Physics* **2003,** *56* (1), 50-57.

246. Zygmanski, P.; Abkai, C.; Han, Z.; Shulevich, Y.; Menichelli, D.; Hesser, J., Low-cost flexible thin-film detector for medical dosimetry applications. *Journal of Applied Clinical Medical Physics* **2014,** *15* (2), 311-326.

247. Ravichandran, R.; Binukumar, J. P.; Amri, I. A.; Davis, C. A., Diamond detector in absorbed dose measurements in high-energy linear accelerator photon and electron beams. *Journal of Applied Clinical Medical Physics* **2016,** *17* (2), 291-303.

248. Dreindl, R.; Georg, D.; Stock, M., Radiochromic film dosimetry: Considerations on precision and accuracy for EBT2 and EBT3 type films. *Zeitschrift für Medizinische Physik* **2014,** *24* (2), 153-163.

249. Devic, S.; Tomic, N.; Lewis, D., Reference radiochromic film dosimetry: Review of technical aspects. *Physica Medica* **2016,** *32* (4), 541-556.

250. Lecavalier, M.-E.; Goulet, M.; Allen, C. N.; Beaulieu, L.; Larivière, D., Water-dispersable colloidal quantum dots for the detection of ionizing radiation. *Chemical Communications* **2013,** *49* (99), 11629-11631.

251. Doty, F. P.; Bauer, C. A.; Skulan, A. J.; Grant, P. G.; Allendorf, M. D., Scintillating Metal-Organic Frameworks: A New Class of Radiation Detection Materials. *Advanced Materials* **2008,** *21* (1), 95-101.

252. Abtahi, S. M., Characteristics of a novel polymer gel dosimeter formula for MRI scanning: Dosimetry, toxicity and temporal stability of response. *Physica Medica: European Journal of Medical Physics* **2016,** *32* (9), 1156-1161.

253. Saha, K.; Agasti, S. S.; Kim, C.; Li, X.; Rotello, V. M., Gold Nanoparticles in Chemical and Biological Sensing. *Chemical Reviews* **2012,** *112* (5), 2739-2779.

254. Huang, H.-C.; Barua, S.; Sharma, G.; Dey, S. K.; Rege, K., Inorganic nanoparticles for cancer imaging and therapy. *Journal of Controlled Release* **2011,** *155* (3), 344-357.

255. Urie, R.; Ghosh, D.; Ridha, I.; Rege, K., Inorganic Nanomaterials for Soft Tissue Repair and Regeneration. *Annual Review of Biomedical Engineering* **2018,** *20* (1), 353-374.

256. Pushpavanam, K.; Inamdar, S.; Chang, J.; Bista, T.; Sapareto, S.; Rege, K., Detection of Therapeutic Levels of Ionizing Radiation Using Plasmonic Nanosensor Gels. *Advanced Functional Materials* **2017,** *27* (21), 1606724.

257. Tagiling, N.; Ab Rashid, R.; Azhan, S. N. A.; Dollah, N.; Geso, M.; Rahman, W. N., Effect of scanning parameters on dose-response of radiochromic films irradiated with photon and electron beams. *Heliyon* **2018,** *4* (10), e00864-e00864.

258. Risholm, P.; Balter, J.; Wells, W. M., Estimation of delivered dose in radiotherapy: the influence of registration uncertainty. *Medical image computing and computer-assisted intervention : MICCAI ... International Conference on Medical Image Computing and Computer-Assisted Intervention* **2011,** *14* (Pt 1), 548-555.

259. Spinks, J. W. T.; Woods, R. J., *An Introduction to Radiation Chemistry*. Wiley: 1990.

260. Akisada, H.; Kuwahara, J.; Koga, A.; Motoyama, H.; Kaneda, H., Unusual behavior of CMC for binary mixtures of alkyltrimethylammonium bromides: Dependence on chain length difference. *Journal of Colloid and Interface Science* **2007,** *315* (2), 678-684.

261. Takenaka, Y.; Kawabata, Y.; Kitahata, H.; Yoshida, M.; Matsuzawa, Y.; Ohzono, T., Effects of surfactant concentration on formation of high-aspect-ratio gold nanorods. *Journal of Colloid and Interface Science* **2013,** *407*, 265-272.

262. Polte, J., Fundamental growth principles of colloidal metal nanoparticles – a new perspective. *CrystEngComm* **2015,** *17* (36), 6809-6830.

263. Pernodet, N.; Maaloum, M.; Tinland, B., Pore size of agarose gels by atomic force microscopy. *ELECTROPHORESIS* **1997,** *18* (1), 55-58.

264. Morris, T.; Copeland, H.; Szulczewski, G., Synthesis and Characterization of Gold Sulfide Nanoparticles. *Langmuir* **2002,** *18* (2), 535-539.

265. Bearden, J. A., X-Ray Wavelengths. *Reviews of Modern Physics* **1967,** *39* (1), 78-124.

266. Nealon, G. L.; Donnio, B.; Greget, R.; Kappler, J.-P.; Terazzi, E.; Gallani, J.-L., Magnetism in gold nanoparticles. *Nanoscale* **2012,** *4* (17), 5244-5258.

267. Charles, P. H.; Cranmer-Sargison, G.; Thwaites, D. I.; Crowe, S. B.; Kairn, T.; Knight, R. T.; Kenny, J.; Langton, C. M.; Trapp, J. V., A practical and theoretical definition of very small field size for radiotherapy output factor measurements. *Medical Physics* **2014,** *41* (4), 041707.

268. Pignol, J.-P.; Keller, B. M.; Ravi, A., Doses to internal organs for various breast radiation techniques--implications on the risk of secondary cancers and cardiomyopathy. *Radiation oncology (London, England)* **2011,** *6*, 5-5.

269. Shymko, R. M.; Hauser, D. L.; Archambeau, J. O., Field size dependence of radiation sensitivity and dose fractionation response in skin. *International Journal of Radiation Oncology*Biology*Physics* **1985,** *11* (6), 1143-1148.

270. Jang, W. H.; Shim, S.; Wang, T.; Yoon, Y.; Jang, W.-S.; Myung, J. K.; Park, S.; Kim, K. H., In vivo characterization of early-stage radiation skin injury in a mouse model by two-photon microscopy. *Scientific Reports* **2016,** *6*, 19216.

271. Padilla, L.; Lee, C.; Milner, R.; Shahlaee, A.; Bolch, W. E., Canine Anatomic Phantom for Preclinical Dosimetry in Internal Emitter Therapy. *Journal of Nuclear Medicine* **2008**.

272. Siegel, R. L.; Miller, K. D.; Jemal, A., Cancer statistics, 2018. *CA Cancer J. Clin.* **2018,** *68* (1), 7-30.

273. Patel, N. M., The Next Hurdle for Personalized Medicine—Radiation Therapy. *Clin. Chem.* **2017,** *63* (3), 791.

274. Tomas Kron and Joerg Lehmann and Peter, B. G., Dosimetry of ionising radiation in modern radiation oncology. *Phys. Med. Biol.* **2016,** *61* (14), R167.

275. Huang, K.; Bice, W. S.; Hidalgo-Salvatierra, O., Characterization of an in vivo diode dosimetry system for clinical use. *J. Appl. Clin. Med. Phys.* **2003,** *4* (2), 132-142.

276. Zhang, W.; Zhang, H.; Feng, Y.; Zhong, X., Scalable Single-Step Noninjection Synthesis of High-Quality Core/Shell Quantum Dots with Emission Tunable from Violet to Near Infrared. *ACS Nano* **2012,** *6* (12), 11066-11073.

277. Zeininger, L.; He, M.; Hobson, S. T.; Swager, T. M., Resistive and Capacitive γ-Ray Dosimeters Based On Triggered Depolymerization in Carbon Nanotube Composites. *ACS Sensors* **2018,** *3* (5), 976-983.

278. Ruyra, À.; Yazdi, A.; Espín, J.; Carné-Sánchez, A.; Roher, N.; Lorenzo, J.; Imaz, I.; Maspoch, D., Synthesis, Culture Medium Stability, and In Vitro and In Vivo Zebrafish Embryo Toxicity of Metal–Organic Framework Nanoparticles. *Chemistry – A European Journal* **2014,** *21* (6), 2508-2518.

279. Nałęcz-Jawecki, G.; Grabińska-Sota, E.; Narkiewicz, P., The toxicity of cationic surfactants in four bioassays. *Ecotoxicol. Environ. Saf.* **2003,** *54* (1), 87-91.

280. Si, S.; Mandal, T. K., Tryptophan-Based Peptides to Synthesize Gold and Silver Nanoparticles: A Mechanistic and Kinetic Study. *Chemistry – A European Journal* **2007,** *13* (11), 3160-3168.

281. Đurović, M. D.; Bugarčić, Ž. D.; Heinemann, F. W.; van Eldik, R., Substitution versus redox reactions of gold(iii) complexes with l-cysteine, l-methionine and glutathione. *Dalton Transactions* **2014,** *43* (10), 3911-3921.

282. Cuadrado, J. A.; Zhang, W.; Hang, W.; Majidi, V., Speciation of gold(III)–L-histidine complex: a multi-instrumental approach. *J. Environ. Monit.* **2000,** *2* (4), 355-359.

283. Skowronek, J., Brachytherapy in the treatment of skin cancer: an overview. *Postepy dermatologii i alergologii* **2015,** *32* (5), 362-367.

284. Carey, B.; Swift, S., The current role of imaging for prostate brachytherapy. *Cancer imaging : the official publication of the International Cancer Imaging Society* **2007,** *7* (1), 27-33.

285. Tanderup, K.; Beddar, S.; Andersen, C. E.; Kertzscher, G.; Cygler, J. E., In vivo dosimetry in brachytherapy. *Medical Physics* **2013,** *40* (7), 070902.

286. Granero, D.; Candela-Juan, C.; Ballester, F.; Ouhib, Z.; Vijande, J.; Richart, J.; Perez-Calatayud, J., Commissioning and quality assurance procedures for the HDR Valencia skin applicators. *Journal of contemporary brachytherapy* **2016,** *8* (5), 441-447.

287. Watanabe, Y.; Warmington, L.; Gopishankar, N., Three-dimensional radiation dosimetry using polymer gel and solid radiochromic polymer: From basics to clinical applications. *World journal of radiology* **2017,** *9* (3), 112-125.

288. Low, D., The importance of 3D dosimetry. *Journal of Physics: Conference Series* **2015,** *573*, 012009.

289. Yin, F.-F.; Oldham, M.; Cai, J.; Wu, Q., Dosimetry challenges for implementing emerging technologies. *Journal of physics. Conference series* **2010,** *250* (1), 8-11.

290. Schreiner, L. J., Review of Fricke gel dosimeters. *Journal of Physics: Conference Series* **2004,** *3*, 9-21.

291. Baldock, C.; De Deene, Y.; Doran, S.; Ibbott, G.; Jirasek, A.; Lepage, M.; McAuley, K. B.; Oldham, M.; Schreiner, L. J., Polymer gel dosimetry. *Physics in medicine and biology* **2010,** *55* (5), R1-R63.

292. Adamovics, J.; Maryanski, M. J., A new approach to radiochromic three-dimensional dosimetry-polyurethane. *Journal of Physics: Conference Series* **2004,** *3*, 172-175.

293. Alqathami, M.; Adamovics, J.; Benning, R.; Blencowe, A., An investigation into ultra-sensitive substituted leucomalachite dye derivatives for use in the PRESAGE®dosimeter. *Journal of Physics: Conference Series* **2013,** *444*, 012034.